CHEMICAL REVIEWS

Review

Cite This: Chem. Rev. XXXX, XXX, XXX−XXX

pubs.acs.org/CR

Approaching Practically Accessible Solid-State Batteries: Stability Issues Related to Solid Electrolytes and Interfaces

Rusong Chen,[†,‡,§] Qinghao Li,[†,§] Xiqian Yu,*[,†,‡] Liquan Chen, and Hong Li*[,†,‡]

[†]Beijing Advanced Innovation Center for Materials Genome Engineering, Key Laboratory for Renewable Energy, Beijing Key Laboratory for New Energy Materials and Devices, Institute of Physics, Chinese Academy of Sciences, Beijing 100190, China

[‡]Center of Materials Science and Optoelectronics Engineering, University of Chinese Academy of Sciences, Beijing 100049, China

ABSTRACT: Solid-state batteries have been attracting wide attention for next generation energy storage devices due to the probability to realize higher energy density and superior safety performance compared with the state-of-the-art lithium ion batteries. However, there are still intimidating challenges for developing low cost and industrially scalable solid-state batteries with high energy density and stable cycling life for large-scale energy storage and electric vehicle applications. This review presents an overview on the scientific challenges, fundamental mechanisms, and design strategies for solid-state batteries, specifically focusing on the stability issues of solid-state electrolytes and the associated interfaces with both cathode and anode electrodes. First, we give a brief overview on the history of solid-state battery technologies, followed by introduction and discussion on different types of solid-state electrolytes. Then, the associated stability issues, from phenomena to fundamental understandings, are intensively discussed, including chemical, electrochemical, mechanical, and thermal stability issues; effective optimization strategies are also summarized. State-of-the-art characterization techniques and *in situ* and *operando* measurement methods deployed and developed to study the aforementioned issues are summarized as well. Following the obtained insights, perspectives are given in the end on how to design practically accessible solid-state batteries in the future.

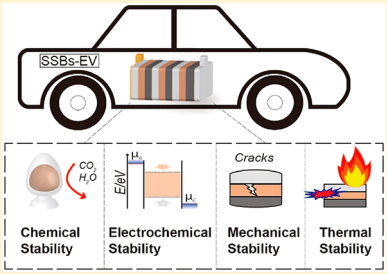

CONTENTS

1. Introduction C
2. Solid-State Battery Technologies C
2.1. Brief Overview of Solid-State Batteries and the Research History C
2.2. State-of-the-Art Solid-State Batteries D
2.3. Solid-State Batteries and Classifications E
2.4. Grand Challenges in Solid-State Batteries F
3. Categorizing and Comparing Various Solid-State Electrolytes F
3.1. Solid Polymer Electrolytes F
3.1.1. PEO Based Solid Polymer Electrolytes F
3.1.2. Other Polymer-Based Electrolytes I
3.1.3. Solid Polymer Composite Electrolytes I
3.2. Inorganic Solid-State Electrolytes I
3.2.1. Oxide Based Solid-State Electrolytes J
3.2.2. Sulfide Based Solid-State Electrolytes K
3.3. Other Types of Solid-State Electrolytes K
3.3.1. Anti-perovskite-type Li_3OX K
3.3.2. LiPON L
4. Stability Issues in Solid-State Batteries L
4.1. Chemical Stability L
4.1.1. Chemical Stability of Solid-State Electrolyte Materials M
4.1.2. Chemical Stability of Solid-State Electrolyte/Electrode Interfaces P
4.2. Electrochemical Stability V
4.2.1. Electrochemical Stability of Solid-State Electrolytes V
4.2.2. Electrochemical Stability at Electrolyte/Electrode Interfaces W
4.2.3. Approaches to Extend the Chemical and Electrochemical Interfacial Stability: Building Interphase AA
4.3. Mechanical Stability AD
4.3.1. Mechanical Properties of Solid-State Electrolytes AD
4.3.2. Mechanical Stability of Solid-State Batteries AF
4.3.3. Approaches to Realize Mechanically Favorable Solid-State Batteries AG
4.4. Thermal Stability AI
4.4.1. Thermal Stability of Materials in Solid-State Batteries AI
4.4.2. Thermal Stability of Interfaces in Solid-State Batteries AJ
5. Characterizations and Novel Methodologies Related to Solid-State Battery AL
5.1. Characterization of the Intrinsic Properties of Solid-State Electrolytes AL
5.2. Characterization of Interfaces between Electrodes and Solid-State Electrolytes AM
6. Conclusions and Perspectives AP

Special Issue: Beyond Li Battery Chemistry

Received: April 30, 2019

Downloaded via INST OF PHYSICS on April 11, 2020 at 08:01:22 (UTC).
See https://pubs.acs.org/sharingguidelines for options on how to legitimately share published articles.

ACS Publications © XXXX American Chemical Society

DOI: 10.1021/acs.chemrev.9b00268
Chem. Rev. XXXX, XXX, XXX−XXX

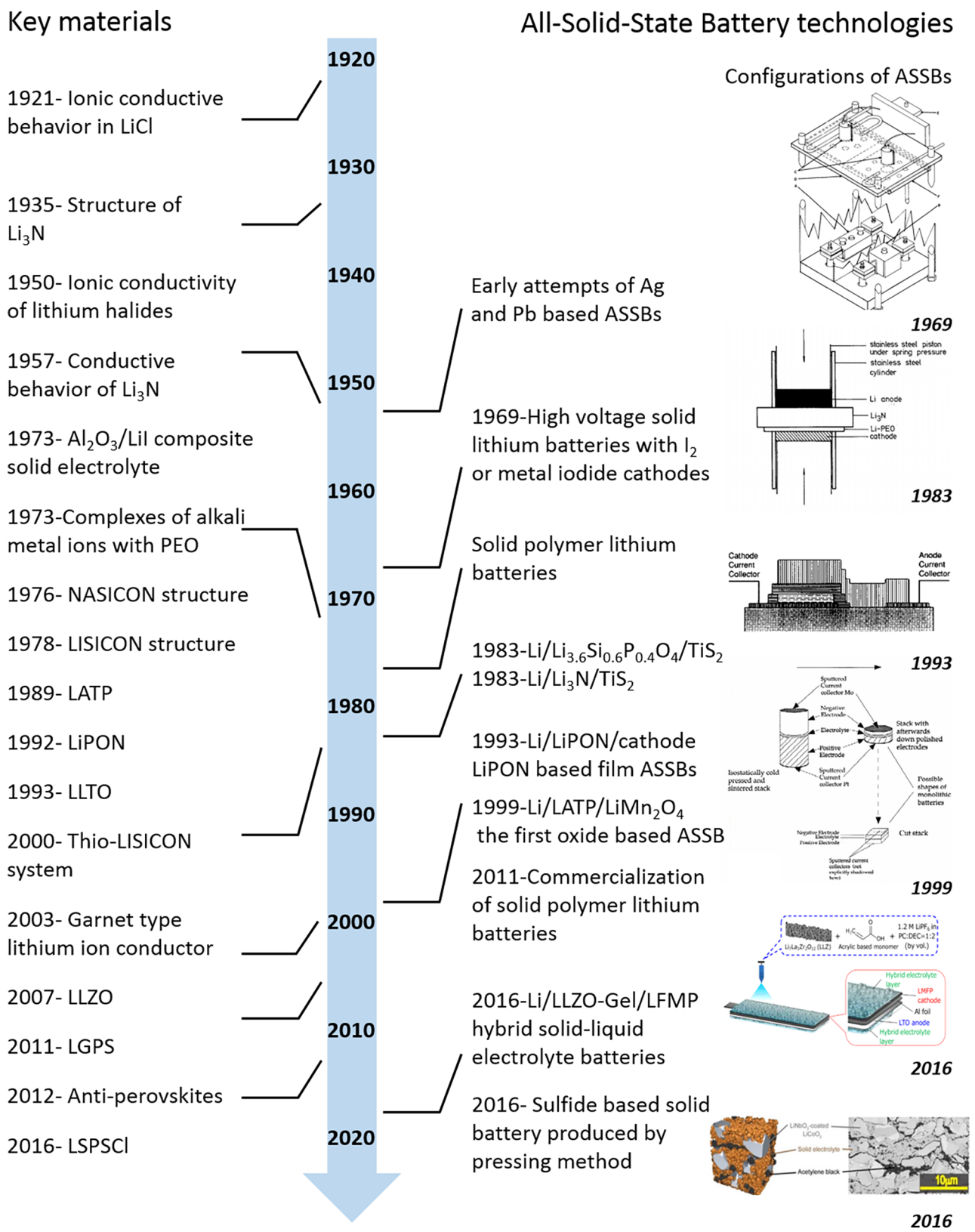

Figure 1. Development history of key materials and technologies of ASSBs. The milestones of progress are based on refs 8−39. Images from top to bottom: Reprinted with permission from ref 33. Copyright 1969 The Electrochemical Society. Reprinted from ref 48, Copyright 1983, with permission from Elsevier. Reprinted from ref 53, Copyright 1993, with permission from Elsevier. Reprinted from ref 36, Copyright 1999, with permission from Elsevier. Reprinted from ref 37, Copyright 2016, with permission from Elsevier. Reprinted from ref 30, Copyright 2016, with permission from Nature Publishing Group.

DOI: 10.1021/acs.chemrev.9b00268
Chem. Rev. XXXX, XXX, XXX−XXX

6.1. Scientific and Fundamental Investigations for Superior SSB Systems AQ
6.1.1. Ionic Conduction Mechanism AQ
6.1.2. Multiscale and Multidimensional Characterizations and Simulations AQ
6.1.3. High Throughput Technologies and Big Data Mining AQ
6.1.4. Novel Battery Chemistries AR
6.2. Engineering and Technical Challenges for Practical SSBs AR
6.2.1. Low-Cost and Large-Scale Production of Key Materials AR
6.2.2. Technical Challenges with Li Metal Anodes AR
6.2.3. Interface Engineering and *in Situ* Solidification AR
6.2.4. Novel Battery Design AR
Author Information AS
Corresponding Authors AS
ORCID AS
Author Contributions AS
Notes AS
Biographies AS
Acknowledgments AS
List of Abbreviations AS
References AT

1. INTRODUCTION

High energy density and high safety batteries are urgently needed with the rapid growth of electric vehicles and grid energy storage demands.[1,2] Conventional lithium ion batteries (LIBs) exploit flammable liquid electrolytes and carbon anodes, suffering from insufficient energy density and potential safety risks.[3] To achieve higher energy density, lithium metal is urged as a potential anode material due to its high specific capacity (~3800 mAh/g). However, uncontrollable lithium dendrite growth and infinite volume expansion during cycling lead to poor electrochemical performance and severe safety challenges.[4,5] Thanks to the high mechanical strength and inflammable nature of solid-state electrolytes, solid-state batteries (SSBs) are expected to completely address the safety and dendrite issues of conventional lithium metal-based batteries with carbonate electrolyte.[6,7] In this regard, all solid-state batteries (ASSBs) are promising to achieve safe and high energy density characteristics.

2. SOLID-STATE BATTERY TECHNOLOGIES

2.1. Brief Overview of Solid-State Batteries and the Research History

The development of SSBs is accompanied by the discovery of solid ionic conductors (Figure 1). The first reported ionic conductor can be traced back to 1833, when Michael Faraday first reported the ionic conducting phenomenon in Ag_2S and proposed the famous "Faraday's law".[40] While SSBs were absent until the 1950s, the research about silver salt based cells (e.g., $Pb/PbCl_2/AgCl/Ag$[41] and $Ag/AgI/I_2$[42]) can be regarded as the very beginning of SSBs. However, SSBs in this period exhibited poor performance with low voltages (<1 V) and low discharge currents.[43] In the subsequent years, lithium metal-based batteries with LiI as electrolyte were introduced in the 1970s, with the discoveries of lithium ion conductivity in lithium halides.[8,10,44] The first patent, submitted by Rao[31] in 1969, disclosed a $Li/LiI/I_2$ solid-state cell with a film LiI SSE, which delivered high open-circuit voltage about 3 V. Later on, Liang and his co-workers proposed the Li/LiI/MI (M = heavy metal, e.g., Ag, Cu, Pb) solid-state cells to address the iodine vapor diffusion issues of I_2 cathodes.[32,33,45] The performance of the Li/LiI/MI cells can be further improved with the addition of Al_2O_3 in the LiI electrolyte.[11] The as-proposed LiI based solid-state lithium batteries delivered high energy density of around 100−200 Wh/kg and were practical as power sources in some electronic devices.[46] However, such SSBs suffer from increasing polarization with continuous LiI formation at the electrode/electrolyte interface, which makes the cell unrechargeable.[43,47]

With the discovery and development of lithium insertion type cathode materials in the late 1970s, rechargeable SSBs were introduced. In 1983, Knutz and Skaarup reported a $Li/Li_3N/TiS_2$ SSB that can cycle more than 200 times.[48] In the same year, researchers at Hitachi, Ltd., prepared a rechargeable solid lithium cell with a configuration of $Li/Li_{3.6}Si_{0.6}P_{0.4}O_4/TiS_2$. The cell exploited a RF-sputtered amorphous film as electrolyte and can deliver a long cycle life of about 2000 times.[35] In 1973, the alkali ion conducting behavior in poly(ethylene oxide) (PEO) was reported by Fenton et al.,[49] and this material obtained applications as SSEs in lithium batteries after Armand et al. suggested this possibility in 1978.[19] Investigations about solid polymer lithium batteries then became the research focus. SSEs with new polymer matrices and lithium salts and their compatibility with various cathodes were reported in subsequent studies.[50,51] Following these pioneering works, solid polymer lithium batteries were successfully commercialized in the Bolloré Group's "Autolib project",[52] which made solid polymer lithium batteries the first commercialized SSBs for electric vehicles (EVs).

During the 1980s and 1990s, high lithium ion conducting compounds with high ionic conductivity attracted increasing research attention for their potential applications in energy storage and conversion devices. A number of solid ionic conductors were reported in this period. In 1976, the Na superionic conductor (NASICON)[12] structure was first designed by Goodenough et al., and its lithium counterpart, $Li_{1.3}Al_{0.3}Ti_{1.7}(PO_4)_3$, with high conductivity was reported by Aono et al. in 1989.[21,22] In 1993, Inaguma et al. reported high bulk conductivity of 10^{-3} S/cm in perovskite $Li_{0.34}La_{0.51}TiO_{2.94}$.[24] Another important oxide SSE, garnet-type material, was first utilized as ionic conductor in 2003 and become famous after the report of fast ionic conductivity of $Li_7La_3Zr_5O_{12}$ in 2007.[27] Generally speaking, oxide-type electrolytes exhibit high ionic conductivity and high mechanical strength. The first oxide based SSB was reported in 1999 by Birke et al.[36] A solid-state cell with a configuration of $Li_4Ti_5O_{12}/Li_{1.3}Al_{0.3}Ti_{1.7}(PO_4)_3/LiMn_2O_4$ was constructed, and 15 wt % $0.44LiBO_2 \cdot 0.56LiF$ was introduced in the cosintering process to obtain intimate contact between electrode and electrolyte. The as-constructed cell delivered small capacity loss after 10 cycles. During this period, LiPON, prepared by RF sputtering of Li_3PO_4 in N_2,[23] was reported, demonstrating high compatibility with both lithium anode and high voltage cathode over the long-term cycling process.[53] Another type of high ionic conductivity materials, sulfide-type SSEs, were brought up in 1980s and showed high lithium ion conductivity because of the weak lithium−sulfur bonding.[54] During the rapid development and commercial success of LIBs based on

DOI: 10.1021/acs.chemrev.9b00268
Chem. Rev. XXXX, XXX, XXX−XXX

Table 1. Performance of Reported SSBs with SSEs[a]

year	initial capacity (mAh/g)	cycle performance	conductivity (S/cm)	battery configuration	classification	ref
2013	100	65% retention after 100 cycles at 0.1 C and 60 °C	5×10^{-4}	$C/75Li_2S{\cdot}25P_2S_5/LiCoO_2$	all solid-state battery	Ohtomo et al.[55]
2014	78	*b*	3.5×10^{-4}	$Li/Li_{6.8}La_{2.95}Ca_{0.05}Zr_{1.75}Nb_{0.25}O_{12}/LiCoO_2$	all solid-state battery	Ohta et al.[56]
2015	144	~84% retention after 30 cycles at 0.1 C and 30 °C	$\sim 10^{-3}$	$In-Li/Li_3PS_4$ + ionic liquids/ $LiFePO_4$	hybrid solid liquid electrolyte battery	Oh et al.[57]
2016	132	99% retention after 150 cycles at 25 °C	4×10^{-4}	$Li/Li_7La_3Zr_2O_{12}$ + ionic liquids/ $LiCoO_2$	hybrid solid liquid electrolyte battery	Kim et al.[58]
2016	*b*	81% retention after 200 cycles at 2 C and 60 °C	5.97×10^{-3}	$Li_4Ti_5O_{12}/Li_7La_3Zr_2O_{12}$ + gel electrolyte/$LiMn_{0.8}Fe_{0.2}PO_4$	hybrid solid liquid electrolyte battery	Yoshima et al.[37]
2016	120	87.5% retention after 640 cycles at 0.6 C and 65 °C	1×10^{-4} (65 °C)	Li/polymer/ceramic/polymer/ $LiFePO_4$	all solid-state battery	Zhou et al.[59]
2016	80	71.2% retention after 10 cycles, 7.3 mA/g at 25 °C	*b*	$Li-In/Li_{10}GeP_2S_{12}/LiNi_{0.5}M_{1.5}O_4$	all solid-state battery	Oh et al.[60]
2017	124	80% retention after 100 cycles at 0.1 C and RT	5×10^{-3}	$Li-In/Li_{10}GeP_2S_{12}/LiCoO_2-Li_2S-P_2S_5$ composite	all solid-state battery	Zhang et al.[61]
2018	106	63% retention after 40 cycles at 0.05 C and 100 °C	1.4×10^{-3}	$Li/Li_7La_3Zr_2O_{12}/Li_7La_3Zr_2O_{12}-Li_{2.3}C_{0.7}B_{0.3}O_3-LiCoO_2$	all solid-state battery	Han et al.[62]

[a]The capacity represents the first discharge capacity of the battery, and the conductivity value is the lithium ion conductivity of the employed SSE at room temperature, if not specified. [b]Not given.

carbonate liquid electrolyte since the 1990s, investigations of SSBs slowed down until the demands for higher energy density and superior safety recalled ASSBs. It should be mentioned that, in 2011, a sulfide SSE with a composition of $Li_{10}GeP_2S_{12}$ was found with even higher conductivity than conventional liquid electrolytes.[28] The lithium ion conductivity of this material was the highest among all SSEs at that time, until this record was broken by the same group in 2016.[30] The high conductivity of this type of SSE showed potential for applications in SSBs, and stable cycling with large currents was achieved in SSBs based on this material.

As can be concluded, SSBs were proposed even earlier than LIBs with liquid electrolyte; however, the unsatisfactory performance of SSBs, together with the successful commercialization of LIBs based on nonaqueous electrolytes, made them less considered for practical applications during the past 20-year "golden age" of LIB development.

2.2. State-of-the-Art Solid-State Batteries

Due to the relative low energy density and safety concerns from flammable electrolytes, conventional LIBs reached a bottleneck period of development. As a result, SSBs were recalled as promising candidates, and inspiring achievements have been made in the last years. Recent advances in SSBs are summarized in Table 1. It can be learned that SSBs with addition of small amounts of liquid electrolytes or polymer electrolytes at the electrolyte/electrode interface demonstrate significantly higher reversible capacity and better cycle durability. However, such batteries with both liquid and solid-state electrolytes are not well-defined. In some papers, the terms "quasi-solid", "hybrid solid", or "solid" batteries were utilized to describe SSBs with a small amount of liquid electrolyte. As drops of liquid electrolyte will make a big difference in battery performance, controversies may arise with such descriptions. Therefore, we classify batteries according to whether they contain liquid or not, to avoid confusion in the following discussions (Figure 2):

(1) Liquid electrolyte battery. Conventional LIBs containing electrodes, separator, and liquid electrolytes, such as nonaqueous and aqueous electrolytes. For gel LIBs, gel polymer is added to liquid electrolyte to enhance the mechanical strength, while the ion transport occurs only in liquid phases. Since there are no SSEs in gel electrolyte batteries, they could also be categorized as a liquid electrolyte battery.

(2) Hybrid solid/liquid electrolyte battery. Batteries containing both liquid and solid-state electrolytes. Usually, the liquid phase is added on the cathode side to obtain sufficient contact between cathode particles and the SSE. In some studies, the term "quasi-solid electrolyte" or "solid battery" is used to describe the electrolyte consisting of solid-state electrolytes with a few drops of liquid electrolytes. To make it clear, here the term "hybrid solid/liquid electrolyte battery" is suggested to

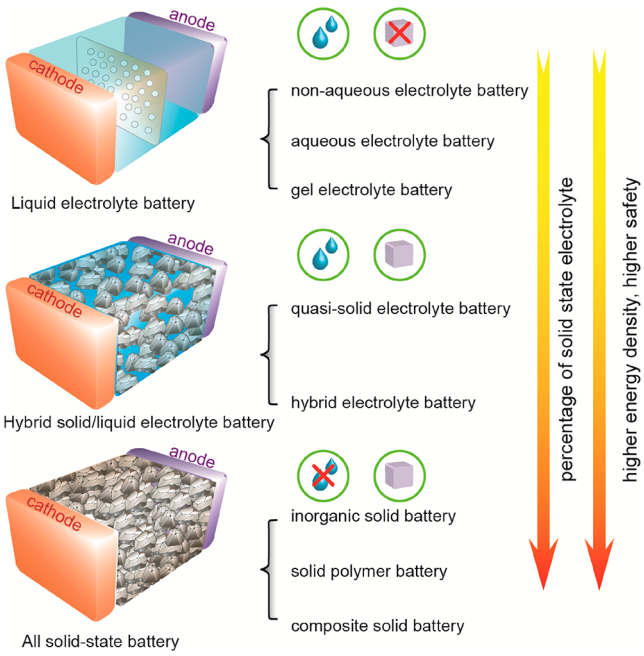

Figure 2. Schematic illustration of the classifications of prevailing lithium ion batteries. Three types of batteries can be classified based on the amount of liquid and percentage of SSE in the assembled batteries.

DOI: 10.1021/acs.chemrev.9b00268
Chem. Rev. XXXX, XXX, XXX−XXX

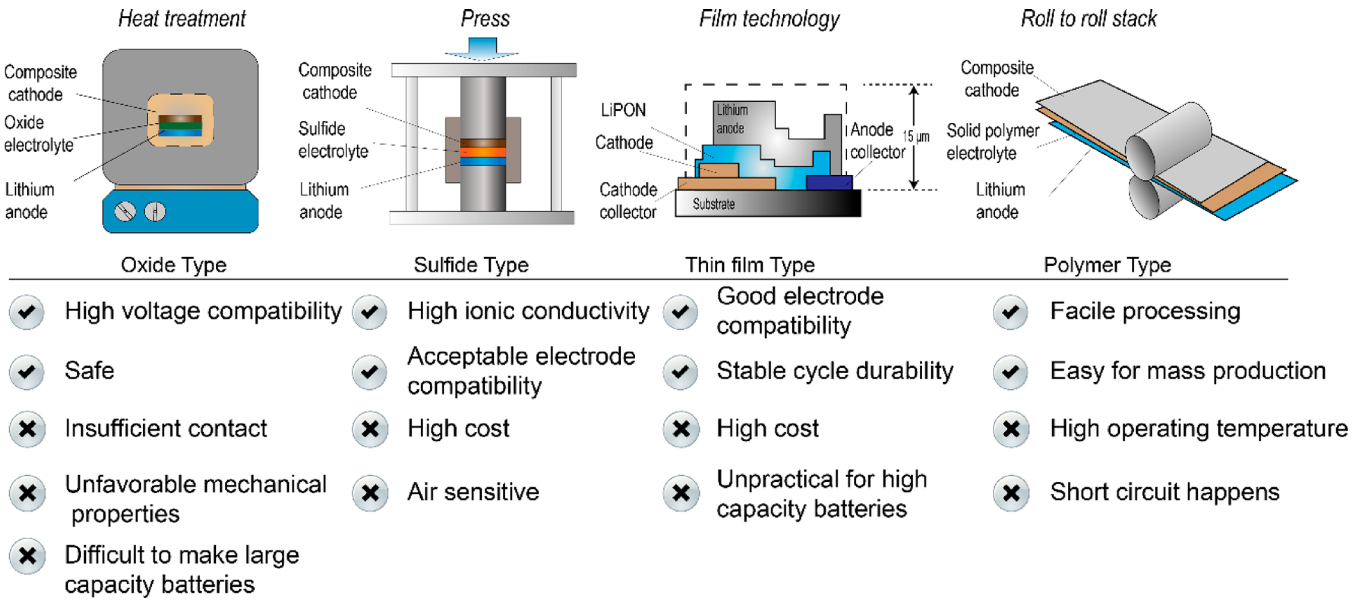

Figure 3. Different types of ASSBs and their basic configuration characteristics. The advantages (√) and disadvantages (×) of each type of SSB are listed below.

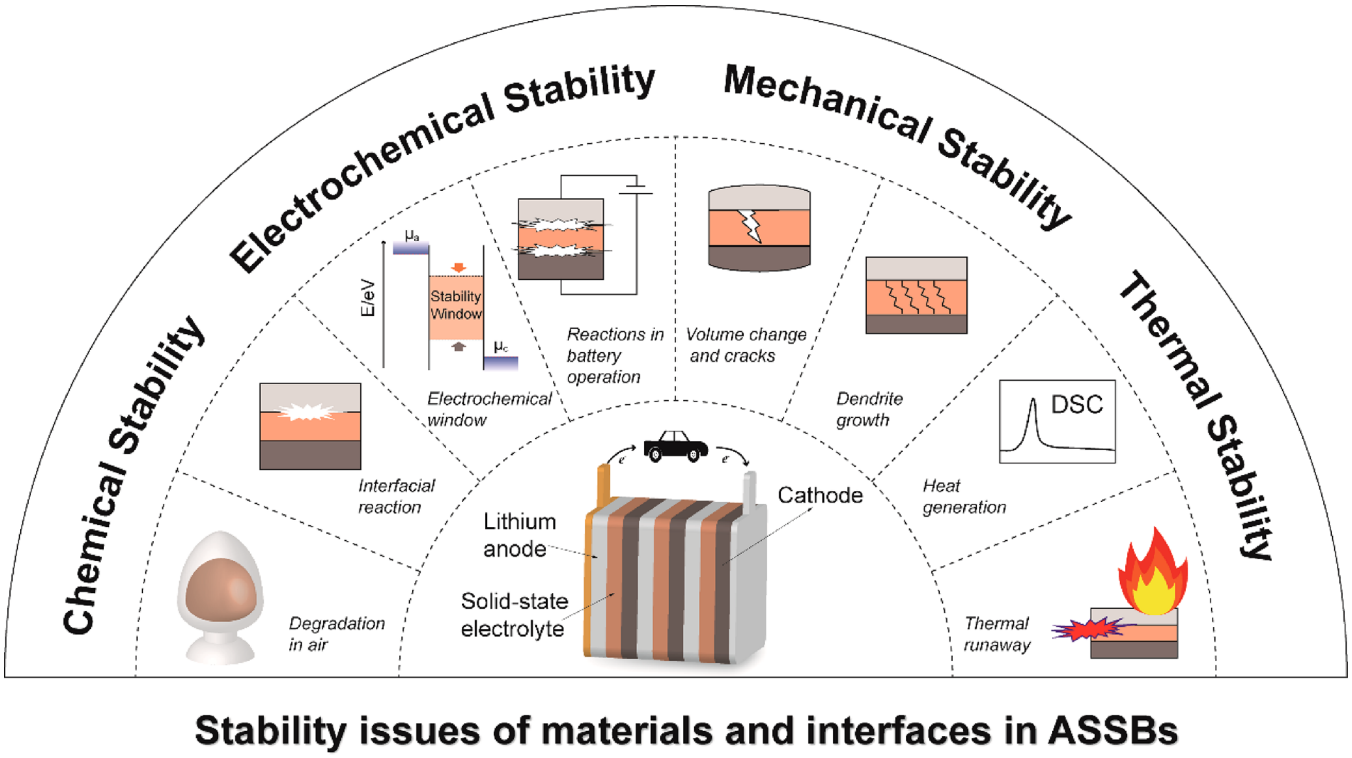

Figure 4. Schematic illustration of stability issues in ASSBs.

represent batteries that contain both SSEs and liquid electrolytes.

(3) All solid-state battery. No liquid phase is present in this type of battery; the cathodes usually composite with the SSEs to provide ionic transport channels, for instance, inorganic ASSBs, polymer solid batteries, composite polymer/ceramic ASSBs, etc. ASSBs are considered as promising candidates compatible with lithium metal anodes.

2.3. Solid-State Batteries and Classifications

Based on battery configurations and the types of SSEs being used, ASSBs can be categorized into four types, as shown in Figure 3.

Thin film-type SSBs with LiPON as SSE demonstrate long cycle life and good compatibility with both lithium metal anodes and high voltage cathodes, which have been commercialized for years. However, this type of battery is difficult to fabricate into large capacity batteries, which limits its applications in large scale energy storage areas. Bulk-type

DOI: 10.1021/acs.chemrev.9b00268
Chem. Rev. XXXX, XXX, XXX−XXX

ASSBs display similar geometry as liquid electrolyte based LIBs and are expected to replace conventional LIBs in electric vehicles and grid energy storage. Based on the applied SSEs, bulk-type ASSBs can be divided into different categories including polymer-based ASSBs, oxide electrolyte based ASSBs, and sulfide electrolyte based ASSBs. The advantages and disadvantages of each type of ASSB are summarized in Figure 3. To note, pretreatments are mostly required in fabrications of inorganic ASSBs. Generally, heat treatments and cold-press are adopted on oxide and sulfide electrolyte based ASSBs, respectively.

2.4. Grand Challenges in Solid-State Batteries

In spite of the incomparable advantages in battery performance of LIBs, there is still a long way to go for practical applications of ASSBs. Intensive studies have been carried out to explore the underlying mechanisms and possible solutions to the above issues. The sluggish ionic transport in SSEs was believed to be the main limitation in early studies. However, it was found later on that ASSBs still exhibited inferior performance even when highly conductive SSEs were employed. Therefore, issues beyond conductive limit obtained increasing research attention. Challenges including continuous interfacial side reactions, limited electrochemical window, contact issues, side reactions in moisture, and cracks or pulverization issues, were then proposed that should be conquered for achieving better performance. For better understanding of challenges in ASSBs, we categorize these challenges into different aspects of stability issues, as shown in Figure 4.

Battery stability can be defined as the ability to retain or recover back to the original structure, composition, and morphology of battery components under external variations. To be specific, the stability issues of materials and interfaces in ASSBs can be divided into four aspects based on different types of variations.

(1) *Chemical Stability*. Chemical stability can be regarded as the ability of the materials and interfaces to remain unchanged during storage and the fabrication process, which occurs even before battery charge/discharge. For materials with poor chemical stability, reactions in ambient air may lead to poor battery performance or safety concerns. Applications of electrolytes in which electrode/electrolyte interfaces are chemically unstable may be limited for high energy density ASSBs. Hence, chemical stability of materials and interfaces determines the production conditions and battery configurations.

(2) *Electrochemical Stability*. Electrochemical stability is utilized to describe the changes of materials and interfaces during the charge/discharge process. Although the electrochemical stability window of SSEs is expected to be wide enough, recent investigations reported the decomposition of SSEs and formation of inactive interfaces under high voltage.[63] Therefore, the stability of materials and interfaces in SSBs deserves a careful revisit in spite of the prevailing understandings.

(3) *Mechanical Stability*. Mechanical stability indicates the ability to remain unchanged in variations of external or internal stress. The stress may be induced by the inevitable volume change in the composite electrode or the electrode/electrolyte interface. The intimate contact of electrode and SSEs is practically a prerequisite to obtain good electrochemical performance. However, dendrite growth, cracks, or pulverization have been reported in SSBs during cycling. These findings indicate non-negligible mechanical instability concerns in ASSBs.[64]

(4) *Thermal Stability*. Thermal stability implies resistance against decomposition or reactions under high temperature. In conventional LIBs, thermal stability of battery components determines the safety of the batteries. In ASSBs, thermal stability of materials and interfaces had been less studied, as the SSEs were believed to be nonflammable and ASSBs were believed to be free from safety risks. However, thermal runaway, heat generation, and gas release have been reported recently. These results demonstrate that thermal stability of materials and interfaces in ASSBs are actually essential to realize practical ASSBs, which is in contrast to the intuitive thoughts.

Therefore, in this review, a framework based on stability issues is established for a comprehensive overview of grand challenges in ASSBs. To be specific, different types of SSEs will be summarized in section 3, the stability issues of materials and interfaces, from phenomenal to fundamental understandings, will be intensively discussed in section 4. State-of-the-art measurement methods and *in situ* characterizations will be illustrated in section 5, and the conclusion and outlook will be given in the last section (section 6). Even though the discussions in this review are based on ASSBs, the fundamental scientific viewpoints and framework can be inspirational for or even applicable to comprehensive understanding of other types of solid-state batteries (SSBs).

3. CATEGORIZING AND COMPARING VARIOUS SOLID-STATE ELECTROLYTES

Solid-state electrolytes are the key components to realize SSBs, and a proper SSE should satisfy several critical criteria. High lithium ion conductivity, low electronic conductivity, and good chemical and electrochemical stability against pairing electrodes will be beneficial to battery performance. In view of practical applications, low cost and environmentally benign materials are favorable for the commercial promotion of SSBs.

Up to now, various types of SSEs have been investigated (Table 2). Among them, solid polymer and solid inorganic electrolytes are two most important series, while solid inorganic electrolytes can be further divided into oxide and sulfide subseries. In addition, other SSEs such as LiPON are developed for specific applications. The properties of each type of SSEs are listed and compared in the following paragraphs.

3.1. Solid Polymer Electrolytes

Solid polymer electrolytes can overcome the problems of liquid electrolyte leakage and flammability in conventional LIBs. Compared with inorganic SSEs, polymer electrolytes demonstrate decent interface contact, good electrochemical stability, easy fabrication, and economic availability. Due to these advantages, solid polymer electrolytes have attracted wide research attention.

3.1.1. PEO Based Solid Polymer Electrolytes. The most representative solid polymer electrolyte is the PEO based system. PEO is a good lithium ion conductor when composited with lithium salts.[65] The chemical structure of PEO is H-(O-CH_2-CH_2)$_n$-OH, and it normally exhibits molecular weight around 20000 g/mol. PEO can be prepared by ring-opening polymerization of ethylene oxide and demonstrates modest lithium ion conductivity of $\sim 10^{-5}$ S/cm at 40−60 °C.

DOI: 10.1021/acs.chemrev.9b00268
Chem. Rev. XXXX, XXX, XXX−XXX

Table 2. Summary of the Basic Properties of Solid-State Electrolytes[a]

classification	material		symmetry	σ_{Li} (s/cm)	T_{mea}[b]	E_a[c] (eV)	synthesis	T_{synt}[d]	ref
				Solid Polymer Electrolyte					
PEO based series and derivatives	PEO−LiFSI		e	1.30×10^{-3}	80 °C	e	solution casting	50 °C	Zhang et al.[68]
	PEO−LiTFSI		e	1.00×10^{-3}	80 °C	e	solution casting	50 °C	Zhang et al.[68]
	PEO−LiDFOB		e	3.18×10^{-5}	RT	0.46	solution casting	50 °C	Polu et al.[69]
	PEO−LiBNFSI		e	2.20×10^{-4}	60 °C	e	solvent cast	RT	Karuppasamy et al.[70]
	PEO−LiTNFSI		e	3.69×10^{-4}	90 °C	e	solution casting	RT	Ma et al.[71]
	PEO−PVP−$LiNO_3$		e	1.13×10^{-3}	RT	0.14	solvent cast	60 °C	B et al.[72]
other organic polymers	PAN−PEO−$LiClO_4$		e	6.79×10^{-4}	RT	e	solution casting	60 °C	Yuan et al.[75]
	PMMA−PVA−$LiBF_4$		e	1.29×10^{-3}	RT	e	solvent-casting	80−100 °C	Rajendran et al.[76]
	PVDF−PEO−$LiClO_4$		e	2.62×10^{-5}	RT	0.55	solvent-casting	70 °C	Jacob et al.[77]
	PAN−$LiClO_4$−Al_2O_3		e	5.70×10^{-4}	RT	0.17	solvent casting	e	Chen-Yang et al.[73]
	PAN−$LiClO_4$−Al_2O_3		e	1.40×10^{-4}	RT	0.17	solvent casting	e	Chen-Yang et al.[73]
	PAN−PVC−EC−$LiClO_4$		e	7.57×10^{-5}	RT	e	solution casting	60 °C	Rajendran et al.[74]
	PAN−PVC−EC−$LiClO_4$−TiO_2		e	4.46×10^{-3}	RT	e	solution casting	60 °C	Rajendran et al.[74]
	poly(alkoxythiophenes)−PEO−PEG		e	7.00×10^{-4}	RT	e	wet chemistry	e	Aldissi[128]
composite electrolyte	PEO−$LiClO_4$ + LATP		e	1.71×10^{-4}	RT	0.03	solution casting	50 °C	Wang et al.[129]
	PEO−LiTF−LGPS		e	1.21×10^{-3}	80 °C	0.36	solution-casting	50 °C	Zhao et al.[130]
	PEO−$LiClO_4$−LAGP		e	1.0×10^{-5}	RT	e	solution casting	80 °C	Jung et al.[131]
	PEO−$LiClO_4$−Al_2O_3		e	7.2×10^{-7}	RT	e	solution casting	80 °C	Jung et al.[131]
	PEO−PVDF−$BaTiO_3$		e	1.2×10^{-4}	RT	e	solution casting	RT	Lee et al.[132]
	PEO−$LiClO_4$−MU−SiO_2		e	1.20×10^{-3}	60 °C	e	hydrolysis reaction	60 °C	Lin et al.[133]
	PEO−$LiClO_4$−$BaTiO_3$		e	1.20×10^{-3}	70 °C	e	solvent casting	RT	Sun et al.[134]
				Inorganic Solid-State Electrolyte					
oxide	perovskite	$Li_{0.34}La_{0.51}TiO_{2.94}$	cubic	7.00×10^{-5}	RT	0.36	solid sintering	800/1150 °C	Itoh et al.[135]
		$Li_{0.34}La_{0.51}TiO_{2.94}$	cubic	1.00×10^{-3}	RT	0.40	solid sintering	800/1150 °C	Inaguma et al.[82]
		$Li_{0.35}La_{0.55}TiO_{3.00}$	cubic	1.00×10^{-3}	RT	0.34	solid sintering	800/1200 °C	Inaguma et al.[136]
		$Li_{0.34}Pr_{0.56}TiO_{3.01}$	orthorhombic	1.00×10^{-6}	RT	0.47	solid sintering	800/1150 °C	Itoh et al.[135]
		$Li_{0.34}Nd_{0.55}TiO_{3.00}$	orthorhombic	8.00×10^{-8}	RT	0.53	solid sintering	800/1150 °C	Itoh et al.[135]
		$Li_{0.38}La_{0.56}Ti_{0.99}Al_{0.01}O_3$	tetragonal	3.17×10^{-4}	RT	0.36	citrate gel-sintering	750/1350 °C	Le et al.[137]
		$Li_{0.06}La_{0.66}Ti_{0.93}Al_{0.06}O_3$	cubic	1.68×10^{-6}	RT	0.36	ground-calcination	1100 °C	Morata-Orrantia et al.[138]
		$Li_{0.25}La_{0.66}Ti_{0.75}Al_{0.25}O_3$	cubic	7.66×10^{-5}	RT	0.35	ground-calcination	1100 °C	Morata-Orrantia et al.[138]
		$Li_{0.475}La_{0.475}Sr_{0.05}TiO_3$	cubic	1.50×10^{-3}	RT	e	solid sintering	800/1200 °C	Inaguma et al.[136]
	NASICON	$LiTi_2(PO_4)_3$	rhombohedral	2.00×10^{-6}	RT	≈0.47	solid sintering	1200 °C	Martínez-Juárez et al.[139] and Fan et al.[140]
		$LiZr_2(PO_4)_3$	rhombohedral	3.80×10^{-5}	RT	0.28	solid sintering	900/1000 °C	Fan et al.[140] and Li et al.[141]
		$LiHf_2(PO_4)_3$	rhombohedral	1.29×10^{-5}	RT	0.33	solid sintering	1000−1200 °C	Martínez-Juárez et al.[139] and Bachman et al.[142]
		$LiTi_2(PO_4)_3$	rhombohedral	3.83×10^{-7}	RT	0.47	solid sintering	1000−1200 °C	Martínez-Juárez et al.[139] and Bachman et al.[142]
		$LiGeTi(PO_4)_3$	rhombohedral	3.48×10^{-8}	RT	0.56	solid sintering	1000−1200 °C	Martínez-Juárez et al.[139] and Bachman et al.[142]
		$LiGe_2(PO_4)_3$	rhombohedral	6.62×10^{-9}	RT	0.60	solid sintering	1000−1200 °C	Martínez-Juárez et al.[139] and Bachman et al.[142]
		$Li_{1.2}Al_{0.2}Ti_{1.8}(PO_4)_3$	rhombohedral	5.00×10^{-3}	RT	0.29	solid sintering	950 °C	Fan et al.[140] and Arbi et al.[143]

DOI: 10.1021/acs.chemrev.9b00268
Chem. Rev. XXXX, XXX, XXX−XXX

Table 2. continued

classification		material	symmetry	σ_{Li} (s/cm)	T_{mea}[b]	E_a[c] (eV)	synthesis	T_{synt}[d]	ref
				Inorganic Solid-State Electrolyte					
		$Li_{1.3}Al_{0.3}Ti_{1.7}(PO_4)_3$	rhombohedral	3.00×10^{-3}	RT	0.35	solid sintering	980/1000 °C	Aono et al.[93]
		$Li_{1.5}Al_{0.5}Ge_{1.5}(PO_4)_3$	e	4.0×10^{-4}	RT	0.37	melt-quenching	300/1450 °C	Fu[99]
		$Li_{1.4}Al_{0.4}Ti_{1.6}(PO_4)_3$	e	2.09×10^{-3}	RT	0.29	sol−gel/calcination	950 °C	Xu et al.[144]
	LISICON	$Li_{2+2x}Zn_{1-x}GeO_4$	tetragonal	3.90×10^{-7}	RT	e	solid sintering	1000/1100 °C	Bruce and West[102]
		$Li_{3.5}Si_{0.5}P_{0.5}O_4$	orthorhombic	3.00×10^{-6}	RT	0.13	solid-state reaction	800 °C	Hu et al.[103]
		$Li_{4-2x}Co_xGeO_4$	orthorhombic	8.40×10^{-6}	RT	0.71	solid-state reaction	700/1000 °C	Sumathipala et al.[101]
		$Li_{3+x}Cr_{1-x}Ge_xO_4$	orthorhombic	1.40×10^{-5}	RT	0.51	ground-sintering	500/800 °C	Dissanayake et al.[100]
		$Li_4GeO_4-Li_3AsO_4$	tetragonal	$3-4 \times 10^{-5}$	RT	~0.45	solid sintering	700/800 °C	Rodger et al.[104]
		$Li_4TiO_4-Li_3VO_4$	tetragonal	$3-4 \times 10^{-5}$	RT	~0.42	solid sintering	700/800 °C	Rodger et al.[104]
		$Li_{3.5}Si_{0.5}P_{0.5}O_4$	tetrahedral	1.31×10^{-7}	RT	0.49	solid-state reaction	900 °C	Bachman et al.[142] and Deng et al.[145]
		$Li_4(Ge, Ti)O_4-Li_3(As, V)O_4$	tetragonal	$3-4 \times 10^{-5}$	RT	~0.50	solid sintering	700/800 °C	Rodger et al.[104]
	garnet	$Li_3Nd_3Te_2O_{12}$	cubic	1.00×10^{-5}	RT	1.22	ground-sintering	700/850 °C	O'Callaghan et al.[106]
		$Li_5La_3Ta_2O_{12}$	cubic	1.54×10^{-6}	RT	0.57	sol−gel/calcination	300/900 °C	Gao et al.[107]
		$Li_6BaLa_2Ta_2O_{12}$	cubic	4.00×10^{-5}	RT	0.40	solids state reaction	700/900 °C	Thangadurai and Weppner[109]
		$Li_6SrLa_2Ta_2O_{12}$	cubic	7.00×10^{-6}	RT	0.50	solids state reaction	700/900 °C	Thangadurai and Weppner[109]
		$Li_7La_3Zr_2O_{12}$	cubic	2.44×10^{-4}	RT	0.31	solid-state reaction	1230 °C	Murugan et al.[110]
		$Li_7La_3Nb_2O_{12}$	cubic	1.00×10^{-5}	RT	0.43	sol−gel/calcination	700−1000 °C	Fan et al.[140] and Peng et al.[108]
		$Li_7La_3Zr_2O_{12}$	tetrahedral	2.0×10^{-6}	RT	0.49	solid sintering	1130 °C	Buschmann et al.[111]
		$Li_7La_3Zr_2O_{12}$ + 0.9% Al	cubic	3.5×10^{-4}	RT	0.34	solid sintering	1130 °C	Buschmann et al.[111]
sulfide	thio-LISICON	Li_2GeS_3	orthorhombic	9.7×10^{-9}	125 °C	e	solid sintering	600−800 °C	Kanno et al.[26]
		Li_4GeS_4	orthorhombic	2.00×10^{-7}	RT	e	solid sintering	600−800 °C	Kanno et al.[26]
		Li_5GaS_4	orthorhombic	5.10×10^{-8}	100 °C	~0.33	solid sintering	600−800 °C	Kanno et al.[26]
		$Li_{3.25}Ge_{0.25}P_{0.75}S_4$	tetragonal	2.20×10^{-3}	RT	0.21	solid sintering	700 °C	Kanno and Murayama[117]
		$Li_{10}GeP_2S_{12}$	tetragonal	1.20×10^{-2}	RT	0.25	solid sintering	550 °C	Kamaya et al.[28]
		$Li_{3.4}Si_{0.4}P_{0.6}S_4$	tetragonal	6.40×10^{-4}	RT	0.29	solid sintering	700 °C	Murayama et al.[146]
		$Li_{4.8}Si_{0.2}Al_{0.8}S_4$	tetragonal	2.3×10^{-7}	RT	0.52	solid sintering	700 °C	Murayama et al.[146]
		$Li_{3.4}Si_{0.4}P_{0.6}S_4$	tetrahedral	6.40×10^{-4}	RT	0.28	solid sintering	700 °C	Fan et al.[140] and Murayama et al.[146]
		Li_2ZnGeS_4	orthorhombic	1.40×10^{-9}	50 °C	e	solid sintering	600−800 °C	Kanno et al.[26]
		$Li_{4-2x}Zn_xGeS_4$	orthorhombic	3.00×10^{-7}	RT	~0.54	solid sintering	600−800 °C	Kanno et al.[26]
		$Li_2S-GeS_2-Ga_2S_3$ system	orthorhombic	6.50×10^{-5}	RT	e	solid sintering	600−800 °C	Kanno et al.[26]
	$Li_2S-M_xS_y$	β-Li_3PS_4	e	1.60×10^{-4}	RT	0.36	coprecipitation-heating	200 °C	Liu et al.[147]
		$0.7Li_2S-0.3P_2S_5$	e	1.7×10^{-2}	RT	0.18	rapid-quenching	700 °C	Seino et al.[148]
		$0.6Li_2S-0.4SiS_2$	e	$1-5 \times 10^{-4}$	RT	0.32	solid sintering	700−900 °C	Pradel and Ribes[149] and Lau et al.[150]
		$0.7Li_2S-0.3P_2S_5$	e	3.2×10^{-3}	RT	0.12	milling-sintering	360 °C	Tatsumisago and Hayashi[151]
		$0.75Li_2S-0.25P_2S_5$	e	3×10^{-4}	RT	e	milling-sintering	200 °C	Sakuda et al.[152]
		$0.3LiCl-0.35Li_2S-0.35SiS_2$	e	2.33×10^{-4}	RT	0.35	milling-sintering	950 °C	Kennedy et al.[153]
		$0.05Li_4SiO_4-0.57Li_2S-0.38SiS_2$	e	2×10^{-3}	RT	0.37	melt-quenching	1000 °C	Hirai et al.[154]
		$0.01Li_3PO_3-0.63Li_2S-0.36SiS_2$	e	1.6×10^{-3}	RT	0.30	melt-quenching	950 °C	Aotani et al.[155]

DOI: 10.1021/acs.chemrev.9b00268
Chem. Rev. XXXX, XXX, XXX−XXX

Table 2. continued

classification	material	symmetry	σ_{Li} (s/cm)	T_{mea} [b]	E_a [c] (eV)	synthesis	T_{synt} [d]	ref
			Other					
anti-perovskite	Li_3OCl	cubic	8.50×10^{-4}	RT	0.26	paste-heating	330−360 °C	Zhao and Daemen[29]
	$Li_3OCl_{0.5}Br_{0.5}$	cubic	1.94×10^{-3}	RT	0.18	paste-heating	330−360 °C	Zhao and Daemen[29]
	$Li_{2.99}Ba_{0.005}ClO$	e	2.5×10^{-2}	RT	<0.6	paste-heating	220−240 °C	Braga et al.[122]
	$A_{2.99}Ba_{0.005}OCl_{1-x}(OH)_x$ (A = Li/Na)	cubic	$>10^{-2}$	RT	<0.1	paste-heating	220−240 °C	Fan et al.[140] and Braga et al.[156]
LiPON	LiPON	e	6.40×10^{-6}	RT	0.47	RF sputtering	50 °C	Suzuki et al.[157]
	LiPON	e	2.30×10^{-6}	RT	0.55	RF sputtering	e	Yu et al.[158]
	$Li_{3.3}PO_{3.9}N_{0.17}$	e	2.00×10^{-6}	RT	~0.65	RF sputtering	e	Bates et al.[23,126]
	$Li_{3\pm x}PO_{4\pm y}N_z$	e	2.00×10^{-6}	RT	0.62	RF sputtering	600 °C	Birke et al.[159]

[a]The lithium transference number for most inorganic SSEs is ~1; for solid polymer electrolyte, it is ~0.1−0.4.[68,70−73,130,134] [b]T_{mea}, measurement temperature. [c]E_a, activation energy of ionic conduction. [d]T_{synt}, synthesis temperature. [e]Not given.

The lithium ion conductivity in PEO originates from the specific molecular structure, where EO units exhibit high donor number for lithium and PEO exhibits high chain flexibility. In PEO matrix, Li^+ is coordinated by oxygen on PEO segmental chains. With the breaking and forming of Li−O bonds and continuous segmental rearrangement, long-range lithium transport can be realized.[66] Note that PEO is found to be a semicrystalline polymer and only amorphous regions favor lithium transport from active chain segments. The glass transition temperature of PEO is around 60 °C, beyond which the amorphous phase may overwhelm the crystallized phase. Therefore, PEO demonstrates only modest lithium ion conductivity at room temperature but much enhanced lithium ion conductivity at elevated temperature.[67]

To further improve the room temperature lithium ion conductivity, numerous trials have been carried out. Increasing carrier density and mitigating PEO crystallization are two major research directions. In past decades, researchers have utilized diverse lithium salts for lower dissociation energy.[68−72] Branch and graft chains have also been introduced to lower the glass transition temperature. Block, graft, or hyperbranched polymer hosts have been further designed to increase the mechanical strength and lithium ion conductivity.

3.1.2. Other Polymer-Based Electrolytes. In addition to the PEO matrix, tremendous research effort has been devoted to developing other solid polymer electrolytes. Various solid polymer electrolytes based on PAN, PVDF, and PMMA have attracted wide research attention, and much progress has been made so far.[73−78] But these solid polymers are still far from satisfying practical applications due to issues, such as low lithium ion conductivity and high voltage instability. Compositing solid polymers with inorganic additives proves promising to further improve the comprehensive properties of solid polymer electrolytes; further study is still needed nonetheless.

3.1.3. Solid Polymer Composite Electrolytes. Solid polymer composite electrolytes come from the combination of solid polymer electrolytes and solid inorganic electrolytes. The initial motivation of such compositing is to increase the mechanical stability of solid polymer electrolytes by adding ceramic additives, that is, "ceramic in polymer".[79] It was found that the obtained SSE presents superior mechanical properties as well as enhanced lithium ion conductivity. The addition of inorganic ceramics mitigates the formation of crystallized phase and increases amorphous regions in the polymer. Moreover, the interfacial interactions between inorganic ceramics and N, F, and O in solid polymer chains further facilitate lithium ion transport, leading to improved lithium ion conductivity.

By compositing solid polymer electrolytes into solid inorganic electrolytes, "polymer in ceramic" can be viewed as another type of composite system.[59,80] Note that the poor mechanical contact between inorganic electrolyte and cathode material has been the key hindrance for most SSEs. Such interfacial problems can be well overcome by adding a slight amount of polymer ingredients to buffer the interfaces. The combination of solid inorganic electrolytes and solid polymers may well exploit the advantages of each component, which is a most promising choice for future applications.

3.2. Inorganic Solid-State Electrolytes

Inorganic SSEs include a giant family of SSEs, which can be categorized into oxide- and sulfide-based series. In the following paragraphs, oxide SSEs will be discussed including

DOI: 10.1021/acs.chemrev.9b00268
Chem. Rev. XXXX, XXX, XXX−XXX

perovskite-type LLTO, NASICON-type LATP and LAGP, LISICON-type LZGO, and garnet-type LLZO. As for sulfide SSEs, we will focus on thio-LISICON-type LGPS and binary sulfide $Li_2S-M_xS_y$ (M = Al, Si, P, etc.).

3.2.1. Oxide Based Solid-State Electrolytes. *3.2.1.1. Perovskite-type LLTO.* The general formula of perovskite structure can be written as ABO_3 within *Pnma* space group. For conventional perovskite materials, the atomic A site is occupied by divalent alkali metal ions (Ba^{2+}, Ca^{2+}, etc.), while the face-centered O atoms form an octahedron that is occupied by tetravalent transition metal element B, such as Ti^{4+}. Perovskite can also be viewed as being constructed by BO_6 octahedra, with the A site coordinated by 12 O from 8 BO_6 octahedral units. Perovskite structure has much tolerance to both radius and valence of A and B site elements, which makes it possible to develop into a big series of functional materials. By replacing the divalent alkali metal at A sites with trivalent rare earth element La^{3+} and monovalent alkali metals such as Li^+ or Na^+, Brous et al. first prepared perovskite $Li_{1/2}La_{1/2}TiO_3$.[81] By controlling the lithium substitution content, Inaguma et al. further prepared perovskite $Li_{3x}La_{2/3-x}\square_{1/3-2x}TiO_3$ (□, vacancy), which presents excellent lithium ion conductivity of $\sim 10^{-3}$ S/cm at room temperature.[82]

Due to their bright potential, numerous investigations have been conducted to explore the fundamental mechanism of the high lithium ion conductivity in perovskite LLTOs. It was found that there are mostly two types of $Li_{3x}La_{2/3-x}\square_{1/3-2x}TiO_3$, in space group of *P*4/*mmm* and *Cmmm*. Due to the asymmetric distribution of La in 1a and 1b sites, alternately stacked La-rich and La-poor layers can be formed and relative lattice distortion can be detected. The conductivity of the perovskite SSE is greatly influenced by the crystal lattice and relative lithium concentration. Whereas in Li-poor orthorhombic structure LLTO the high La occupancy and low concentration of vacancies lead to sluggish lithium transport, Li-rich tetrahedral perovskite LLTO demonstrates higher lithium ion conductivity. Moreover, the relatively low La occupancy in Li-rich LLTO further lowers the energy barrier to lithium diffusion in the [001] direction, leading to 3D lithium conduction channels. Based on temperature dependent conductivity measurements, the increase in external temperature may also lead to lithium transport channels changing from 2D to 3D, which can be attributed to the distortion of the lattice.[83−88]

3.2.1.2. NASICON-type LATP/LAGP. Short for sodium superionic conductor, the NASICON-type SSEs are another big family of electrolyte systems, which have attracted much research attention in recent years. NASICON-type materials can be written with a general formula of $AM_2(PO_4)_3$, in which A = Li or Na and M = Ge, Ti, Zr, etc. The fundamental framework of the NASICON-type SSE can be built up based on a rigid $M_2P_3O_{12}$ skeleton, where two MO_6 octahedra and three PO_4 tetrahedra are linked together by sharing corner O atoms in one unit. Within this skeleton, alkali ions occupy the interstitial A1 and A2 sites and may diffuse via the transport channel established by MO_6 octahedra and PO_4 tetrahedra, offering modest lithium ion conductivity. The two MO_6 octahedra are separated with corner sharing XO_4 tetrahedra, making electronic orbital overlap and delocalization infeasible across the -M-O-M- chains. This feature further favors low electronic conductivity within the NASICON framework. Meanwhile, the relative rigid NASICON framework makes it possible to substitute or dope various elements. Within the overall consistent fundamental skeleton, detailed lattice symmetry can be quite variant based on diverse substituted elements. In the case of M = Ti or Ge, NASICON electrolytes exhibit rhombohedral symmetry in $R\bar{3}m$ space group, while in the case of M = Zr or Hf, with larger atomic radius, NASICON electrolytes present triclinic symmetry in $C\bar{1}$ space group. Following the pioneering report of NASICON as a promising SSE, a series of derivatives and analog materials have been designed and synthesized.[89−92]

Presently, the prevailing NASICON-type SSEs are derived from $LiTi_2(PO_4)_3$ and $LiGe_2(PO_4)_3$ parent lattices. The partial substitution of tetravalent M ion, Ti^{4+} and Ge^{4+}, by trivalent cations, Al^{3+}, Ga^{3+}, Fe^{3+}, etc., is promising to further improve lithium ion conductivity. In the Al-doped NASICON SSE, high room temperature lithium ion conductivity up to $\sim 10^{-3}$ S/cm can be obtained in $Li_{1.3}Al_{0.3}Ti_{1.7}(PO_4)_3$ and $Li_{1+x}Al_xGe_{2-x}(PO_4)_3$ systems, which are abbreviated as LATP and LAGP respectively.[93,94] The enhanced lithium ion conductivity can be attributed to the increase of mobile alkali ion concentration in the skeleton, together with invoking additional migration tunnels with lower excitation energy due to atomic radius effect. Meanwhile, cosintering of NASICON-type SSEs with additive lithium compounds demonstrates a valid strategy to further improve lithium ion conductivity. These cosintering additives may well act as buffer materials to decrease SSE porosity and interfacial resistance at grain boundaries.[95−97] Furthermore, glass-ceramic-type LAGP and LATP have proven promising, where the lithium transport barrier at grain boundaries can be much alleviated.[98,99]

3.2.1.3. LISICON-type LZGO. LISICON is short for lithium superionic conductor and exhibits γ-Li_3PO_4-type structure within the orthorhombic *Pnma* space group. The very first LISICON-type SSE, $Li_{14}ZnGe_4O_{16}$, was reported by Hong[14] and exhibits lithium ion conductivity of $\sim 10^{-7}$ S/cm at room temperature and ~0.125 S/cm at 300 °C. In LISICON-type SSEs, Ge, Zn, and Li occupy tetrahedral sites, and additional Li atoms occupy octahedral interstices, where octahedra share common faces with neighboring tetrahedra. Within the fundamental skeleton of $[Li_{11}ZnGe_4O_{16}]^{3-}$, a 3D lithium transport tunnel can be established, and the partial occupancy of octahedral sites further favors lithium conduction.

Note that LISICON-type SSEs share a common γ-Li_3PO_4-type solid solution structure with diverse analog components, thus representing an effective strategy to design novel materials and tailor electrolyte properties.[26,100−102] A typical example is $Li_{14}ZnGe_4O_{16}$, which can also be viewed as a solid solution of Li_4GeO_4 and Zn_2GeO_4. By combining Li_4XO_4 (X = Si, Ge, Ti, etc.) and Li_3YO_4 (Y = P, As, V, etc.), another series of LISICON SSEs can be built up, formulated as $Li_{3+x}X_xY_{1-x}O_4$.[103,104] Within this series LISICON, $Li_{3.5}Si_{0.5}P_{0.5}O_4$ demonstrates a considerably high lithium ion conductivity of 3×10^{-6} S/cm,[103] while As or V containing LISICON SSE presents an even higher value.[104]

3.2.1.4. Garnet-type LLZO. Traditional garnet structure can be written in general chemical formula of $A_3B_2(XO_4)_3$, where A = Ca, Mg, Y, La, etc., B = Al, Fe, Ga, Ge, Mn, Ni, V, etc., and X = Si, Ge, Al, etc. Garnet structure $A_3B_2(XO_4)_3$ crystallizes in face centered cubic $Ia\bar{3}d$ space group, and A, B, and X are 8-fold, 6-fold, and 4-fold coordinated cations, respectively. When X sites within this frame are occupied by Li atoms, garnet-type structure becomes a promising lithium conductor through the interconnected empty polyhedral sites. In 2003, Thangadurai

DOI: 10.1021/acs.chemrev.9b00268
Chem. Rev. XXXX, XXX, XXX−XXX

et al. first reported garnet electrolyte $Li_5La_3M_2O_{12}$ (M = Nb or Ta) with lithium ion conductivity ~10^{-6} S/cm at room temperature.[105] Within the garnet skeleton, aliovalent doping has been widely investigated with extra lithium in the structure and brings in a series of garnet-type electrolytes. Presently, prevailing garnet-type electrolytes generally contain 5−7 Li atoms per chemical formula, also known as Li-rich garnet. Based on the lithium content per formula, garnet-type electrolyte can be classified into several groups including Li3 series, $Li_3Ln_3Te_2O_{12}$ (Ln = Y, Pr, Nd, etc.),[106] Li5 series, $Li_5La_3M_3O_{12}$ (M = Nb, Ta, Sn, etc.),[107,108] Li6 series, $Li_6ALa_2M_2O_{12}$ (A = Ca, Sr, Ba, etc., and M = Nb, Ta, etc.),[109] and L7 series, $Li_7La_3M_2O_{12}$ (M = Zr, Sn, Hf, etc.).[110−112]

Lithium ion conductivity in garnet-type structure is determined by several factors, in which lithium concentration, lithium coordination environment, crystal structure, and grain boundaries are the most important ones. More specifically, higher lithium concentration favors higher lithium ion conductivity, as can be supported from the lithium ion conductivity change from Li3 to Li7 series. In-depth research indicates that the increased lithium ion conductivity is directly related to the lithium coordination environment in garnet structure. As in Li3 series, all three Li atoms occupy 24d tetrahedral sites, while in Li5−L7 series, the further induced extra Li ions occupy octahedral sites. Note that octahedral site Li demonstrates facile lithium transport, while tetrahedral site Li does not; the Li fraction in octahedral coordination is hence directly related to the measured lithium ion conductivity. Li7 series were found with two more subtypes, cubic LLZO in $Ia\bar{3}d$ space group with fully disordered lithium arrangement and tetrahedral LLZO in $I4_1/acd$ space group with fully ordered lithium occupancy. The cubic LLZO exhibits higher symmetry and more lithium equivalent sites, which favors 1−2 orders of magnitude higher lithium ion conductivity compared with tetrahedral LLZO. To stabilize cubic LLZO phase at lower sintering temperature, Al doping is verified to be an effective strategy, owing to the preferred occupancy of Al in tetrahedral sites. In addition, Al and Si doping are further expected to benefit increasing SSE densification and reducing grain boundary resistance, which are also favorable to higher lithium ion conductivity.[113,114]

3.2.2. Sulfide Based Solid-State Electrolytes. *3.2.2.1. Thio-LISICON-type LGPS.* Thio-LISICON-type electrolytes exhibit γ-Li_3PO_4 structure within orthorhombic *Pnma* space group and are built up by replacing O in LISICON-type structure with S. Li_2ZrS_3, Li_2GeS_3, Li_4GeS_4, Li_5GaS_4, and Li_3PS_4 are typical examples of thio-LISICON-type electrolytes, but they only exhibit low lithium ion conductivity, ~10^{-6} to 10^{-7} S/cm.[26,115,116] By aliovalent doping or various analogue solid solutions, the thio-LISICON system grows into a big family of materials, which can be written in the form of $Li_xM_{1-y}M'_yS_4$. Compared with LISICON electrolyte, S substitution exhibits larger radius and higher polarization.[117] These two features may well expand the lithium transport tunnel and mitigate the strong constraint from the O based skeleton, leading to enhanced lithium ion conductivity.

As mentioned previously, Kanno et al. developed a series of $Li_{4-x}Ge_{1-x}P_xS_4$ thio-LISICON systems, which exhibit high lithium ion conductivity even comparable to liquid electrolyte at room temperature.[26,28,117] By aliovalent doping, thio-LISICON electrolyte can further improve lithium ion conductivity to 2.5 × 10^{-2} S/cm in $Li_{9.54}Si_{1.74}P_{1.44}S_{11.7}Cl_{0.3}$ material.[30] Based on first-principles calculations and molecular dynamics calculations, the extremely high lithium ion conductivity in $Li_{10}GeP_2S_{12}$ can be attributed to the fast 1D lithium transport tunnel in the *c* axis combined with the 2D lithium transport tunnel in the *ab* plane.[118] These pioneering works on thio-LISICON electrolyte attracted wide attention and demonstrated the promising future of SSEs in replacing conventional liquid carbonate electrolytes.

3.2.2.2. Amorphous Sulfide Li_2S−M_xS_y. Binary sulfide Li_2S−M_xS_y (M = Al, Si, P, etc.) electrolyte is another type of important amorphous electrolyte, which exhibits high room temperature lithium ion conductivity of ~10^{-4} to 10^{-3} S/cm.[119] Compared with oxygen based amorphous systems, the sulfide system generally exhibits higher lithium ion conductivity, which can be attributed to the larger ionic polarization and weaker interaction of sulfur with lithium ions. The higher mechanical ductility and lower interfacial resistance makes it promising for practical applications. Presently, low cost production has been realized in ASSBs based on sulfide amorphous SSEs.

In order to further improve lithium ion conductivity, diverse sulfide amorphous electrolytes have been investigated. Following early studies, Li_2S concentration and sulfide compound M_xS_y selection on lithium ion conductivity have been optimized. The addition of lithium based oxides such as Li_4SiO_4 was further verified to effectively enhance room temperature lithium ion conductivity approaching 10^{-3} S/cm.[120] Based on NMR and XPS characterizations, it is verified that the different coordination environments between O and S facilitate Li activation and transport. The preparation procedure is further verified to play an important role in influencing lithium ion conductivity.

3.3. Other Types of Solid-State Electrolytes

3.3.1. Anti-perovskite-type Li_3OX. Anti-perovskite-type SSEs can be written as Li_3OX within cubic $Pm\bar{3}m$ space group and share consistent fundamental crystal structure with perovskite-type SSEs. Anti-perovskite-type structure can be built up by inverting occupancy of perovskite lattice sites, where X^- ions occupy the cubic corner sites, O^{2-} ions occupy the body center sites, and Li^+ ions occupy the cubic face center sites forming octahedral units. Due to the abundant lithium concentration in the chemical formula, anti-perovskite Li_3OX is also named Li-rich anti-perovskite (LiRAP).[29,121,122] And the Li-rich formula also facilitates higher conductive lithium concentration, favoring higher lithium ion conductivity.

Perovskite/anti-perovskite-type structure exhibits large tolerance to both atomic radius and valence state variation. Hence structural tailoring through chemical substitution is feasible to manipulate properties of SSEs, and plentiful investigations have been carried out correspondingly. $Li_3OCl_{0.5}Br_{0.5}$ was reported to exhibit improved lithium ion conductivity of ~1.94 × 10^{-3} S/cm,[29] $Li_{3-2x}Ba_xOCl$ (x = 0.005) was further reported to exhibit 2.5 × 10^{-2} S/cm lithium ion conductivity at room temperature.[122] In addition, Li et al. further prepared $Li_2(OH)_{0.9}F_{0.1}Cl$, which presents lithium ion conductivity of ~10^{-2} S/cm with wide electrochemical stability window.[123]

Many works focus on clarifying the physical mechanism of the high lithium ion conductivity in anti-perovskite-type electrolytes. It was found that the sintering procedure and material texture are key to improved lithium ion conductivity. These findings indicate that microstructural changes such as vacancy formation, local distortion, and local order−distortion

DOI: 10.1021/acs.chemrev.9b00268
Chem. Rev. XXXX, XXX, XXX−XXX

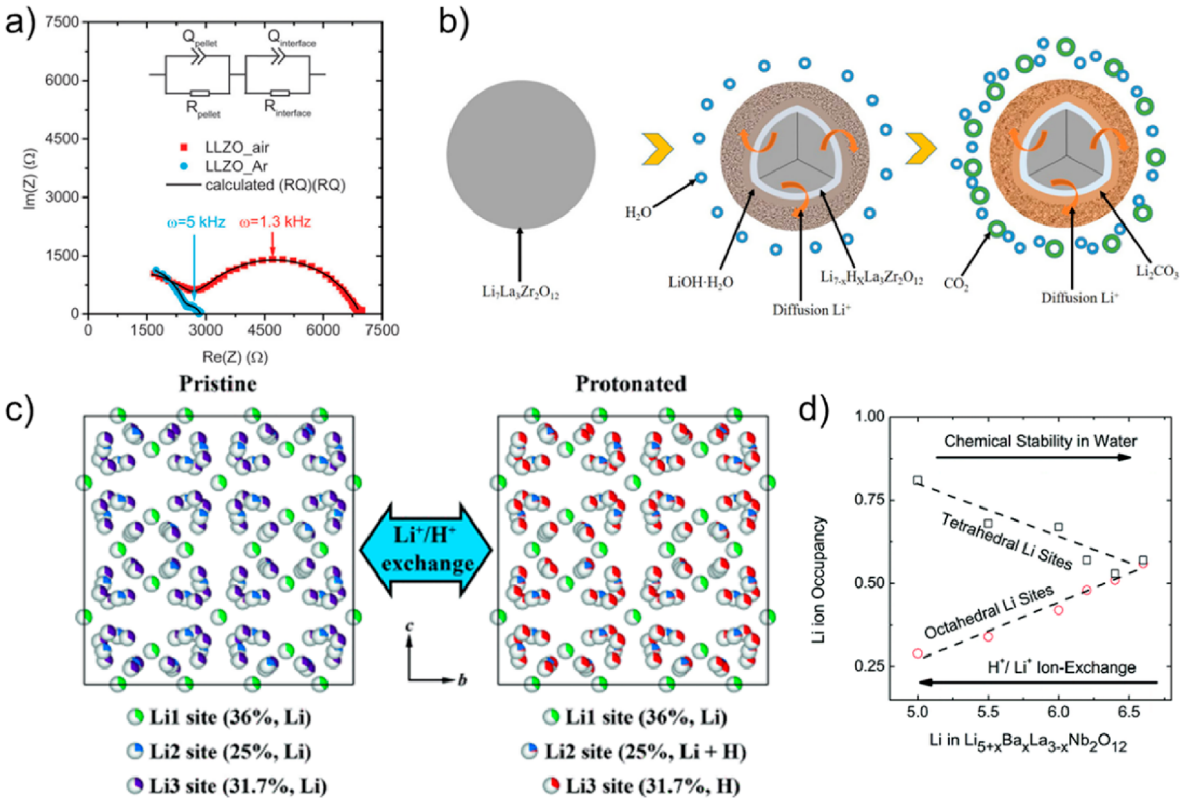

Figure 5. Degradation of SSEs in ambient air. (a) Nyquist plots of Li/LLZO/Li symmetric cells in air and in Ar. The significantly reduced resistance of Li/LLZO/Li in Ar atmosphere demonstrates the highly resistant interface of LLZO, which may result from surface impurities in moist air.[165] Reproduced from ref 165. with permission from the PCCP Owner Societies. (b) Scheme of the mechanism proposed for Li^+/H^+ exchange reaction of LLZO with CO_2 and H_2O.[166] Reprinted with permission from ref 166. Copyright 2017 American Ceramic Society. (c) Schematic illustration of the Li^+/H^+ exchange reaction of $Li_{6.5}La_3Zr_{1.5}Ta_{0.5}O_{12}$ SSE with water. Lithium ions located on Li3 sites and Li2 sites are more likely to be exchanged by protons.[167] Reprinted from ref 167 with permission. Copyright 2015 John Wiley and Sons. (d) Variation of occupancy of Li ion sites in $Li_{5+x}Ba_xLa_{3-x}Nb_2O_{12}$ and their different extent of Li^+/H^+ exchange reaction.[168] Reprinted with permission from ref 168. Copyright 2011 American Chemical Society.

transition may be the reasons for the phenomenally high lithium ion conductivity. By theoretical calculations, several models have also been proposed to explain the lithium transport process. Molecular dynamics simulations indicate that local structural disorder and lithium vacancy formation instead of perfect structure will promote lithium ion conductivity.[121] Emly et al. then proposed a collective hop-migration mechanism involving lithium interstitial dumbbells to explain the low excitation energy.[124] Later, Mouta et al. further employed a Schottky defect induced vacancies model to calculate lithium vacancy concentration and proposed the dominant transport scenario.[125]

3.3.2. LiPON. The typical constitution of LiPON, which demonstrates room temperature lithium ion conductivity of ~3.3×10^{-6} S/cm with excitation energy ~0.54 eV, can be written as $Li_{2.88}PO_{3.73}N_{0.14}$. LiPON was first proposed by Bates et al. and fabricated by magnetron sputtering of Li_3PO_4 in N_2 atmosphere.[126] LiPON is mostly widely utilized in thin film batteries with a thickness of hundreds of nanometers.[127] Within thin film structure, the relatively low lithium ion conductivity will not be a problem. And thin film batteries based on LiPON electrolyte have been successfully commercialized for specific applications including microsized medical apparatus, microelectronic devices, etc. However, due to the small size of thin film batteries, the capacity has always been small, which has limited the widespread application of this system. The high production cost further hinders its practical development. On the other hand, the inertness of LiPON against both lithium anode and high voltage cathode makes it a promising interfacial buffer layer that can be implemented in other SSBs.

In the above discussion, we briefly review various prevailing SSEs, focusing on fundamental structure, lithium ion conducting properties, and preparation methods, as summarized in Table 2. Presently, only solid polymer-based ASSBs have been successfully commercialized for practical applications among diverse SSEs. By combining advantages of both polymer and inorganic materials, the solid composite battery is a promising candidate for the next phase of ASSB development. Meanwhile, inorganic component based ASSBs seem an even longer-range perspective of the research field due to the higher energy density and superior safety performance. In past years, numerous investigations have been devoted to developing practical accessible ASSBs with inorganic SSEs, and much progress has been achieved so far. In the following discussions, we will focus on the instability issues of some prevailing SSEs, which contain sulfides, oxides, and polymer electrolytes.

4. STABILITY ISSUES IN SOLID-STATE BATTERIES

4.1. Chemical Stability

The capability of the SSEs and the electrolyte/electrode interfaces to maintain the initial composition and structure

DOI: 10.1021/acs.chemrev.9b00268
Chem. Rev. XXXX, XXX, XXX−XXX

before the cycling process is of great significance to practical battery design and fabrication. The stability of SSEs against moisture determines the condition requirements for SSE synthesis and transport, while the chemical instability of the electrode/electrolyte interfaces drives the degradation of battery performance during storage, which is also called "calendar failure".[160] Therefore, it is essential to obtain a comprehensive understanding on the chemical stability of materials and interfaces in ASSBs, from phenomena to mechanism.

4.1.1. Chemical Stability of Solid-State Electrolyte Materials. The chemical stability of SSEs determines the storage and fabrication conditions. However, degradation will happen when some SSEs are exposed to ambient air, and some decomposed products may even do harm to their usage. In this section, degradation behaviors of different types of SSEs will be discussed, and the comparison of their stability in ambient environments will be given. Particularly, H_2S generation in sulfides and Li^+/H^+ exchange reaction in oxides will be emphasized, and the approaches to enhance air stability will be summarized.

4.1.1.1. H_2S Generation in Sulfides. The release of H_2S in sulfide electrolytes is no surprise, as some sulfides can be described by the formula $xLi_2S{\cdot}P_2S_5$, in which the Li_2S is highly moisture sensitive and facilely releases H_2S.[161] However, the reaction mechanism between sulfide electrolytes and moisture is far from well clarified. In 2011, Muramatsu et al.[162] first studied the structural change of $xLi_2S{\cdot}(100-x)P_2S_5$ with different Li_2S contents in ambient air by Raman spectroscopy. It was found that sulfides with composition of 67% Li_2S experienced the most significant structural change. $P_2S_7^{4-}$ ions, the main structural unit of $67Li_2S{\cdot}33P_2S_5$, decomposed to OH and SH groups under water attack. It was reported that the amount of H_2S released is highly dependent on the $Li_2S{\cdot}P_2S_5$ composition, and $75Li_2S_5{\cdot}25P_2S_5$ generates the least H_2S gas. However, deep understanding of the decomposition behavior of sulfide electrolytes still remains to be developed. Sahu et al.[163] attempted to clarify the chemical stability behavior of sulfides by using the hard and soft acids and bases (HASB) theory.[164] Soft acids and bases exhibit larger atomic or ionic radius and larger polarization, while the hard acids and bases are more compact and less polarizable. Based on this theory, oxygen, as a hard base, is harder than sulfur and, therefore, is more prone to react with hard acid P. Since Sn and As exhibit softer acid properties and prefer to bond with sulfur rather than oxygen, a new As-substituted Li_4SnS_4 SSE was designed and demonstrated high chemical stability against moist air. However, a comprehensive understanding of the chemical stability of sulfide electrolyte materials needs further study.

4.1.1.2. Li^+/H^+ Exchange in Oxides. H^+/Li^+ exchange has been widely observed in oxide lithium conductors, both electrodes and ionic conductive electrolytes.[169,170] This phenomenon was even utilized to design the LLTO based pH sensors and has potential applications in the food industry.[171] The famous garnet-type SSE, LLZO, was widely accepted as air stable in the early stage of its discovery.[27] However, Cheng et al.[165] reported that a high Li/Zr atomic ratio layer formed on the surface after LLZO pellet exposure to air for 2 months. SEM, XRD, XPS, and XAS studies proved that the as-formed layer contains Li_2CO_3. The authors therefore considered the surface impurity, caused by chemical instability of LLZO, as the origin of the large interfacial resistance between LLZO and Li (Figure 5a). Similarly, Sharafi et al.[172] reported that the presence of surface contaminants led to poor wettability and large interfacial resistance. After removal of the surface impurities by combining simple wet polishing and heat treatment, a significant increase in lithium wettability and interfacial conductivity can be achieved.

It was reported that a protonated phase forms as a result of lithium site replacement by proton. Recently, Brugge et al.[173] observed obvious proton diffusion from the surface to the inner bulk phase, and estimated the diffusion length to be 1.5 μm. Based on FIB-SIMS depth profiling and EIS measurements, the conductivity of protonated Ga-LLZO was determined to be 8.6×10^{-6} S cm^{-1}, indicating that the large interfacial resistance should be attributed to not only newly formed LiOH and Li_2CO_3 but also protonated garnet. In addition, Jin and McGinn[174] claimed that for LLZO pellets exposure to moisture not only degrades its conductive properties but also impacts its mechanical integrity, which may result from the preferable reaction activity on the grain boundaries of LLZO pellet.

To obtain deep insights into the Li^+/H^+ exchange mechanism, theoretical and experimental studies were carried out. Duran et al.[175] reported that immersion of LLTO in pure water does not greatly change the initial crystal structure except a slight expansion of the lattice parameters. Similar results were also found in garnet materials; as reported by Li et al.,[176] the ion-exchanged sample exhibited similar XRD patterns to that of pristine garnet, while the lattice parameters increased from the asymmetric O−H···O bonds.[177] Kang and Sholl[178] first examined the chemical stability of three garnet electrolytes with respect to moisture and carbon dioxide by DFT calculations. They proposed that Li_2CO_3 and LiOH, accompanied by the La_2O_3 and MO_2 (M = Zr, Hf, or Sn), tended to form when LLMOs were in the presence of CO_2 and H_2O. Although Wang and Lai[179] reported that partial tetragonal−cubic phase transition still can be observed after 40 h of CO_2 exposure at 350 °C, Xia et al.[166] claimed that direct reaction of a garnet pellet with CO_2 is rather difficult and the formation of Li_2CO_3 was due to transformation from LiOH as a result of Li^+/H^+ exchange, as illustrated in Figure 5b. A similar two-step mechanism was also proposed for perovskite systems.[180−182] The LLTO tends to first react with water on the grain surface, exchanging H^+ for Li^+ in the crystalline framework, transforming LLTO to protonated $(Li_{0.30-y}H_y)$-$La_{0.57}TiO_3$, which follows a topotactic reaction process. Then LiOH would be formed on the surface and further transform to Li_2CO_3.

NMR and neutron diffraction were utilized to identify the preferred locations of the replaced lithium atoms. It was reported by Truong et al.[183] that, in garnet-type materials, H preferentially replaces Li in the distorted octahedral sites. A quantitative study conducted by Li et al.[176] revealed that lithium occupancy of Li1 (tetrahedral 24d sites) in garnet LLZT stayed constant while Li2 and Li3, located at the 48g and 96h sites, occupancy decreased by 8.6% and 16.9%, accompanying distortion of Li−O octahedra at these sites, as shown in Figure 5c.

4.1.1.2.1. Temperature, Humidity, and pH. The ion exchange behaviors of oxide conductors were also controlled by the following kinetic factors. Generally, higher temperature leads to faster Li^+/H^+ exchange kinetics. As reported by Bhuvanesh et al.,[184] the ion exchange reaction is topotactic and completed at 60 °C; a single protonated phase $La_{2/3-x}TiO_{3-3x}(OH)_{3x}$ was obtained in 5 days. The reaction

DOI: 10.1021/acs.chemrev.9b00268
Chem. Rev. XXXX, XXX, XXX−XXX

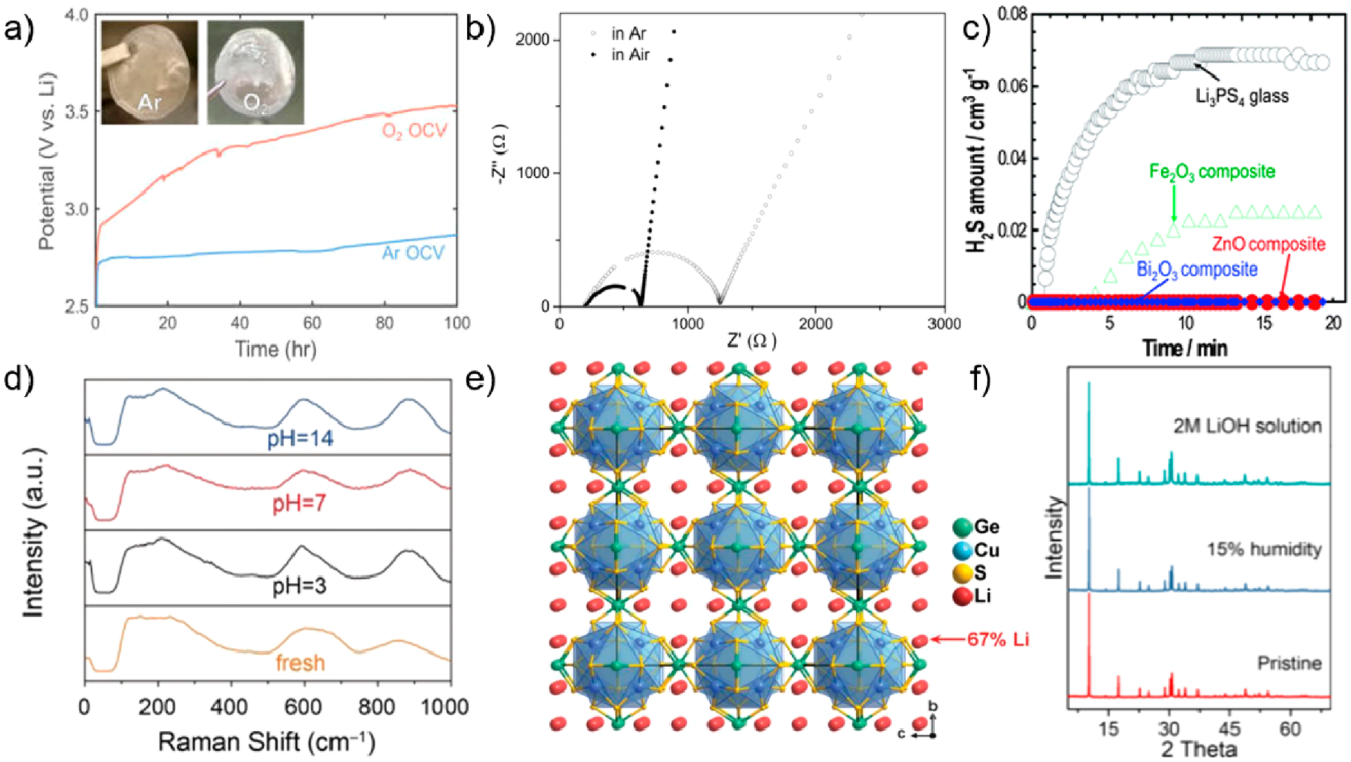

Figure 6. Air stability of polymer and NASICON-type SSEs, and strategies to improve the chemical stability of ambient sensitive materials. (a) Time-dependent open-circuit potential curves of polymer Li−O_2 batteries in Ar and O_2, the continuous increasing open-circuit potential results from the oxidation of the polymer electrolyte.[195] Reprinted with permission from ref 195. Copyright 2015 American Chemical Society. (b) Impedance spectra of LATP pellet with ion-block electrodes, tested in air and Ar atmosphere. The LATP SSE exhibits even higher ionic conductivity in air. Reprinted from ref 201, Copyright 2018, with permission from Elsevier. (c) Amount of H_2S generation for Li_3PS_4 SSE with different oxide additives. Reproduced from ref 206 with permission from The Royal Society of Chemistry. (d) Raman spectra of $Li_{0.38}Sr_{0.44}Ta_{0.7}Hf_{0.3}O_{2.95}F_{0.05}$, after the pellet was immersed in water with different pH = 0, 3, 7, or 14 for 2 weeks. The air stability of this material is confirmed by the unchanged Raman spectra. Reprinted from ref 209 with permission. Copyright 2018 John Wiley and Sons. (e) Crystal structure of an air stable sulfide electrolyte, $Li_4Cu_8Ge_3S_{12}$ (LCGS), which is designed based on hard and soft acids and bases (HASB) theory. (f) XRD results of LCGS in different states (15% moist and 2 M LiOH aqueous solution). No decomposition happens. Panels e and f are reprinted from ref 210 with permission. Copyright 2019 John Wiley and Sons.

at room temperature is rather slow, and it is hard to reach 100% exchange efficiency. However, when the temperature reaches around 300 °C, the protonated LLTO begins to dehydrate, resulting in a $La_{2/3-x}TiO_{3-3x/2}$ phase. In addition, the LiOH and Li_2CO_3 formed by the ion exchange on the surface of LLTO would decompose resulting in the recovery of LLTO.[180,181] Humidity impacts the reaction kinetics as well. It was reported that a lower content of Li_2CO_3 on the LLZO pellets was obtained under dry air (humidity ∼0.5%) than in ambient air (humidity ∼50%). Therefore, a much lower Li/LLZO interfacial resistance was achieved on LLZO stored in dry air. Besides humidity, the pH value of aqueous medium also plays a role on the ion exchange process. Two new phases, La_2TiO_3 and Li_2TiO_3, were observed in LLTO after immersion in HCl solution, while the crystal structure of a sample immersed in pure water remained unchanged.[175] Reasonable stability in 1 M LiCl solution was also observed for LLZO electrolytes as well as Y and Li doped garnets.[185,186] Moreover, the Li^+/H^+ exchange degree was also reported to vary in different solvents, and it turns out that acetonitrile causes less Al-LLZO decomposition compared to water,[187] which makes acetonitrile more suitable as the dispersion agent for garnet powders.

4.1.1.2.2. Microstructure and Element Composition. Besides the environment, the microstructure and element composition of the material itself also affect the ion exchange. Smaller particle sizes generally lead to larger degrees of exchange and higher reaction rate.[175] As reported by Bohnke et al.,[182] LLTO nanoparticles undergo fast reaction with water and CO_2 even under Ar gas in a glovebox. Xia et al.[188] synthesized a denser LLZO pellet, which contains fewer grain boundaries, by solid-state reaction in a Pt crucible. Since the ion exchange of oxide electrolytes was reported to start at grain boundaries, pellets with a lower amount of grain boundaries, which was achieved by removing the Al from alumina crucibles, may minimize the ion exchange degree and prevent the pellet from further degradation. This work also emphasized the role of element composition in chemical stability of oxide electrolytes against air. Galven et al.[177] reported that $Li_{7-x}H_xLa_3Sn_2O_{12}$ and $Li_{5-x}H_xLa_3Nb_2O_{12}$ experience different phase transition behavior in the ion exchange process. It was reported that a higher degree of exchange occurs with higher lithium concentration. Galven et al.[177] and Truong and Thangadurai[168] reported that ion exchange becomes more favorable if the concentration of Li^+ ions is greater than what can be occupy the tetrahedral sites (Figure 5d), confirming Li^+ on tetrahedral sites as the preferable reactive sites.

In fact, proton/Li^+ exchange has been reported to exist widely in ionic conductors and electrode materials, such as sodium zirconium phosphate (NZP) family,[189−191] LTO,[169]

DOI: 10.1021/acs.chemrev.9b00268
Chem. Rev. XXXX, XXX, XXX−XXX

Table 3. Chemical Stability of Different Solid-State Electrolytes in Air

material	stability in ambient air	reaction mechanism	ref
$Li_7La_3M_2O_{12}$ (M = Zr, Sn, Hf)	H^+/Li^+ exchange	$2Li_7La_3M_2O_{12} + 7H_2O \leftrightarrow 14LiOH + 3La_2O_3 + 4MO_2$	Kang and Sholl[178]
$Li_{6.5}La_3Zr_{1.5}Ta_{0.5}O_{12}$	H^+/Li^+ exchange	(1) $Li_{6.5}La_3Zr_{1.5}Ta_{0.5}O_{12} + xH_2O \rightarrow Li_{6.5-x}H_xLa_3Zr_{1.5}Ta_{0.5}O_{12} + xLiOH$ (2) $LiOH + H_2O \rightarrow LiOH{\cdot}H_2O$ (3) $2LiOH{\cdot}H_2O + CO_2 \rightarrow Li_2CO_3 + 3H_2O$	Xia et al.[166]
$Li_{0.3}La_{0.57}TiO_3$	H^+/Li^+ exchange	(1) $Li_{0.3}La_{0.57}TiO_3 + yH_2O_{(g)} \rightarrow (Li_{0.3-y}H_y)La_{0.57}TiO_3 + yLiOH_{(s)}$ (2) $2LiOH(s) + CO_{2(g)} \rightarrow Li_2CO_3 + 3H_2O_{(g)}$	Boulant et al.[180]
$67Li_2S{\cdot}33P_2S_5$	H_2S generation	$P_2S_7^{4-} + H_2O \rightarrow PS_3^{2-}-SH + PS_3^{2-}-OH + H_2O \rightarrow 2PS_3^{2-}-OH + H_2S_{(g)}$	Muramatsu et al.[162]
PEO	water absorption in ambient air; oxidized in pure O_2 environment	*a*	Harding et al.[195]
$Li_{1+x}Al_xTi_{1-x}(PO_4)_3$	nearly stable, slow Li^+/H^+ exchange	*a*	Thokchom and Kumar[196] and Hasegawa et al.[197]

[a]Not given.

and LMO.[192] Dahn et al.[170] studied the stability of lithium intercalation compounds in aqueous solution. They calculated the equilibrium voltage of lithium transition metal oxide intercalation compounds in water. It was found that the more tightly Li atoms are bound, the higher the Li insertion voltage, thus resulting in higher stability. The difference in the chemical stability under moisture may be explained by this theory, since high Li^+ conductivity often comes from weak Li−M bonding, which may result in lower stability under moisture attacks. However, the reactions between these materials and aqueous solutions have not been well understood yet. Very recently, two reviews provided by Duan et al.[193] and Hofstetter et al.[194] gave comprehensive discussion on stability issues of garnet SSEs, while intensive studies on other types of oxide SSEs are still needed.

4.1.1.3. Chemical Stability of Other Solid-State Electrolytes in Ambient Air. Unlike the sulfides and oxides, polymer electrolytes usually display reasonable chemical stability in air. Still, polymer SSEs need to be handled in inert environments to prevent water adsorption, which can be removed by drying in vacuum oven.[68] However, slight degradation of PEO/LiTFSI electrolyte still can be observed in oxygen rich environments (Figure 6a), which should be prevented in practical applications.[195] Meanwhile, thin film type LiPON exhibits modest stability in dry air but demonstrates chemical instability in moisture. Hydrolysis reaction brings about Li_2CO_3 formation and PH_3/NH_3 gas release after 24 h storage in moist air with humidity 40%, demonstrating new phase evolution and obvious morphology change from SEM.[198] On the other hand, NASICON electrolytes, which are also oxide ionic conductors, show slow degradation in water and $LiNO_3$ aqueous solutions.[197] Cretin et al.[199] reported that, after 100 h of water immersion, $Li_{1.3}Al_{0.3}Ti_{1.7}(PO_4)_3$ pellets demonstrated only 0.9% weight loss. Shimonishi et al.[200] examined the conductivity of LATP before and after immersion in solutions with different pH values at 50 °C for 3 weeks. It was found that LATP pellet is stable in solution at pH = 7 and the conductivity exhibits no change after immersion. In addition, Dashjav et al.[201] reported that LATP even demonstrates enhanced ionic conductivity after moisture exposure; pellets after exposure in ambient air and pellets immersed in water for 24 h deliver conductivity of 1×10^{-3} S/cm and 2.8×10^{-3} S/cm (Figure 6b), respectively. It was found that the grain boundary resistance significantly decreased after water immersion, which may originate from Li^+/H^+ exchange at grain boundaries. Owning to its high chemical stability, LATP was utilized as a protecting layer in aqueous $Li-O_2$ batteries.[197,202,203] Therefore, it can be concluded that the NASICON electrolytes show better chemical stability in ambient air compared with other SSEs (Table 3). The chemical stability rank of various SSEs can be given as NASICON > polymer > garnet and perovskite > sulfide. Stability of NASICON electrolytes is at the highest level showing even enhanced conductivity in ambient air. Note that the detrimental impacts of polymer and other oxide electrolytes brought by moisture could be eliminated through relatively facile methods, which demonstrate acceptable chemical stability in practical productions. However, the irreversible decomposition of sulfides and health-threatening reaction products require it to be treated in strict environments from production to device operation, which cause a short supply of sulfide electrolytes and limits their large-scale applications.

4.1.1.4. Approaches to Enhance the Chemical Stability of Solid-State Electrolytes in Ambient Air. 4.1.1.4.1. Additives. The utilization of additives is efficient in inhibiting unwanted reactions in ambient air. Li et al. proved that addition of 2 wt % LiF suppresses Li_2CO_3 formation on the grain surface of LLZO, and 2 wt % LiF-LLZO demonstrates smaller interfacial resistance with lithium metal.[204] The addition of oxides is reported to be an efficient way to suppress H_2S generation, as displayed in Figure 6c, Li_2O[205] and M_xO_y (M = Fe_2O_3, ZnO, and Bi_2O_3)[206] were utilized to improve the stability of sulfide electrolytes against moisture, which was well summarized by Chen et al. in their recent review.[207] The oxides can act as H_2S absorbents, and the reaction mechanism can be written as $M_xO_y + H_2S \rightarrow M_xS_y + H_2O$, when oxides have a large negative Gibbs energy change for this reaction. However, the stability may increase at the expense of the conductivity, as Hood et al.[208] pointed out that the oxide fillers may increase the activation energy of ion hopping, thus exhibiting ion blocking effect and leading to a decrease of ion conductivity.

4.1.1.4.2. Composition Optimization. Another approach to reach better chemical stability is tuning the chemical composition of materials. As has been mentioned, oxide ionic conductive materials with different stoichiometry display different ionic exchange behaviors.[177] Therefore, optimizing the element composition of oxides should be an effective way to enhance the chemical stability of materials. For example, thermodynamic calculations predicted that the chemical

DOI: 10.1021/acs.chemrev.9b00268
Chem. Rev. XXXX, XXX, XXX−XXX

Table 4. DFT Predictions and Experimental Results Concerning Chemical Reactions between Cathodes and SSEs

solid-state electrolyte	cathode	interfacial behavior	T (K)	method	ref
$Li_7La_3Zr_2O_{12}$	$LiCoO_2$	$4Li_7La_3Zr_2O_{12} \rightarrow 4La_2Zr_2O_7 + 7O_2 + 2La_2O_3$	0	DFT	Richards et al.[224]
$Li_7La_3Zr_2O_{12}$	$LiFePO_4$	$10LiFePO_4 + 3Li_7La_3Zr_2O_{12} \rightarrow 5Fe_2O_3 + 7Li_3PO_4 + 3LaPO_4 + 3La_2Zr_2O_7$	0	DFT	Richards et al.[224]
$Li_7La_3Zr_2O_{12}$	$LiMnO_2$	$7LiMnO_2 + 2Li_7La_3Zr_2O_{12} \rightarrow La_2O_3 + 2La_2Zr_2O_7 + 7Li_2MnO_3$	0	DFT	Richards et al.[224]
Li_3PS_4	$LiCoO_2$	$3LiCoO_2 + 2Li_3PS_4 \rightarrow Co(PO_3)_2 + 2CoS_2 + 4S$	0	DFT	Richards et al.[224]
Li_3PS_4	$LiFePO_4$	$2Li_3PS_4 \rightarrow P_2S_7 + S$	0	DFT	Richards et al.[224]
Li_3PS_4	$LiMnO_2$	$14LiMnO_2 + 8Li_3PS_4 \rightarrow 3Mn_2S_3 + 4Mn_2P_2O_7 + 23S$	0	DFT	Richards et al.[224]
$Li_{10}GeP_2S_{12}$	$LiCoO_2$	$7LiCoO_2 + 2Li_{10}GeP_2S_{12} \rightarrow 2GeP_2O_7 + 10S + 7CoS_2$	0	DFT	Richards et al.[224]
$Li_{10}GeP_2S_{12}$	$LiFePO_4$	$Li_{10}GeP_2S_{12} \rightarrow 3S + P_2S_7 + GeS_2$	0	DFT	Richards et al.[224]
$Li_{10}GeP_2S_{12}$	$LiMnO_2$	$14LiMnO_2 + 4Li_{10}GeP_2S_{12} \rightarrow 4Mn_2P_2O_7 + 31S + 4GeS_2 + 3Mn_2S_3$	0	DFT	Richards et al.[224]
$Li_{10}GeP_2S_{12}$	$LiNiO_2$	$171LiNiO_2 + 22Li_{10}GeP_2S_{12} \rightarrow 22Li_4P_2O_7 + 22GeO_2 + 36Li_2SO_4 + 57Ni_3S_4$	0	DFT	Richards et al.[224]
$Li_7La_3Zr_2O_{12}$	$LiCoO_2$	La_2CoO_4 formation	298	TEM	Kim et al.[216]
$Li_7La_3Zr_2O_{12}$	$LiCoO_2$	tetragonal $Li_7La_3Zr_2O_{12}$ phase formation	973	XRD	Park et al.[218]
$Li_{6.6}La_3Zr_{1.6}Ta_{0.4}O_{12}$	$LiMnCoO_4$	$11.6Li_{6.6}La_3Zr_{1.6}Ta_{0.4}O_{12} + 39.9LiMnCoO_4 \rightarrow 0.25O_2 + La_2MnCoO_6 + 0.2La_2O_3 + 9.3La_2Zr_2O_7 + 4.7La_3TaO_7 + 38.9Li_2MnO_3 + 38.9LiCoO_2$	873	XRD	Miara et al.[217]
$Li_{6.6}La_3Zr_{1.6}Ta_{0.4}O_{12}$	$Li_2Mn_3NiO_8$	$36.9Li_{6.6}La_3Zr_{1.6}Ta_{0.4}O_{12} + 61.3Li_2Mn_3NiO_8 \rightarrow 0.25O_2 + 3.2La_2O_3 + 29.5La_2Zr_2O_7 + 14.7La_3TaO_7 + LaMnO_3 + 182.9Li_2MnO_3 + 61.3NiO$	873	XRD	Miara et al.[217]
$Li_{6.6}La_3Zr_{1.6}Ta_{0.4}O_{12}$	$Li_2Mn_3FeO_8$	$5.3Li_{6.6}La_3Zr_{1.6}Ta_{0.4}O_{12} + 7.25Li_2Mn_3FeO_8 + 1.8O_2 \rightarrow 4.3La_2Zr_2O_7 + 2.1La_3TaO_7 + LaFeO_3 + 21.8Li_2MnO_3 + 6.25LiFeO_2$	873	XRD	Miara et al.[217]
$Li_{1+x}Al_xGe_{2-x}(PO_4)_3$	$LiMn_{1.5}Ni_{0.5}O_4$	formation of $LiMnPO_4$ and CeO_2	873	XRD	Robinson et al.[225]
$Li_{1.5}Al_{0.5}Ti_{1.5}(PO_4)_3$	$LiCoO_2$	formation of $LiTiPO_5$, Li_3PO_4, and Co_3O_4	873	XRD	Gellert et al.[226]
$Li_{1.5}Al_{0.5}Ti_{1.5}(PO_4)_3$	$LiMn_2O_4$	formation of $AlPO_4$, Li_3PO_4, and Mn_2O_3	973	XRD	Gellert et al.[226]
$Li_{1.5}Al_{0.5}Ti_{1.5}(PO_4)_3$	$LiFePO_4$	formation of $Li_2FeTi(PO_4)_3$ and $AlPO_4$	1073	XRD	Gellert et al.[226]

stability against humidity follows the order $Li_7La_3Sn_2O_{12}$ > $Li_7La_3Hf_2O_{12}$ > $Li_7La_3Zr_2O_{12}$,[178] and a perovskite-type electrolyte with chemical composition of $Li_{0.38}Sr_{0.44}Ta_{0.7}Hf_{0.3}O_{2.95}F_{0.05}$ shows no reaction with water in $3 \leq pH \leq 14$, which was confirmed by Raman spectra at different states (Figure 6d).[209] In addition, better chemical stability of sulfides can be achieved by substitution of P by Sn or As, and As partially substituted Li_4SnS_4 delivers high air stability without compromise of conductivity.[163] Very recently, a series of newly reported sulfide SSEs, such as $Li_4Cu_8Ge_3S_{12}$ (Figure 6e)[210] and $Li_{4-x}Sb_xSn_{1-x}S_4$,[211] designed based on HSAB theory, show high air stability (Figure 6f).

4.1.1.4.3. Postsynthesis Treatments. As the additives and composition modifications usually lead to the compromises in ionic conductivity, the postsynthesis treatments of the SSEs can be regarded as efficient and low-cost methods to achieve impurity-free SSEs, especially for dense oxide SSE pellets. High temperature treatment has been utilized to remove surface Li_2CO_3; for example, Wu et al.[212] reported that a Li_2CO_3-free garnet pellet and stable Li−LLZTO interface can be achieved by sintering the pellet at 900 °C. However, it should be noted that the temperature should be chosen carefully, as high temperature leads to Li loss and thus low ionic conductivity, while insufficient calcination cannot fully remove the surface Li_2CO_3; Li et al.[213] reported that residual surface impurities exist even after heat treatment at 750 °C. Combining thermal processes with other treatments, like polishing and Li_2CO_3 scavengers, was reported to produce clean SSE pellets. Sharafi et al.[172] suggested that wet polishing combined with heat treatment is preferable in removing the surface impurities. Li et al. reported that heating LLZTO pellets with introduced carbon at 750 °C can remove the surface Li_2CO_3 completely, and stable cycle durability of a Li/Li symmetric cell without short circuit was realized. Very recently, Hou et al.[214] reported a facile, rapid acid treatment process enabling a pure LLZTO surface and stable Li plating/stripping for over 700 h. However, for SSEs, the critical parameters of materials with good chemical stability against air and moisture still remain to be discovered, as does the relationship between chemical composition and stability.

4.1.2. Chemical Stability of Solid-State Electrolyte/Electrode Interfaces. It is generally recognized that a passivation layer forms at the electrolyte/electrode interface to extend the stability window of the liquid electrolytes. In SSBs, interphase layers are also reported to form at electrode/electrolyte, on both cathode and anode sides. In addition, the formation of interphases is driven by chemical and electrochemical processes simultaneously. Note that chemically driven interphase formation happens without external voltage and can be regarded as a slow, static process. Meanwhile, the electrochemical process brings about dynamical evolution with lithium stripping and plating. In this section, the interface

DOI: 10.1021/acs.chemrev.9b00268
Chem. Rev. XXXX, XXX, XXX−XXX

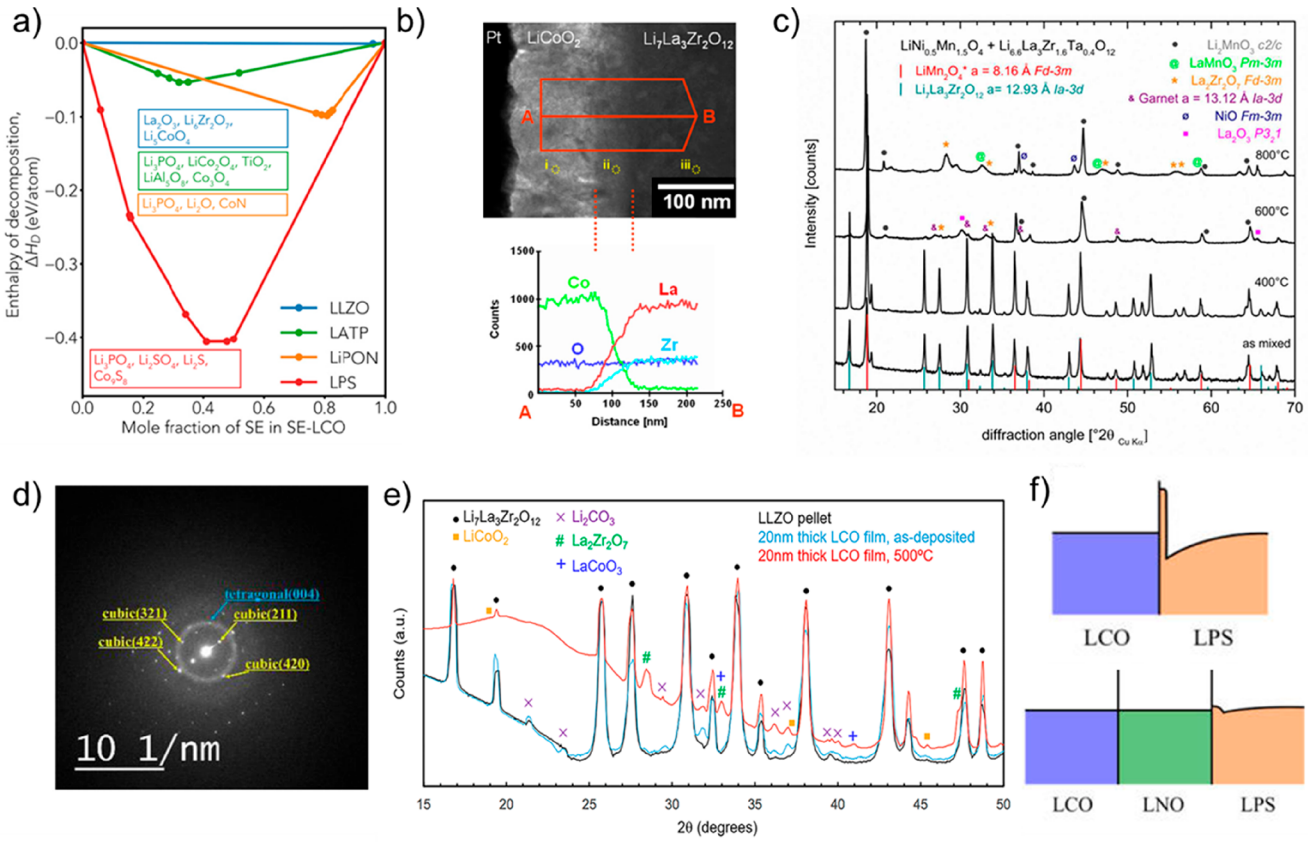

Figure 7. Chemical and structural evolution at cathode/SSE interface. (a) Pseudobinary phase diagram of $LiCoO_2$ and different SSEs calculated by thermodynamic calculations. New phases form exothermically, indicating that the two materials are not chemically stable in contact. The decomposition products with maximum driving force are marked in a box.[215] Reprinted from ref 215, Copyright 2018, with permission from Elsevier. (b) Cross-sectional TEM image and EDS line profiles of $Li_7La_3Zr_2O_{12}/LiCoO_2$ interface.[216] Reprinted from ref 216, Copyright 2011, with permission from Elsevier. (c) XRD patterns of $LiNi_{0.5}Mn_{1.5}O_4$ and $Li_{6.6}La_3Zr_{1.6}Ta_{0.4}O_{12}$ mixture at elevated temperature, new phases begin to appear when temperature reaches 600 °C.[217] Reprinted with permission from ref 217. Copyright 2016 American Chemical Society. (d) TEM images and electron diffraction patterns of $LiCoO_2$ and $Li_7La_3Zr_2O_{12}$ mixture after annealing at 700 °C for 1 h. The tetragonal LLZO phase was observed.[218] Reprinted with permission from ref 218. Copyright 2016 American Chemical Society. (e) Synchrotron XRD profile of the LLZO and LCO interface after 500 °C sintering.[219] Reprinted with permission from ref 219. Copyright 2018 American Chemical Society. (f) Equilibrium interfacial Li concentrations predicted by DFT calculations for the LCO/LPS ($LiCoO_2/\beta$-Li_3PS_4) interface (top) and LCO/LNO/LPS ($LiCoO_2/LiNbO_3/\beta$-Li_3PS_4, bottom). A space charge layer with sharp voltage drop was predicted to form at LCO/LPS interface without LNO coating.[220] Reprinted with permission from ref 220. Copyright 2014 American Chemical Society.

reaction mechanism driven by chemical processes will be discussed.

4.1.2.1. Cathode/Solid-State Electrolyte Interfaces. With the rapid development of novel SSEs, higher lithium ion conductivity comparable to that of liquid electrolytes can be realized. Even so, the assembled ASSBs still exhibit inferior electrochemical performance to their liquid counterparts. The huge resistance between cathodes and electrolytes is the main cause for the poor battery performance. In this section, the main concerns focus on the instability issues involved with chemical reactions. Interdiffusion and the space charge layer effect contribute to the formation of a high-resistance layer, which will be discussed in detail.

4.1.2.1.1. Interdiffusion Issue. Chemical stability of cathode/SSE interfaces was studied by theoretical calculations. Systematic calculations were conducted, and a series of reactions were predicted to occur after the contact between SSEs and cathodes, which are summarized in Table 4. Decomposition reactions were predicted for cathode and SSE (Figure 7a). As shown in Figure 7b, a 100 and 50 nm interdiffusion layer can be detected by TEM combined with EDS line profile for $LiCoO_2$/LLZO[216] and $LiCoO_2/Li_3PS_4$,[221] respectively. The as formed interphase between LLZO and thin film $LiCoO_2$ cathode was suggested to be La_2CoO_4, as reported by Kim et al.[216] However, no observable decomposition products can be found experimentally if the cathodes and SSEs particles are simply mixed together,[222] indicating the cathode/SSE reaction may be kinetically slow when contact is insufficient or at room temperature, which makes it hard to detect by bulk characterization techniques like XRD. Nevertheless, the cathode/SSE reactions become more pronounced at high temperature, since a high temperature cosintering process is widely adopted in oxide electrolyte based ASSBs to obtain an intimate contact between cathodes and SSE particles. As shown in Table 4, it was found that the mixture of LATP and oxide materials exhibits rapid decomposition even at temperatures as low as 500 °C. The interfacial reactions can be explained by the thermodynamically favorable formation of lithium-free compounds, whereas the extracted lithium is likely to form Li_3PO_4 when contacting with cathodes, thus leading to a lower decomposition temperature. A similar reaction was also observed in a $LiNi_{0.5}Mn_{1.5}O_4/Li_{6.6}La_3Zr_{1.6}Ta_{0.4}O_{12}$ mixture at

DOI: 10.1021/acs.chemrev.9b00268
Chem. Rev. XXXX, XXX, XXX−XXX

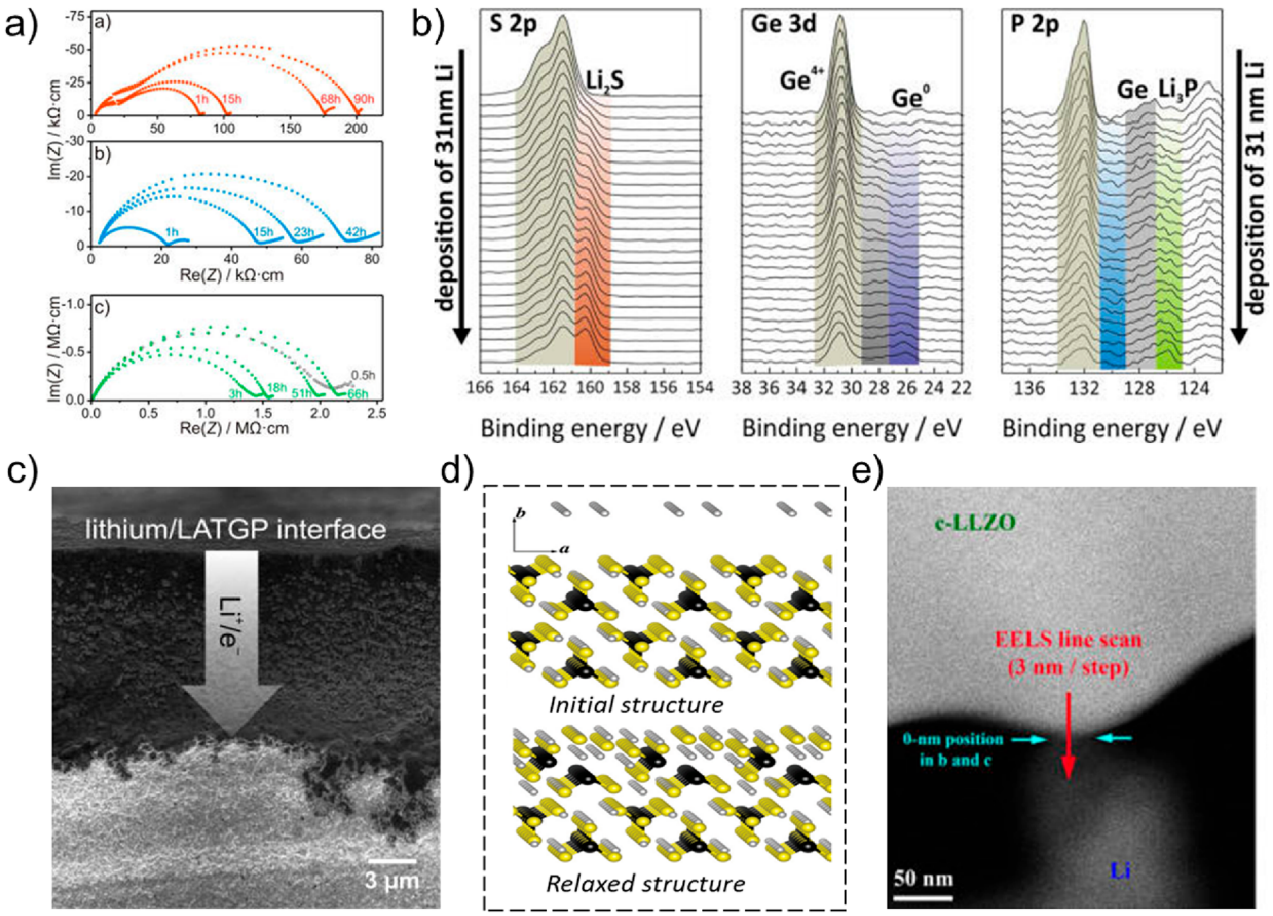

Figure 8. Interphase formation at lithium anode/SSE interface. (a) Time dependent impedance spectra of Li/NASICON SSE/Li symmetric batteries.[229] (b) *In situ* XPS spectra during Li deposition on $Li_{10}GeP_2S_{12}$. The formation of Li−Ge alloys were observed.[228] Reprinted with permission from ref 228. Copyright 2016 American Chemical Society. (c) SEM cross-section image of LATGP/Li interface after approximately 12 h contact.[229] Panels a and c are reprinted with permission from ref 229. Copyright 2013 American Chemical Society. (d) Initial structure and relaxed structure of Li_3PS_4 with Li on the surface. The Li, P, and S atoms are displayed in gray, black, and yellow colors. A Li_2S layer is predicted to form after full structure relaxation. Reprinted with permission from ref 231. Copyright 2013 by the American Physical Society. (e) HAADF-STEM image of LLZO/Li interface. The O K-edge across the interface was obtained by EELS with a 3 nm step size. A 6 nm layer (less than the length of 5 unit cells) with different chemistry or structure was formed at the LLZO/Li interface.[241] Reprinted with permission from ref 241. Copyright 2016 American Chemical Society.

high temperature (Figure 7c,d). Vardar and co-workers carried out a detailed structure and composition study to prove that Li_2CO_3, $La_2Zr_2O_7$, and $LaCoO_3$ are the most likely interfacial reaction products during the sintering process. (Figure 7e) It should be noted that Li-free decomposition products may block the ionic transport and result in high interfacial resistance, which brings in large polarization and poor full cell performance. Therefore, the architecture of oxide based ASSBs still calls for further research efforts to achieve intimate interfacial contact at low temperature.

4.1.2.1.2. Space Charge Layer Theory. The space charge layer model was also used to describe the high cathode interfacial resistance, especially for sulfide based ASSBs, as sulfide electrolytes were soft enough to achieve intimate contact with active materials when external pressure was applied.[152] Haruyama et al.[220] carried out the first DFT calculations on the space charge layer effect between LCO and Li_3PS_4. The lithium ion is expected to transfer to the LCO side under the different chemical potential between electrolyte and cathode. However, when the active materials exhibit both ionic and electronic conductive properties, the Li^+ concentration gradient will be compensated by electrons, which results in continuous transport of Li^+ from the sulfides. The lithium ion redistribution thus leads to a carrier depletion zone on the sulfide side, which hinders lithium transport in the charge/discharge process (Figure 7f). This depletion was confirmed by a steep drop of potential across the cathode/electrolyte interface, which was detected by Yamamoto et al.[223] with electron holography. Although the space charge layer is utilized to understand the large interfacial resistance, the chemical nature of this layer is still unclear. In addition, the interfacial behaviors may become more complicated with the application of external potential, which will be further discussed in section 4.2.

4.1.2.2. Lithium/Solid-State Electrolyte Interfaces. 4.1.2.2.1. Formation of Lithium/Solid-State Electrolyte Interphases. It was reported that Li−Li symmetric batteries with SSEs demonstrate an increase in resistance, which was observed from polymer to inorganic electrolyte-based batteries, as shown in Figure 8a. These studies on resistance were carried out at time scale ranging from several hours to hundreds of hours. The measured resistance of the passivation layer is reported to be proportional to its thickness, and the resistance increase can therefore be attributed to the growth of lithium/

DOI: 10.1021/acs.chemrev.9b00268
Chem. Rev. XXXX, XXX, XXX−XXX

Table 5. Interfacial Reactions of Different SSEs with Metallic Lithium

material type	material composition	reaction behavior with Li metal	characterization method	ref
garnet	$Li_7La_3Zr_2O_{12}$	not observed	preliminary color change	Murugan et al.[27]
	$Li_7La_3Zr_2O_{12}$	6 nm tetragonal LLZO-like interphase formation	EELS	Ma et al.[241]
	$Li_{6.4}Fe_{0.2}La_3Zr_2O_{12}$	130 μm interphase layer formation	Raman mapping	Rettenwander et al.[242]
perovskite	$Li_{0.33}La_{0.56}TiO_3$	Reduction of Ti^{4+} to Ti^{3+} and oxidized Li insertion	XPS, SIMS	Yang et al.[243]
NASICON	$Li_{1.5}Al_{0.5}Ti_{1.5}(PO_4)_3$	Formation of TiAl, Li_3P, Li_2O, Ti_3P	DFT	Zhu et al.[233]
	$Li_{1.5}Al_{0.5}Ti_{0.83}Ge_{0.67}(PO_4)_3$	$6Li_{1.5}Al_{0.5}Ti_{0.83}Ge_{0.67}(PO_4)_3 + 13Li \rightarrow 3AlPO_4 + 6Li_3PO_4 + 5TiPO_4 + 4LiGePO_4$	DFT	Wu et al.[244]
	$Li_{1.5}Al_{0.5}Ge_{1.5}(PO_4)_3$	$Li_{1.5}Al_{0.5}Ge_{1.5}(PO_4)_3 + aLi + bC \rightarrow Li_{1.5+x}Al_{0.5}Ge^{4+/3+}{}_{1.5}(PO_{4-\delta})_3 + cLi_2O + dLi_2O_2 + bLi_2CO_3$	XPS	Chung et al.[245]
	$Li_{1.6}Al_{0.5}Ti_{0.95}Ta_{0.5}(PO_4)_3$	Reduction from Ti^{4+} to Ti^{3+}	XPS	Hartmann et al.[229]
	$LiZr_2(PO_4)_3$	$LiZr_2(PO_4)_3 + 24Li \rightarrow 2Li_8ZrO_6 + 3Li_3P$	XRD	Li et al.[141]
sulfide	$Li_7P_3S_{11}$	$Li_7P_3S_{11} + 24Li \rightarrow 11Li_2S + 3Li_3P$	XPS	Wenzel et al.[230]
	$Li_{10}GeP_2S_{12}$	$Li_{10}GeP_2S_{12} + 23.75Li \rightarrow 12Li_2S + 2Li_3P + 1/4\ Ge_4Li_{15}$ or $Li_{10}GeP_2S_{12} + 20Li \rightarrow 12Li_2S + 2Li_3P + Ge$	XPS	Wenzel et al.[228,232]
	Li_3PS_4	Li_2S formation	DFT	Lepley et al.[231]
	Li_4GeS_4	$7.75Li + Li_4GeS_4 \rightarrow 0.25Li_{15}Ge_4 + 4Li_2S$	DFT	Zhu et al.[247]
	Li_6PS_5X (X= Cl, Br, I)	$Li_6PS_5X + 8\ Li \rightarrow 5\ Li_2S + Li_3P + LiX$	XPS	Wenzel et al.[248]
polymer	PEO/LiTFSI	Formation of a passive layer which consists of RO-Li[a] and LiF	XPS	Xu et al.[236]
	NP[b]/LiTFSI	LiF formation	XPS	Ismail et al.[235]
	NP[b]/$LiBF_4$	LiF formation	XPS	Ismail et al.[235]
	PEO/$LiClO_4$	Formation of a passive layer	EIS	Munichandraiah et al.[249]

[a]RO-Li represents lithium alkoxide species defined by the O 1s XPS peak at 530.6 eV. [b]NP is a solid polymer electrolyte prepared from monoacrylated and triacrylated copolymer of ethylene oxide and propylene oxide.

SSE interphases. In addition, greater and sharper increments of resistance were observed in SSEs with Ti and Ge elements, which may be related to the reduction of Ti^{4+} and Ge^{4+}.[227] It should be noted that the resistance of Li/polymer/Li became stable after 25 days, while the electrolyte pellet was totally broken down in the case of LAGP, which may illustrate the different reaction behaviors between inorganic and polymer electrolytes. To quantify the increment of interfacial resistance, Wenzel et al.[228] observed the LGPS/Li interfacial reaction by *in situ* XPS (Figure 8b) and verified the dependence of the interphase layer thickness on the reaction time, by assuming Li_2S as the main component of the interphase. It can be inferred from the obtained relationship that the growth of the interphase may be controlled by a diffusion process, and a 370 nm thickness interphase was predicted for LGPS/Li after one year of contact.

Hartmann et al.[229] observed that an interphase layer with a thickness of 20 μm formed after NASICON LATTP electrolyte contact with Li metal (Figure 8c). The ionic and electronic properties of the newly formed interphases were further studied, and the obtained electronic conductivity for the interface layer was found to be about 3 orders of magnitude higher than that of the bare SSE. The interfacial ionic/electronic region was therefore defined as a "mixed conducting interphase" (MCI), and the electronic conductive nature of the interphases was attributed to the formation of Li−Ti/Ge alloys, which were confirmed by *ex-situ* XPS characterization. Later on, an *in situ* XPS approach developed by Wenzel et al.[230] was further utilized to study the interfacial reactions of another Ti containing SSE, LLTO. The argon ion beam in the XPS system was used to sputter lithium, the interphases formed and then were studied by *in situ* XPS. Ti^{3+}, Ti^{2+}, and Ti^0 species were found as Ti^{4+} reduction products, which implied compositions of Ti_2O_3, TiO, Ti, and Li_2O. The resulting MCI layer, as well as in NASICON electrolytes, was believed responsible for the continuous degradation of the SSE/Li metal interface. Similar electronic conductive products and interfacial degradation behavior were also found in interphases of Li/LGPS. However, some sulfide electrolytes, such as β-Li_3PS_4, were reported to be compatible with Li metal and can deliver long cycle life in Li−Li symmetric cells.[147] First-principles calculations conducted by Lepley et al.[231] revealed that metallic Li could react with Li_3PS_4, leading to formation of Li_2S as represented in Figure 8d. The Li_2S layer was considered to form in the first few cycles, which was believed to be beneficial to the cycle compatibility with Li metal. Similarly, a 2 nm passive layer, which contains Li_2S species, was also observed at the Li/$Li_7P_3S_{11}$ interface.[232] The reaction of Li metal and sulfide electrolytes was further confirmed by DFT calculations.[224,233] Moreover, the thin Li_2S layer that formed in the first few cycles was claimed to serve as a passive layer, which inhibited further reduction of electrolytes. The passive layer, which is much like the SEI in liquid electrolytes, was also reported in thin film LiPON based lithium batteries.[234] The stable ionic conductive interphases were considered as the origin of the good cycle performance. Nevertheless, a similar passivation layer, which mainly contains LiF and lithium alkoxide species, was also observed by XPS in polymer SSBs[235,236]. Since the LiF exhibits relatively slow ionic transport dynamics,[237] the kinetics of the solid polymer batteries may be controlled by this LiF containing interphase. It is worth noting that within polymer−inorganic composite electrolytes, the polymer component may act as a buffer layer to isolate the direct contact and severe reaction between organic species and Li metal. In a specially designed SSE with $Li_7P_3S_{11}$ wrapped with PEO−$LiClO_4$, the interface reaction between $Li_7P_3S_{11}$ and Li anode can be effectively suppressed.[238] Hence, the chemical stability of polymer−inorganic

DOI: 10.1021/acs.chemrev.9b00268
Chem. Rev. XXXX, XXX, XXX−XXX

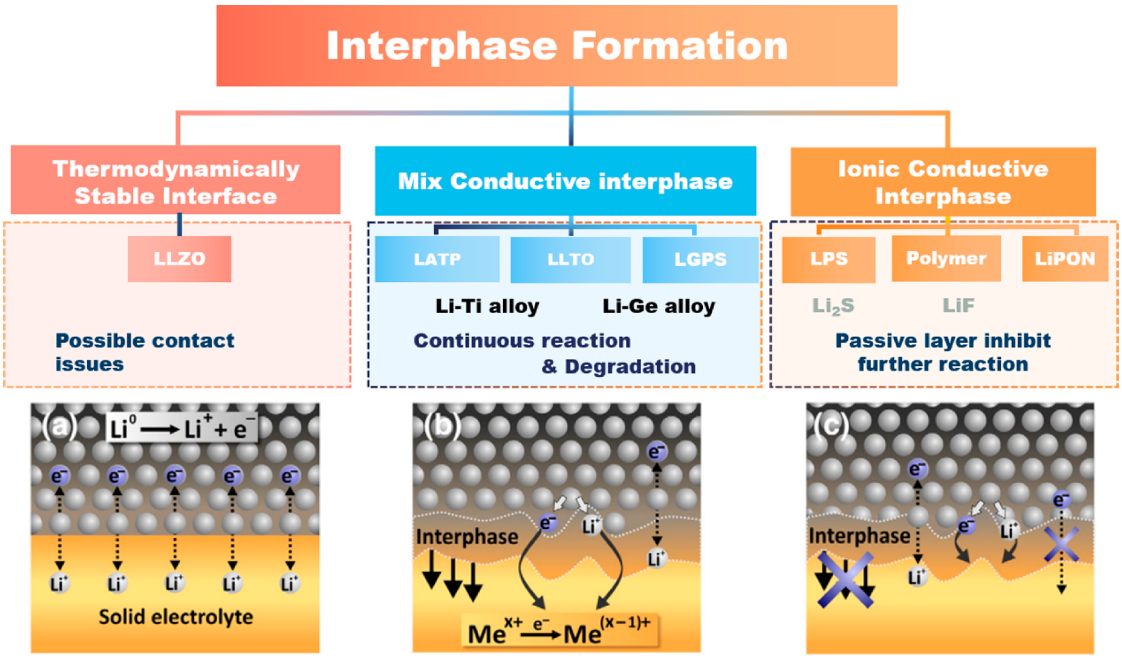

Figure 9. Illustration of three types of interphases between SSE and metallic lithium.[230] Reprinted from ref 230, Copyright 2015, with permission from Elsevier.

composite electrolyte against Li metal is a very complicated issues, which is determined not only by the stability of each component itself but also by the spatial distribution of each species. Moreover, chemical instability between polymer and inorganic components will further add to the interface reaction process. In PEO−$Li_{10}SnP_2S_{12}$ based composite electrolyte, the formation of polysulfides, P-[S]$_n$-P like bridged PS_4^{3-} units, and sulfite, SO_3^{2-}, were demonstrated due to the chemical degradation between LSPS with PEO.[239,240] These studies reveal the essential role of the interphase properties.

On the other hand, for garnet SSEs, especially for LLZO based electrolytes, both experiments and DFT calculations demonstrated their stability. Kotobuki et al.[114] examined the XRD patterns of the LLZO after Li contact, and the characteristic peaks remained the same. Then Wolfenstine et al.[250] compared the Li 1s XPS spectra of LLZO before and after contact with molten lithium; it was revealed that the oxidation state of Li was identical before and after contact. The authors also reported that the color of the garnet pellet turned gray after immersion into molten Li, which was also reported by Rettenwander et al.[242] Nevertheless, this phenomenon could be well explained by the formation of color centers;[251] when Li metal contacts the pellet, Li atoms diffuse into the LLZO to form Li ions and electrons, followed by the formation of a color center, which originates from electron trapping by oxygen. Ma et al.[241] observed that a 6 nm Li-rich tetragonal-LLZO-like layer formed after contact with Li (Figure 8e), which further supports the "color center" theory. The stability between Li and LLZO was also studied by first-principles calculations. Zhu et al.[252] reported that garnet electrolytes show the lowest reduction potential of 0.05 V and the least favorable reaction energy of 49 kJ/mol. Wu et al.[244] determined that the Gibbs free energies for all the possible reaction formulas between Li and LLZO are positive, which indicates that these reactions are thermodynamically unfavorable. It therefore can be concluded that both experimental studies and theoretical calculations confirm the thermodynamic stability of the Li/LLZO interface, as summarized in Table 5. However, on the other hand, some recent studies have shown that the stability of garnets against metallic lithium may be cation dependent. Zhu et al.[253] combined experimental and computational methods and reported that the stability of LLZO with different dopants exhibits unequal extents of reduction. Obvious Nb^{5+} to Nb^{4+} and Nb^{3+} reduction when lithium was deposited onto polished Nb doped LLZO (LLZNO) was observed by *in situ* XPS method, accompanied by a small amount of Zr^{4+} to Zr^{2+} reduction, while the Ta doped LLZO showed a much lower extent of reduction under lithium deposition. Therefore, a deeper understanding about the element-dominated interfacial chemistry between SSEs and lithium is expected.

4.1.2.2.2. Classifications of Interphases. Based on the above discussions, interfaces between SSEs and metallic lithium can be categorized into three types based on their electronic and ionic conducting properties (Figure 9): (1) thermodynamically stable interfaces, which do not react with Li metal; (2) mixed conducting interphases (MCI), which can transport ions and electrons simultaneously and thus lead to continuous interfacial degradation; (3) ionic conductive but electronic insulating interphases, which prevent the electrolytes from direct reaction but allow Li ion conduction, much like the "SEI" concept in conventional LIBs.[254,255] This classification was first proposed by Janek and co-workers[230] in 2015. Specifically, the interfaces of Li with LLZO, Li with LLTO and LATP/LAGP, and Li with β-Li_3PS_4 fall into the three types of interface, respectively. The thermodynamically stable interface, which allows decent ion transport, was proposed as the most ideal interface. It should be noted that dendrite growth has been widely observed for type 1 LLZO/Li interfaces, while this phenomenon was less reported in lithium reactive type 2 and type 3 interfaces.[256−261] It was found that interfacial contact loss and the resulting localized electrical field will promote dendrite propagation, which will be detailed in section 4.3; thus the dendrite issues of LLZO/Li interfaces may be raised

DOI: 10.1021/acs.chemrev.9b00268
Chem. Rev. XXXX, XXX, XXX−XXX

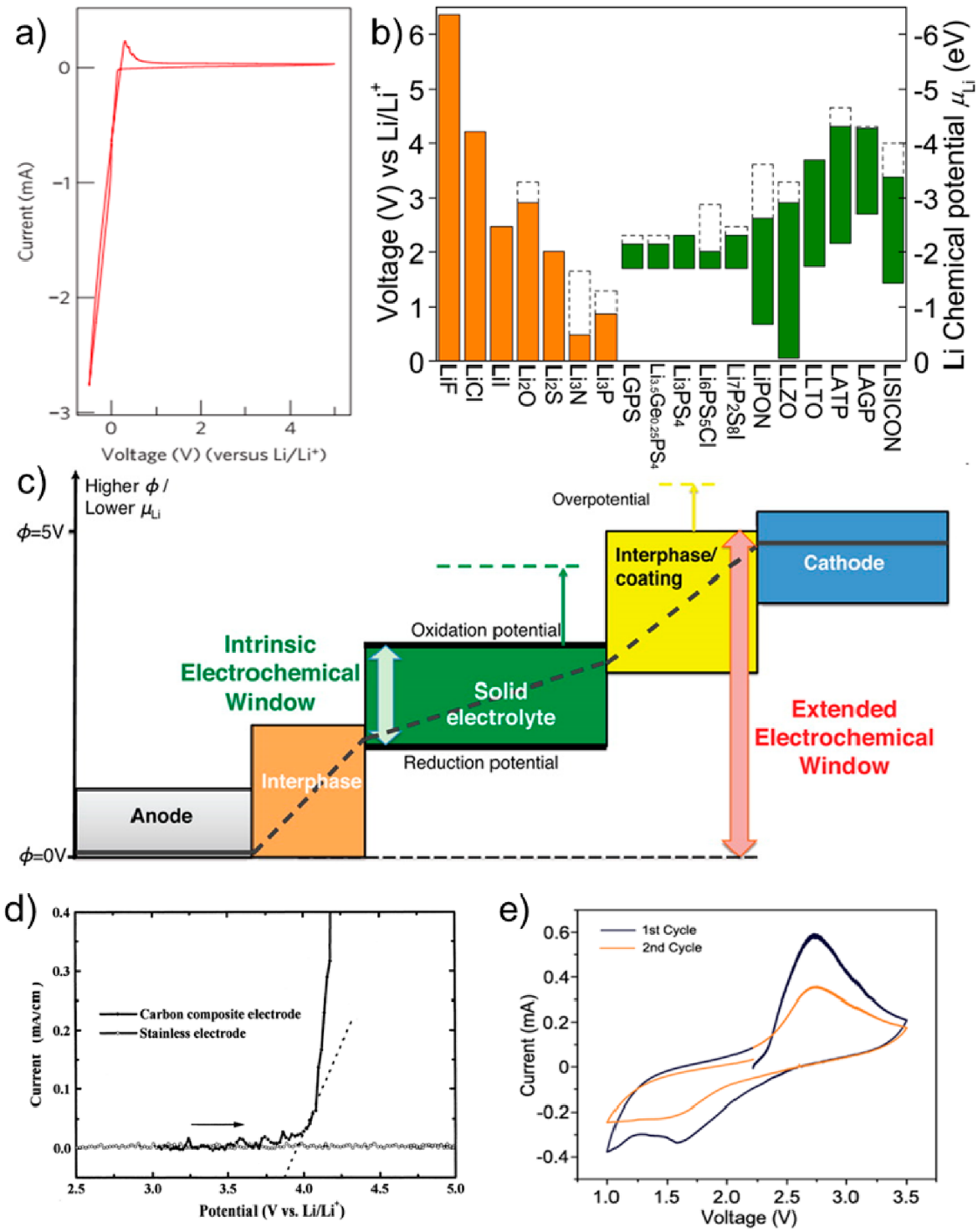

Figure 10. Experiment results and theoretical predictions on electrochemical stability of SSEs. (a) Electrochemical window of LGPS examined by CV test with semiblocking electrode setup.[28] Reprinted with permission from ref 28. Copyright 2011 Nature Publishing Group. (b) Electrochemical stability predicted by DFT calculations.[252] (c) Schematic illustration of the extended electrochemical stability by polarization and interphase formation.[252] Panels b and c are reprinted with permission from ref 252. Copyright 2015 American Chemical Society. (d) LSV of a PEO/LiTFSI electrolyte sandwiched between a lithium disc and a stainless disc or a carbon composite electrode.[281] Reprinted from ref 281, Copyright 2001, with permission from Elsevier. (e) CV test with Li/LGPS/LGPS-C composite electrode. The oxidation and reduction peaks of LGPS were observed in the 0−2 V region and 1.6−2.7 V region, respectively.[285] Reprinted from ref 285 with permission. Copyright 2018 John Wiley and Sons.

from the more significant contact issues, as the contact degradation in reactive SSE based batteries can be alleviated by reaction with surface metallic lithium.[244,262] In addition, once the deposited Li contacts the reactive SSE, penetrating lithium

DOI: 10.1021/acs.chemrev.9b00268
Chem. Rev. XXXX, XXX, XXX−XXX

can be consumed by type 2 and type 3 SSEs. However, for type 2 interfaces, the MCI becomes thicker during cycling, which leads to increased impedance and large polarization and eventually terminates the cell.[229] Hence, not type 1 or type 2 but type 3, the electronic insulating and ionic conducting interface, is highly desirable. Wang's group reported the electronic conductivity of SSEs as the origin of lithium dendrite deposition,[263] which further emphasizes the critical role of type 3 interphases.

4.2. Electrochemical Stability

The high electrochemical stability of many SSEs was considered as an advantage in their early studies. However, the poor battery performance of SSBs reported in recent years challenged this point of view.

4.2.1. Electrochemical Stability of Solid-State Electrolytes. It was reported that, even for some SSEs that exhibit electrochemical windows up to 5 V (Figure 10a), poor cathode compatibility was observed. In addition, theoretical studies displayed different results regarding the electrochemical stability of SSEs. In this section, the high electrochemical stability and unsatisfactory battery performance, the deviation between experiments and calculations, and their hidden mechanisms will be discussed.

4.2.1.1. Electrochemical Stability of Inorganic Solid-State Electrolytes. Inorganic electrolytes were expected to exhibit much wider electrochemical windows because they are not limited by lithium salts and organic components. In fact, the electrochemical window obtained by CV with a Li/SSE/block electrode setup was indeed far beyond the upper limits of conventional liquid electrolytes, as summarized in Table 6.

For sulfides, although a wide electrochemical window was observed, irreversible initial capacity loss was also demonstrated in sulfide electrolyte based full cells.[221] AC impedance analysis was conducted showing the large polarization on the cathode. The cathode side interfacial resistance demonstrates continuous growth under high potential or long cycle processes.[55] An interphase layer on the cathode side was therefore proposed as the origin of the increased polarization,[264] which will be further discussed later.

Oxides exhibit a similar dilemma as sulfide electrolytes. CV tests with semiblocking setup electrodes demonstrate the wide electrochemical windows of oxides, as summarized in Table 6. Based on the observed wide electrochemical window, oxide electrolytes are expected to well match the high voltage electrodes, such as LNMO[265] and LCO.[266,267] However, acceptable battery performances are rarely reported when oxide SSEs match with those cathode materials.

4.2.1.2. Electrochemical Stability of Solid Polymer Electrolytes. The electrochemical stability of polymer electrolytes has long been considered a main challenge for SSE applications in high voltage battery systems. Therefore, cathodes with low charge/discharge platform, such as $LiFePO_4$[268] and V_2O_5,[269,270] were usually utilized in solid polymer lithium batteries. LSV was performed to examine the electrochemical window of solid polymer electrolytes, and it was reported that the electrochemical stability of polyether-derived electrolytes was in the range 3.7−4.5 V.[134,271,272]

However, it was also found that copolymer SSEs exhibited enhanced electrochemical stability; for example, a solid polymer electrolyte with the composition PAN−PEO−$LiClO_4$ was reported to be stable up to 4.8 V[75] vs Li/Li^+. In addition, a block copolymer electrolyte with the configuration P(STFSILi)-*b*-PEO-*b*-P(STFSILi) delivered high electrochemical stability up to at least 5 V. These findings demonstrate the feasibility to enhance electrochemical stability of polymer electrolytes by copolymer strategy.[273]

Still, there are some other issues that affect the observed electrochemical stability. Some LSV or CV tests with a semiblocking electrode setup revealed the high electrochemical stability of polymer electrolytes above 4.5 V,[274,275] which should be suitable for 4 V class cathodes (e.g., $LiCoO_2$, $LiMnO_2$, etc.). However, a reasonable electrochemical performance of solid polymer batteries was rarely reported. Li et al.[276] examined the critical voltage of solid polymer

Table 6. Electrochemical Window (EW) for Different SSEs Examined by Experimental or Theoretical Methods

solid-state electrolyte	EW (V)	method	ref
PEO/LiTFSI	0−4.7	LSV	Wen et al.[277]
P(STFSILi)−PEO−P(STFSILi)[a]	0−5	CV	Bouchet et al.[273]
20 wt % poly-Ac1b[b] + 80 wt % PEO/LiTFSI	0−4.9	LSV	Wen et al.[277]
PEO/$LiClO_4$	0−4	LSV	Michael et al.[278]
PEO/$LiClO_4$−$BaTiO_3$	0−4	LSV	Michael et al.[278]
PEO/$LiClO_4$−10 wt % γ-$LiAlO_2$	0−4	LSV	Capuano et al.[272]
PEO/$LiBF_4$ + 20 wt % γ-$LiAlO_2$	0−3.7	LSV	Appetecchi et al.[271]
PAN−PEO−$LiClO_4$[a]	0−4.7	LSV	Yuan et al.[75]
PEO/LiTFSI	0−4.25	LSV and CV	Zhang et al.[279]
PEO/LiTFSI−LLZTO	0−4.75	LSV and CV	Zhang et al.[279]
PEO/LiTFSI	0−4	LSV	Wang et al.[280]
PEO/LiTFSI−LLTO	>4.5	LSV	Wang et al.[280]
PEO/LiTFSI	0−3.8	LSV with composite electrode	Xia et al.[281]
Li_3PS_4	0−5	CV	Liu et al.[147]
$Li_{3.25}Ge_{0.25}P_{0.75}S_4$	0−5	CV	Kanno and Murayama[117]
$Li_{9.42}Si_{1.02}P_{2.1}S_{9.96}O$	0−5	CV	Hori et al.[282]
$Li_{9.81}Sn_{0.81}P_{2.19}S_{12}$	0−5	CV	Hori et al.[282]
$Li_{10}GeP_2S_{12}$	0−5	CV	Hori et al.[282]
$80Li_2S{\cdot}20P_2S_5$	0−10	CV	Hayashi et al.[283]
Li_6PS_5Cl	0−7	CV	Boulineau et al.[284]
$Li_{10}GeP_2S_{12}$	1.7−2.1	CV with composite electrode	Han et al.[285]
$Li_{7-x}La_3(Zr_{2-x}, Nb_x)O_{12}$ (x = 0−2)	0−9	CV	Ohta et al.[286]
$Li_{1.5}Al_{0.5}Ge_{1.5}(PO_4)_3$	0−6	CV	Feng et al.[227]
$Li_7La_3Zr_2O_{12}$	0−4.0	CV with composite electrode	Han et al.[285]
$Li_{10}GeP_2S_{12}$	1.71−2.15	DFT	Zhu et al.[233]
Li_3PS_4	1.71−2.31	DFT	Zhu et al.[233]
Li_6PS_5Cl	1.71−2.01	DFT	Zhu et al.[252]
$Li_7P_2S_8I$	1.71−2.31	DFT	Zhu et al.[252]
$Li_7La_3Zr_2O_{12}$	0.05−2.91	DFT	Zhu et al.[233]
$Li_{0.33}La_{0.56}TiO_3$	1.75−3.71	DFT	Zhu et al.[233]
$Li_{1.3}Al_{0.3}Ti_{1.7}(PO_4)_3$	2.16−4.31	DFT	Zhu et al.[233]
$Li_{1.5}Al_{0.5}Ge_{1.5}(PO_4)_3$	2.70−4.27	DFT	Zhu et al.[252]

[a]P(STFSILi), poly(styrene trifluoromethanesulfonylimide of lithium). [b]poly-Ac1b, hyperbranched poly[bis(triethylene glycol)-benzoate] with terminal acetyl groups.

DOI: 10.1021/acs.chemrev.9b00268
Chem. Rev. XXXX, XXX, XXX−XXX

batteries by applying different cutoff voltages, as it is difficult to exactly distinguish the small currents in the high voltage range.[276] Interestingly, the capacity loss of the batteries demonstrates dependency on cutoff voltages, in which the capacity loss rate was much steeper when the cutoff voltage reached 4 V. In addition, the potential catalytic effect of the electrode and redox reaction between high valence transition metals or even oxygen against reductive polymers will play important parts in interface reactions, while rare literature reports have been published so far particularly focusing on clarifying the detailed interface reaction mechanism. Therefore, it was concluded that 3.9 V should be the upper limit of PEO−$Li(CF_3SO_2)_2N$ polymer electrolyte.[276] The impacts of non-conductive and ionic conductive fillers are also compared in Table 6; a slightly extended electrochemical window resulted from ionic conductive ceramic compositing, even though no detailed investigations have been carried out on clarifying the origin of such effect from different fillers on electrochemical window. The interface interaction between electrolyte components, together with the generally wider electrochemical stability window from ceramic electrolytes can be speculated as the fundamental origin of such experimental phenomenon, while further investigation is still needed.

Therefore, the upper limit of the electrochemical stability with PEO based solid polymer electrolytes may lie around 4 V, and a deeper understanding of the chemical behavior of the cathode/polymer interfaces needs to be further investigated.

4.2.1.3. Theoretic Predictions for Electrochemical Stability of Solid-State Electrolytes. The electrochemical stability or electrochemical windows of SSEs determine the compatibility with high voltage operation. To understand the electrochemical stability of SSEs as well as their compatibility with high voltage cathodes, the intrinsic electrochemical stability on the anode side and cathode side should be examined precisely.

Theoretical studies were utilized to identify the intrinsic electrochemical stability of the SSEs, which attracted great attention in recent years. First-principles calculations were conducted by Zhu et al. and Ceder's group,[224,233,252] and the calculated electrochemical windows of numerous SSEs, including most sulfides and garnets, were much lower than experimental results, as shown in Table 6 and Figure 10b.

The deviation between theoretical and experimental results was attributed to kinetic barriers (Figure 10c). In the reduction limit, for different SSEs, as has been discussed in last section, the decomposition products form an interphase layer between electrolyte and electrode, inhibiting further decomposition. Since the electrochemical potential of lithium is constant across the interface, the electronic insulting interphase results in a drop of electrochemical potential of electrons, which leads to the decrease of chemical potential of lithium along the interphase.[252] The electronic insulting nature of the interphase is essential for passivation, which can explain why some SSEs, for example, LGPS, LAGP, and LLTO, experience continuous interfacial degradation, as the reduction of these electrolytes leads to mixed electronic and ionic conductive interphases.[230] The passivation mechanism was also utilized in liquid batteries, for example, the "water in salt" aqueous electrolyte, of which the electrochemical window was broadened to >3 V by designing a LiF containing interphase.[287] For the oxidation limit, multiple factors can be responsible for the kinetic barriers. First, on the cathode side, most of the oxidation products are electronic insulators, which inhibit continuous reaction. Second, the release of some oxidized products, like O_2, may display slow kinetics.[252] Third, the electrochemical stability of SSEs was usually examined by CV with a Li/SSE/Au(Pt) semiblocking electrode setup. This setup results in sluggish interfacial reaction kinetics, due to the limited contact between the SSE and the current collector. The small anodic and cathodic currents, as a result of insufficient contact, as well as the high Li deposition/stripping peak, make the reaction peaks of the electrolytes too difficult to detect.[63,285]

4.2.1.4. Examining the Intrinsic Electrochemical Stability. To estimate the intrinsic electrochemical windows of SSEs, Han et al.[63] developed a new Li/SSE/SSE+carbon/Pt construction for CV. The improved contact between carbon and electrolytes enables fast reaction kinetics, thus making it possible to identify the intrinsic electrochemical window. Using this setup, CV shows that the reduction of LGPS started from 1.7 V, while oxidation occurred after 2.1 V (Figure 10d); the examined 1.7−2.1 V electrochemical window agrees well with previous theoretical reports. Actually, the composite electrode setup was first reported in 2001.[281] It was found that the onset of the oxidizing potential determined by LSV or CV with a blocking electrode (e.g., stainless steel) was generally 1 V higher than the starting voltage of decomposition in a real battery system. A composite electrode consisting of 60 wt % polymer electrolytes and 40 wt % carbon was prepared by hot-pressing technique and utilized in LSV. The obtained upper limit voltage of PEO based electrolytes was about 3.8 V vs Li/Li^+ (Figure 10e), which is highly consistent with the practical upper limit voltage determined by controlling the cutoff voltage.[276,281] Therefore, CV/LSV with a composite electrode setup can be an efficient way to determine the intrinsic electrochemical stability window of SSEs.

Examining the lithiation/delithiation potential also provides information about the electrochemical stability of SSEs. For example, the Li_3PS_4/carbon composite electrode exhibits a charging voltage plateau at around 3.0 V,[288] and Hua et al. reported that the lithiation potential of LLTO was around 1.5 V,[289] which is highly consistent with the calculated upper and lower limit of electrochemical windows of Li_3PS_4 and LLTO, respectively.

It should be noted that the impurities involved in materials synthesis may disturb the detected electrochemical window even with the improved test method. As demonstrated by Li et al.,[213] the electrochemical decomposition of LLZO above 3 V may come from the surface adsorbed Li_2CO_3; the as prepared Li_2CO_3-free LLZO demonstrates high electrochemical stability and well matches with $LiCoO_2$. Therefore, the influence of the secondary phase on the measurements of electrochemical stability should be carefully considered.

4.2.2. Electrochemical Stability at Electrolyte/Electrode Interfaces. Actually, the SSE/electrode interfacial reactions at the cathode and anode sides determine the electrochemical stability of SSEs. The interfacial reactions driven by chemical processes have been discussed in section 4.1.2. In this section, interfacial behaviors during charge/discharge will be summarized. For the cathode side, reactions and interphase formation under high voltage are discussed, while at the Li anode side, the chemical stability of Li metal is equivalent to the electrochemical stability at 0 V vs Li/Li^+. To distinguish the dynamic electrochemical process from the interfacial chemical reactions, the evolution of Li/SSE interphases will be emphasized in this section.

4.2.2.1. Cathode/Solid-State Electrolyte Interfaces. On the cathode side, interphase formation driven by electrochemical

DOI: 10.1021/acs.chemrev.9b00268
Chem. Rev. XXXX, XXX, XXX−XXX

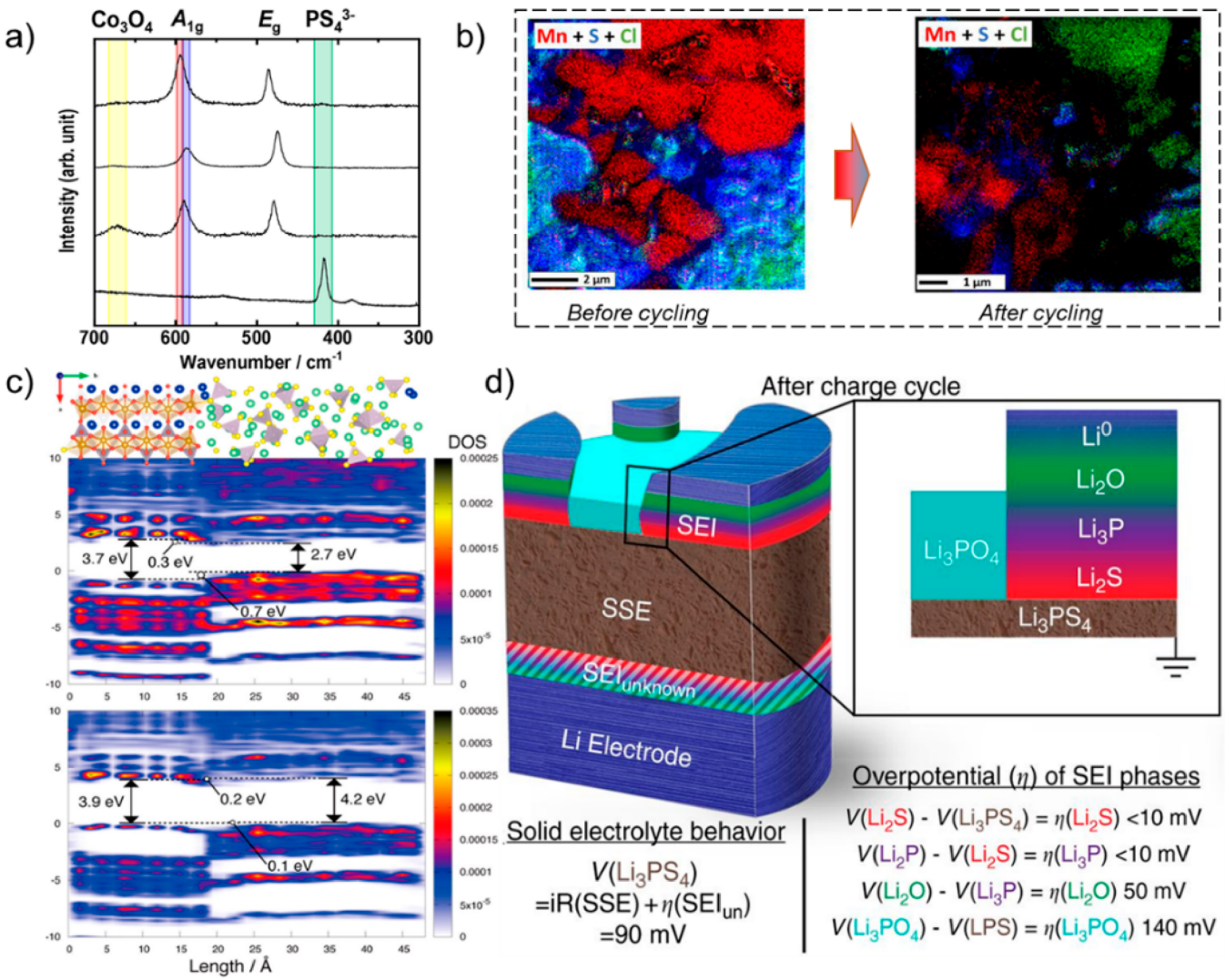

Figure 11. Chemical and structural evolution of electrode/SSE interfaces during charge/discharge. (a) Raman spectra of the $LiCoO_2/Li_2S-P_2S_5$ composite cathode in an ASSB with sulfide electrolyte. Co_3O_4 was observed on the cathode surface after the initial charge.[290] Reprinted from ref 290, Copyright 2016, with permission from Elsevier. (b) SEM image and scanning Auger microscopy (SAM) mapping for $LiMn_2O_4/Li_6PS_5Cl/Li-In$ cell before (left) and after (right) cycling. The continuous connected S-rich area and Cl-rich area become separated after cycling, which indicates the decomposition of the Li_6PS_5Cl electrolyte.[292] Reprinted with permission from ref 292. Copyright 2017 American Chemical Society. (c) Contour maps of beta electron layered density of states (LDOS) at the $Li_3PS_4/LiFePO_4$ interface. Top and bottom LDOS calculated with the +U level and HSE06 hybrid functional level (two calculation methods). The valence band maximum (VBM) of Li_3PS_4 is slightly higher than that of $LiFePO_4$.[296] Reprinted with permission from ref 296. Copyright 2017 American Chemical Society. (d) 3D schematic illustration of SEI composition and morphology on sulfide SSE after charge, which displays an inhomogeneous interphase layer of Li/sulfide electrolyte interface. The overpotential for each component of the SEI is given.[307] Reprinted with permission from ref 307. Copyright 2018 Nature Publishing Group.

potential will happen during charge/discharge. The interfacial behaviors under external voltage are different for various electrolytes and strongly affected by cell pretreatment conditions, which makes the interfacial behavior more complicated.

4.2.2.1.1. Sulfide Electrolyte/Cathode Interfaces. For sulfide SSEs, to obtain the chemical nature of interphases, both experimental and theoretical works were performed. Mutual diffusion of elements and interphase formation with Co and S after initial charge[221] were observed by TEM combined with EDS line profiles; both were claimed to contribute to the large interfacial resistance.[221] Raman and XPS measurements were carried out to clarify the chemical nature of the as formed interphases. Otoyama et al.[290] reported the composition and distribution of sulfide/cathode interfacial reaction products with Raman imaging technique. Co_3O_4, which was reported to be detrimental to battery performance and normally appeared in liquid systems when $LiCoO_2$ was overcharged, was observed (Figure 11a).[291] In addition, the distribution of the Co_3O_4 was not uniform, which suggested that overcharge may occur locally in composite electrodes. Auvergniot et al.[292] reported that Li_6PS_5Cl oxidized into S, LiCl, P_2S_x, and LiCl as determined by Auger electron spectroscopy (Figure 11b). The reaction behavior on the sulfide side was also examined by XPS; the oxidation of sulfur was observed, and this reaction was more pronounced when carbon additives were involved. The accumulation of sulfur at the interface isolates the ionic conduction and hinders the subsequent oxidation process, which may explain the more severe electrochemical decom-

DOI: 10.1021/acs.chemrev.9b00268
Chem. Rev. XXXX, XXX, XXX−XXX

Table 7. Behaviors of Different SSEs at High Potential

type	solid-state electrolyte	applied potential (vs Li/Li^+)	behavior	method	ref
polymer	PEO/LiDFOB	4.45 V	ring-opening reaction of $DFOB^-$ anion	FTIR	Ma et al.[297]
sulfide	Li_3PS_4	potential of $FePO_4$ (charged $LiFePO_4$)	S−S bonds formation	DFT+U for MD	Sumita et al.[295]
	Li_3PS_4	potential of $FePO_4$ (charged $LiFePO_4$)	PS_4 polymerization	DFT+U for MD	Sumita et al.[296]
	LiP_3S_4	2.31 V	formation of elemental sulfur and P_2S_5	DFT	Zhu et al.[252]
	$Li_7P_3S_{11}$	potential of CoO_2 (charged $LiCoO_2$)	formation of CoS_2, P_2S_5, Li_3PO_4	*ab initio* molecular dynamics (AIMD) simulations	Chu et al.[294]
	Li_6PS_5Cl	4.9 V	formation of elemental sulfur, phosphates, and LiCl	XPS	Auvergniot et al.[292]
	Li_6PS_5Cl	4.0 V	reversible formation of elemental sulfur and polysulfurs	XPS	Auvergniot et al.[292]
	Li_6PS_5Cl	4.6 V	sulfur-containing species (S, Li_2S_n, and P_2S_x) and LiCl	XPS and AES	Auvergniot et al.[292]
	$Li_{10}GeP_2S_5$	2.14 V	formation of LiP_3S_4, GeS_2, and S	DFT	Zhu et al.[252]
garnet	$Li_7La_3Zr_2O_{12}$	2.91 V	formation of Li_2O_2, La_2O_3, and $Li_6Zr_2O_7$	DFT	Zhu et al.[252]
NASICON	$Li_{1.5}Al_{0.5}Ge_{1.5}(PO_4)_3$	4.27 V	formation of $Ge_5O(PO_4)_6$, O_2, $Li_4P_2O_7$, $AlPO_4$	DFT	Zhu et al.[252]
	$Li_{1.3}Al_{0.3}Ti_{1.7}(PO_4)_3$	4.21 V	formation of $Ti_5P_4O_{20}$, $AlPO_4$, TiP_2O_7, O_2	DFT	Zhu et al.[252]
perovskite	$Li_{0.33}La_{0.56}TiO_3$	3.71 V	formation of TiO_2, O_2, $La_2Ti_2O_7$	DFT	Zhu et al.[252]

position in the carbon containing system due to its enhanced electronic conductivity.[293]

Moreover, the interfacial behaviors on the cathode side interface were also reported to be affected by the type of cathode materials. Chu et al.[294] compared the electrochemical decomposition of SSE with different cathodes, as summarized in Table 7; the decomposition products of $LiCoO_2$ based interphases were more distinguished for their better electronic conductivity, which may lead to continuous reaction, as has been discussed before. However, Sumita et al.[295] reported that the VBM of sulfides is higher than that of oxides (Figure 11c). Therefore, even the reaction of sulfide electrolyte and $LiFePO_4$ cathode was limited at the fully discharge state; charge compensation of LPS may be introduced, making the cathode side of LPS become active materials and finally resulting in a lithium depletion zone. The depletion area was further developed due to the formation of S−S bonds and PS_4 polymerization processes.[296] Recently, reversible S−S bond formation was also reported in the charge/discharge process of LPS, which demonstrated the oxidation ability of sulfide electrolytes even at a relatively low potential.[288] Therefore, it is rather difficult for sulfides to obtain high electrochemical stability up to more than 5 V.[28,147] The electrochemical interfacial reactions at the cathode side may be inevitable, while the interfacial reactions are governed by many factors, which make the interfaces become complicated and hard to characterize.

4.2.2.1.2. Oxide Electrolyte/Cathode Interfaces. As for oxide electrolytes, owing to the solid−solid contact between oxide electrolytes and cathode particles, a cosintering process was generally adopted to improve contact, which may bring new interphases and make the interfacial behaviors more complicated.[56,298] Interphases introduced by mutual diffusion in the thermal process were observed and reported to be responsible for the huge interfacial resistance.[216] Low temperature cosintering may partially suppress the mutual diffusion from high temperature. Kim et al.[299] fabricated an LCO/LATP/LiPON/Li film battery by sputtering a 500 nm $LiCoO_2$ film on the NASCION SSE substrate. Although the battery delivered limited charge/discharge capacity, the cathode and SSEs remain intact, and no interphase layer can be observed under high resolution TEM. Rutherford backscattering spectroscopy (RBS) analysis was performed and further confirmed that the $LiCoO_2$/NASCION interface remains unchanged after 50 cycles. However, for garnet electrolytes, irreversible electrochemical decomposition of $LiCoO_2$/LLZO was observed around 3.0 V.[218] In addition, a clear sharp potential drop of the $LiMn_{1.5}Ni_{0.5}O_2$/LLZO/Li battery was observed when the voltage was above 3.8 V. Chemical composition of the high resistance layer was determined by XRD; a new phase of Li_2MnO_3, $(Li_{0.35}Ni_{0.05})NiO_2$, and other impurities was observed on the cycled composite electrodes. The newly formed impurities were attributed to the electrochemical reaction rather than chemical reaction between cathode and SSEs under high voltage, as the thermal process was at a low temperature of 100 °C, which is far lower than the thermal reaction temperature of cathode and garnets.[300] The compatibility of NASICON electrolytes with LNMO cathode was also investigated; it was found that the secondary phases introduced by heat treatment could improve the contact of cathode interphases, while the as assembled ASSBs can only deliver about 2% of the theoretical capacity of $LiMn_{1.5}Ni_{0.5}O_4$.[225] The electrochemical performance was also affected by the type of the cathodes. As summarized in Table 7, the electrochemical decomposition products display different ionic and electronic transport properties, and as has been discussed before, electronic conductive interphases may lead to continuous interfacial reactions. And it was found that, $LiCoO_2$/oxide perovskite electrolytes deliver a higher interfacial resistance, about 6 times larger than $LiMn_2O_4$/oxide perovskite interface.[301] Moreover, the space charge layer effects, as discussed in section 2, may also play a role for inferior electrochemical performance of ASSBs. A sharp voltage drop zone of $LiCoO_2$/NASICON interface was observed in the charge/discharge process, which may result from the formation of a lithium depletion zone.[223] Theoretical studies

DOI: 10.1021/acs.chemrev.9b00268
Chem. Rev. XXXX, XXX, XXX−XXX

Table 8. Modification of SSE/Cathode Interfaces

type	solid-state electrolyte	cathode	modification layer	method	ref
polymer	P(EO/MEEGE)/LiTFSI[a]	$LiCoO_2$	Li_3PO_4	spray coating	Kobayashi et al.[314]
	P(EO/MEEGE)/ $LiN(SO_2CF_2CF_3)_2$[a]	$LiCoO_2$	Li_3PO_4	simple mixing	Seki et al.[305]
	P(EO/MEEGE/AGE)/ $LiBF_4$[b]	$LiCoO_2$	Al_2O_3	spray coating	Miyashiro et al.[315]
	P(EO/MEEGE/AGE)/ $LiBF_4$[b]	$LiCoO_2$	$Li_{1.5}Al_{0.5}Ge_{1.5}(PO_4)_3$	mechanical mixing	Kobayashi et al.[316]
	PEO/$LiClO_4$	$LiNi_{0.6}Co_{0.2}Mn_{0.2}O_2$	$Li_{1.4}Al_{0.4}Ti_{1.6}(PO_4)_3$	sol−gel method	Liang et al.[310]
sulfide	$Li_2S-P_2S_5$	$LiCoO_2$	Li_2SiO_3	sol−gel method	Sakuda et al.[317]
	Li_3PS_4	$Li(Ni_{1/3}Mn_{1/3}Co_{1/3})O_2$	$LiAlO_2$	sol−gel method associated with ultrasonic irradiation	Okada et al.[318]
	$Li_2S-P_2S_5$	$LiNi_{0.8}Co_{0.15}Al_{0.05}O_2$	Li_2O-ZrO_2	sol−gel method	Ito et al.[319]
	$Li_2S-P_2S_5$	$LiCoO_2$	Li_2CO_3	solution method	Kim et al.[320]
	$Li_2S-P_2S_5$	$LiNi_{0.5}Mn_{1.5}O_4$	Li_3PO_4	pulsed laser deposition	Yubuchi et al.[321]
	$Li_{3.25}Ge_{0.25}P_{0.75}S_4$	$LiCoO_2$	$LiNbO_3$	spray-coating	Ohta et al.[322]
	$Li_{3.25}Ge_{0.25}P_{0.75}S_4$	$LiCoO_2$	$Li_4Ti_5O_{12}$	spray-coating	Ohta et al.[323]
	$Li_{10}GeP_2S_{12}$	$LiNi_{0.5}Mn_{1.5}O_4$	$LiNbO_3$	sol−gel method	Oh et al.[60]
	$Li_{10}GeP_2S_{12}$	$LiCoO_2$	$LiNbO_3$	ALD	Wang et al.[324]
	$Li_{3.25}Ge_{0.25}P_{0.75}S_4$	$LiCoO_2$	$LiTaO_3$	spray-coating	Takada et al.[325]
garnet	$Li_7La_3Zr_2O_{12}$	$LiCoO_2$	Nb	pulsed laser deposition	Kato et al.[311]
	Nb doped $Li_7La_3Zr_2O_{12}$	$LiCoO_2$	Li_3BO_3	screen printing	Ohta et al.[326]
	$Li_7La_3Zr_2O_{12}$	$LiFePO_4$	Li_2CO_3	thermal process with $Li_{2.3}C_{0.7}B_{0.3}O_3$	Han et al.[62]
	$Li_7La_3Zr_2O_{12}$	$LiMn_{0.8}Fe_{0.2}PO_4$	gel electrolyte−($LiPF_6$/DEC/PC)	coating and heating	Yoshima et al.[37]
NASICON	$Li_{1.5}Al_{0.5}Ge_{1.5}(PO_4)_3$	$LiFePO_4$	PEO/$LiClO_4$	spin coating	Zhang et al.[327]

[a]P(EO/MEEGE), poly[ethylene oxide-*co*-2-(2-methoxy-ethoxy) ethyl glycidyl ether). [b]AGE, allyl glycidyl ether.

were conducted to make up for the difficulties of examining interfacial behavior at high potential in experiments;[302] it was founded that LMO and LFP strongly react with garnets under high potential, while LCO is relatively stable, which is consistent with the stable performance of film LCO/$Li_{6.75}La_3Zr_{1.75}Nb_{0.25}O_{12}$ batteries.[303]

Therefore, the poor performance of the ASSBs based on oxide electrolytes associated with the cathode/SSE interfacial behavior was controlled by more than one factor,[304] which can be summarized as follows: (1) huge polarization caused by the poor contact between SSEs and cathodes; (2) high resistance layer formed during the thermal process, which was generally adopted to achieve an intimate contact; (3) the interphase layer caused by electrochemical decomposition when high voltage was applied; (4) the space charge layer effect; as the Li^+ was permitted to rapidly transport in SSEs while the host ions were confined within their primary sites, a Li-depletion zone was easily formed and limited the lithium transport in subsequent discharge processes. The electrochemical stability of cathode/SSE interfaces may, therefore, be hidden behind other effects and is difficult to explore.

4.2.2.1.3. Polymer Electrolyte/Cathode Interfaces. Attempts to fabricate solid polymer batteries with high voltage cathodes, such as $LiCoO_2$ and $LiMnO_2$, generally result in fast capacity loss and poor cycle stability compared with low voltage cathode systems. Seki et al.[305] examined the electrochemical performance of Li/SPE/$LiCoO_2$ based batteries, which displayed poor cycle stability with 58% of the initial capacity retained after 10 cycles. However, the charge/discharge of $LiCoO_2$ agreed well with that determined in liquid electrolyte-based batteries. The capacity loss, therefore, may be related to the degradation of electrode/electrolyte interfaces. AC impedance analysis was carried out to examine the behavior of the lithium polymer batteries at high cathode potential.[306] It was found that the resistance contribution from the cathode side greatly increased with the holding time at high voltage, while the resistance from bulk and anode side are nearly the same. The high resistance cathode/electrolyte interfaces, which result from polymer degradation, may grow in proportion with time and are the main source for the large polarization.[306] XRD and XPS analyses were performed. A clear peak corresponding to Co_3O_4 was observed by XRD in solid polymer batteries based on P(EO/MEEGE/AGE). Recently, Ma et al.[297] confirmed weak interaction between PEO and Li-salt (LiDFOB) by FTIR and identified the decomposition of Li-salt by XPS, which reveals that the stability of solid polymer electrolytes is mainly impacted by the decomposition of lithium salts rather than the polymer matrix.

4.2.2.2. Solid-State Electrolyte/Li Interphase Evolution. As discussed before, for most SSEs, an interphase layer is already formed before battery operation. However, the subsequent reaction behavior of Li/SSE interphases during charge/discharge should also be considered, as the dynamic variation of Li/SSE interphases during charge/discharge may also play a role in electrochemical performance of batteries, like SEI evolution in conventional LIBs.[308,309]

As has been discussed, interphases between lithium metal and SSEs were classified into three types,[230] and the ionic conductive/electronic insulating SEI was desirable for SSBs. However, further discussions about the change of the SEI during the charge/discharge process were absent. Recently, a decent experimental approach was designed to clarify the dynamic variation of SEI on Li/$Li_2S-P_2S_5$ interphases.[307] Visualization of the charge/discharge process was realized by a "virtual electrode" design. The charge/discharge process was successfully simulated by exposing the LPS surface to fluxes of

DOI: 10.1021/acs.chemrev.9b00268
Chem. Rev. XXXX, XXX, XXX−XXX

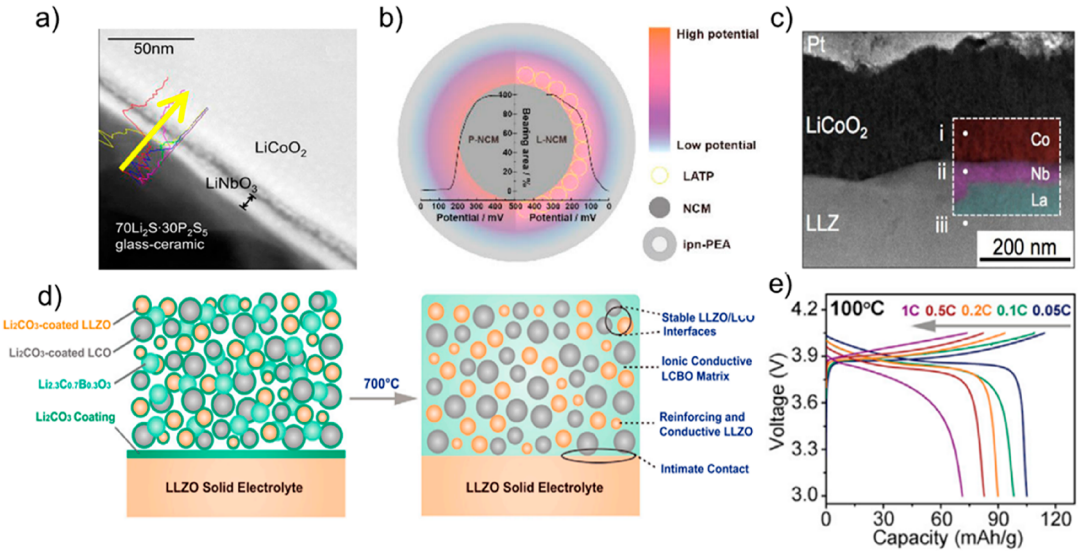

Figure 12. Modification of cathode/SSE interfaces. (a) HADDF image of interface between $70Li_2S{\cdot}30P_2S_5$ and $LiNbO_3$ coated $LiCoO_2$.[55] Reprinted from ref 55, Copyright 2013, with permission from Elsevier. (b) Schematic diagram of LATP coating layer on $LiCoO_2$ to mitigate the polarization and enhance the interfacial dynamics in solid polymer batteries.[310] Reprinted with permission from ref 310. Copyright 2018 American Chemical Society. (c) Cross-sectional HAADF-STEM image of LLZO/$LiCoO_2$ interface with Nb modification.[311] Reprinted from ref 311, Copyright 2014, with permission from Elsevier. (d) Schematic illustration of the $Li_{2.3}C_{0.7}B_{0.3}O_3$ modified $LiCoO_2/L_7La_3Zr_2O_{12}$ interface and (e) enhanced electrochemical performance of interfacially modified all ceramic cell with a configuration of $LiCoO_2/L_7La_3Zr_2O_{12}$/Li.[62] Panels d and e are reprinted from ref 62, Copyright 2018, with permission from Elsevier.

low energy electrons or UV photons. This study revealed that the redox active components in the SEI changed dynamically during charge/discharge, such as Li_3P and Li_2O, and the *in situ* AES mapping demonstrated the heterogeneity of the SEI. Based on their results, the authors proposed a 3D model of SEI composition and structure, as shown on Figure 11d.[307] This study first provided information on the SEI during the charge/discharge process; however, the evolution of the SEI in a real working full solid-state cell, as well as the evolution of other types of interphases, has not been well understood.

4.2.3. Approaches to Extend the Chemical and Electrochemical Interfacial Stability: Building Interphase. The discussions in section 4.2 and section 4.3 illustrate the inevitable interfacial reactions for most electrolyte/electrode interfaces. Although Wu et al.[312] reported a high potential stable core−shell structure sulfide electrolyte, it should be noted that the oxidation of SSEs originates from the instability of their anions,[215] which makes it difficult to suppress the reduction by regulating composition. Therefore, interface modifications are required on both the cathode and the anode side. In this section, modification strategies on the cathode side and the lithium anode side to build favorable interphases are summarized, discussed, and compared.

4.2.3.1. Modifications for Cathode Side Interfaces. The introduced secondary layers for different cathodes and electrolytes are summarized in Table 8. It is interesting that most of the surface modified layers were ionic conductive and electronic insulating materials, except Nb. This sharp difference may originate from different design principles for different SSE/cathode interfaces. It is obvious that all the interfacial layers designed for polymer and sulfide-based electrolytes are good electronic insulators. As discussed above, polymers and sulfides suffer from chemical or electrochemical reactions between cathodes and electrolytes; therefore, good interphases should meet the requirements of (1) high electrochemical stability against cathode to prevent the formation of a new passivation layer (therefore, the interphase layers are generally stable at high voltage, as calculated by Zhu et al.)[233] and (2) ionic conductive and electronic insulating properties, such as $LiNbO_3$ (Figure 12a) and LATP (Figure 12b). The introduced layer protects the SSEs from oxidation without blocking lithium transport; enhanced performance for solid polymer and sulfide batteries can therefore be achieved. For example, a 5 V $LiNi_{0.5}Mn_{1.5}O_4$ cathode was successfully applied in a sulfide SSE based on $LiNbO_3$ or Li_3PO_4 coating strategies. Techniques such as sol−gel, spray coating, MLD, PLD, and ALD can well realize conformal coating and thus can effectively mitigate side reactions at the interface (Table 8).[313] However, the complicated operation procedures and high production cost might be a practical hindrance for large-scale fabrication. Meanwhile simple mechanical mixing, while it cannot provide a perfect coating layer, has also been reported to improve the interface stability to some extent. The facile preparation and low cost make it an alternative way for interface modification and competitive for practical applications. However, things may be different in oxide electrolyte based batteries. The high resistance mainly comes from poor contact, which is not so pronounced for polymers and sulfides, as the latter two electrolytes are soft enough to obtain intimate contact. Nevertheless, in oxide based SSBs, the chemical or electrochemical processes may be largely inhibited for huge kinetics barriers of solid−solid contacts. Therefore, the principle to modify the interface should first address the contact issues. As a result, Nb metal, Li_3BO_3, gel electrolytes, and even liquid electrolytes were introduced and proved effective to greatly improve the electrochemical performance of all solid oxide batteries (Figure 12c). Han et al.[62] achieved an intimate contact LLZO/$LiCoO_2$ interface by introducing $Li_{2.3}C_{0.7}B_{0.3}O_3$ additive (Figure 12d), and the all ceramic cell exhibited significantly improved performance (Figure 12e). In addition, it also can be learned that the modification of cathode/SSEs was mainly focused on polymers, sulfides, and garnet based

DOI: 10.1021/acs.chemrev.9b00268
Chem. Rev. XXXX, XXX, XXX−XXX

Table 9. New Phase Layers Introduced to Modify the SSE/Li Interfaces

type	material	type of coated material	conductive property of introduced layer	introduced layer	method	ref
NASICON	$Li_{1.5}Al_{0.5}Ge_{1.5}(PO_4)_3$	polymer	SEI[a]	PEO based electrolyte	spin coating	Zhang et al.[327]
	$Li_2O-Al_2O_3-SiO_2-P_2O_5-TiO_2-GeO_2$	inorganic compound	SEI[a]	LiPON	sputter deposition	West et al.[342]
	$Li_{1.5}Al_{0.5}Ti_{1.5}(PO_4)_3$	inorganic compound	SEI[a]	Li_3PO_4	PPA[c]/DMSO[d] immersion	Liu et al.[333] and Liu et al.[334]
	$Li_{1.5}Al_{0.5}Ge_{1.5}(PO_4)_3$	inorganic compound	SEI[a]	LiF/Li_3N	electrochemical precycling	Hou et al.[335]
	$Li_{1.5}Al_{0.5}Ge_{1.5}(PO_4)_3$	metal	MCI[b]	Ge	sputtering	Liu et al.[330]
	$Li_{1.5}Al_{0.5}Ti_{1.5}(PO_4)_3$	oxides	SEI[a]	Li−Al−O layer	Al_2O_3 PLD	Liu et al.[334]
	$Li_{1.5}Al_{0.5}Ti_{1.5}(PO_4)_3$	liquid electrolytes	SEI[a]	$LiPF_6$−EC[e]/EMC[f]/DMC[g]	liquid electrolyte immersion	Liu et al.[333]
	$Li_{1.4}Al_{0.4}Ti_{1.6}(PO_4)_3$	oxides	SEI[a]	Zn@Li_2O	magnetron sputtering	Hao et al.[336]
garnet	$Li_{6.5}La_3Zr_{1.5}Ta_{0.5}O_{12}$	metal	MCI[b]	Li	vacuum evaporation	Basappa et al.[343]
	$Li_7La_3Zr_2O_{12}$	metal	MCI[b]	Ge	evaporation	Luo et al.[344]
	$Li_{6.375}La_3Zr_{1.375}Nb_{0.625}O_{12}$	metal	MCI[b]	Sn	magnetron sputtering	He et al.[345]
	$Li_7La_3Zr_2O_{12}$	metal	MCI[b]	Au	sputtering	Tsai et al.[256]
	$Li_{6.5}La_3Zr_{1.5}Ta_{0.5}O_{12}$	nonmetallic	SEI[b]	Li_3N	lithium evaporation in N_2	Xu et al.[346]
	$Li_{6.85}La_{2.9}Ca_{0.1}Zr_{1.75}Nb_{0.25}O_{12}$	nonmetallic	MCI[b]	Si	PECVD	Luo et al.[331]
	$Li_{5.9}Al_{0.2}La_3Zr_{1.75}W_{0.25}O_{12}$	nonmetallic	MCI[b]	C	drawing by pencil	Shao et al.[347]
	$Li_7La_{2.75}Ca_{0.25}Zr_{1.75}Nb_{0.25}O_{12}$	oxide	SEI[a]	Li−Al−O layer	ALD	Han et al.[328]
	$Li_{6.85}La_{2.9}Ca_{0.1}Zr_{1.75}Nb_{0.25}O_{12}$	oxide	MCI[b]	Li−Zn alloy	ZnO-ALD	Wang et al.[348]
	$Li_7La_{2.75}Ca_{0.25}Zr_{1.75}Nb_{0.25}O_{12}$	alloy	MCI[b]	Cu_6Sn_5	magnetron cosputtered and *in situ* alloying method	Feng et al.[349]
sulfide	$Li_{10}SnP_2S_{12}$	ionic liquid	SEI[a]	LiTFSI/IL	spread	Zheng et al.[350]
	$Li_{10}SnP_2S_{12}$	inorganic/organic composite	SEI[a]	alucone[h]	MLD	Wang et al.[329]
	$Li_7P_3S_{11}$	nonmetallic	SEI[a]	LiF/LiI	*in situ* formation	Xu et al.[351]
	Li_3PS_4	metal	MCI[b]	Au	vacuum evaporation	Kato et al.[352]

[a]SEI, only ionic conductive. [b]MCI, mixed ionic and electronic conductive. [c]PPA, polyphosphoric acid. [d]DMSO, dimethyl sulfoxide. [e]EC, ethylene carbonate. [f]EMC, ethyl methyl carbonate. [g]DMC, dimethyl carbonate. [h]Alucone, an inorganic−organic hybrid thin film, the chemical structure is shown in Figure 13.

systems. The relatively fewer investigations of perovskite-type and NASICON electrolytes may result from the severe degradations on the Li side, which brings the Li/SSE interfacial challenges more urgently to the fore.

4.2.3.2. Modifications for Lithium Anode Side Interfaces. Various approaches were performed to improve the stability against metallic Li and were mainly focused on Ti/Ge containing electrolytes and garnet LLZO based electrolytes. The electrolytes suffer from chemical instability or lithiophobicity, and the modification approaches can be classified into two categories.

4.2.3.2.1. Artificial SEI. The comparison of the modification layers induced by different methods is summarized in Table 9. For garnet electrolytes, which are chemically stable with lithium metal, the introduced layers were utilized to enhance the lithium wettability and improve the contact between SSEs and Li, such as ALD@Al_2O_3 layer (Figure 13a). As the huge interfacial resistance was blamed on the inhomogeneous SSE/Li contact due to low lithium wettability,[331] numerous alloy materials, which could be alloyed with lithium and thus enhance the lithium wettability, were utilized to reduce the interfacial resistance (Table 9). However, a recent study from Janek's group challenged the capability of the interlayer alloy materials,[332] and it was found that even though interfacial degradation can be delayed by employing an interfacial Li-alloy layer, the fundamental lithium nucleation kinetics did not change, which means the long-term or high rate lithium plating/striping process cannot be fully addressed by utilizing Li-alloy interlayers. For Ti/Ge containing electrolytes, the interphase layers were introduced to prevent reduction of SSEs by Li.[333−336] This layer acts as an "artificial SEI", as has been proposed in research on conventional LIBs.[337] Hao et al.[336] reported a Zn@Li_2O interphase layer with low electronic conductivity and high lithium wettability that can improve the LATP/Li interfacial compatibility. Gao et al.[338] recently reported that an organic−inorganic nanocomposite interphase, which formed *in situ* by the electrochemical decomposition of liquid electrolyte, enabled a stable lithium plating/stripping process up to 3000 h. Wang et al.[339] designed a solid-state plastic crystal electrolyte to act as an interphase between metallic lithium and SSE to prevent side reactions and dendrite formation at the interface. The artificial SEI should be ion conductive but electronic insulating based on the discussions above (such as alucone, the molecular structure is shown in Figure 13b). More specifically, the inserted interfacial layer should exhibit lower electronic conductivity than the matrix

DOI: 10.1021/acs.chemrev.9b00268
Chem. Rev. XXXX, XXX, XXX−XXX

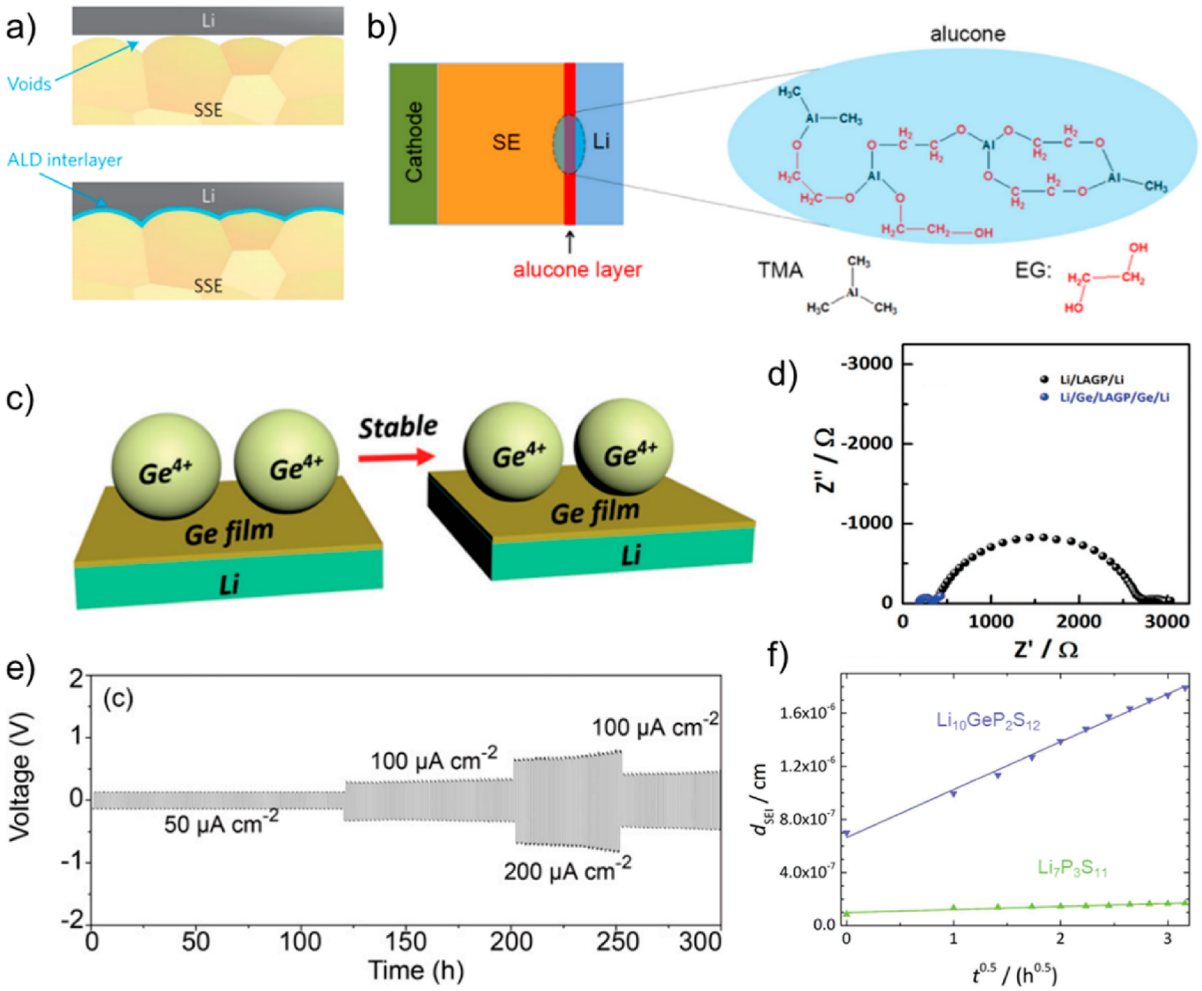

Figure 13. Approaches developed to address the challenges at Li/SSE interface. (a) Schematic illustration of the wetting behavior of garnet surface with molten Li upon Al_2O_3 ALD coating.[328] Reprinted with permission from ref 328. Copyright 2017 Nature Publishing Group. (b) Scheme of Alucone layer modified Li surface and its chemical structure.[329] Reprinted from ref 329, Copyright 2018, with permission from Elsevier. (c) Schematic illustrations of Ge film modification of the LAGP/Li metal interface.[330] (d) Comparison of impedance spectra of Li/LAGP/Li with or without Ge layer.[330] Panels c and d are reprinted from ref 330 with permission. Copyright 2018 John Wiley and Sons. (e) Cycle stability of Li/$LiZr_2PO_4$/Li symmetric cell at different currents. Stable cell polarization indicates the high stability of $LiZr_2PO_4$ against Li.[141] (f) SEI growth thickness of $Li_{10}GeP_2S_{12}$ and $Li_7P_3S_{11}$ depending on the square of time. The $Li_7P_3S_{11}$ shows a much slower SEI growth rate.[228] Reprinted with permission from ref 228. Copyright 2016 American Chemical Society.

SSE to reduce the potential between Li and SSE and prevent reduction of the SSE;[340] if not, even if the interfacial resistance can be restrained by better lithium wettability, the battery degradation is inevitable after long-term cycling.[341] However, it is interesting that the introduced metallic interphases improve lithium stability as well;[330] an amorphous Ge film was coated on LATP pellet (Figure 13c), and it was found that the Li−Ge alloy between the SSE and lithium efficiently suppressed the Ge^{4+} reduction (Figure 13d), which seems to conflict with previous studies. Therefore, the design principles of the interphase layer remain to be further investigated.

4.2.3.2.2. Composition Optimization. Since Zhu et al.[247] reported that the reduction products are mainly governed by redox species, tuning the element composition may lead to a stable Li/electrolyte interface without the penalty of electrolyte conductivity. For example, Li et al.[141] reported that NASICON electrolytes, $LiZr_2(PO)_4$, can form a thin and stable interface layer containing Li_3P and Li_8ZrO_6. The formation of this stable interface provides ion transport channels but prevents dendrite growth, resulting in good electrochemical performance (Figure 13e). In addition, the Ti/Ge-free sulfide electrolytes like $Li_{10}SiP_2S_{12}$[353] and $Li_7P_3S_{11}$,[228,232] exhibit better Li compatibility than $Li_{10}GeP_2S_{12}$,[28] as displayed in Figure 13f, which demonstrates the feasibility of tuning the chemical composition of inorganic electrolytes to achieve a stable SEI.

To conclude, experimental and theoretical investigations illustrated the much narrower electrochemical window of SSEs, as summarized in Figure 14. In oxidation limits, oxides display better stability at high potential than polymers and sulfides, while sulfide electrolytes were found to exhibit the lowest oxidation limit among prevailing SSEs. In reduction limits, the electrochemical stability at 0 V vs Li/Li^+ can be regarded as the chemical stability versus metallic Li, and the reductive reactions are cation controlled. Therefore, the Ti/Ge-containing electrolytes, like LATP/LAGP, generally exhibit a high reductive limit, while the LLZO are stable with metallic Li. However, the stability on the lithium anode side is governed by both thermodynamics and kinetics; the intrinsic high reduction limit of some sulfides can be improved by adding ionic conductive interface layers, which kinetically

DOI: 10.1021/acs.chemrev.9b00268
Chem. Rev. XXXX, XXX, XXX−XXX

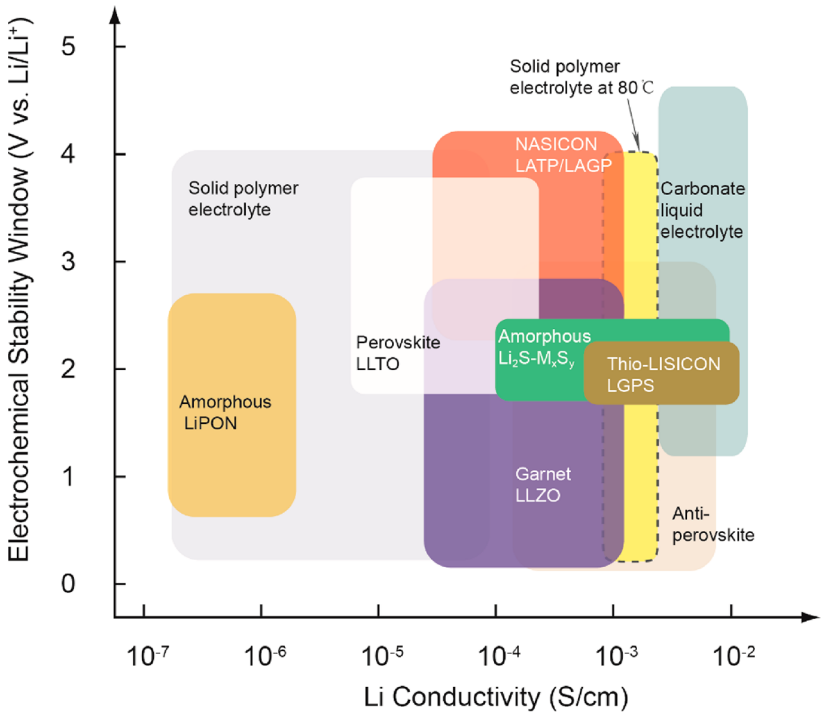

Figure 14. Electrochemical window and lithium ion conductivity of different SSEs. To note, the summary of the ionic conductivity of each type of SSE is based on the experimental values summarized in Table 2; the conductivity values are examined at room temperature except that labeled with dashed line. The electrochemical window of SSEs is obtained from works of the Ceder[224] and Mo groups,[233,252] and the polymer and liquid electrolyte data come from experimental works.

Table 10. Mechanical Properties of Different SSEs[a]

type	material	E (GPa)	G (GPa)	Pugh's ratio[b] (B/G)	K_{IC}[c] (MPa m$^{1/2}$)	ref
polymer	UP + PEO-*b*-PPO-*b*-PEO[d]	1−5	[e]	[e]	0.4−0.6	Builes et al.[355]
	PEO	6.9×10^{-4}	[e]	[e]	[e]	Ramesh et al.[356]
sulfide	$Li_2S{\cdot}P_2S_5$	18.5	7.1 ± 0.3	[e]	0.23 ± 0.04	McGrogan et al.[357]
	$25Li_2S{\cdot}75P_2S_5$	13	5	2.18	[e]	Kato et al.[358]
	$10Li_2O{\cdot}60Li_2S{\cdot}30P_2S_5$	23.3	8.9	2.34	[e]	Kato et al.[358]
	$Li_{10}GeP_2S_{12}$	21.7[f]	7.9[f]	3.44[f]	[e]	Deng et al.[359]
	$Li_{10}SnP_2S_{12}$	29.1[f]	11.2[f]	2.09[f]	[e]	Deng et al.[359]
	Li_5PS_5Cl	22.1[f]	8.1[f]	3.57[f]	[e]	Deng et al.[359]
oxide	$Li_{1.3}Al_{0.3}Ti_{1.7}(PO_4)_3$	115	[e]	[e]	1.1 ± 0.3	Jackman and Cutler[360]
	$Li_{0.33}La_{0.56}TiO_3$	200	80	1.66	~1	Cho et al.[361] and Deng et al.[359]
	$Li_{6.24}Al_{0.24}La_3Zr_2O_{11.98}$	150	58.1	1.74	[e]	Yu et al.[362]
	$Li_{6.5}La_3Zr_{1.5}Ta_{0.5}O_{12}$	147	55.7	1.59	[e]	Yu et al.[362]
	$Li_7La_3Zr_2O_{12}$	149.8 ± 0.4	59.6 ± 0.1	1.72	0.97	Ni et al.[363] and Kim et al.[364]
metal	Al-2219-T851	[e]	[e]	[e]	32	Boresi et al.[365]
	stainless steel-403	[e]	[e]	[e]	77	Boresi et al.[365]

[a]The relationship of the bulk modulus (B), Young's modulus (E), and shear modulus (G) obeys the following equations: $E = 2G(1 + \nu)$, $B = E/3(1 - 2\nu)$, where ν is Poisson's ratio. [b]Pugh's ratio, defined as the ratio of B to G, can be utilized to estimate the brittleness or ductility of a material. [c]K_{IC}, fracture toughness; Al-2219-T851 is a type of aluminum material and stainless steel-403 is a type of steel. The K_{IC} values of these two materials are listed for reference. [d]UP, unsaturated polyester; UP + PEO-*b*-PPO-*b*-PEO, UP/poly(ethylene oxide-*b*-propylene oxide-*b*-ethylene oxide). [e]Not given. [f]Data come from calculation works.

extend the low limit of some sulfide electrolytes. Although many efforts have been carried out to extend the electrochemical window of SSEs, high voltage SSBs still remain challenging to achieve.

4.3. Mechanical Stability

4.3.1. Mechanical Properties of Solid-State Electrolytes. For SSEs, high shear modulus was expected, as Newman and Monroe predicted the dendrite growth can be suppressed when the shear modulus of SSEs is large enough. Another requirement for SSEs is the ability to accommodate the stress from battery assembly and the cycling process.

4.3.1.1. Elastic Properties. Shear modulus (G) is defined as the ratio of shear stress and shear strain, which can be derived from the equation $2G(1 + \nu) = E$, where E is Young's modulus and ν is Poisson's ratio. The shear moduli of different SSEs are summarized in Table 10. It can be learned that solid polymer electrolytes exhibit Young's modulus of <5 GPa, while the critical shear modulus for dendrite inhabitation is about 9 GPa. Therefore, polymers are too "soft" to suppress dendrite growth,

DOI: 10.1021/acs.chemrev.9b00268
Chem. Rev. XXXX, XXX, XXX−XXX

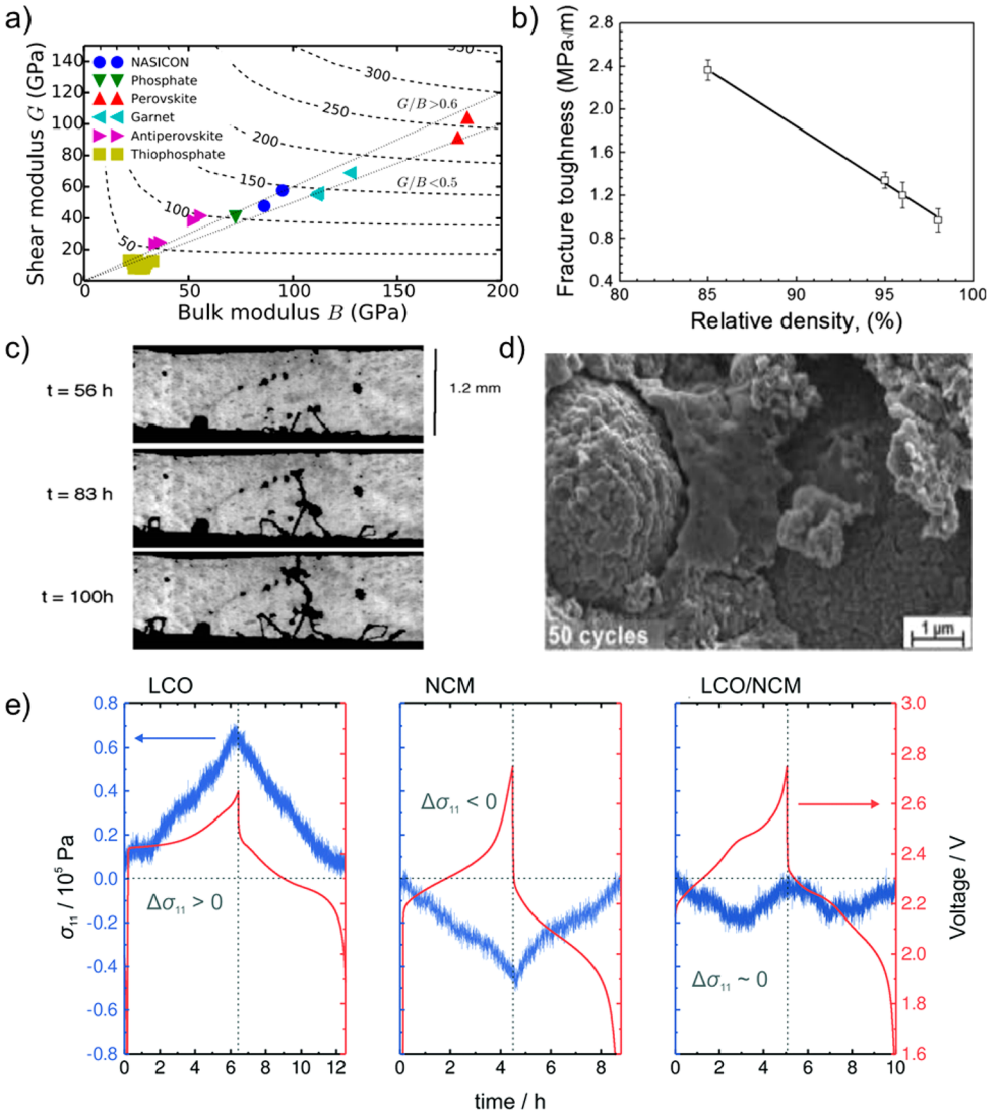

Figure 15. (a) Calculations of shear modulus (G) and bulk modulus (B) of different types of SSEs.[359] Reprinted with permission from ref 359. Copyright 2016 The Electrochemical Society. (b) Fracture toughness of $Li_{6.19}Al_{0.27}La_3Zr_2O_{12}$ as a function of relative density. The fracture toughness decreases with higher pellet density.[364] Reprinted from ref 364 with permission. Copyright 2016 John Wiley and Sons. (c) Time dependent SEM image of lithium dendrite growth in solid polymer batteries.[354] Reprinted from ref 354, Copyright 1999, with permission from Elsevier. (d) Sulfide electrolyte/cathode interface after 50 cycles. Contact loss happens with mechanical deflation/expansion during charge/discharge.[367] Reprinted with permission from ref 367. Copyright 2017 American Chemical Society. (e) Volume change of different cathodes in the lithiation process: (left) $LiCoO_2$; (middle) $LiNi_{0.8}Co_{0.1}Mn_{0.1}O_2$; (right) $LiCoO_2$ + $LiNi_{0.8}Co_{0.1}Mn_{0.1}O_2$. A minimal volume change was achieved by careful mechanical balance.[64] Reproduced from ref 64 with permission from The Royal Society of Chemistry.

Table 11. Volume Change and Mechanical Properties of Electrode Materials[a]

material	volume change (%)	E (GPa)	G (GPa)	Pugh's ratio[b] (B/G)	K_{IC}[c] (MPa m$^{1/2}$)	ref
$LiCoO_2$	−9.9	178 ± 5	*d*	*d*	0.94 ± 0.09	Mukhopadhyay and Sheldon[369] and Swallow et al.[370]
$LiCoO_2$	*d*	191	80	1.53	*d*	Cheng et al.[371]
$LiFePO_4$	−7.2	125.9	48.9	2.02	*d*	Mukhopadhyay and Sheldon[369] and Chong et al.[372]
$LiMn_2O_4$	−6.8	86.67 ± 11.29	*d*	*d*	0.49 ± 0.13	Mughal et al.[373]
graphite	10	32	12	2.34	*d*	Qi et al.[375]
metallic Li	*d*	12.6	4.8	2.75	*d*	Yu et al.[362] and Slotwinski and Trivisonno[376]

[a]Volume variation is based on the volume after fully delithiated over pristine volume. The relationship of the bulk modulus (B), Young's modulus (E), and shear modulus (G) obeys the following equations: $E = 2G(1 + \nu)$, $B = E/3(1 - 2\nu)$, where ν is the Poisson's ratio. [b]The Pugh's ratio, defined as the ratio of B to G, can be utilized to estimate the brittleness or ductility of a material. [c]K_{IC}, fracture toughness. [d]Not given.

and lithium dendrite growth was confirmed by experiments.[354] Sulfides were also reported to exhibit poor mechanical strength. However, the shear modulus of sulfide is closed to the critical value, which should be sufficient for dendrite growth limitation after composition and structure optimizations. Oxides exhibit the highest shear modulus among all

DOI: 10.1021/acs.chemrev.9b00268
Chem. Rev. XXXX, XXX, XXX−XXX

electrolytes, which is 10 times larger than the value of lithium metal, as illustrated in Figure 15a. Such high mechanical strength may well allow the oxides to suppress dendrite growth. However, dendrite growth and short circuit were still observed in oxide based all solid batteries.[259,261] Instead of the mechanical properties of oxide electrolytes, lithium penetration was attributed to insufficient contact of electrolyte and electrode, as well as cracks along grain boundaries.[256] As can be concluded here, the value of shear modulus is an important but not the only factor to determine whether lithium dendrites grow.

4.3.1.2. Brittle Properties. Another issue that should be considered is the brittleness or fracture properties of SSEs. Pugh's ratio (B/G) can be adopted to evaluate the brittleness of materials.[366] The critical value of Pugh's ratio is 1.74,[362] and those materials with B/G below this value can be regarded as brittle materials. The comparison of Pugh's ratio for different materials is shown in Tables 10 and 11. It is clear that sulfide electrolytes exhibit higher B/G than oxides, demonstrating better ductility than oxides. Therefore, sulfide electrolytes can be regarded as "soft materials" and can accommodate the stress generated from cell assembly or cycling. Another parameter to evaluate the brittleness of materials is the fracture toughness, K_{IC}, which reflects the resistance for crack propagations. K_{IC} is defined as $K_{IC} = \xi(E/H)^{0.5}P/C_0^{1.5}$, where ξ is a constant depended on materials, H is the hardness, E is Young's modulus, C_0 is the length of the crack, and P represents the applied stress.[365] Higher K_{IC} is demonstrated in high ductile materials, for example, stainless steel delivers a high K_{IC} value of 70 MPa·m$^{1/2}$. As summarized in Table 10, oxide ceramics usually exhibit low K_{IC} values of about 1 MPa·m$^{1/2}$,[360,361,364] which further confirm their extreme brittleness. However, McGrogan et al.[357] reported that sulfide electrolytes also display low fracture toughness of 0.23−0.34 MPa/cm^2, which is controversial with the high B/G value of sulfides; therefore, the mechanical properties of SSEs still need to be further clarified. What makes the brittleness of materials important is that the inevitable volume change of electrode materials leads to stress concentration. Cracks may open for those brittle electrolyte/electrode interfaces, which is fatal to a working battery.

4.3.1.3. Determining Factors for Mechanical Properties of Solid-State Electrolytes. The mechanical properties of materials are mainly determined by chemical bonding, crystal structures, and microstructures. For example, the lower bonding energy in sulfides results in higher ductility.[358] It was reported that different types of bonding result in different hardness/shear modulus (H/G) values.[368] Deng et al.[359] calculated the mechanical properties of 23 SSEs; it was found that similar chemical compositions usually give similar elastic modulus, and it was also reported that the mechanical properties are affected by composition and lattice structure. In addition, Kim et al.[364] reported that higher relative density of SSE leads to lower fracture resistance (Figure 15b), while higher compaction is required for SSEs to obtain higher ionic conductivity. Therefore, a dilemma between conductivity and ductility may occur, which should be considered in further investigations.

4.3.2. Mechanical Stability of Solid-State Batteries. During battery cycling, dendrite growth and crack formation may happen. The mechanical properties of SSEs play vital but diverse roles in determining the final mechanical behaviors in SSBs. As a result, it is very necessary to first figure out the phenomena contributed by mechanical issues of prevailing SSEs, as will be discussed in the following sections.

4.3.2.1. Dendrite Penetration. Suppressing dendrite growth is considered one important motivation to develop ASSBs, especially ceramic SSBs, as dendrite growth still happens in solid polymer batteries (Figure 15c). However, the internal short circuit was still widely reported in ASSBs with high shear modulus,[261] and efforts were carried out to prove that the short circuit was caused by lithium dendrite formation inside SSEs.[256,261,377] Early studies attributed the growth of dendrite to the grain boundaries in SSEs. Sudo et al. reported that in Al doped LLZO based ASSBs, the lifespan and the critical current increased with higher grain boundary resistance. A similar phenomenon was later reported by Ishiguro et al.[258,259] in ASSBs using Nb-doped and Ta-doped garnet electrolytes. In addition, Suzuki et al.[257] found that dendrite formation was more pronounced in opaque SSEs, which contain more grain boundaries than transparent ones. However, the "grain boundary related dendrite formation mechanism" was challenged by the reports of dendrite growth in highly dense SSEs.[378] Cheng et al.[260] compared the critical shirt-circuit currents of SSEs with different microstructures. They found that the surface layer in ceramic pellets with small grains is favorable for dendrite suppression. Then work of Tasi et al.[256] confirmed the importance of surface; the interfacial contact issues were believed to be responsible for dendrite growth. The insufficient contact between electrolytes and electrodes results in large local currents, which finally leads to dendrite growth, and the battery lifespan can be extended by interfacial modification with a Au layer. Later on, Krauskopf's work proved that current collectors had an impact on lithium dendrite growth kinetics,[332] the high nucleation and inhomogeneous lithium deposition may lead to fast lithium dendrite penetration and short circuit. Dendrite growth can be delayed by employing a Au current collector, as Au−Li can be formed at the interface to enhance interfacial contact. The above results highlight the importance of intimate interfacial contact and a homogeneous lithium plating/stripping process in preventing the dendrite penetration. Very recently, Han et al.[263] proposed electronic conductivity of SSEs as the origin of lithium dendrite growth, and the critical electronic conductivity for different SSEs to limit the dendrite growth was given. The relatively high electronic conductivity of LLZO was confirmed by the DFT calculations of Qi's group;[379] they found some additional states of revealed on the surface of LLZO, which may trap the excess electrons around La atoms, thus providing pathways for lithium penetration. It seems that these results challenged the prediction made by Newman and Monroe.[380] However, their calculation still works if the shear modulus of the grain boundaries is concerned, as the shear modulus of grain boundaries is reported to be 0.2−0.6 of the bulk value.[381] It is worth noting various models have been proposed on the role of grain boundaries in Li dendrite growth, based on grain boundary conductivity, grain size and surface structure, relative density of SSE, and defect or microcrack formation, as well as electronic conductivity. These investigations have been carried out in different research groups on various SSE materials with diverse microstructure, morphology, and size, prepared by different methods. All these factors may contribute to the diverse dendrite formation behaviors reported so far. From the fundamental driving force point of view, the inhomogeneous Li deposition or Li dendrite formation actually comes from the inhomogeneous over-

DOI: 10.1021/acs.chemrev.9b00268
Chem. Rev. XXXX, XXX, XXX−XXX

potential distribution at the interface. As a result, Li dendrite growth may be overcome by guiding homogeneous Li deposition at the interface, where smoothing electric field distribution at grain boundaries will be determinative. Further studies are still very necessary to clarify these issues.

4.3.2.2. Volume Change Driven Cracks and Contact Loss. In LIBs, most electrode materials experience phase transitions, lattice expansion/contraction, or structural changes during lithiation/delithiation, resulting in volume change after charge/discharge.[369] The volume change value is briefly summarized in Table 11. The repeated expansion and contraction leads to mechanical instability, such as deformation, pulverization, and contact loss between current collector and electrode particles, leading to capacity fade and poor cycle stability. In this regard, the volume change of electrodes is attributed as one of the critical causes for battery degradation. Mechanical stability is critical to achieve high performance batteries; however, corresponding investigations in SSBs were less common. Since the stress induced by volume change cannot be transferred to uniform hydraulic pressure, the pressure changes are taken up by the SSE itself. In addition, the cathodes of SSBs often consist of active materials, conductive additives, binders, and SSEs to obtain good contact between SSEs and cathode particles; usually, the content of SSEs is up to 50% in composite cathodes.[382] Therefore, the stress in ASSBs will occur not only between electrodes and SSEs but also within cathode and SSE composites. Actually, reversible resistance change, as well as the delamination of SSEs and active materials after cycling, has been reported by Koerver et al.,[367] as displayed in Figure 15d. However, this phenomenon was not linked to volume change at that time. The critical role of mechanical stability was also emphasized by theoretical calculations; Tian and Qi[383] simulated the contact area change during cycling based on the 1D Nerman battery model and Poisson's contact mechanics theory. They reported that contact loss occurs after cycling, which leads to a capacity drop; thus external applied pressure is needed to recover the insufficient contact. Bucci et al.[384] developed a cohesive zone model (CZM) to simulate crack evolution induced by electrode expansion; the calculated results indicate that the fracture propagation happens under large electrode expansion ($\Delta V > 7\%$) and low fracture energy ($G_c < 4$ J m^{-2}). These studies demonstrate the critical role of mechanical stabilities of SSEs. External pressure is also necessary to obtain ultimate contact in battery assembling process. Therefore, cracks may happen during assembly or the cycling process as both cathode and electrolytes are brittle (Table 11).

However, the mechanical properties and mechanical instability of SSEs were ignored by the battery community in early studies. Janek's group[385] first monitored the pressure change in a working SSB, fabricated with In metal anode, sulfide electrolyte, and $LiCoO_2$ cathode. With the assistance of the homemade pressure measurement apparatus, the "cell breathing" phenomenon was demonstrated as a result of reversible volume change of electrode materials. In addition, the blending of SSE and several cracks at the edge area were also observed, without external applied pressure. Recently, Koerver et al.[64] further analyzed the chemomechanical expansion of state-of-the-art electrodes in ASSBs. Although volume change can be reduced by exploring a zero strain anode electrode, $Li_4Ti_5O_{12}$, the reversible volume changes induced by the cathode side still can be observed in all the electrodes, which leads to reversible compression and tension of SSEs. Therefore, SSEs with higher ductility were expected to accommodate the reversible volume change of electrodes.

In summary, oxide electrolytes exhibit Pugh's ratio below 1.7, and fracture toughness of about 1 MPa·m$^{1/2}$, which is the same magnitude of the value of oxide cathode materials. Sulfide electrolytes display lower shear modulus and higher B/G, which results in soft nature to accommodate the external pressure. Polymer electrolytes often deliver elastic modulus less than 0.1 GPa, which may be too low to inhibit dendrite growth. As predicted by Monroe and Newman,[380,386] dendrites can be prevented if the SSEs have a modulus higher than 8.5 GPa. Therefore, the polymer may be too "soft" to inhibit dendrite growth, while the oxide electrolytes may be too "hard" to accommodate the reversible volume change during cycling. In this regard, sulfide electrolytes have an intermediate modulus and high B/G value, which may meet the demands of mechanical properties. Moreover, enhancement of the electrochemical performance of assembled In−Li/LGPS/Ti_2S solid-state cells under an external pressure of 228 MPa was also reported.[374] Hence, it was considered that the sulfide electrolytes deliver the most favorable mechanical stability among the typical SSEs.[152] However, Chiang et al.[357] reported that the LPS electrolytes exhibit low fracture toughness, which demonstrates the brittle nature of the sulfides and may compromise their favorable mechanical stability. Therefore, the mechanical properties of SSEs and chemical−mechanical compatibility issues of electrodes and SSEs remain to be further studied.

4.3.3. Approaches to Realize Mechanically Favorable Solid-State Batteries. A mechanically stable SSB requires a mechanically stable interface. Strategies for both materials and battery designs have developed. Materials with both flexibility and enough mechanical strength are desirable but difficult to achieve. However, novel designs at the battery level are more efficient and show their practical feasibility.

4.3.3.1. Mechanical Favorable Solid-State Electrolyte Materials. As mentioned above, polymer electrolytes exhibit a relatively low mechanical strength to suppress lithium dendrite growth, while the high hardness ceramic electrolytes suffer from volume change of electrodes in the charge/discharge process, and the resulting insufficient contact between electrodes and SSEs. Hence, a thoughtful approach to solve the dilemma is to design a composite polymer/ceramic electrolyte, which combines the advantages of both electrolytes. For example, Wang et al.[280] developed a 3D composite polymer electrolyte that contains a PEO matrix and a 3D LLTO backbone. The composite electrolyte displays enhanced mechanical stability (0.98 GPa of Young's modulus) compared with pure solid polymer electrolytes. Moreover, very recently, Pervez et al.[387] reported that compositing of LLZO particles into PEO polymer electrolytes significantly enhanced the toughness of the neat polymer electrolytes. When a crack initiates in the composite electrolytes, the polymer−oxide particle interfaces would hinder further crack propagations, which can be called a "crack-pinning" toughening mechanism. Therefore, the composite polymer/ceramic may be the final solution to reach appropriate mechanical stability.[388] However, it still remains unknown whether the introduction of polymer components compromises the safety and conductivity, as polymers exhibit inferior room-temperature conductive properties and thermal stability. In addition, the different electrochemical stability of polymer and ceramic electrolytes makes the reactions in charge/discharge process more complicated.

DOI: 10.1021/acs.chemrev.9b00268
Chem. Rev. XXXX, XXX, XXX−XXX

Therefore, systematic studies of the variations in conductive properties, chemical and electrochemical stability, and mechanical strength after compositing the polymer and ceramic remain to be further developed.

4.3.3.2. Novel Battery Designs. Proper mechanical properties of materials are important but difficult to control. Therefore, optimizing the designs of SSBs can be a more efficient way to achieve mechanically stable SSBs.

4.3.3.2.1. Mechanical Balancing. As discussed above, the reversible volume change is reported in most electrode materials, especially anode materials like graphite. Hence, the zero strain materials, $Li_4Ti_5O_{12}$, can be considered as the anode in solid electrochemical systems, which results in a 20 times smaller volume change for the whole cell. In addition, combination of cathode and anode with different volume change behaviors allows the chemical expansion of cathode to be taken up by the contraction of anode, which decreases the cell volume change. However, the cathode of a solid cell usually consists of cathode/electrolyte composites; thus the contact loss between them, which is detrimental to the ionic conduction and battery performance, may happen as a result of repeated volume change of cathode particles. Therefore, it is critical to minimize the volume change of cathode materials. As summarized by Koever et al.,[64] most electrode materials experience volume expansion in the charge process, except $LiCoO_2$, which makes it possible to realize a "zero strain" cathode by carefully composition balancing. It has been reported that the volume change of cathode materials can be minimized by combining positive and negative volume changing cathodes, LCO and NCM, respectively. This mechanical balance battery design makes the cycled composite cathodes free from the delamination of cathode/SSE (Figure 15e).

4.3.3.2.2. Hybrid Solid−Liquid Electrolyte Batteries. As the huge interfacial resistance on cathode/electrolyte interface leads to significant decrease in battery capacity, especially in oxide-type ASSBs, adding a liquid phase into the electrode/electrolyte interfaces can be an efficient approach to solve the mechanical stability challenges, which makes the battery become a hybrid solid−liquid (quasi-solid) type. In 2016, Yoshima et al. proposed a practical hybrid solid−liquid battery design, which contains about 4 wt % gel electrolytes. The as-prepared hybrid solid−liquid batteries displayed high ionic conductivity and small interfacial resistance. The 12 V pouch-type bipolar batteries based on this design illustrated its feasibility for large scale production as well. Another type of hybrid solid−liquid electrolyte is based on the existing production process for LIBs. SSEs are coated on one side or both sides of conventional PP or PE separators.[389,390] In addition, an *in situ* solidification was reported in ceramic coated separators, which decreased the liquid/solid phase ratio and suppressed the short circuit risk.[391]

Those results show their practical feasibility for large scale applications, and mechanical issues can be solved based on those hybrid designs. However, the introduction of a liquid phase may lead to compromise on thermal stability and safety, and the technical challenges for the introduction of a small amount of liquid phase with good wetting properties for large scale batteries should be further clarified.

4.3.3.2.3. Batteries with Hierarchical Structures. Another design strategy to enhance the mechanical stability is to contrast the hierarchical SSEs or electrodes. For 3D hierarchical SSEs, typically, the inner compact layer with high density offers high mechanical strength to suppress lithium dendrite permeation, and the outer porous layer confirms the intimate contact with electrode particles. This architecture was achieved by Fu et al.[392] with a simple tape casting method; an all solid-state Li−sulfur battery was fabricated by melting sulfur into the porous layer. Moreover, the same group reported that further improved interfaces between 3D oxide electrolyte and electrode can be achieved by surface coating on the 3D SSE matrix or depositing a current collector on the bottom of the electrolyte scaffold.[382,393] However, rigid high voltage oxide cathodes may not be practical for this architecture. Very recently, Huo et al.[394] extended this concept into composite ASSBs; "ceramic-in-polymer" and "polymer-in-ceramic" sandwich-type electrolytes were designed, which contained a relative rigid inner layer and a soft outer layer. Contact loss and local stress were limited by its soft layer, and the highly elastic rigid inner layer provided a dendrite-free charge/discharge process. Li/LFP full batteries with enhanced battery performance were achieved at 30 °C by this design, while the competition with rigid high voltage cathodes still needs to be further investigated. A similar strategy was also introduced in sulfide-based solid batteries; recently, Xu et al.[395] integrated Li_3PS_4 into a three-dimensional Kevlar nonwoven scaffold to fabricate a cathode supported all solid lithium sulfur battery, which delivered the best electrochemical performance among the reported all-solid-state lithium−sulfur batteries. On the other hand, 3D electrode designs were also proven to be beneficial in constructing mechanically stable SSE/electrode interfaces. Li et al.[396] employed the Neutron Depth Profile (NDP) method to visualize the lithium plating/stripping behavior in Li/LLZTO/3D Ti SSB. It was found that most of the plated lithium deposited in the void between the Ti electrode, maintaining the intimate contact between the electrode and electrolyte and inhibiting interfacial degradation. Therefore, the 3D structural design for both electrolyte and electrode is critical in constructing stable electrode/electrolyte interfaces.

4.3.3.2.4. Solution Method Based Sheet-Type Solid-State Batteries. For sulfide based SSEs, although the soft nature provides the ability to accommodate volume change, contact loss on composite cathodes was reported.[367] Owing to the solubility of sulfides in some solvents, a solution process was developed to obtain complete infiltration between sulfide electrolytes and porous cathodes.[397] The SSE solutions can be directly coated on a porous electrode layer to obtain stable ionic contact composite cathodes. For example, Kim et al.[398] reported that the LPSCl infiltrated electrodes display even higher capacities than their liquid counterparts. Compared to typical cold-pressed solid sulfide pellets, sulfides fabricated through the solution process are more practical to realize large scale and thin SSE layers, which are compatible with commercial roll-to-roll fabrication processes. Large size pouch-type all solid-state full cells were achieved with slurry-coated composited electrodes,[399,400] which further demonstrates its practical significance. However, the ionic block polymer binders, which are often added to enhance adherence, may coat active materials and limit ionic transport and harm battery performance.[400] In addition, finding an inexpensive, nontoxic, and inert solvent is also greatly challenging and hinders large scale production by the solution method. A similar strategy can be realized in polymer-based SSEs with bipolar designs. Chen et al.[401] reported a cathode-supported SSB by directly tape casting the electrolyte slurry onto the

DOI: 10.1021/acs.chemrev.9b00268
Chem. Rev. XXXX, XXX, XXX−XXX

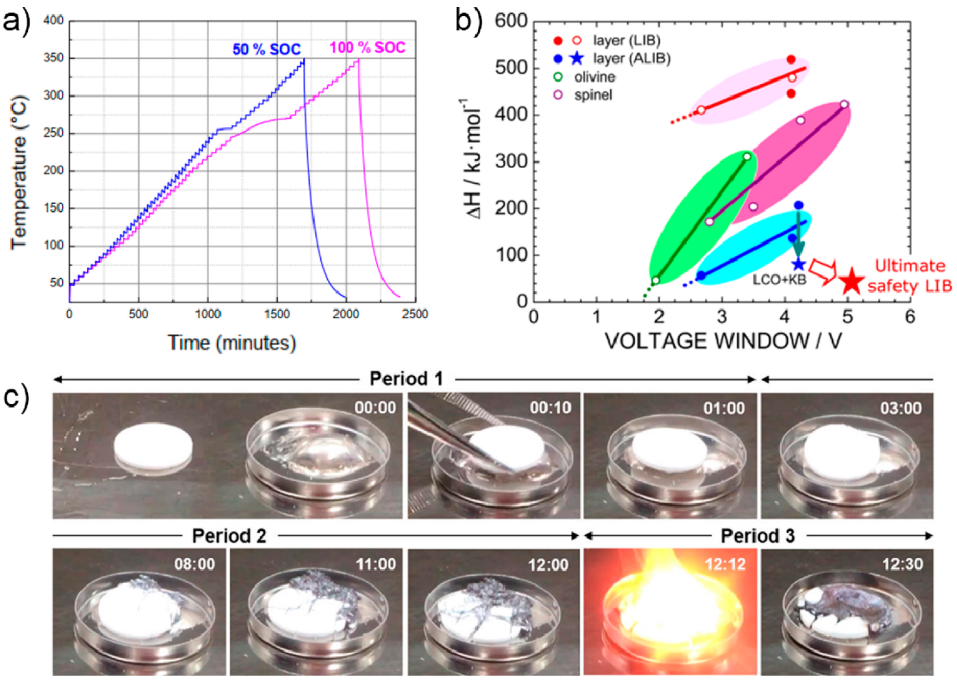

Figure 16. (a) Thermal runaway behavior of Li/$LiFePO_4$ half-cells at 50% and 100% SOC with solid polymer electrolytes, examined by adiabatic rate calorimeter (ARC) test. No thermal runaway was observed within the test temperature range (50−300 °C).[406] Reprinted from ref 406, Copyright 2017, with permission from Elsevier. (b) Safety map comparison on heat generation for LIBs and ASSLIBs (all-solid-state lithium ion batteries). The total heat generation under 420 °C of ASSLIBs is about 30% of the value in traditional LIBs.[407] Reprinted with permission from ref 407. Copyright 2017 American Chemical Society. (c) Thermal runaway behavior for LAGP in contact with metallic lithium when the temperature reach 200 °C.[245] Reprinted with permission from ref 245. Copyright 2017 American Chemical Society.

cathode layer; interfacial contact was improved compared with a stack process, and a 9 V ASSB was achieved with 3 layers of parallel batteries. The wettability of polymer and sulfide solutions make them practical to obtain mechanically stable interfaces with rigid cathode particles, while the electrochemical stability, as well as the challenges to large scale production, remains to be developed.

4.3.3.2.5. Batteries with Liquid Electrode. The mechanical dilemma of ceramic electrolytes is attributed to the rigid nature of the inorganic electrolytes. Although some sulfide electrolytes display relatively favorable mechanical properties, blending and delamination still occur in cycling without external pressure. However, the electrode volume change problem is relatively less serious in conventional LIBs. The stress generated from the electrode expansion can be transformed to homogeneous hydraulic pressure in a solid−liquid contact interface, which minimizes the local stress and prevents contact loss. Hence, liquid electrodes can be utilized to construct a liquid/solid interface. Actually, liquid metal batteries have been known for many years,[402] using molten metal salts. The proposed liquid metal batteries, for example, the well-known Na−S batteries, exhibit long lifespan and have been commercialized in grid energy storage. However, to melt the metal salts, high temperature is inevitably required, which brings additional manufacturing costs and safety risks. Lu et al.[403] employed Na−C alloy as anode and β-Al_2O_3 as the electrolyte, which enabled the assembled Na−S and Na−$NiCl_2$ to operate at a temperature low as 95 °C. Recently, Jin et al.[404] reported the utilization of garnet electrolyte to fabricate a Li/LLZTO/Sn−Pb liquid metal cell, which delivers good electrochemical performance at temperatures above the lithium melting point. In addition, a room temperature liquid Na metal anode was also reported to be prepared by dissolving Na into biphenyl and DME solutions.[405] Therefore, this is a decent approach to solve the mechanical stability issues if the liquid metal batteries can operate at room temperature.

To summarize, although volume expansion can be suppressed by careful mechanical balancing, a soft−rigid electrolyte/electrode interface in a composite cathode is critical for maintaining continuous contact and accommodating volume change. An SSE material with both high elastic modulus and high flexibility can be a fundamental solution to solve mechanical issues, while it is difficult for a material to simultaneously satisfy all the requirements in chemical and mechanical properties. In this regard, proper battery design could be more efficient toward practical applications. A soft−rigid contact can be achieved by a well-designed electrolyte/electrode interface. However, technique challenges remain to be addressed, each type of design has its drawbacks, and new battery geometries should be further studied for practical SSBs.

4.4. Thermal Stability

4.4.1. Thermal Stability of Materials in Solid-State Batteries. For conventional LIBs with organic electrolytes, a series of side reactions occur as the temperature increases,[408,409] which results in failure or thermal runaway of LIBs. First, the SEI begins to decompose around 80−120 °C, accompanied by gas (CO_2, O_2, C_2H_4, etc.) release. Second, the PE/PP separators start to melt at around 130 °C, which would lead to internal short circuit and further heat release. Finally, when the temperature continues increasing, cathode oxide materials break down accompanied by oxygen release, which results in a sharp increase in temperature and pressure inside LIBs and eventually leads to thermal runaway. For safety issues with liquid electrolytes, it is generally accepted to be an effective solution to replace flammable liquid electrolytes with

DOI: 10.1021/acs.chemrev.9b00268
Chem. Rev. XXXX, XXX, XXX−XXX

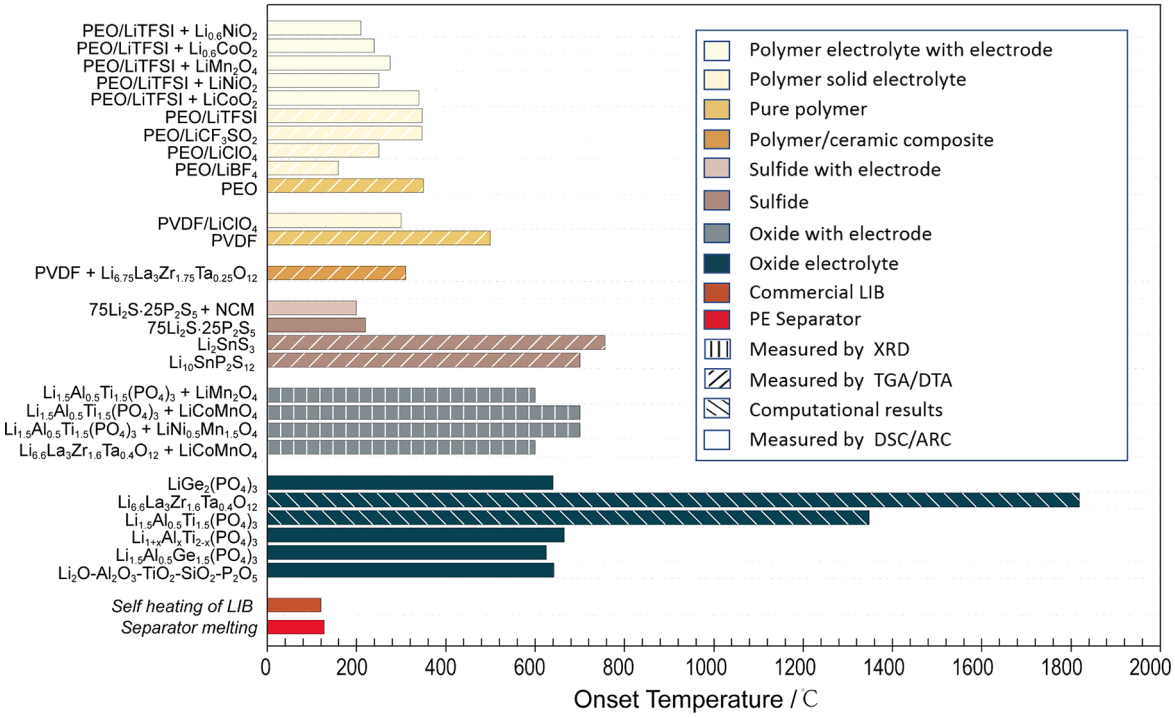

Figure 17. Comparison of onset temperature of exothermal behaviors for different SSEs. The commercial LIB self-heating reaction temperature and PE melting temperature are provided for reference, based on temperature values summarized in Table 12. Different colors represent different sample composition, and patterns inside the column distinguish the values obtained by different methods. Abbreviations: PVDF, poly(vinylidene fluoride); PEO, poly(ethylene oxide); PAN, polyacrylonitrile; PEG, poly(ethylene glycol); EMITFSI, 1-ethyl-3-methylimidazolium bis-(trifluoromethylsulfonyl)imide; PE, polyether; LiTFSI, lithium bis(trifluoromethanesulfonyl)imide.

SSEs, which was proven by ARC test results carried out by Perea et al.[406] (Figure 16a). However, Inoue and Mukai[407] reported that exothermal reactions still can be observed in ASSBs by DSC at elevated temperature (Figure 16b). Chung and Kang[245] found that thermal runaway occurred at 200 °C when the solid oxide electrolyte contacted lithium metal (Figure 16c). These studies reveal that the intrinsic safety and thermal behavior of ASSBs should be further clarified.

Thermal behaviors of various SSEs at elevated temperature observed by different methods are summarized in Figure 17 and Table 12. It should be noted that, as the safety of SSBs were less considered in previous investigations, the onset temperature was chosen as the temperature at which the first exothermal reaction occurs rather than the temperature of thermal runaway.

As shown in Figure 17, it is obvious that oxide electrolytes exhibit the best thermal stability. The initial temperature of oxygen loss and thermal decomposition for LATP and LLZO were predicted to be 1270 and 1600 °C, respectively. Although it is reported that LATP glass electrolyte undergoes a crystallization process at about 650 °C,[410] it still has better thermal stability than sulfide electrolytes ($75Li_2S{\cdot}25P_2S_5$, ~220 °C).[411] However, the newly discovered sulfide electrolyte $Li_{10}SnP_2S_{12}$, which is considered as a stable and low-cost solid sulfide electrolyte, shows excellent thermal stability up to 700 °C.

Most solid polymer electrolytes have good thermal stability compared with liquid electrolytes. In other words, we found that the decomposition onset temperature of polymer electrolytes containing lithium salts shifts lower compared with pure polymer counterparts. For example, the decomposition temperature of PEO is 400 °C,[412] but solid polymer electrolytes PEO/$LiClO_4$, PEO/$LiCF_3SO_3$, and PEO/$LiBF_4$ display lower onset temperatures of thermal decomposition, as can be seen in Figure 17. Among these polymer electrolytes, PEO with $LiBF_4$, reported by Xia et al.,[281] displays the worst thermal stability. However, $LiBF_4$, as well as other lithium salts, were found to be stable at relatively high temperature (~300 °C for $LiBF_4$).[413,414] It is therefore necessary to study the interplay between Li-salts and solid polymer electrolytes and the impact on thermal stability behavior. It should be noted that the exothermal onset temperatures of all SSEs are higher than the self-heating temperature (~120 °C), separator breakdown temperature (~130 °C) in conventional LIBs, and onset temperature of LIB thermal runaway, indicating the relatively superior thermal stability of SSBs to some extent.

4.4.2. Thermal Stability of Interfaces in Solid-State Batteries. It can be learned that all the electrolytes deliver lower onset decomposition temperature when contact with electrodes, as shown in Figure 17. Miara et al.[217] investigated the decomposition behavior by experiments and theoretical calculations. It was found that a mixture of oxide electrodes and electrolytes starts to decompose at 600 °C, which is lower than the decomposition temperature of pure electrolytes or electrodes. Moreover, as a thermal process is widely adopted to obtain intimate contact between the ceramic and the electrode, high temperature driven decomposition and mutual diffusion between cathode and SSEs would happen. Similarly, Gellert et al.[226] reported that a mixture of LATP and oxide materials exhibits rapid decomposition even at a temperature as low as 500 °C, which can be explained by the thermodynamically favorable formation of Li-free compounds and the extracted lithium being likely to form Li_3PO_4 when ing contact with LATP, thus leading to a lower decomposition temperature.

DOI: 10.1021/acs.chemrev.9b00268
Chem. Rev. XXXX, XXX, XXX−XXX

Table 12. Thermal Behaviors of SSEs at Different States, Examined by Experimental and Theoretical Methods

type	material	temp (°C)	behavior	heat flow (J/g)	method	ref
inorganic electrolytes	$2[Li_{1.8}Al_{0.4}Ti_{1.6}Si_{0.4}P_{2.6}O_{12}]\cdot AlPO_4$	642	crystallization	*b*	DSC	Chen et al.[410]
	$Li_{1.5}Al_{0.5}Ge_{1.5}(PO_4)_3$	~625	crystallization	*b*	DSC	Rodrigues et al.[415]
	$Li_{1+x}Al_xTi_{2-x}(PO_4)_3$	665	crystallization	*b*	DSC	Narvaez-Semanateet al.[416]
	$Li_{1.5}Al_{0.5}Ti_{1.5}(PO_4)_3$	1348	decomposition	*b*	DFT prediction	Miara et al.[217]
	$Li_{6.6}La_3Zr_{1.6}Ta_{0.4}O_{12}$	1819	decomposition	*b*	DFT prediction	Miara et al.[217]
	$LiGe_2(PO_4)_3$	640	crystallization	*b*	DSC	Cruz et al.[417]
	$Li_{10}SnP_2S_{12}$	700	decomposition	*b*	TGA/DCS	Bron et al.[418]
	Li_2SnS_3	756	crystallization	*b*	DTA	Brant et al.[419]
	$75Li_2S\cdot 25P_2S_5$	220	crystallization	*b*	DSC	Tsukasaki et al.[411]
	$Li_{6.75}La_3Zr_{1.75}Nb_{0.25}O_{12}$	>480	*b*	*b*	DSC	Inoue et al.[407]
polymer electrolytes	$PVDF/LiClO_4$	~300	decomposition	*b*	DSC	Zhang et al.[420]
	$PEO/LiBF_4$	160	decomposition	*b*	DSC	Xia et al.[281]
	$PAN/LiBF_4$	~279	decomposition	*b*	DTA/TGA	Nippani et al.[421]
	$PEO/LiClO_4$	250	decomposition	*b*	DSC	Xia et al.[281]
	$PEO/LiCF_3SO_3$	>300	decomposition	*b*	DSC	Xia et al.[281]
	$PEO/LiN(CF_3SO_2)_2$	>300	decomposition	*b*	DSC	Xia et al.[281]
	PEG/EMITFSI	~350	decomposition	*b*	TGA	You et al.[422]
composite electrolytes	PVDF + LLZTO	310	decomposition	*b*	TGA	Zhang et al.[420]
solid-state electrolytes contact with electrodes	PEO/LiTFSI + $LiCoO_2$	340	decomposition	660	DSC	Xia et al.[281]
	PEO/LiTFSI + $LiNiO_2$	250	decomposition	926	DSC	Xia et al.[281]
	PEO/LiTFSI + $LiMn_2O_4$	275	decomposition	312	DSC	Xia et al.[281]
	PEO/LiTFSI + $LiCoO_2$ (charged state)	240	decomposition	600	DSC	Xia et al.[281]
	PEO/LiTFSI + $LiNiO_2$ (charged state)	210	decomposition	640	DSC	Xia et al.[281]
	PEO/LiTFSI + $LiMn_2O_4$ (charged state)	230	decomposition	420	DSC	Xia et al.[281]
	$Li_{6.75}La_3Zr_{1.75}Nb_{0.25}O_{12}$ + graphite	>480	*b*	*b*	DSC	Inoue et al.[407]
	$Li_{6.75}La_3Zr_{1.75}Nb_{0.25}O_{12}$ + Li	>480	*b*	*b*	DSC	Inoue et al.[407]
	$Li_{6.75}La_3Zr_{1.75}Nb_{0.25}O_{12}$ + $Li_{0.47}CoO_2$	>480	*b*	*b*	DSC	Inoue et al.[407]
	$Li_{6.6}La_3Zr_{1.6}Ta_{0.4}O_{12}$ + $LiCoMnO_4$	600	decomposition	*b*	XRD	Miara et al.[217]
	$Li_{1.5}Al_{0.5}Ti_{1.5}(PO_4)_3$ + $LiNi_{0.5}Mn_{1.5}O_4$	700	decomposition	*b*	XRD	Miara et al.[217]
	$Li_{1.5}Al_{0.5}Ti_{1.5}(PO_4)_3$ + $LiCoMnO_4$	700	decomposition	*b*	XRD	Miara et al.[217]
	$Li_{1.5}Al_{0.5}Ti_{1.5}(PO_4)_3$ + $LiMn_2O_4$	600	decomposition	*b*	XRD and DTA	Gellert et al.[226]
	$75Li_2S\cdot 25P_2S_5$ + $LiNi_{1/3}Mn_{1/3}Co_{1/3}O_2$	200	crystallization	*b*	DSC	Tsukasaki et al.[411]
LIB[a]	$LiCoO_2$/carbon	123	self-heating exothermic reactions	1104	ARC and DSC	Maleki et al.[423]
separator[a]	PE	~130	separator melting	−190	DSC	Biensan et al.[424]

[a]The commercial LIB self-heating reaction temperature and PE melting temperature are provided for reference. [b]Not given.

These works pointed out that the cosintering temperature and cathodes should be chosen carefully. However, as these exothermal reactions were detected by XRD, heat flows of these reactions have not been reported yet.

On the lithium anode side, thermal runaway of inorganic electrolyte in contact with lithium was first observed by Chung and Kang.[245] The LAGP electrolytes in contact with a lithium foil were observed to first pulverize, and thermal runaway finally occurred at elevated temperature (Figure 16c). The authors attributed the thermal runaway behavior to the sharp reaction of oxygen, released from the chemically formed interface layer.

To clarify whether the ASSBs are really thermally stable at high temperature and how safe they are, Inoue and Mukai[407] first developed an all-inclusive-microcell (AIM) for DSC analysis to quantify the safety performance of SSBs. According to their work, although Nb-LLZO is stable with electrodes up to 480 °C, exothermal reactions occur when the full cell is assembled, which is attributed to reaction with cathodes and anodes. Normalizing all the ΔH values based on the weight of positive materials, the heat flow for ASSBs was found to be

DOI: 10.1021/acs.chemrev.9b00268
Chem. Rev. XXXX, XXX, XXX−XXX

around 30% of its liquid state counterparts, as shown in Figure 16b, which confirms the superior thermal stability of ASSBs. However, the as-reported AIMs still cannot reflect the real charging process as the SEI formation is absent in the construction. Perea et al.[406] presented the different thermal stability of a Li/$LiFePO_4$ pouch cell with liquid and solid polymer electrolytes. The ARC results reveal that the self-heating temperature for the all solid-state pouch cell shifted to a higher temperature of 247 °C compared to conventional LIBs (90 °C), which further supports the high thermal stability of ASSBs. The influence of state of charge (SOC) on the thermal stability was also investigated; it was found that higher SOC results in lower thermal runaway temperature, no matter whether solid or liquid-type cells.

Those findings prove the superior safety performance of ASSBs to some extent. However, there is still little knowledge about thermal runaway in ASSBs. The critical temperatures of various thermal behaviors for SSBs are still unclear. It is important to clarify the highest operating temperature even if we assume that ASSBs are safe. Furthermore, the reaction mechanisms of SSBs at high temperatures, for example the chain reactions for liquid batteries at elevated temperatures, are still far from being profoundly understood.

On the other hand, unlike commercial LIBs, consensus is not reached for the architectural designs of ASSBs, and a common approach still has not been established to obtain ultimate contact between ceramic electrolyte and electrode. Therefore, it may be not so significant to investigate the thermal behavior at the cell level if the configuration of the ASSB is not well-defined.

5. CHARACTERIZATIONS AND NOVEL METHODOLOGIES RELATED TO SOLID-STATE BATTERY

In order to overcome the instability issues and realize practical and accessible ASSBs, deep and fundamental understandings are the prerequisites.[39,62,215,224,425] The investigations on SSBs involve complicated material analysis related to crystal structure, particle morphology, valence state, elemental distribution, etc. In this entangled research field, diverse characterization tools have been utilized to gain insights from different aspects.[409,426,427] Novel techniques have even been specifically designed and established to disclose fundamental mechanisms. In this section, we will focus on the prevailing characterization techniques and the emerging novel tools for this hot topic. Note that the two foremost problems in SSBs are superior SSE design and electrode−electrolyte interface failure. About these two topics, the research focuses are quite distinct from each other. For the intrinsic characterization of SSEs, the research priority is on lithium ion conductivity and the lithium transport mechanism.[428,429] Particularly, the diversity of SSEs makes it a grand topic involving multiphase, crystal−amorphous composite and potential synergistic effect. On the other hand, interface regions are buried between two solid components. Such specific geometry makes it challenging to prepare samples with the exact interface region exposed for study,[409,425,427] and proper technique selection or even methodology development to probe the buried interface becomes a key point. Due to the distinct research focus, it is necessary to discuss the characterization of intrinsic SSEs and interface regions separately in the following paragraphs.

5.1. Characterization of the Intrinsic Properties of Solid-State Electrolytes

As a most important component in SSBs, SSEs have been widely investigated by researchers from diverse backgrounds with various techniques. To build up the overall crystal structure, XRD or neutron diffraction patterns with precise refinements can be a prevailing choice; meanwhile, the local atom stacking can be revealed by diverse electron microscopy techniques with atomic scale resolution.[183,250,430,431] To figure out the detailed chemical constitution of a certain system, spectroscopy including XAS, XPS, and SIMS, will be the perfect probe, and the probe depth difference from various detection modes together with etching strategies may well provide constitutional distribution from surface to bulk.[165,230,243,432] As for the key parameters, the electronic and ionic conductivities and electrochemical stability window can be obtained from various electrochemical characterizations.[433−435] Such conventional characterizations have been widely utilized in previous research on diverse SSEs.

Even so, we would like to emphasize the detailed characterization of intrinsic properties of SSEs. Seemingly, the characterization of bulk SSEs is quite direct and straightforward, but it may be a tricky issue to ensure that the obtained information actually represents the intrinsic properties of the SSEs instead of an artificial effect. The detection of the electrochemical stability window is a typical example. As discussed above, LSV has been established as a decent method that validated a wide stability window of ∼6 V for garnet electrolytes.[436] However, by designing an optimized carbon coated SSE for the measurement, a narrow intrinsic electrochemical stability window is indicated, which is consistent with theoretical calculations.[63,233] As for the lithium ion conductivity, the bulk and grain boundary resistance can be well distinguished from each other by AC impedance analysis and equivalent circuit fitting. The presence of grain boundaries in the polycrystalline electrolytes generally play a non-negligible role, giving rise to reduced total (bulk + grain boundary) conductivity, but the lithium ion conducting mechanisms for several SSEs have not reached consensus. In LISICON-type $Li_{3.1}Zn_{0.45}GeO_4$ and perovskite-type $Li_{0.34}La_{0.51}TiO_3$, the grain boundary conductivities are reported to be 1−2 orders of magnitude lower than that of bulk conductivity.[82,102] In garnet $Li_5La_3Bi_2O_{12}$ and $Li_6SrLa_2Bi_2O_{12}$, Murugan et al. quantified the grain boundary contribution appreciably up to 54% and 61%, respectively.[437] However, in the case of $Li_6SrLa_2Ta_2O_{12}$ and $Li_6BaLa_2Ta_2O_{12}$ based garnet electrolytes, the total and bulk conductivity are found to be nearly the same magnitude, exhibiting mainly a bulk contribution with rather small grain boundary contribution.[109] Although such discrepancy can be explained by material composition and structural differences, it should be noted that the full picture of how lithium ions are conducted in SSEs is still far from being clear for many SSE systems. Still, numerous reported lithium ion conductivities in the literature may not even distinguish conductivities from bulk and grain boundaries, where their intrinsic values are mingled altogether. As can be concluded here, further validation from impedance analysis or even developing new characterization techniques will be necessary to clarify lithium ion conductivity of SSEs.

To figure out the detailed lithium ion conductivity mechanism, direct experimental probe of the lithium diffusion channel within the SSE skeleton will be of vital significance. However, the direct probe of Li ions in the crystal lattice has

DOI: 10.1021/acs.chemrev.9b00268
Chem. Rev. XXXX, XXX, XXX−XXX

been challenging due to the low atomic number and its weak interaction with conventional probe media like X-ray photons or electron beams. Thanks to the sensitivity of neutrons to Li atoms, neutron scattering had become an effective method to fingerprint lithium ion transport in the structure. The combination of neutron diffraction and maximum entropy method (MEM) may further provide direct visualization of lithium ion diffusion schemes, which is presently the only direct characterization technique to map out lithium transport channels. In previous investigations on $LiFePO_4$ cathodes, Nishimura et al. first combined high temperature powder neutron diffraction and MEM to visualize lithium distribution in $LiFePO_4$ along the [010] direction, verifying a curved 1D lithium diffusion path in this prevailing electrode.[438] This characterization methodology was then transferred to SSE research; Kwon et al. first utilized neutron diffraction and MEM to visualize the lithium conduction pathways in LGPS electrolyte.[430] It was found that the 2D distribution of Li along the *ab* plane became apparent at high temperature, and the ionic conduction mechanism transitions from a 1D to a 3D pathway with temperature increase from 4.8 to 750 K. Later, the same research group further visualized 3D conduction pathways in the LGPS-type structure at room temperature, where high ionic conductivity comparable to liquid electrolyte can be obtained by small amount of chlorine substitution in the Cl(1)(8g) sites within $P(2b)X_4$ tetrahedra.[30] The combination of advanced characterizations and theoretical calculations proves indispensable in clarifying the detailed lithium transport behavior.

As discussed above, composite electrolytes consisting of various components have been proven effective in achieving superior performance and mitigating the shortcomings of each single component. However, such composite systems make the characterization and clarification of intrinsic lithium transport properties even more complicated and challenging.[439] As first reported by Liang, the ionic conduction of the two-phase system $LiI-Al_2O_3$ was anomalously high in comparison with pure phases.[11] After intense discussion, Maier revealed the scenario that the space charge region contributes to conduction enhancement in the composite electrolytes.[440,441] To gain further insights into such an entangled system, a combination of techniques sensitive to not only each component but also potential interface regions will be preferred. Note that typical PEO based polymer electrolytes contain crystallized and amorphous phases with distinguished transport properties at room temperature. Prevailing composite electrolytes combine inorganic and organic components, which further adds to the challenges for characterization and clarification in the multiphase system. In LLZO−PEO based composite electrolyte, Zheng et al. utilized high resolution Li NMR to monitor Li diffusion within the LLZO-PEO SSE. By using NMR active isotopes, lithium diffusion pathways in SSEs can be tracked among distinct components. In contrast to prevailing understanding, Li prefers transit through LLZO ceramics rather than in PEO polymer or in interfaces between LLZO and PEO.[442] Considering the significance of solid composite electrolytes in realizing SSBs in the near future, detailed investigations on the lithium ion conductivity are urgent and vital and need to be more meticulous and detailed.

5.2. Characterization of Interfaces between Electrodes and Solid-State Electrolytes

Based on previous reports, the properties of the interface region are practically the bottleneck for the development of SSBs, which has been the focus in many literature reports. Note that the interface region is often well buried between the electrode and the SSE; this feature makes it challenging to directly probe it. Surface sensitive techniques such as XPS with shallow probe depth cannot penetrate through the solid sample, while bulk sensitive techniques such as XRD collect information from overall samples with interface signal overwhelmed in the total signal from bulk. As a result, specific sample preparation will be key to achieve direct characterization of the interface region. Utilizing microfabrication techniques such as FIB or XPS etching is a most straightforward strategy to expose the cross section interface region for direct probe.[216,443] But possible damage under high energy ion flux cannot be excluded. Thin film deposition is another promising choice to obtain "quasi-interface" samples. With well controlled deposition film thickness, the interfacial reactions between electrolyte and lithium anode can be directly characterized.[230] Powder sample mixing may be another subtle method to magnify the ratio of interface region in the total sample.[217] Particularly, the utilization of nanometer scale powder mixing can well make the interface signal comparable to or even stronger than bulk signal. Moreover, specific characterization technique design or modification has been proven effective to obtain depth resolved information, which empowers direct detection of the interface layer.[444] Even though the interface region is hidden, delicate sample preparation and characterization development may well strengthen interface signal or even enable direct experimental probe, while detailed and insightful interface study still calls for more subtle interface sample design and preparation that can represent the intrinsic properties of interface layer.

It is worth noting that the interface region is actually a transition layer from one phase to another, which involves inhomogeneous spatial distribution of particular elements or newly formed phases. Meanwhile, chemical or electrochemical instability may lead to irreversible interfacial reactions with valence change of key elements. Consequently, characterizations with high spatial resolution and high element and chemical sensitivity will be preferred. The combination of electron microscopy and spectroscopy will be a good choice to realize such a goal. With the extremely high spatial resolution from electron microscopy and the chemical environment sensitivity from affiliated spectroscopy, the interface layer can be well investigated. As reported by Kim et al., the decent spatial resolution of EDS line profiles (∼5 nm) across the $LLZO/LiCoO_2$ interface demonstrates Co, La, and Zr concentration varying gradually across the intermediate layer, which validates formation of the novel reaction phase La_2CoO_4 by mutual diffusion.[216] Cheng et al. further combined HAADF-STEM and EELS to monitor chemical instability between cubic LLZO and metallic Li.[165] With the atomic image intensity contrast probed by HAADF-STEM and the evolution of electronic structure probed by EELS, a tetrahedral-like LLZO interphase can be detected upon lithium contact. The thickness of the newly formed layer is small as ∼5 unit cells, which prevents further interfacial reactions, and the cubic to tetrahedral transition is key to the electrochemically benign interface of LLZO.[241] In recent years, high resolution TOF-SIMS has been further demonstrated to be able to reveal

DOI: 10.1021/acs.chemrev.9b00268
Chem. Rev. XXXX, XXX, XXX−XXX

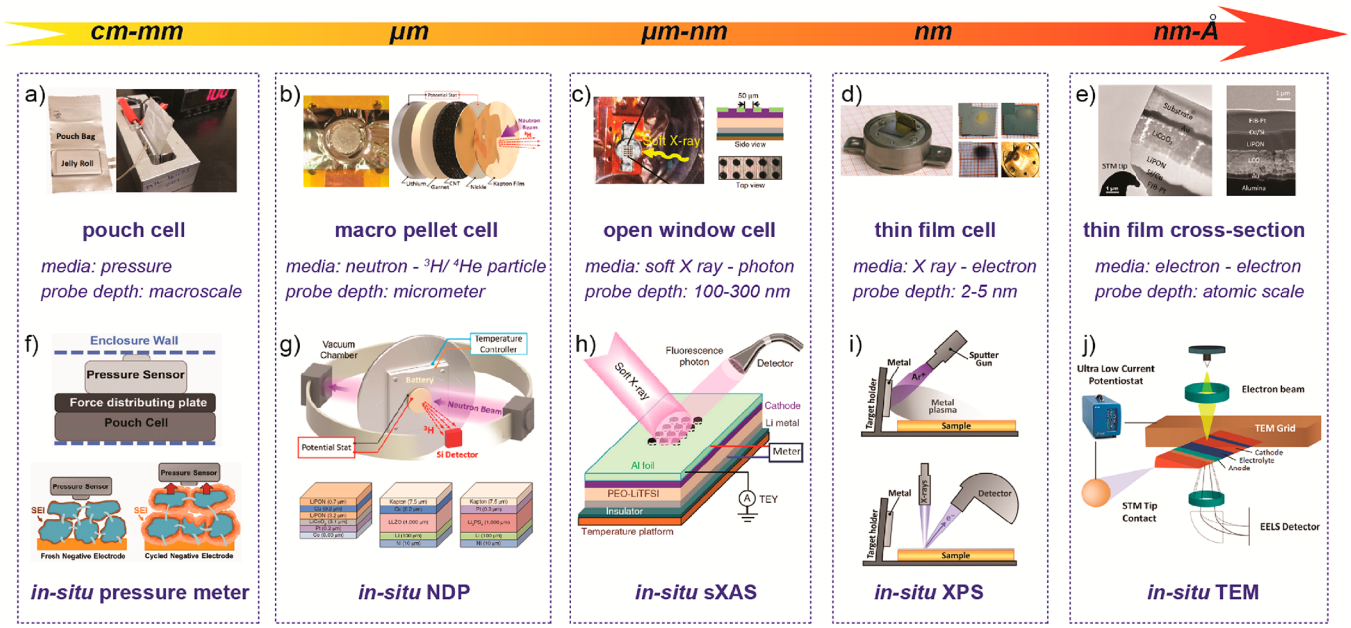

Figure 18. Schematic illustration of *in situ* cell design and characterization of SSBs. Based on the different probing depths of difference characterization techniques, different model cells can be designed accordingly to conduct *in situ* and *operando* characterizations, and different spatial resolutions can be achieved. Panel a is reprinted with permission from ref 445. Copyright 2017 The Electrochemical Society. Panel b is reprinted with permission from ref 447. Copyright 2017 American Chemical Society. Panels c and h are reprinted with permission from ref 448. Copyright 2013 Nature Publishing Group. Panels d and i are reprinted from ref 230, Copyright 2015, with permission from Elsevier. Panels e and j are reprinted with permission from ref 246. Copyright 2016 American Chemical Society. Panel f is reprinted from ref 446, Copyright 2019, with permission from Elsevier. Panel g is reprinted with permission from ref 263. Copyright 2019 Nature Publishing Group.

3D distribution of key elements from interfacial reaction products. At the interface between $LiCoO_2$ and cubic LLZO, element diffusion at high temperature, particularly Al, leads to a tetrahedral LLZO phase at the interface, which exhibits less lithium ion conductivity and has a profound influence on the electrochemical properties and chemical stability against moist air.[262] The widespread applications of these combined characterizations and development of novel techniques bring about significant information on the interface layer with high spatial and elemental resolution.

With the deepening of interface investigations, researchers begin to realize that the interface region may not simply be an inert layer that maintains its original form upon contact but evolves with battery cycle. As a result, *in situ* and *operando* characterizations are very necessary to clarify the interface change upon cycling. Compared with conventional *ex situ* characterization techniques, which are static and often destructive, *in situ* and *operando* characterizations have significant advantages. Upon electrode−electrolyte contact and interface formation, metastable phases may well form that can be omitted in *ex situ* characterizations. Wenzel et al. investigated the interface chemical stability of $Li_7P_3S_{11}$ in contact with metallic lithium.[232] By virtue of *in situ* XPS, the measurement reveals the growth of an interfacial layer consisting of Li_2S and Li_3P, which coincides with time dependent EIS evolution, while in the case of *ex situ* XPS investigations, only Li_2S can be detected due to the facial decomposition of Li_3P even with the protection of pure Ar or UHV atmosphere. On the other hand, the interface region may demonstrate dynamic evolution upon electrochemical operation, which can be completely missed in *ex situ* characterizations. A typical example is the *operando* XPS and AES study of the SEI formation and evolution process in Li_2S−P_2S_5 SSEs, as investigated by Wood et al.[307] Redox active SEI components, including Li_3P and Li_2O, and stable SEI components, including Li_2S, can be established by such *operando* characterizations. Such dynamic information is irreplaceable to build up fundamental and comprehensive understanding of interface evolution.

In the last years, SSBs have seen rapid development of *in situ* and *operando* characterizations, which provide valuable insights disclosing interface response with battery cycle (Figure 18). However, *in situ* characterizations typically require delicate battery design and meticulous detection; these challenges limit widespread applications. The special *in situ* battery design is mostly limited by the detection mode and probe depth confinement of various techniques. Most directly, the overall mechanical or pressure change can be detected with sensors; as a result, a typical pouch cell can be utilized for *in situ* measurement. Louli et al. developed a homemade *in situ* characterization method to monitor mechanical stress evolution.[445] With Archimedes-type *in situ* volume measurement, thickness detection, and pressure monitoring, the effect of electrode mechanical expansion and contraction of the pouch cell can be well obtained. In a recent work by Luoli et al., an inversely proportional relationship was established between irreversible pressure growth and capacity fade.[446] To gain more detailed insights, techniques with modest macroscale probe depth can be adopted for *in situ* and *operando* characterizations. Neutron based techniques are good candidates for direct probe of battery operation due to the large probe depth of incident neutrons. Wang et al. a assembled Li/garnet pellet/Li symmetric cell with excellent Li/garnet contact for *in situ* neutron depth profiling (NDP) measurement. The interface behavior of the garnet electrolyte in contact with metallic lithium can be monitored, and short

DOI: 10.1021/acs.chemrev.9b00268
Chem. Rev. XXXX, XXX, XXX−XXX

Table 13. Evaluation of Stability Issues of Different Electrolytes[a]

★ Unacceptable
★★★ Sufficient for a working battery
★★★★★ Good performance

Solid electrolytes	Thermal stability	Chemical stability	Stability against Li	Electrochemical stability	Mechanical stability	Ionic conductivity
Polymer	★★	★★★	★★★	★★	★★	★★★
Garnet	★★★★★	★★	★★★	★★★	★	★★★
NASICON	★★★★★	★★★★	★	★★★★	★	★★★
Sulfide	★★★	★	★★★	★	★★	★★★★
Liquid electrolyte	★	★	★★	★★★	★★★★	★★★★★

[a]"Stability against Li" indicates the chemical and electrochemical stability versus lithium metal anode. "Electrochemical stability" indicates the upper voltage limits of the SSEs. One star indicates a critical challenge of the SSE toward practical applications. Three stars suggest that the stability is sufficient to support solid-state cell operation, but further improvements are still needed. For example, despite the LLZO exhibiting thermodynamic stability with lithium, the interfacial modifications or some treatments (high temperature, pressure) are still needed for achieving reasonable cycle stability. Five stars indicate the stability of the SSEs is rather high, which is supreme over other electrolytes.

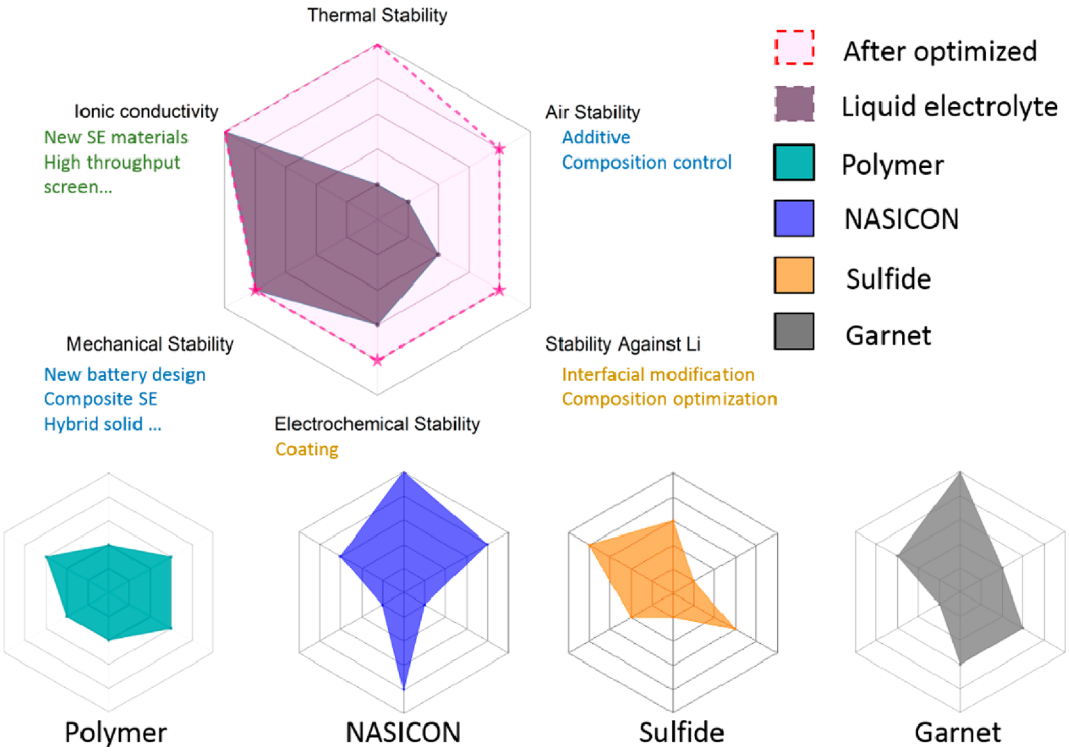

Figure 19. Radar maps of the stability issues of different types of electrolytes. The scores of different electrolytes in various aspects are given based on Table 13.

circuiting of the SSB can be diagnosed.[447] In a recent report by Han et al., researchers further utilized *in situ* and *operando* NDP to monitor the dynamic evolution of lithium concentration profiles in three conventional SSEs including LiPON, LLZO, and amorphous L_3PS_4.[263] Electronic conductivity is validated to be responsible for lithium dendrite formation in SSEs. With a shallow penetration depth of hundreds of nanometers, *in situ* sXAS calls for specific cell design compatible with a vacuum chamber. Liu et al.[448] utilized a PEO based SSE for *operando* soft X-ray spectroscopy characterizations. A specially designed probing window allows emitted photon collection with photon-in−photon-out mode. Distinct dynamic response between NMC and LFP based SSB can be detected.[448] With even thinner escape depth of emitted electrons, *in situ* XPS only allows an extremely thin lithium deposit to cover the interface. Wenzel et al.[228,230] utilized a standard argon ion gun in the XPS chamber to sputter a target lithium metal onto the SSE and build a desired interface by a "bottom-up" approach. The interface instability of SSEs against lithium anode can be characterized by *in situ* XPS.[228,230,234]

DOI: 10.1021/acs.chemrev.9b00268
Chem. Rev. XXXX, XXX, XXX−XXX

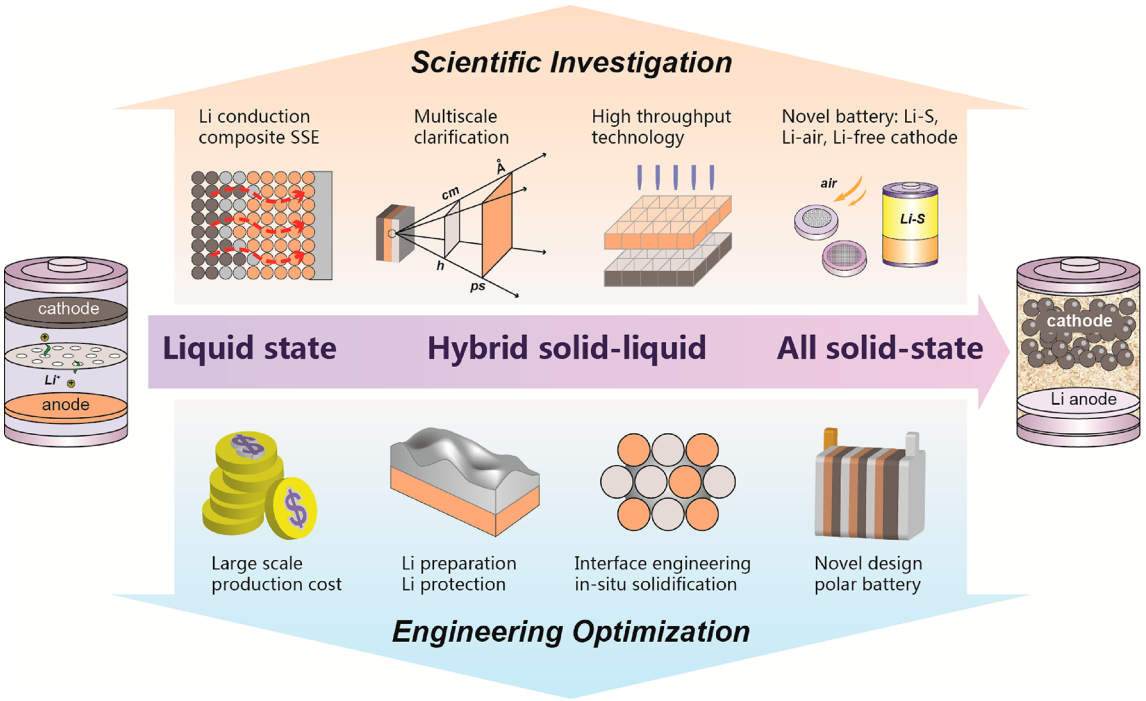

Figure 20. Perspectives for future studies on SSBs

The reduction of Ti and Ge by metallic lithium and decomposition of LiPON can be directly probed from new XPS peaks rising or peak shifting. To further investigate the microscale interface behavior, the combination of thin film deposition and microscale or even nanoscale manufacturing is a proper strategy. With a thin film battery and FIB sculpture, the atomic scale interface behavior can be detected. Wang et al.[246] prepared ASSBs by RF magnetron sputtering and designed a novel nanobattery enabling galvanostatic charge in a TEM chamber. When combined with *in situ* STEM-EELS, a disordered interfacial layer growth can be detected between $LiCoO_2$ and LiPON. Moreover, intermediate Li_2O/Li_2O_2 formation can be verified by *in situ* characterization, which will generally decay to rock salt structure as probed by *ex situ* characterization.[246] Within thin film battery structure, Yamamoto et al. further developed *in situ* electron holography to investigate the 2D electric potential distribution in a $LiCoO_2/Li_{1+x+y}Al_yTi_{2-y}Si_xP_{3-x}O_{12}$ thin film battery upon cycling.[223,449] By combination of this technique with EELS, the detailed redox process can be verified and the source of interfacial reaction resistance can be determined.[223] Later, Yamamoto et al. utilized *in situ* electron holography to monitor the lithium shuttling in SSE and negative electrode in thin film $LCO/Li_{1+x+y}Al_yTi_{2-y}Si_xP_{3-x}O_{12}$(LATSPO)/Pt battery. The 1600 nm wide retardant region of Li^+ transfer can be detected within LATSPO, which can be attributed to a small amount Li^+ trapped within the SSE.[449] Even though *in situ* characterizations are still confined within model systems in specially designed cells in past years, the rapid development of *in situ* characterization techniques has provided valuable and complementary information in clarifying the dynamic response of interface layer and attracted broad research attention. Following the intense research enthusiasm, more and more *in situ* and *operando* techniques will be developed in the near future, which will play an even more important role for future investigations.

6. CONCLUSIONS AND PERSPECTIVES

In this review, a historical retrospective on solid-state batteries and SSEs is presented. The stability issues of key materials with their associated interfaces and the main hindrance for practical application of SSBs are summarized and highlighted. Characterization techniques for investigating these related problems are also briefly overviewed. Focusing on the stability

Table 14. Safety Standards and Testing Subjects for LIBs

test subject	standards			
	GB 31241[a]	JIS C8714[b]	IEC 62133[c]	UL 1642[d]
heating	√	√	√	√
thermal cycling	√	√	√	√
shock	√	√	√	√
vibration	√	√	√	√
drop	√	√	√	
impact	√			√
projectile	√			√
crush	√	√	√	√
external short circuit	√	√	√	√
internal short circuit		√		√
abnormal charge	√	√	√	√
forced discharge	√	√	√	√
low pressure	√	√	√	√

[a]GB 31241, lithium ion cells and batteries used in portable electronic equipment - safety requirements, proposed by Chinese Standardization Administration. [b]JIS C8714, safety tests for portable lithium-ion secondary cells and batteries for use in portable electronic applications, proposed by Japanese Standards Association. [c]IEC 62133, secondary cells and batteries containing alkaline or other nonacid electrolytes - safety requirements for portable sealed secondary cells, and for batteries made from them, for use in portable applications, proposed by International Electrotechnical Commission. [d]UL 1642, UL Standard for Safety for Lithium Batteries, proposed by Underwriters Laboratories Inc.

DOI: 10.1021/acs.chemrev.9b00268
Chem. Rev. XXXX, XXX, XXX−XXX

of SSBs, four types of stability issues are categorized and clarified in detail, including chemical stability, electrochemical stability, mechanical stability, and thermal stability. These stability issues are determinative to the practical development of SSBs in the near future. For a comprehensive evaluation of these stability challenges in SSBs, here we compare the four prevailing types of SSEs in Table 13 and Figure 19 based on the discussions above. In the summary table, one star is defined as unacceptable stability for practical applications, three stars imply that the stability is sufficient to support SSB operation but further improvements are still needed, while five stars indicate that the stability of the SSEs is rather high and superior to other electrolytes. As mentioned in the footnote, "Stability against Li" indicates the chemical and electrochemical stability versus lithium metal anode.

It is somewhat frustrating that none of the prevailing SSEs can simultaneously satisfy all the stability requirements. The stability of polymer electrolytes from different aspects is more balanced than that of ceramic electrolytes, which is the closest choice for practical applications presently. For sulfide electrolytes, the overriding limitation lies in the narrow electrochemical windows, poor air stability, and resulting deleterious H_2S gas production. Nevertheless, the favorable mechanical properties of sulfide electrolytes do provide intimate electrolyte/electrode contact, which allows sulfide based ASSBs to perform reasonably well in conventional sandwich battery geometry. Considering the compatibility of sulfide electrolytes with roll-to-roll industrial fabrication, there are likely possibilities for the large applications of sulfide based ASSBs in the near future. For oxide electrolytes, although lithium wettability and lithium stability issues can be overcome by interfacial engineering, the inherent solid−solid point contact hinders the ionic transport pathways, making the performance of oxide ASSBs far from satisfactory, not to mention the cracking issues of ceramic pellet-based batteries. Based on existing oxide electrolyte materials and battery configurations, the above challenges are critical but difficult to solve simply by material and interface modifications. There is still a long way to go for the commercialization of oxide based ASSBs.

A general overview of SSB development during past decades demonstrates two interconnected but in-tandem historical stages. Early research efforts mostly focused on the discovery and design of SSEs with high lithium ion conductivity. During this period, numerous polymer and ceramic SSEs were reported, shaping the basic framework of the present rich variety of SSE families. The pursuit of fast Li ion conductors even led to SSEs with Li ion conductivity higher than conventional liquid electrolytes. However, when high Li conductors were integrated into SSBs, the as-fabricated SSBs only demonstrated modest electrochemical performance, in contrast to the intuitive and optimistic anticipations. As a result, the second stage of SSB development begins to focus on testing the electrochemical performance of the as-fabricated SSBs on the whole. The complicated interfacial challenges instead of conductivity issues are found to practically hinder the exploitation of SSBs capacity, and intensive investigations are shifted toward addressing the interfacial challenges in SSBs. Therefore, the past decades-long SSB development history highlighted not only the importance of intrinsic property optimization of key components in SSBs but also the necessity to re-evaluate these properties in the specific and integrated SSB scheme. In addition, to fulfill large-scale production and commercialization of SSBs in the near future, top-level schematization and rational coordination of scientific investigation as well as engineering exploration will be essential to the R&D of SSBs. Here, in the following discussions, we highlight several points that we believe deserve more attention in the future development of SSBs (Figure 20).

6.1. Scientific and Fundamental Investigations for Superior SSB Systems

Even though rapid and significant progress has been obtained from continuous research efforts in past decades, SSBs are still hindered by a great many unsolved scientific challenges. During the second phase of SSB development, more open questions even begin to arise within assembled SSB structures, which calls for more fundamental investigations.

6.1.1. Ionic Conduction Mechanism. Since the very first reported solid ionic conductors, the intrinsic ionic transportation in SSEs has been studied for over 100 years. Fundamental understanding or physical models have been built up for almost each type of SSEs. However, for some cases, even more than one scenario has been proposed for one single material, leaving fierce debates yet to be clarified. As for the next stage of SSB development, the clarification of ionic transport properties and mechanisms beyond intrinsic ionic conduction within certain SSEs will become even more critical in SSBs, particularly the Li ion conduction at complicated and complex interfaces of polymers/ceramic fillers, SSEs/electrodes, and sometimes interface between SSEs and liquid electrolytes. These interface regions involve various materials with different forms; corresponding investigations on the ionic conduction mechanism will be even more challenging, which calls for tremendous research efforts.

6.1.2. Multiscale and Multidimensional Characterizations and Simulations. Note that practical SSB operation involves orders of spreading at different time and space scales; such features make it challenging for both experimental characterization and theoretical simulations. Although prevailing techniques or models can present valuable insights in one way or another, the integrated and comprehensive understanding of SSB operation is still missing. As a result, combination of multiscale and multidimensional characterizations and simulations are urgently needed at the present stage. In certain aspects, novel methodology utilization or even development are indispensable. Particularly, *in situ* and *operando* characterizations will play an essential role in elaborating the complicated interface behaviors in SSBs, with time scale covering from picosecond for electron excitation to hour for macroscopic variation, while length scale covers from angstrom for atomic arrangement to millimeter for battery level architecture. On such basis, a full picture of SSB operation can be mapped out with not only macrocontours but also focusing on specific details, and the knowledge gap between laboratory-based models and practical SSBs can be bridged and remedied.

6.1.3. High Throughput Technologies and Big Data Mining. During the first stage of SSB development, high throughput technology and Materials Genome Initiative (MGI) projects have promoted the discovery and screening of fast lithium ion conductors. At the present stage, to further accelerate practical SSB development, more appropriate chemical and mechanical parameters should be taken into considerations besides modest ionic conductivity, in both high throughput calculations and experiments. In addition, recent progress in theoretical calculations have even enabled

DOI: 10.1021/acs.chemrev.9b00268
Chem. Rev. XXXX, XXX, XXX−XXX

predicting the interfacial chemo-electrochemical behaviors by DFT, which is promising in providing more precise and practical information on design of future SSBs. Above all, a most significant and thriving advance in the past few years lies in artificial intelligence (AI) and machine learning technologies, which may even shift the fundamental paradigms of SSB investigations and material selection via big data mining strategy. With the strong support from these techniques, there are good reasons to expect even more important roles for calculations and simulations in SSB research and thriving SSB development in the near future.

6.1.4. Novel Battery Chemistries. With the prosperity of SSEs, new battery chemistries beyond conventional schemes become feasible options, which may open up another avenue for future SSB design and development. Presently, Li−S and Li−air batteries are widely accepted as promising energy storage devices for future applications, while SSE development may well benefit or promote corresponding investigations. For Li−S battery chemistry, employing SSEs can greatly suppress the "shuttle effect" in carbonate liquid electrolytes, while the cathode side polarization in Li−air systems can also be alleviated with SSE utilization. More importantly, the SSB framework makes metallic Li practically accessible; the almost inexhaustible Li source liberates cathode options from conventional TM lithium oxide confinement. Therefore, numerous Li-free cathodes become practically accessible candidates, which could potentially provide higher energy density than prevailing cathode materials, as demonstrated by a recent calculation by Wang et al.[450] Even so, the compatibility and the additional instability issues brought up by these new materials and new mechanisms should be further clarified.

6.2. Engineering and Technical Challenges for Practical SSBs

In addition to the scientific challenges, there are even more engineering hurdles before practically accessible SSBs can be built. In principle, SSBs exhibit inspiring advantages over conventional LIBs. However, successful commercialization of SSBs needs to comprise extrinsic factors including manufacturing cost, compatibility of large-scale production, and practical feasibility.

6.2.1. Low-Cost and Large-Scale Production of Key Materials. It should be noted that most available SSEs require much higher production cost than conventional carbonate-based liquid electrolytes, especially for some SSEs containing rare earth or costly elements, such as LLZO or LGPS. As a result, it becomes highly desirable to substitute these elements by some abundant ones. One preliminary attempt is the successful prediction and design of LGPS analogues without Ge, such as $Li_2SnP_2S_{12}$ and $Li_2SiP_2S_{12}$, which exhibit comparable ionic conductivity. On the other hand, prevailing SSE synthesis methods generally demand high temperature sintering at ∼600−1000 °C. The high energy consumption during this process will not only add to SSB production cost but also lead to environmental penalty. Moreover, most current SSBs are incompatible with large-scale roll-to-roll fabrication widely used in conventional LIBs. As can be inferred, development of novel low-cost SSE synthesis methods as well as facile SSB construction strategies should be further developed in the years to come.

6.2.2. Technical Challenges with Li Metal Anodes. The practically accessible Li metal anode has been widely believed to be a most significant advantage of SSBs, while from the energy density point of view, the application of Li metal in SSBs is actually an inevitable choice to make SSBs competitive against conventional LIBs. As calculated by Wu et al.,[451] the densities of SSEs are mostly higher than prevailing liquid electrolytes, which brings about even lower energy density of SSBs. However, the extremely high chemical reactivity of metallic Li brings new technical challenges in not only thin Li foil production but also metallic Li storage and transport during SSB manufacturing.[452] Extra protection systems and safety concerns should be taken into consideration. Meanwhile, the technical challenges from Li metal anode will further add to the production cost and make SSBs less competitive economically.

6.2.3. Interface Engineering and *in Situ* Solidification. Based on previous discussion, interfacial engineering has been extensively explored and verified to be effective in promoting SSB performance. However, a general design principle of the interphase layer is still unclear. On SSE/Li interfaces, different viewpoints hold on the practical roles of MCI (alloy materials, for example) and SEI materials (LiF, LiPON), while on SSE/cathode interfaces, the rigid−rigid contact and related stability issues are the prerequisites to SSB operation. The selection and adoption of proper materials to construct suitable SSE/electrode interfaces call for more research attention. Moreover, many interfacial modification approaches reported to date utilize thin film techniques, like ALD, PLD, and sputtering, which should further reduce the manufacturing cost and improve the production efficiency for practical application, while some current available low-cost and efficient methods, like spray coating or solution based methods, are also preferable. At the present stage, wetting the interface by addition of small amount of liquid is found to be the most straightforward and efficient way, where an *in situ* solidification process is expected to transform the liquid into solid phase. As described by Li et al.,[391] the conversion of organic liquid electrolytes to solid phases can effectively mitigate lithium dendrite growth and enable stable cycling. Nonetheless, some manufacturing challenges in large scale production should be further verified.

6.2.4. Novel Battery Design. Besides the above-mentioned issues, reducing the proportion of inactive materials (electrolytes and collectors, for example) is essential to promoting the energy density of SSBs. In 2015, McCloskey[453] pointed out that SSBs will deliver even lower volumetric energy density than commercial LIBs when SSE thickness exceeds 99 μm, which is smaller than most reported values. However, reducing SSE thickness at the cost of mechanical strength will make ceramic pellets fragile. In addition, reduction of the SSE proportion in cathode composite is also critical to enhance SSB energy density, as 30−40 wt % SSE particles are composited into cathodes in previous reports. As can be inferred, innovations in SSB design and new synthesis methods may well play a vital role in future SSB development. For example, a current LIB module is constructed by connecting a number of LIB units with external wiring to prevent internal short-circuiting and electrolyte leakage, while nonfluidic SSEs enable internal series connections in SSBs, which can be regarded as an efficient way to simultaneously enhance the energy density and lower the costs. Therefore, the development of techniques in advanced manufacturing are critical and urgently required to guarantee highly efficient and accurate bipolar SSB fabrications.

DOI: 10.1021/acs.chemrev.9b00268
Chem. Rev. XXXX, XXX, XXX−XXX

In the very end, we would like to recall the safety issue of SSBs, which are essentially the primitive driving force for developing SSBs and also the precondition for SSB application. Although SSBs have been widely believed to be intrinsically safe, such claim still lacks support from safety test data in real SSBs. The quantitative determination of the safety boundary and the related key parameters are very necessary. To properly evaluate the safety performance of SSBs, corresponding safety standards will be the paramount guideline (Table 14). The well-established international safety standards for conventional LIBs might provide eligibility reference for assessing SSBs at the current stage. However, the distinct characteristics of SSBs demand dedicated safety standards of their own, which can be expected to gradually be established upon further development of SSBs. The past decades have witnessed rapid development of SSBs accompanying intense research enthusiasm involving government funding, industrial investment, and scientific efforts. Throughout the text, although we have outlined tremendous hindrances and daunting challenges for the next stage of SSB development, we believe that there are good opportunities to embrace the forthcoming era of SSBs, particularly with these ongoing worldwide thriving investigations.

AUTHOR INFORMATION

Corresponding Authors

*E-mail: hli@iphy.ac.cn.
*E-mail: xyu@iphy.ac.cn.

ORCID

Xiqian Yu: 0000-0001-8513-518X
Hong Li: 0000-0002-8659-086X

Author Contributions

[§]R.C. and Q.L. contributed equally.

Notes

The authors declare no competing financial interest.

Biographies

Rusong Chen is now a Ph.D. candidate in Institute of Physics, Chinese Academy of Sciences (IOP, CAS). He obtained his Bachelor degree in functional materials at 2017, from Huazhong University of Science and Technology (HUST). His research works mostly focus on the instability issues in all solid-state batteries including interface decay and heat generation, as well as the design of novel solid-state batteries for practical applications.

Qinghao Li is now a postdoctoral researcher in Institute of Physics, Chinese Academy of Sciences (IOP, CAS). He received his Bachelor degree in Physics from Shandong University (2011) and his Ph.D. degree in condensed matter physics from Shandong University (2017). He worked at Advanced Light Source in Lawrence Berkeley National Laboratory as a visiting Ph.D. candidate in 2014−2016. His research interest focuses on high energy density lithium ion battery materials, solid state electrolytes, particularly with synchrotron radiation based soft and hard X ray spectroscopy.

Xiqian Yu is a professor at Institute of Physics, Chinese Academy of Sciences (IOP, CAS). He received this Bachelor's degree in applied physics (2005) from Wuhan University and Ph.D. degree in condensed matter physics (2010) from IOP, CAS. Prior to IOP, he worked at Brookhaven National Laboratory as a postdoctoral fellow (2010−2013) and Physics Associate (2013−2016). His research interest is in the field of electrochemical energy storage with the main focus on the characterization of the electrode materials for rechargeable batteries.

Liquan Chen is a professor at the Institute of Physics, Chinese Academy of Sciences (IOP, CAS). He has been devoted to the field of lithium ion batteries for decades. His research activities are related to ion or electron transport in materials. He is especially interested in design and development of new materials and new systems for the next generation of energy storage devices, particularly the development of novel solid-state batteries for vehicle and large-scale applications.

Hong Li is a professor in Institute of Physics, Chinese Academy of Science. His research interests include fundamental research on batteries, such as transport of ions and electrons, size effect, interface phenomena, and structural evolution, and application research, including high energy density Li-ion batteries using Si based anodes, solid lithium batteries, and battery failure analysis. He leads a CAS SPRP "Battery for EV" 5-year program and serves as a committee member for Advanced Energy in Ministry of Science and Technology of China since 2012.

ACKNOWLEDGMENTS

The work was supported by funding from National Key R&D Program of China (Grant No. 2016YFB0100100), National Natural Science Foundation of China (Grant Nos. 51822211 and U1932220), and the Foundation for Innovative Research Groups of the National Natural Science Foundation of China (Grant No. 51421002).

LIST OF ABBREVIATIONS

LIB	Li ion battery
ASSB	all solid-state battery
ASSLIB	all solid-state lithium ion battery
SSB	solid-state battery
SSE	solid-state electrolyte
LISICON	lithium superionic conductor
NASICON	sodium superionic conductor
PEO	poly(ethylene oxide)
PAN	poly(acrylonitrile)
PVDF	poly(vinylidene fluoride)
PMMA	poly(methyl methacrylate)
LiTFSI	$LiN(CF_3SO_2)_2$
LLZO	$Li_7La_3Zr_2O_{12}$
LATP	$Li_{1+x}Al_xTi_{2-x}(PO_4)_3$ (x = 0.3, 0.4, 0.5)
LAGP	$Li_{1+x}Al_xGe_{2-x}(PO_4)_3$ (x = 0.3, 0.4, 0.5)
LZGO	$Li_{14}ZnGe_4O_{16}$
LGPS	$Li_{10}GeP_2S_{12}$
LLTO	$Li_{3x}La_{2/3-x}TiO_3$
LiDFOB	$LiF_2BC_2O_4$
LPSCl	Li_6PS_5Cl
LNMO	$LiNi_{0.5}Mn_{1.5}O_4$
LPS	Li_3PS_4
LCO	$LiCoO_2$
LTO	$Li_4Ti_5O_{12}$
NCM	$Li(Ni_xCo_yMn_z)O_2$ ($x + y + z = 1$)
LFP	$LiFePO_4$
SEM	scanning electron microscope
XRD	X-ray diffraction
XPS	X-ray photoelectron spectroscopy
FIB	focused ion beam etching
SIMS	secondary ion mass spectrometry
NMR	nuclear magnetic resonance
DFT	density functional theory

DOI: 10.1021/acs.chemrev.9b00268
Chem. Rev. XXXX, XXX, XXX−XXX

XAS	X-ray absorption spectroscopy
CZM	cohesive zone model
MEM	maximum-entropy method
CV	cyclic voltammetry
LSV	linear sweep voltammetry
EDS	energy dispersive spectroscopy
HAADF	high-angle annular dark field
STEM	scanning transmission electron microscope
EELS	electron energy loss spectroscopy
TOF-SIMS	time of flight secondary ion mass spectrometry
RBS	Rutherford backscattering spectroscopy
FTIR	Fourier transform infrared spectroscopy
AES	Auger electron spectroscopy
UV	ultraviolet
DSC	differential scanning calorimetry
AIM	all-inclusive microcell
ARC	adiabatic rate calorimeter
UHV	ultrahigh vacuum
EIS	electrochemical impedance spectroscopy
HSAB	hard and soft acids and bases theory
MCI	mixed ionic/electronic conducting interphase
VBM	valence band maximum
SEI	solid electrolyte interphase
DME	dimethyl ether
PE/PP	polyethylene/polypropylene
B/*G*	Pugh's ratio
H/*G*	hardness/shear modulus
3D	three-dimensional
2D	two-dimensional
1D	one-dimensional
ALD	atomic layer deposition
PLD	pulsed laser deposition
MS	magnetron sputtering
TGA	thermal gravimetric analysis

REFERENCES

(1) Tarascon, J. M.; Armand, M. Issues and Challenges Facing Rechargeable Lithium Batteries. *Nature* **2001**, *414*, 359−367.

(2) Armand, M.; Tarascon, J. M. Building Better Batteries. *Nature* **2008**, *451*, 652−657.

(3) Wang, Q. S.; Ping, P.; Zhao, X. J.; Chu, G. Q.; Sun, J. H.; Chen, C. H. Thermal Runaway Caused Fire and Explosion of Lithium Ion Battery. *J. Power Sources* **2012**, *208*, 210−224.

(4) Cheng, X. B.; Zhang, R.; Zhao, C. Z.; Zhang, Q. Toward Safe Lithium Metal Anode in Rechargeable Batteries: A Review. *Chem. Rev.* **2017**, *117*, 10403−10473.

(5) Xu, W.; Wang, J. L.; Ding, F.; Chen, X. L.; Nasybulin, E.; Zhang, Y. H.; Zhang, J. G. Lithium Metal Anodes for Rechargeable Batteries. *Energy Environ. Sci.* **2014**, *7*, 513−537.

(6) Hu, Y. S. Getting Solid. *Nat. Energy* **2016**, *1*, 16042.

(7) Janek, J.; Zeier, W. G. A Solid Future for Battery Development. *Nat. Energy* **2016**, *1*, 16141.

(8) Benrath, A.; Drekopf, K. On the Electric Conductivity of Salts and Salt Mixtures. *Z. Phys. Chem.* **1921**, *99*, 57−70.

(9) Vaillant, P. The Conductivity of Solid Salts at Raised Temperatures. *C. R. Hebd. Seances Acad. Sci.* **1924**, *179*, 530−532.

(10) Haven, Y. The Ionic Conductivity of Li-Halide Crystals. *Recl. Trav. Chim. Pays-Bas* **1950**, *69*, 1471−1489.

(11) Liang, C. C. Conduction Characteristics of the Lithium Iodide-Aluminum Oxide Solid Electrolytes. *J. Electrochem. Soc.* **1973**, *120*, 1289−1292.

(12) Goodenough, J. B.; Hong, H. Y. P.; Kafalas, J. A. Fast Na^+-Ion Transport in Skeleton Structures. *Mater. Res. Bull.* **1976**, *11*, 203−220.

(13) Whittingham, M. S. Electrical Energy-Storage and Intercalation Chemistry. *Science* **1976**, *192*, 1126−1127.

(14) Hong, H. Y. P. Crystal Structure and Ionic Conductivity of $Li_{14}Zn(GeO_4)_4$ and Other New Li^+ Superionic Conductors. *Mater. Res. Bull.* **1978**, *13*, 117−124.

(15) Armand, M. B.; Duclot, M. J.; Rigaud, P. Polymer Solid Electrolytes - Stability Domain. *Solid State Ionics* **1981**, *3*−*4*, 429−430.

(16) Armand, M.; Chabagno, J.; Duclot, M. *Fast Ion Transport in Solids*; North Holland: Amsterdam, 1979; p 52.

(17) Mizushima, K.; Jones, P. C.; Wiseman, P. J.; Goodenough, J. B. Li_xCoO_2 ($0<x \leq 1$): a New Cathode Material for Batteries of High-Energy Density. *Mater. Res. Bull.* **1980**, *15*, 783−789.

(18) Mercier, R.; Malugani, J. P.; Fahys, B.; Robert, G.; Douglade, J. Structure du tetrathiophosphate de lithium. *Acta Crystallogr., Sect. B: Struct. Crystallogr. Cryst. Chem.* **1982**, *38*, 1887−1890.

(19) Armand, M. B.; Chabagno, J. M.; Duclot, M. "Second International Meeting on Solid Electrolytes, St. Andrews, Scotland, September 20−22." Extended Abstracts. 1978.

(20) Latie, L.; Villeneuve, G.; Conte, D.; Leflem, G. Ionic Conductivity of Oxides with General Formula $Li_xLn_{1/3}Nb_{1-x}Ti_xO_3$ (Ln = La, Nd). *J. Solid State Chem.* **1984**, *51*, 293−299.

(21) Aono, H.; Sugimoto, E.; Sadaoka, Y.; Imanaka, N.; Adachi, G. Y. Ionic-Conductivity of the Lithium Titanium Phosphate ($Li_{1+X}M_XTi_{2-X}(PO_4)_3$, M = Al, Sc, Y, and La) systems. *J. Electrochem. Soc.* **1989**, *136*, 590−591.

(22) Aono, H.; Sugimoto, E.; Sadaoka, Y.; Imanaka, N.; Adachi, G. Ionic-Conductivity of Solid Electrolytes Based on Lithium Titanium Phosphate. *J. Electrochem. Soc.* **1990**, *137*, 1023−1027.

(23) Bates, J. B.; Dudney, N. J.; Gruzalski, G. R.; Zuhr, R. A.; Choudhury, A.; Luck, C. F.; Robertson, J. D. Electrical Properties of Amorphous Lithium Electrolyte Thin Films. *Solid State Ionics* **1992**, *53*−*56*, 647−654.

(24) Inaguma, Y.; Chen, L. Q.; Itoh, M.; Nakamura, T.; Uchida, T.; Ikuta, H.; Wakihara, M. High Ionic-Conductivity in Lithium Lanthanum Titanate. *Solid State Commun.* **1993**, *86*, 689−693.

(25) Padhi, A. K.; Nanjundaswamy, K. S.; Goodenough, J. B. Phospho-Olivines as Positive-Electrode Materials for Rechargeable Lithium Batteries. *J. Electrochem. Soc.* **1997**, *144*, 1188−1194.

(26) Kanno, R.; Hata, T.; Kawamoto, Y.; Irie, M. Synthesis of a New Lithium Ionic Conductor, Thio-Lisicon-Lithium Germanium Sulfide System. *Solid State Ionics* **2000**, *130*, 97−104.

(27) Murugan, R.; Thangadurai, V.; Weppner, W. Fast Lithium Ion Conduction in Garnet-Type $Li_7La_3Zr_2O_{12}$. *Angew. Chem., Int. Ed.* **2007**, *46*, 7778−7781.

(28) Kamaya, N.; Homma, K.; Yamakawa, Y.; Hirayama, M.; Kanno, R.; Yonemura, M.; Kamiyama, T.; Kato, Y.; Hama, S.; Kawamoto, K.; et al. A Lithium Superionic Conductor. *Nat. Mater.* **2011**, *10*, 682−686.

(29) Zhao, Y.; Daemen, L. L. Superionic Conductivity in Lithium-Rich Anti-Perovskites. *J. Am. Chem. Soc.* **2012**, *134*, 15042−15047.

(30) Kato, Y.; Hori, S.; Saito, T.; Suzuki, K.; Hirayama, M.; Mitsui, A.; Yonemura, M.; Iba, H.; Kanno, R. High-Power All-Solid-State Batteries Using Sulfide Superionic Conductors. *Nat. Energy* **2016**, *1*, 16030.

(31) Rao, M. L. B. High energy density solid electrolyte cells. U.S. Patent US 3455742 A, 1969.

(32) Liang, C. C.; Bro, P. A High-Voltage, Solid-State Battery System I. Design Considerations. *J. Electrochem. Soc.* **1969**, *116*, 1322−1323.

(33) Liang, C. C.; Epstein, J.; Boyle, G. H. A High-Voltage, Solid-State Battery System 2. Fabrication of Thin-Film Cells. *J. Electrochem. Soc.* **1969**, *116*, 1452−1454.

(34) Liang, C. Electrolyte materials for high voltage solid electrolyte battery systems. U.S. Patent US 3713897 A, 1973.

(35) Kanehori, K.; Matsumoto, K.; Miyauchi, K.; Kudo, T. Thin Film Solid Electrolyte and Its Application to Secondary Lithium Cell. *Solid State Ionics* **1983**, *9*−*10*, 1445−1448.

(36) Birke, P.; Salam, F.; Döring, S.; Weppner, W. A First Approach to a Monolithic All Solid State Inorganic Lithium Battery. *Solid State Ionics* **1999**, *118*, 149−157.

DOI: 10.1021/acs.chemrev.9b00268
Chem. Rev. XXXX, XXX, XXX−XXX

(37) Yoshima, K.; Harada, Y.; Takami, N. Thin Hybrid Electrolyte Based on Garnet-Type Lithium-Ion Conductor $Li_7La_3Zr_2O_{12}$ for 12 V-Class Bipolar Batteries. *J. Power Sources* **2016**, *302*, 283−290.
(38) Kengo, H.; Suzuki, T.; Ose, N.; Hayashi, A.; Inoue, H., Uchiyama, T.; Hasegawa, H.; Otaki, M.; Hama, S.; Yamaguchi, H.; Kato, D. Method of producing all-solid battery. U.S. Patent US 20180294531 A1, 2018.
(39) Wu, B.; Wang, S.; Evans, W. J., IV; Deng, D. Z.; Yang, J.; Xiao, J. Interfacial Behaviours between Lithium Ion Conductors and Electrode Materials in Various Battery Systems. *J. Mater. Chem. A* **2016**, *4*, 15266−15280.
(40) Faraday, M. Iv. Experimental Researches in Electricity-Third Series. *Philos. Trans. R. Soc. London* **1833**, *123*, 23−54.
(41) Sator, A. Pile Reversible Dont Lelectrolyte Est Un Cristal Depose En Lame Mince Par Evaporation. *C. R. Hebd. Seances Acad. Sci.* **1952**, *234*, 2283−2285.
(42) Lehovec, K.; Broder, J. Semiconductors as Solid Electrolytes in Electrochemical Systems. *J. Electrochem. Soc.* **1954**, *101*, 208−209.
(43) Liang, C. C. In *Applied Solid State Science*; Wolfe, R., Ed.; Elsevier, 1974; p 4.
(44) Vaillant, P. The Passage of a Current in Solid Salts. *C. R. Hebd. Seances Acad. Sci.* **1926**, *182*, 1335−1337.
(45) Liang, C. C. A High-Voltage Solid-State Battery System. 3. Li/Lii/Cui Thin-Film Cell. *J. Electrochem. Soc.* **1970**, *117*, C243.
(46) Julien, C. In *Materials for Lithium-Ion Batteries*; Julien, C., Stoynov, Z., Eds.;Springer: Dordrecht, Netherlands, 2000.
(47) Scrosati, B. Recent Advances in Lithium Solid State Batteries. *J. Appl. Electrochem.* **1972**, *2*, 231−238.
(48) Knutz, B.; Skaarup, S. Cycling of $Li/Li_3N/TiS_2$ Solid-State Cells. *Solid State Ionics* **1983**, *9−10*, 371−374.
(49) Fenton, D. E.; Parker, J. M.; Wright, P. V. Complexes of Alkali-Metal Ions with Poly(Ethylene Oxide). *Polymer* **1973**, *14*, 589−589.
(50) Weston, J. E.; Steele, B. C. H. Thermal History - Conductivity Relationship in Lithium Salt-Poly(Ethylene Oxide) Complex Polymer Electrolytes. *Solid State Ionics* **1981**, *2*, 347−354.
(51) Angell, C. A.; Liu, C.; Sanchez, E. Rubbery Solid Electrolytes with Dominant Cationic Transport and High Ambient Conductivity. *Nature* **1993**, *362*, 137.
(52) https://en.wikipedia.org/wiki/Bollore_Bluecar, 2011.
(53) Bates, J. B.; Dudney, N. J.; Gruzalski, G. R.; Zuhr, R. A.; Choudhury, A.; Luck, C. F.; Robertson, J. D. Fabrication and Characterization of Amorphous Lithium Electrolyte Thin Films and Rechargeable Thin-Film Batteries. *J. Power Sources* **1993**, *43*, 103−110.
(54) Ribes, M.; Barrau, B.; Souquet, J. L. Sulfide Glasses: Glass Forming Region, Structure and Ionic Conduction of Glasses in Na_2S-XS_2 (X = Si; Ge), Na_2S - P_2S_5 and Li_2S - GeS_2 Systems. *J. Non-Cryst. Solids* **1980**, *38−39*, 271−276.
(55) Ohtomo, T.; Hayashi, A.; Tatsumisago, M.; Tsuchida, Y.; Hama, S.; Kawamoto, K. All-Solid-State Lithium Secondary Batteries Using the $75Li_2S \bullet 25P_2S_5$ Glass and the $70Li_2S \bullet 30P_2S_5$ Glass-Ceramic as Solid Electrolytes. *J. Power Sources* **2013**, *233*, 231−235.
(56) Ohta, S.; Seki, J.; Yagi, Y.; Kihira, Y.; Tani, T.; Asaoka, T. Co-Sinterable Lithium Garnet-Type Oxide Electrolyte with Cathode for All-Solid-State Lithium Ion Battery. *J. Power Sources* **2014**, *265*, 40−44.
(57) Oh, D. Y.; Nam, Y. J.; Park, K. H.; Jung, S. H.; Cho, S.-J.; Kim, Y. K.; Lee, Y.-G.; Lee, S.-Y.; Jung, Y. S. Excellent Compatibility of Solvate Ionic Liquids with Sulfide Solid Electrolytes: Toward Favorable Ionic Contacts in Bulk-Type All-Solid-State Lithium-Ion Batteries. *Adv. Energy Mater.* **2015**, *5*, 1500865.
(58) Kim, H. W.; Manikandan, P.; Lim, Y. J.; Kim, J. H.; Nam, S.-c.; Kim, Y. Hybrid Solid Electrolyte with the Combination of $Li_7La_3Zr_2O_{12}$ Ceramic and Ionic Liquid for High Voltage Pseudo-Solid-State Li-Ion Batteries. *J. Mater. Chem. A* **2016**, *4*, 17025−17032.
(59) Zhou, W.; Wang, S.; Li, Y.; Xin, S.; Manthiram, A.; Goodenough, J. B. Plating a Dendrite-Free Lithium Anode with a Polymer/Ceramic/Polymer Sandwich Electrolyte. *J. Am. Chem. Soc.* **2016**, *138*, 9385−9388.
(60) Oh, G.; Hirayama, M.; Kwon, O.; Suzuki, K.; Kanno, R. Bulk-Type All Solid-State Batteries with 5 V Class $LiNi_{0.5}Mn_{1.5}O_4$ Cathode and $Li_{10}GeP_2S_{12}$ Solid Electrolyte. *Chem. Mater.* **2016**, *28*, 2634−2640.
(61) Zhang, W. B.; Weber, D. A.; Weigand, H.; Arlt, T.; Manke, I.; Schroder, D.; Koerver, R.; Leichtweiss, T.; Hartmann, P.; Zeier, W. G.; et al. Interfacial Processes and Influence of Composite Cathode Microstructure Controlling the Performance of All-Solid-State Lithium Batteries. *ACS Appl. Mater. Interfaces* **2017**, *9*, 17835−17845.
(62) Han, F.; Yue, J.; Chen, C.; Zhao, N.; Fan, X.; Ma, Z.; Gao, T.; Wang, F.; Guo, X.; Wang, C. Interphase Engineering Enabled All-Ceramic Lithium Battery. *Joule* **2018**, *2*, 497−508.
(63) Han, F. D.; Zhu, Y. Z.; He, X. F.; Mo, Y. F.; Wang, C. S. Electrochemical Stability of $Li_{10}GeP_2S_{12}$ and $Li_7La_3Zr_2O_{12}$ Solid Electrolytes. *Adv. Energy Mater.* **2016**, *6*, 1501590.
(64) Koerver, R.; Zhang, W.; de Biasi, L.; Schweidler, S.; Kondrakov, A. O.; Kolling, S.; Brezesinski, T.; Hartmann, P.; Zeier, W. G.; Janek, J. Chemo-Mechanical Expansion of Lithium Electrode Materials − on the Route to Mechanically Optimized All-Solid-State Batteries. *Energy Environ. Sci.* **2018**, *11*, 2142−2158.
(65) Wright, P. V. Electrical Conductivity in Ionic Complexes of Poly(Ethylene Oxide). *Br. Polym. J.* **1975**, *7*, 319−327.
(66) Ratner, M. A.; Shriver, D. F. Ion Transport in Solvent-Free Polymers. *Chem. Rev.* **1988**, *88*, 109−124.
(67) Xu, K. Nonaqueous Liquid Electrolytes for Lithium-Based Rechargeable Batteries. *Chem. Rev.* **2004**, *104*, 4303−4418.
(68) Zhang, H.; Liu, C.; Zheng, L.; Xu, F.; Feng, W.; Li, H.; Huang, X.; Armand, M.; Nie, J.; Zhou, Z. Lithium Bis(Fluorosulfonyl)Imide/Poly(Ethylene Oxide) Polymer Electrolyte. *Electrochim. Acta* **2014**, *133*, 529−538.
(69) Polu, A. R.; Kim, D. K.; Rhee, H.-W. Poly(Ethylene Oxide)-Lithium Difluoro(Oxalato)Borate New Solid Polymer Electrolytes: Ion−Polymer Interaction, Structural, Thermal, and Ionic Conductivity Studies. *Ionics* **2015**, *21*, 2771−2780.
(70) Karuppasamy, K.; Kim, D.; Kang, Y. H.; Prasanna, K.; Rhee, H. W. Improved Electrochemical, Mechanical and Transport Properties of Novel Lithium Bisnonafluoro-1-Butanesulfonimidate (LiBNFSI) Based Solid Polymer Electrolytes for Rechargeable Lithium Ion Batteries. *J. Ind. Eng. Chem.* **2017**, *52*, 224−234.
(71) Ma, Q.; Qi, X.; Tong, B.; Zheng, Y.; Feng, W.; Nie, J.; Hu, Y.-S.; Li, H.; Huang, X.; Chen, L.; et al. Novel $Li[(CF_3SO_2)(n\text{-}C_4F_9SO_2)N]$-Based Polymer Electrolytes for Solid-State Lithium Batteries with Superior Electrochemical Performance. *ACS Appl. Mater. Interfaces* **2016**, *8*, 29705−29712.
(72) B, J.; KM, A.; M, M.; V.S, P.; S, J. Development of a Novel Type of Solid Polymer Electrolyte for Solid State Lithium Battery Applications Based on Lithium Enriched Poly (Ethylene Oxide) (PEO)/Poly (Vinyl Pyrrolidone) (PVP) Blend Polymer. *Electrochim. Acta* **2017**, *235*, 210−222.
(73) Chen-Yang, Y. W.; Chen, H. C.; Lin, F. J.; Chen, C. C. Polyacrylonitrile Electrolytes 1. A Novel High-Conductivity Composite Polymer Electrolyte Based on PAN, LiClO4 and α-Al_2O_3. *Solid State Ionics* **2002**, *150*, 327−335.
(74) Rajendran, S.; Babu, R. s.; Sivakumar, P. Investigations on PVC/PAN Composite Polymer Electrolytes. *J. Membr. Sci.* **2008**, *315*, 67−73.
(75) Yuan, F.; Chen, H.-Z.; Yang, H.-Y.; Li, H.-Y.; Wang, M. PAN−PEO Solid Polymer Electrolytes with High Ionic Conductivity. *Mater. Chem. Phys.* **2005**, *89*, 390−394.
(76) Rajendran, S.; Sivakumar, M.; Subadevi, R. Effect of Salt Concentration in Poly(Vinyl Alcohol)-Based Solid Polymer Electrolytes. *J. Power Sources* **2003**, *124*, 225−230.
(77) Jacob, M. M. E.; Prabaharan, S. R. S.; Radhakrishna, S. Effect of PEO Addition on the Electrolytic and Thermal Properties of PVDF-LiClO4 Polymer Electrolytes. *Solid State Ionics* **1997**, *104*, 267−276.
(78) Manuel Stephan, A.; Nahm, K. S. Review on Composite Polymer Electrolytes for Lithium Batteries. *Polymer* **2006**, *47*, 5952−5964.

DOI: 10.1021/acs.chemrev.9b00268
Chem. Rev. XXXX, XXX, XXX−XXX

(79) Wieczorek, W.; Such, K.; Wyciślik, H.; Płocharski, J. Modifications of Crystalline Structure of PEO Polymer Electrolytes with Ceramic Additives. *Solid State Ionics* **1989**, *36*, 255−257.
(80) Chen, L.; Li, Y.; Li, S.-P.; Fan, L.-Z.; Nan, C.-W.; Goodenough, J. B. PEO/Garnet Composite Electrolytes for Solid-State Lithium Batteries: From "Ceramic-in-Polymer" to "Polymer-in-Ceramic. *Nano Energy* **2018**, *46*, 176−184.
(81) Brous, J.; Fankuchen, I.; Banks, E. Rare Earth Titanates with a Perovskite Structure. *Acta Crystallogr.* **1953**, *6*, 67−70.
(82) Inaguma, Y.; Liquan, C.; Itoh, M.; Nakamura, T.; Uchida, T.; Ikuta, H.; Wakihara, M. High Ionic Conductivity in Lithium Lanthanum Titanate. *Solid State Commun.* **1993**, *86*, 689−693.
(83) Abe, M.; Uchino, K. X-Ray Study of the Deficient Perovskite $La_{23}TiO_3$. *Mater. Res. Bull.* **1974**, *9*, 147−155.
(84) Fourquet, J. L.; Duroy, H.; Crosnier-Lopez, M. P. Structural and Microstructural Studies of the Series $La_{2/3-x}Li_{3x}\square_{1/3-2x}TiO_3$. *J. Solid State Chem.* **1996**, *127*, 283−294.
(85) Ibarra, J.; Várez, A.; León, C.; Santamaría, J.; Torres-Martínez, L. M.; Sanz, J. Influence of Composition on the Structure and Conductivity of the Fast Ionic Conductors $La_{2/3-x}Li_{3x}TiO_3$ ($0.03 \leq x \leq 0.167$). *Solid State Ionics* **2000**, *134*, 219−228.
(86) Inaguma, Y.; Katsumata, T.; Itoh, M.; Morii, Y. Crystal Structure of a Lithium Ion-Conducting Perovskite $La_{2/3-x}Li_{3x}TiO_3$ (x = 0.05). *J. Solid State Chem.* **2002**, *166*, 67−72.
(87) Yashima, M.; Itoh, M.; Inaguma, Y.; Morii, Y. Crystal Structure and Diffusion Path in the Fast Lithium-Ion Conductor $La_{0.62}Li_{0.16}TiO_3$. *J. Am. Chem. Soc.* **2005**, *127*, 3491−3495.
(88) Zou, Y.; Inoue, N. Structure and Lithium Ionic Conduction Mechanism in $La_{4/3-y}Li_{3y}Ti_2O_6$. *Ionics* **2005**, *11*, 333−342.
(89) Losilla, E. R.; Aranda, M. A. G.; Martínez-Lara, M.; Bruque, S. Reversible Triclinic-Rhombohedral Phase Transition in $LiHf_2(PO_4)_3$: Crystal Structures from Neutron Powder Diffraction. *Chem. Mater.* **1997**, *9*, 1678−1685.
(90) Giarola, M.; Sanson, A.; Tietz, F.; Pristat, S.; Dashjav, E.; Rettenwander, D.; Redhammer, G. J.; Mariotto, G. Structure and Vibrational Dynamics of Nasicon-Type $LiTi_2(PO_4)_3$. *J. Phys. Chem. C* **2017**, *121*, 3697−3706.
(91) Catti, M.; Stramare, S.; Ibberson, R. Lithium Location in Nasicon-Type Li^+ Conductors by Neutron Diffraction. I. Triclinic α'-$LiZr_2(PO_4)_3$. *Solid State Ionics* **1999**, *123*, 173−180.
(92) Arbi, K.; Mandal, S.; Rojo, J. M.; Sanz, J. Dependence of Ionic Conductivity on Composition of Fast Ionic Conductors $Li_{1+x}Ti_{2-x}Al_x(PO_4)_3$, $0 \leq x \leq 0.7$. A Parallel Nmr and Electric Impedance Study. *Chem. Mater.* **2002**, *14*, 1091−1097.
(93) Aono, H.; Sugimoto, E.; Sadaoka, Y.; Imanaka, N.; Adachi, G. y. Ionic Conductivity of Solid Electrolytes Based on Lithium Titanium Phosphate. *J. Electrochem. Soc.* **1990**, *137*, 1023−1027.
(94) Aono, H.; Sugimoto, E.; Sadaoka, Y.; Imanaka, N.; Adachi, G.-y. Electrical Properties and Sinterability for Lithium Germanium Phosphate $Li_{1+x}M_xGe_{2-x}(PO_4)_3$, M = Al, Cr, Ga, Fe, Sc, and in Systems. *Bull. Chem. Soc. Jpn.* **1992**, *65*, 2200−2204.
(95) Aono, H.; Sugimoto, E.; Sadaoka, Y.; Imanaka, N.; Adachi, G.-y. Electrical Property and Sinterability of $LiTi_2(PO_4)_3$ Mixed with Lithium Salt (Li_3PO_4 or Li_3BO_3). *Solid State Ionics* **1991**, *47*, 257−264.
(96) Kobayashi, Y.; Tabuchi, M.; Nakamura, O. Ionic Conductivity Enhancement in $LiTi_2(PO_4)_3$-Based Composite Electrolyte by the Addition of Lithium Nitrate. *J. Power Sources* **1997**, *68*, 407−411.
(97) Xiong, L.; Ren, Z.; Xu, Y.; Mao, S.; Lei, P.; Sun, M. LiF Assisted Synthesis of $LiTi_2(PO_4)_3$ Solid Electrolyte with Enhanced Ionic Conductivity. *Solid State Ionics* **2017**, *309*, 22−26.
(98) Fu, J. Superionic Conductivity of Glass-Ceramics in the System Li $_2O$- Al_2O_3-TiO_2-P_2O_5. *Solid State Ionics* **1997**, *96*, 195−200.
(99) Fu, J. Fast Li^+ Ion Conducting Glass-Ceramics in the System Li_2O−Al_2O_3−GeO_2−P_2O_5. *Solid State Ionics* **1997**, *104*, 191−194.
(100) Dissanayake, M. A. K. L.; Gunawardane, R. P.; Sumathipala, H. H.; West, A. R. New Solid Electrolytes and Mixed Conductors: $Li_{3+x}Cr_{1-x}M_xO_4$: M = Ge, Ti. *Solid State Ionics* **1995**, *76*, 215−220.
(101) Sumathipala, H. H.; Dissanayake, M. A. K. L.; West, A. R. Novel LISICON Mixed Conductors, $Li_{4-2x}Co_xGeO_4$. *Solid State Ionics* **1996**, *86*−*88*, 719−724.
(102) Bruce, P. G.; West, A. R. The A-C Conductivity of Polycrystalline LISICON, $Li_{2+2x}Zn_{1-x}GeO_4$, and a Model for Intergranular Constriction Resistances. *J. Electrochem. Soc.* **1983**, *130*, 662−669.
(103) Hu, Y. W.; Raistrick, I. D.; Huggins, R. A. Ionic Conductivity of Lithium Orthosilicate—Lithium Phosphate Solid Solutions. *J. Electrochem. Soc.* **1977**, *124*, 1240−1242.
(104) Rodger, A. R.; Kuwano, J.; West, A. R. Li^+ Ion Conducting γ Solid Solutions in the Systems Li_4XO_4-Li_3YO_4: X = Si, Ge, Ti; Y = P, As, V; Li_4XO_4-$LiZO_2$: Z = Al, Ga, Cr and Li_4GeO_4-Li_2CaGeO_4. *Solid State Ionics* **1985**, *15*, 185−198.
(105) Thangadurai, V.; Kaack, H.; Weppner, W. J. F. Novel Fast Lithium Ion Conduction in Garnet-Type $Li_5La_3M_2O_{12}$ (M = Nb, Ta). *J. Am. Ceram. Soc.* **2003**, *86*, 437−440.
(106) O'Callaghan, M. P.; Lynham, D. R.; Cussen, E. J.; Chen, G. Z. Structure and Ionic-Transport Properties of Lithium-Containing Garnets $Li_3Ln_3Te_2O_{12}$ (Ln = Y, Pr, Nd, Sm−Lu). *Chem. Mater.* **2006**, *18*, 4681−4689.
(107) Gao, Y. X.; Wang, X. P.; Wang, W. G.; Fang, Q. F. Sol−Gel Synthesis and Electrical Properties of $Li_5La_3Ta_2O_{12}$ Lithium Ionic Conductors. *Solid State Ionics* **2010**, *181*, 33−36.
(108) Peng, H.; Wu, Q.; Xiao, L. Low Temperature Synthesis of $Li_5La_3Nb_2O_{12}$ with Cubic Garnet-Type Structure by Sol−Gel Process. *J. Sol-Gel Sci. Technol.* **2013**, *66*, 175−179.
(109) Thangadurai, V.; Weppner, W. $Li_6ALa_2Ta_2O_{12}$ (A = Sr, Ba): Novel Garnet-Like Oxides for Fast Lithium Ion Conduction. *Adv. Funct. Mater.* **2005**, *15*, 107−112.
(110) Murugan, R.; Thangadurai, V.; Weppner, W. Fast Lithium Ion Conduction in Garnet-Type $Li_7La_3Zr_2O_{12}$. *Angew. Chem., Int. Ed.* **2007**, *46*, 7778−7781.
(111) Buschmann, H.; Dölle, J.; Berendts, S.; Kuhn, A.; Bottke, P.; Wilkening, M.; Heitjans, P.; Senyshyn, A.; Ehrenberg, H.; et al. Structure and Dynamics of the Fast Lithium Ion Conductor "$Li_7La_3Zr_2O_{12}$. *Phys. Chem. Chem. Phys.* **2011**, *13*, 19378−19392.
(112) Awaka, J.; Kijima, N.; Hayakawa, H.; Akimoto, J. Synthesis and Structure Analysis of Tetragonal $Li_7La_3Zr_2O_{12}$ with the Garnet-Related Type Structure. *J. Solid State Chem.* **2009**, *182*, 2046−2052.
(113) Kumazaki, S.; Iriyama, Y.; Kim, K.-H.; Murugan, R.; Tanabe, K.; Yamamoto, K.; Hirayama, T.; Ogumi, Z. High Lithium Ion Conductive $Li_7La_3Zr_2O_{12}$ by Inclusion of Both Al and Si. *Electrochem. Commun.* **2011**, *13*, 509−512.
(114) Kotobuki, M.; Kanamura, K.; Sato, Y.; Yoshida, T. Fabrication of All-Solid-State Lithium Battery with Lithium Metal Anode Using Al_2O_3-added $Li_7La_3Zr_2O_{12}$ Solid Electrolyte. *J. Power Sources* **2011**, *196*, 7750−7754.
(115) Liu, Z.; Huang, F.; Yang, J.; Wang, B.; Sun, J. New Lithium Ion Conductor, Thio-LISICON Lithium Zirconium Sulfide System. *Solid State Ionics* **2008**, *179*, 1714−1716.
(116) Homma, K.; Yonemura, M.; Kobayashi, T.; Nagao, M.; Hirayama, M.; Kanno, R. Crystal Structure and Phase Transitions of the Lithium Ionic Conductor Li_3PS_4. *Solid State Ionics* **2011**, *182*, 53−58.
(117) Kanno, R.; Murayama, M. Lithium Ionic Conductor Thio-LISICON: The Li_2S-GeS_2-P_2S_5 System. *J. Electrochem. Soc.* **2001**, *148*, A742−A746.
(118) Mo, Y.; Ong, S. P.; Ceder, G. First Principles Study of the $Li_{10}GeP_2S_{12}$ Lithium Super Ionic Conductor Material. *Chem. Mater.* **2012**, *24*, 15−17.
(119) Hayashi, A. Preparation and Characterization of Glassy Materials for All-Solid-State Lithium Secondary Batteries. *J. Ceram. Soc. Jpn.* **2007**, *115*, 110−117.
(120) Hayashi, A.; Tatsumisago, M.; Minami, T.; Miura, Y. Structural Investigation of $95(0.6Li_2S_{0.4}SiS_2)5Li_4SiO_4$ Oxysulfide Glass by Using X-Ray Photoelectron Spectroscopy. *J. Am. Ceram. Soc.* **1998**, *81*, 1305−1309.

DOI: 10.1021/acs.chemrev.9b00268
Chem. Rev. XXXX, XXX, XXX−XXX

(121) Zhang, Y.; Zhao, Y.; Chen, C. Ab Initio Study of the Stabilities of and Mechanism of Superionic Transport in Lithium-Rich Antiperovskites. *Phys. Rev. B: Condens. Matter Mater. Phys.* **2013**, *87*, 134303.
(122) Braga, M. H.; Ferreira, J. A.; Stockhausen, V.; Oliveira, J. E.; El-Azab, A. Novel Li_3ClO Based Glasses with Superionic Properties for Lithium Batteries. *J. Mater. Chem. A* **2014**, *2*, 5470−5480.
(123) Li, Y.; Zhou, W.; Xin, S.; Li, S.; Zhu, J.; Lü, X.; Cui, Z.; Jia, Q.; Zhou, J.; Zhao, Y.; et al. Fluorine-Doped Antiperovskite Electrolyte for All-Solid-State Lithium-Ion Batteries. *Angew. Chem., Int. Ed.* **2016**, *55*, 9965−9968.
(124) Emly, A.; Kioupakis, E.; Van der Ven, A. Phase Stability and Transport Mechanisms in Antiperovskite Li_3OCl and Li_3OBr Superionic Conductors. *Chem. Mater.* **2013**, *25*, 4663−4670.
(125) Mouta, R.; Melo, M. Á. B.; Diniz, E. M.; Paschoal, C. W. A. Concentration of Charge Carriers, Migration, and Stability in Li_3OCl Solid Electrolytes. *Chem. Mater.* **2014**, *26*, 7137−7144.
(126) Bates, J. B.; Dudney, N. J.; Neudecker, B.; Ueda, A.; Evans, C. D. Thin-Film Lithium and Lithium-Ion Batteries. Solid State Ionics. *Solid State Ionics* **2000**, *135*, 33−45.
(127) Hamon, Y.; Douard, A.; Sabary, F.; Marcel, C.; Vinatier, P.; Pecquenard, B.; Levasseur, A. Influence of Sputtering Conditions on Ionic Conductivity of LiPON Thin Films. *Solid State Ionics* **2006**, *177*, 257−261.
(128) Aldissi, M. Multi-Layered Polymer Electrolytes Towards Interfacial Stability in Lithium Ion Batteries. *J. Power Sources* **2001**, *94*, 219−224.
(129) Wang, W.; Yi, E.; Fici, A. J.; Laine, R. M.; Kieffer, J. Lithium Ion Conducting Poly(ethylene oxide)-Based Solid Electrolytes Containing Active or Passive Ceramic Nanoparticles. *J. Phys. Chem. C* **2017**, *121*, 2563−2573.
(130) Zhao, Y.; Wu, C.; Peng, G.; Chen, X.; Yao, X.; Bai, Y.; Wu, F.; Chen, S.; Xu, X. A New Solid Polymer Electrolyte Incorporating $Li_{10}GeP_2S_{12}$ into a Polyethylene Oxide Matrix for All-Solid-State Lithium Batteries. *J. Power Sources* **2016**, *301*, 47−53.
(131) Jung, Y.-C.; Lee, S.-M.; Choi, J.-H.; Jang, S. S.; Kim, D.-W. All Solid-State Lithium Batteries Assembled with Hybrid Solid Electrolytes. *J. Electrochem. Soc.* **2015**, *162*, A704−A710.
(132) Lee, L.; Park, S.-J.; Kim, S. Effect of Nano-Sized Barium Titanate Addition on PEO/PVDF Blend-Based Composite Polymer Electrolytes. *Solid State Ionics* **2013**, *234*, 19−24.
(133) Lin, D.; Liu, W.; Liu, Y.; Lee, H. R.; Hsu, P.-C.; Liu, K.; Cui, Y. High Ionic Conductivity of Composite Solid Polymer Electrolyte Via in Situ Synthesis of Monodispersed SiO_2 Nanospheres in Poly(ethylene oxide). *Nano Lett.* **2016**, *16*, 459−465.
(134) Sun, H. Y.; Sohn, H. J.; Yamamoto, O.; Takeda, Y.; Imanishi, N. Enhanced Lithium-Ion Transport in PEO-Based Composite Polymer Electrolytes with Ferroelectric $BaTiO_3$. *J. Electrochem. Soc.* **1999**, *146*, 1672−1676.
(135) Itoh, M.; Inaguma, Y.; Jung, W.-H.; Chen, L.; Nakamura, T. High Lithium Ion Conductivity in the Perovskite-Type Compounds $Ln_{12}Li_{12}TiO_3$ (Ln = La, Pr, Nd, Sm). *Solid State Ionics* **1994**, *70−71*, 203−207.
(136) Inaguma, Y.; Chen, L.; Itoh, M.; Nakamura, T. Candidate Compounds with Perovskite Structure for High Lithium Ionic Conductivity. *Solid State Ionics* **1994**, *70−71*, 196−202.
(137) Le, H. T. T.; Kalubarme, R. S.; Ngo, D. T.; Jang, S.-Y.; Jung, K.-N.; Shin, K.-H.; Park, C.-J. Citrate Gel Synthesis of Aluminum-Doped Lithium Lanthanum Titanate Solid Electrolyte for Application in Organic-Type Lithium−Oxygen Batteries. *J. Power Sources* **2015**, *274*, 1188−1199.
(138) Morata-Orrantia, A.; García-Martín, S.; Morán, E.; Alario-Franco, M. Á. A New $La_{2/3}Li_xTi_{1-x}Al_xO_3$ Solid Solution: Structure, Microstructure, and Li+ Conductivity. *Chem. Mater.* **2002**, *14*, 2871−2875.
(139) Martínez-Juárez, A.; Pecharromán, C.; Iglesias, J. E.; Rojo, J. M. Relationship between Activation Energy and Bottleneck Size for Li^+ Ion Conduction in Nasicon Materials of Composition $LiMM'(PO_4)_3$; M, M' = Ge, Ti, Sn, Hf. *J. Phys. Chem. B* **1998**, *102*, 372−375.
(140) Fan, L.; Wei, S.; Li, S.; Li, Q.; Lu, Y. Recent Progress of the Solid-State Electrolytes for High-Energy Metal-Based Batteries. *Adv. Energy Mater.* **2018**, *8*, 1702657.
(141) Li, Y.; Zhou, W.; Chen, X.; Lü, X.; Cui, Z.; Xin, S.; Xue, L.; Jia, Q.; Goodenough, J. B. Mastering the Interface for Advanced All-Solid-State Lithium Rechargeable Batteries. *Proc. Natl. Acad. Sci. U. S. A.* **2016**, *113*, 13313−13317.
(142) Bachman, J. C.; Muy, S.; Grimaud, A.; Chang, H.-H.; Pour, N.; Lux, S. F.; Paschos, O.; Maglia, F.; Lupart, S.; Lamp, P.; et al. Inorganic Solid-State Electrolytes for Lithium Batteries: Mechanisms and Properties Governing Ion Conduction. *Chem. Rev.* **2016**, *116*, 140−162.
(143) Arbi, K.; Rojo, J. M.; Sanz, J. Lithium Mobility in Titanium Based Nasicon $Li_{1+x}Ti_{2-x}Al_x(PO_4)_3$ and $LiTi_{2-x}Zr_x(PO_4)_3$ Materials Followed by NMR and Impedance Spectroscopy. *J. Eur. Ceram. Soc.* **2007**, *27*, 4215−4218.
(144) Xu, X.; Wen, Z.; Wu, J.; Yang, X. Preparation and Electrical Properties of NASICON-Type Structured $Li_{1.4}Al_{0.4}Ti_{1.6}(PO_4)_3$ Glass-Ceramics by the Citric Acid-Assisted Sol−Gel Method. *Solid State Ionics* **2007**, *178*, 29−34.
(145) Deng, Y.; Eames, C.; Chotard, J.-N.; Lalère, F.; Seznec, V.; Emge, S.; Pecher, O.; Grey, C. P.; Masquelier, C.; Islam, M. S. Structural and Mechanistic Insights into Fast Lithium-Ion Conduction in Li_4SiO_4−Li_3PO_4 Solid Electrolytes. *J. Am. Chem. Soc.* **2015**, *137*, 9136−9145.
(146) Murayama, M.; Kanno, R.; Irie, M.; Ito, S.; Hata, T.; Sonoyama, N.; Kawamoto, Y. Synthesis of New Lithium Ionic Conductor Thio-LISICON — Lithium Silicon Sulfides System. *J. Solid State Chem.* **2002**, *168*, 140−148.
(147) Liu, Z.; Fu, W.; Payzant, E. A.; Yu, X.; Wu, Z.; Dudney, N. J.; Kiggans, J.; Hong, K.; Rondinone, A. J.; Liang, C. Anomalous High Ionic Conductivity of Nanoporous β-Li_3PS_4. *J. Am. Chem. Soc.* **2013**, *135*, 975−978.
(148) Seino, Y.; Ota, T.; Takada, K.; Hayashi, A.; Tatsumisago, M. A Sulphide Lithium Super Ion Conductor Is Superior to Liquid Ion Conductors for Use in Rechargeable Batteries. *Energy Environ. Sci.* **2014**, *7*, 627−631.
(149) Pradel, A.; Ribes, M. Ionically Conductive Chalcogenide Glasses. *J. Solid State Chem.* **1992**, *96*, 247−257.
(150) Lau, J.; DeBlock, R. H.; Butts, D. M.; Ashby, D. S.; Choi, C. S.; Dunn, B. S. Sulfide Solid Electrolytes for Lithium Battery Applications. *Adv. Energy Mater.* **2018**, *8*, 1800933.
(151) Tatsumisago, M.; Hayashi, A. Superionic Glasses and Glass-Ceramics in the Li_2S-P_2S_5 System for All-Solid-State Lithium Secondary Batteries. *Solid State Ionics* **2012**, *225*, 342−345.
(152) Sakuda, A.; Hayashi, A.; Tatsumisago, M. Sulfide Solid Electrolyte with Favorable Mechanical Property for All-Solid-State Lithium Battery. *Sci. Rep.* **2013**, *3*, 2261.
(153) Kennedy, J. H.; Sahami, S.; Shea, S. W.; Zhang, Z. Preparation and Conductivity Measurements of SiS_2•Li_2S Glasses Doped with Libr and LiCl. *Solid State Ionics* **1986**, *18−19*, 368−371.
(154) Hirai, K.; Tatsumisago, M.; Minami, T. Thermal and Electrical Properties of Rapidly Quenched Glasses in the Systems Li_2S-SiS_2-Li_xMO_y (Li_xMO_y = Li_4SiO_4, Li_2SO_4). *Solid State Ionics* **1995**, *78*, 269−273.
(155) Aotani, N.; Iwamoto, K.; Takada, K.; Kondo, S. Synthesis and Electrochemical Properties of Lithium Ion Conductive Glass, Li_3PO_4-Li_2S-SiS_2. *Solid State Ionics* **1994**, *68*, 35−39.
(156) Braga, M. H.; Grundish, N. S.; Murchison, A. J.; Goodenough, J. B. Alternative Strategy for a Safe Rechargeable Battery. *Energy Environ. Sci.* **2017**, *10*, 331−336.
(157) Suzuki, N.; Inaba, T.; Shiga, T. Electrochemical Properties of LiPON Films Made from a Mixed Powder Target of Li_3PO_4 and Li_2O. *Thin Solid Films* **2012**, *520*, 1821−1825.
(158) Yu, X.; Bates, J. B.; Jellison, G. E.; Hart, F. X. A Stable Thin-Film Lithium Electrolyte: Lithium Phosphorus Oxynitride. *J. Electrochem. Soc.* **1997**, *144*, 524−532.

DOI: 10.1021/acs.chemrev.9b00268
Chem. Rev. XXXX, XXX, XXX−XXX

(159) Birke, P.; Chu, W. F.; Weppner, W. Materials for Lithium Thin-Film Batteries for Application in Silicon Technology. *Solid State Ionics* **1996**, *93*, 1−15.
(160) Ma, J.; Chen, B. B.; Wang, L. L.; Cui, G. L. Progress and Prospect on Failure Mechanisms of Solid-State Lithium Batteries. *J. Power Sources* **2018**, *392*, 94−115.
(161) Greenwood, N. N.; Earnshaw, A. *Chemistry of the Elements*, 2nd ed.; Butterworth-Heinemann: Oxford, 1997.
(162) Muramatsu, H.; Hayashi, A.; Ohtomo, T.; Hama, S.; Tatsumisago, M. Structural Change of Li_2S-P_2S_5 Sulfide Solid Electrolytes in the Atmosphere. *Solid State Ionics* **2011**, *182*, 116−119.
(163) Sahu, G.; Lin, Z.; Li, J. C.; Liu, Z. C.; Dudney, N.; Liang, C. D. Air-Stable, High-Conduction Solid Electrolytes of Arsenic-Substituted Li_4SnS_4. *Energy Environ. Sci.* **2014**, *7*, 1053−1058.
(164) Pearson, R. G. Hard and Soft Acids and Bases. *J. Am. Chem. Soc.* **1963**, *85*, 3533−3539.
(165) Cheng, L.; Crumlin, E. J.; Chen, W.; Qiao, R. M.; Hou, H. M.; Franz Lux, S. F.; Zorba, V.; Russo, R.; Kostecki, R.; Liu, Z.; et al. The Origin of High Electrolyte-Electrode Interfacial Resistances in Lithium Cells Containing Garnet Type Solid Electrolytes. *Phys. Chem. Chem. Phys.* **2014**, *16*, 18294−18300.
(166) Xia, W. H.; Xu, B. Y.; Duan, H. A.; Tang, X. Y.; Guo, Y. P.; Kang, H. M.; Li, H.; Liu, H. Z. Reaction Mechanisms of Lithium Garnet Pellets in Ambient Air: The Effect of Humidity and CO_2. *J. Am. Ceram. Soc.* **2017**, *100*, 2832−2839.
(167) Ma, C.; Rangasamy, E.; Liang, C.; Sakamoto, J.; More, K. L.; Chi, M. Excellent Stability of a Lithium-Ion-Conducting Solid Electrolyte Upon Reversible Li^+/H^+ Exchange in Aqueous Solutions. *Angew. Chem., Int. Ed.* **2015**, *54*, 1063−1063.
(168) Truong, L.; Thangadurai, V. Soft-Chemistry of Garnet-Type $Li_{5+x}Ba_xLa_{3-x}Nb_2O_{12}$ (x = 0, 0.5, 1): Reversible $H^+ \leftrightarrow Li^+$ Ion-Exchange Reaction and Their X-Ray, ^{7}Li MAS NMR, IR, and AC Impedance Spectroscopy Characterization. *Chem. Mater.* **2011**, *23*, 3970−3977.
(169) Simon, D. R.; Kelder, E. M.; Wagemaker, M.; Mulder, F. M.; Schoonman, J. Characterization of Proton Exchanged $Li_4Ti_5O_{12}$ Spinel Material. *Solid State Ionics* **2006**, *177*, 2759−2768.
(170) Li, W.; Mckinnon, W. R.; Dahn, J. R. Lithium Intercalation from Aqueous-Solutions. *J. Electrochem. Soc.* **1994**, *141*, 2310−2316.
(171) Bohnke, C.; Duroy, H.; Fourquet, J. L. pH Sensors with Lithium Lanthanum Titanate Sensitive Material: Applications in Food Industry. *Sens. Actuators, B* **2003**, *89*, 240−247.
(172) Sharafi, A.; Kazyak, E.; Davis, A. L.; Yu, S. H.; Thompson, T.; Siegel, D. J.; Dasgupta, N. P.; Sakamoto, J. Surface Chemistry Mechanism of Ultra-Low Interfacial Resistance in the Solid-State Electrolyte $Li_7La_3Zr_2O_{12}$. *Chem. Mater.* **2017**, *29*, 7961−7968.
(173) Brugge, R. H.; Hekselman, A. K. O.; Cavallaro, A.; Pesci, F. M.; Chater, R. J.; Kilner, J. A.; Aguadero, A. Garnet Electrolytes for Solid State Batteries: Visualization of Moisture-Induced Chemical Degradation and Revealing Its Impact on the Li-ion Dynamics. *Chem. Mater.* **2018**, *30*, 3704−3713.
(174) Jin, Y.; McGinn, P. J. $Li_7La_3Zr_2O_{12}$ Electrolyte Stability in Air and Fabrication of a $Li/Li_7La_3Zr_2O_{12}/Cu_{0.1}V_2O_5$ Solid-State Battery. *J. Power Sources* **2013**, *239*, 326−331.
(175) Duran, T.; Climent-Pascual, E.; Perez-Prior, M. T.; Levenfeld, B.; Varez, A.; Sobrados, I.; Sanz, J. Aqueous and Non-Aqueous Li^+/H^+ Ion Exchange in $Li_{0.44}/La_{0.52}TiO_3$ Perovskite. *Adv. Powder Technol.* **2017**, *28*, 514−520.
(176) Li, Y. T.; Han, J. T.; Vogel, S. C.; Wang, C. A. The Reaction of $Li_{6.5}La_3Zr_{1.5}Ta_{0.5}O_{12}$ with Water. *Solid State Ionics* **2015**, *269*, 57−61.
(177) Galven, C.; Dittmer, J.; Suard, E.; Le Berre, F.; Crosnier-Lopez, M. P. Instability of Lithium Garnets against Moisture. Structural Characterization and Dynamics of $Li_{7-x}H_xLa_3Sn_2O_{12}$ and $Li_{5-x}H_xLa_3Nb_2O_{12}$. *Chem. Mater.* **2012**, *24*, 3335−3345.
(178) Kang, S. G.; Sholl, D. S. First-Principles Study of Chemical Stability of the Lithium Oxide Garnets $Li_7La_3M_2O_{12}$ (M = Zr, Sn, or Hf). *J. Phys. Chem. C* **2014**, *118*, 17402−17406.
(179) Wang, Y. X.; Lai, W. Phase Transition in Lithium Garnet Oxide Ionic Conductors $Li_7La_3Zr_2O_{12}$: The Role of Ta Substitution and H_2O/CO_2 Exposure. *J. Power Sources* **2015**, *275*, 612−620.
(180) Boulant, A.; Bardeau, J. F.; Jouanneaux, A.; Emery, J.; Buzare, J. Y.; Bohnke, O. Reaction Mechanisms of $Li_{0.30}La_{0.57}TiO_3$ powder with ambient air: H^+/Li^+ exchange with water and Li_2CO_3 Formation. *Dalton Trans* **2010**, *39*, 3968−3975.
(181) Bohnke, O.; Lorant, S.; Roffat, M.; Berger, P. Fast H^+/Li^+ Ion Exchange in $Li_{0.30}La_{0.57}TiO_3$ Nanopowder and Films in Water and in Ambient Air. *Solid State Ionics* **2014**, *262*, 563−567.
(182) Bohnke, O.; Pham, Q. N.; Boulant, A.; Emery, J.; Salkus, T.; Barre, M. H^+/Li^+ Exchange Property of $Li_{3x}La_{2/3-x}TiO_3$ in Water and in Humid Atmosphere. *Solid State Ionics* **2011**, *188*, 144−147.
(183) Truong, L.; Howard, M.; Clemens, O.; Knight, K. S.; Slater, P. R.; Thangadurai, V. Facile Proton Conduction in H^+/Li^+ Ion-Exchanged Garnet-Type Fast Li-Ion Conducting $Li_5La_3Nb_2O_{12}$. *J. Mater. Chem. A* **2013**, *1*, 13469−13475.
(184) Bhuvanesh, N. S. P.; Bohnké, O.; Duroy, H.; Crosnier-Lopez, M. P.; Emery, J.; Fourquet, J. L. Topotactic H^+/Li^+ Ion Exchange on $La_{2/3-x}Li_{3x}TiO_3$: New Metastable Perovskite Phases $La_{2/3-x}TiO_{3-3x}(OH)_{3x}$ and $La_{2/3-x}TiO_{3-3x/2}$ Obtained by Further Dehydration. *Mater. Res. Bull.* **1998**, *33*, 1681−1691.
(185) Narayanan, S.; Ramezanipour, F.; Thangadurai, V. Dopant Concentration-Porosity-Li-Ion Conductivity Relationship in Garnet-Type $Li_{5+2x}La_3Ta_{2-x}Y_xO_{12}$ ($0.05 \leq X \leq 0.75$) and Their Stability in Water and 1 M LiCl. *Inorg. Chem.* **2015**, *54*, 6968−6977.
(186) Nemori, H.; Matsuda, Y.; Mitsuoka, S.; Matsui, M.; Yamamoto, O.; Takeda, Y.; Imanishi, N. Stability of Garnet-Type Solid Electrolyte $Li_xLa_3A_{2-y}B_yO_{12}$ (a = Nb or Ta, B = Sc or Zr). *Solid State Ionics* **2015**, *282*, 7−12.
(187) Kun, R.; Langer, F.; Delle Piane, M.; Ohno, S.; Zeier, W. G.; Gockeln, M.; Columbi Ciacchi, L.; Busse, M.; Fekete, I. Structural and Computational Assessment of the Influence of Wet-Chemical Post-Processing of the Al-Substituted Cubic $Li_7La_3Zr_2O_{12}$. *ACS Appl. Mater. Interfaces* **2018**, *10*, 37188−37197.
(188) Xia, W. H.; Xu, B. Y.; Duan, H. N.; Guo, Y. P.; Kang, H. M.; Li, H.; Liu, H. Z. Ionic Conductivity and Air Stability of Al-Doped $Li_7La_3Zr_2O_{12}$ Sintered in Alumina and Pt Crucibles. *ACS Appl. Mater. Interfaces* **2016**, *8*, 5335−5342.
(189) Komorowski, P.; Argyropoulos, S.; Hancock, R.; Gulens, J.; Taylor, P.; Canaday, J.; Kuriakose, A.; Wheat, T.; Ahmad, A. Characterization of Protonically Exchanged Nasicon. *Solid State Ionics* **1991**, *48*, 295−301.
(190) Canaday, J. D.; Chehab, S. F.; Kuriakose, A. K.; Ahmad, A.; Wheat, T. A. Protonic Conductivity of Hyceramtm, a Bonded Hydronium Nasicon. *Solid State Ionics* **1991**, *48*, 113−121.
(191) Fuentes, R. O.; Figueiredo, F.; Marques, F. M. B.; Franco, J. I. Reaction of NASICON with Water. *Solid State Ionics* **2001**, *139*, 309−314.
(192) Feng, Q.; Miyai, Y.; Kanoh, H.; Ooi, K. Li^+ Extraction/Insertion with Spinel-Type Lithium Manganese Oxides. Characterization of Redox-Type and Ion-Exchange-Type Sites. *Langmuir* **1992**, *8*, 1861−1867.
(193) Duan, H. N.; Zheng, H. P.; Zhou, Y.; Xu, B. Y.; Liu, H. Z. Stability of Garnet-Type Li Ion Conductors: An Overview. *Solid State Ionics* **2018**, *318*, 45−53.
(194) Hofstetter, K.; Samson, A. J.; Narayanan, S.; Thangadurai, V. Present Understanding of the Stability of Li-Stuffed Garnets with Moisture, Carbon Dioxide, and Metallic Lithium. *J. Power Sources* **2018**, *390*, 297−312.
(195) Harding, J. R.; Amanchukwu, C. V.; Hammond, P. T.; Shao-Horn, Y. Instability of Poly(ethylene oxide) Upon Oxidation in Lithium-Air Batteries. *J. Phys. Chem. C* **2015**, *119*, 6947−6955.
(196) Thokchom, J. S.; Kumar, B. Water Durable Lithium Ion Conducting Composite Membranes from the Li_2O-Al_2O_3-TiO_2-P_2O_5 Glass-Ceramic. *J. Electrochem. Soc.* **2007**, *154*, A331−A336.
(197) Hasegawa, S.; Imanishi, N.; Zhang, T.; Xie, J.; Hirano, A.; Takeda, Y.; Yamamoto, O. Study on Lithium/Air Secondary

DOI: 10.1021/acs.chemrev.9b00268
Chem. Rev. XXXX, XXX, XXX−XXX

Batteries—Stability of NASICON-Type Lithium Ion Conducting Glass-Ceramics with Water. *J. Power Sources* **2009**, *189*, 371−377.
(198) Liu, W. Y.; Li, C. L.; Fu, Z. W. Stability of Lithium Phosphorous Oxynitride Thin Films in Humid Air. *Acta Phys.-Chim. Sin.* **2006**, *22*, 1413−1418.
(199) Cretin, M.; Fabry, P.; Abello, L. Study of $Li_{1+x}Al_xTi_{2-x}(PO_4)_3$ for Li^+ Potentiometric Sensors. *J. Eur. Ceram. Soc.* **1995**, *15*, 1149−1156.
(200) Shimonishi, Y.; Zhang, T.; Imanishi, N.; Im, D.; Lee, D. J.; Hirano, A.; Takeda, Y.; Yamamoto, O.; Sammes, N. A Study on Lithium/Air Secondary Batteries-Stability of the Nasicon-Type Lithium Ion Conducting Solid Electrolyte in Alkaline Aqueous Solutions. *J. Power Sources* **2011**, *196*, 5128−5132.
(201) Dashjav, E.; Ma, Q. L.; Xu, Q.; Tsai, C. L.; Giarola, M.; Mariotto, G.; Tietz, F. The Influence of Water on the Electrical Conductivity of Aluminum-Substituted Lithium Titanium Phosphates. *Solid State Ionics* **2018**, *321*, 83−90.
(202) Zhang, T.; Imanishi, N.; Shimonishi, Y.; Hirano, A.; Takeda, Y.; Yamamoto, O.; Sammes, N. A Novel High Energy Density Rechargeable Lithium/Air Battery. *Chem. Commun.* **2010**, *46*, 1661−1663.
(203) Imanishi, N.; Hasegawa, S.; Zhang, T.; Hirano, A.; Takeda, Y.; Yamamoto, O. Lithium Anode for Lithium-Air Secondary Batteries. *J. Power Sources* **2008**, *185*, 1392−1397.
(204) Li, Y. T.; Xu, B. Y.; Xu, H. H.; Duan, H. N.; Lu, X. J.; Xin, S.; Zhou, W. D.; Xue, L. G.; Fu, G. T.; Manthiram, A.; et al. Hybrid Polymer/Garnet Electrolyte with a Small Interfacial Resistance for Lithium-Ion Batteries. *Angew. Chem., Int. Ed.* **2017**, *56*, 753−756.
(205) Ohtomo, T.; Hayashi, A.; Tatsumisago, M.; Kawamoto, K. Glass Electrolytes with High Ion Conductivity and High Chemical Stability in the System LiI-Li_2O-Li_2S-P_2S_5. *Electrochemistry* **2013**, *81*, 428−431.
(206) Hayashi, A.; Muramatsu, H.; Ohtomo, T.; Hama, S.; Tatsumisago, M. Improvement of Chemical Stability of Li_3PS_4 Glass Electrolytes by Adding M_xO_y (M = Fe, Zn, and Bi) Nanoparticles. *J. Mater. Chem. A* **2013**, *1*, 6320−6326.
(207) Chen, S.; Xie, D.; Liu, G.; Mwizerwa, J. P.; Zhang, Q.; Zhao, Y.; Xu, X.; Yao, X. Sulfide Solid Electrolytes for All-Solid-State Lithium Batteries: Structure, Conductivity, Stability and Application. *Energy Storage Mater.* **2018**, *14*, 58−74.
(208) Hood, Z. D.; Wang, H.; Li, Y. C.; Pandian, A. S.; Paranthaman, M. P.; Liang, C. D. The "Filler Effect": A Study of Solid Oxide Fillers with Beta-Li_3PS_4 for Lithium Conducting Electrolytes. *Solid State Ionics* **2015**, *283*, 75−80.
(209) Li, Y. T.; Xu, H. H.; Chien, P. H.; Wu, N.; Xin, S.; Xue, L. G.; Park, K.; Hu, Y. Y.; Goodenough, J. B. A Perovskite Electrolyte That Is Stable in Moist Air for Lithium-Ion Batteries. *Angew. Chem., Int. Ed.* **2018**, *57*, 8587−8591.
(210) Wang, Y.; Lü, X.; Zheng, C.; Liu, X.; Chen, Z.; Yang, W.; Lin, J.; Huang, F. Chemistry Design Towards a Stable Sulfide-Based Superionic Conductor $Li_4Cu_8Ge_3S_{12}$. *Angew. Chem., Int. Ed.* **2019**, *58*, 7673.
(211) Zhang, Z.; Zhang, J.; Sun, Y.; Jia, H.; Peng, L.; Zhang, Y.; Xie, J. $Li_{4-x}Sb_xSn_{1-x}S_4$ Solid Solutions for Air-Stable Solid Electrolytes. *J. Energy Chem.* **2020**, *41*, 171−176.
(212) Wu, J.-F.; Pu, B.-W.; Wang, D.; Shi, S.-Q.; Zhao, N.; Guo, X.; Guo, X. In Situ Formed Shields Enabling Li_2CO_3-Free Solid Electrolytes: A New Route to Uncover the Intrinsic Lithiophilicity of Garnet Electrolytes for Dendrite-Free Li-Metal Batteries. *ACS Appl. Mater. Interfaces* **2019**, *11*, 898−905.
(213) Li, Y. T.; Chen, X.; Dolocan, A.; Cui, Z. M.; Xin, S.; Xue, L. G.; Xu, H. H.; Park, K.; Goodenough, J. B. Garnet Electrolyte with an Ultralow Interfacial Resistance for Li-Metal Batteries. *J. Am. Chem. Soc.* **2018**, *140*, 6448−6455.
(214) Huo, H.; Chen, Y.; Zhao, N.; Lin, X.; Luo, J.; Yang, X.; Liu, Y.; Guo, X.; Sun, X. In-Situ Formed Li_2CO_3-free Garnet/Li Interface by Rapid Acid Treatment for Dendrite-Free Solid-State Batteries. *Nano Energy* **2019**, *61*, 119−125.
(215) Nolan, A. M.; Zhu, Y.; He, X.; Bai, Q.; Mo, Y. Computation-Accelerated Design of Materials and Interfaces for All-Solid-State Lithium-Ion Batteries. *Joule* **2018**, *2*, 2016−2046.
(216) Kim, K. H.; Iriyama, Y.; Yamamoto, K.; Kumazaki, S.; Asaka, T.; Tanabe, K.; Fisher, C. A. J.; Hirayama, T.; Murugan, R.; Ogumi, Z. Characterization of the Interface between $LiCoO_2$ and $Li_7La_3Zr_2O_{12}$ in an All-Solid-State Rechargeable Lithium Battery. *J. Power Sources* **2011**, *196*, 764−767.
(217) Miara, L.; Windmuller, A.; Tsai, C. L.; Richards, W. D.; Ma, Q. L.; Uhlenbruck, S.; Guillon, O.; Ceder, G. About the Compatibility between High Voltage Spinel Cathode Materials and Solid Oxide Electrolytes as a Function of Temperature. *ACS Appl. Mater. Interfaces* **2016**, *8*, 26842−26850.
(218) Park, K.; Yu, B. C.; Jung, J. W.; Li, Y. T.; Zhou, W. D.; Gao, H. C.; Son, S.; Goodenough, J. B. Electrochemical Nature of the Cathode Interface for a Solid-State Lithium-Ion Battery: Interface between $LiCoO_2$ and Garnet-$Li_7La_3Zr_2O_{12}$. *Chem. Mater.* **2016**, *28*, 8051−8059.
(219) Vardar, G.; Bowman, W. J.; Lu, Q.; Wang, J.; Chater, R. J.; Aguadero, A.; Seibert, R.; Terry, J.; Hunt, A.; Waluyo, I.; et al. Structure, Chemistry, and Charge Transfer Resistance of the Interface between $Li_7La_3Zr_2O_{12}$ Electrolyte and $LiCoO_2$ Cathode. *Chem. Mater.* **2018**, *30*, 6259−6276.
(220) Haruyama, J.; Sodeyama, K.; Han, L. Y.; Takada, K.; Tateyama, Y. Space-Charge Layer Effect at Interface between Oxide Cathode and Sulfide Electrolyte in All-Solid-State Lithium-Ion Battery. *Chem. Mater.* **2014**, *26*, 4248−4255.
(221) Sakuda, A.; Hayashi, A.; Tatsumisago, M. Interfacial Observation between $LiCoO_2$ Electrode and Li_2S−P_2S_5 Solid Electrolytes of All-Solid-State Lithium Secondary Batteries Using Transmission Electron Microscopy. *Chem. Mater.* **2010**, *22*, 949−956.
(222) Kato, T.; Yoshida, R.; Yamamoto, K.; Hirayama, T.; Motoyama, M.; West, W. C.; Iriyama, Y. Effects of Sintering Temperature on Interfacial Structure and Interfacial Resistance for All-Solid-State Rechargeable Lithium Batteries. *J. Power Sources* **2016**, *325*, 584−590.
(223) Yamamoto, K.; Iriyama, Y.; Asaka, T.; Hirayama, T.; Fujita, H.; Fisher, C. A. J.; Nonaka, K.; Sugita, Y.; Ogumi, Z. Dynamic Visualization of the Electric Potential in an All-Solid-State Rechargeable Lithium Battery. *Angew. Chem., Int. Ed.* **2010**, *49*, 4414−4417.
(224) Richards, W. D.; Miara, L. J.; Wang, Y.; Kim, J. C.; Ceder, G. *Chem. Mater.* **2016**, *28*, 266−273.
(225) Robinson, J. P.; Kichambare, P. D.; Deiner, J. L.; Miller, R.; Rottmayer, M. A.; Koenig, G. M. High Temperature Electrode-Electrolyte Interface Formation between $LiMn_{1.5}Ni_{0.5}O_4$ and $Li_{1.4}Al_{0.4}Ge_{1.6}(PO_4)_3$. *J. Am. Ceram. Soc.* **2018**, *101*, 1087−1094.
(226) Gellert, M.; Dashjav, E.; Gruner, D.; Ma, Q. L.; Tietz, F. Compatibility Study of Oxide and Olivine Cathode Materials with Lithium Aluminum Titanium Phosphate. *Ionics* **2018**, *24*, 1001−1006.
(227) Feng, J. K.; Lu, L.; Lai, M. O. Lithium Storage Capability of Lithium Ion Conductor $Li_{1.5}Al_{0.5}Ge_{1.5}(PO_4)_3$. *J. Alloys Compd.* **2010**, *501*, 255−258.
(228) Wenzel, S.; Randau, S.; Leichtweiss, T.; Weber, D. A.; Sann, J.; Zeier, W. G.; Janek, J. Direct Observation of the Interfacial Instability of the Fast Ionic Conductor $Li_{10}GeP_2S_{12}$ at the Lithium Metal Anode. *Chem. Mater.* **2016**, *28*, 2400−2407.
(229) Hartmann, P.; Leichtweiss, T.; Busche, M. R.; Schneider, M.; Reich, M.; Sann, J.; Adelhelm, P.; Janek, J. Degradation of NASICON-Type Materials in Contact with Lithium Metal: Formation of Mixed Conducting Interphases (MCI) on Solid Electrolytes. *J. Phys. Chem. C* **2013**, *117*, 21064−21074.
(230) Wenzel, S.; Leichtweiss, T.; Kruger, D.; Sann, J.; Janek, J. Interphase Formation on Lithium Solid Electrolytes-an in Situ Approach to Study Interfacial Reactions by Photoelectron Spectroscopy. *Solid State Ionics* **2015**, *278*, 98−105.
(231) Lepley, N. D.; Holzwarth, N. A. W.; Du, Y. J. A. Structures, Li^+ Mobilities, and Interfacial Properties of Solid Electrolytes Li_3PS_4 and

DOI: 10.1021/acs.chemrev.9b00268
Chem. Rev. XXXX, XXX, XXX−XXX

Li_3PO_4 from First Principles. *Phys. Rev. B: Condens. Matter Mater. Phys.* **2013**, *88*, 104103.
(232) Wenzel, S.; Weber, D. A.; Leichtweiss, T.; Busche, M. R.; Sann, J.; Janek, J. Interphase Formation and Degradation of Charge Transfer Kinetics between a Lithium Metal Anode and Highly Crystalline $Li_7P_3S_{11}$ Solid Electrolyte. *Solid State Ionics* **2016**, *286*, 24−33.
(233) Zhu, Y. Z.; He, X. F.; Mo, Y. F. First Principles Study on Electrochemical and Chemical Stability of Solid Electrolyte-Electrode Interfaces in All-Solid-State Li-Ion Batteries. *J. Mater. Chem. A* **2016**, *4*, 3253−3266.
(234) Schwobel, A.; Hausbrand, R.; Jaegermann, W. Interface Reactions between LiPON and Lithium Studied by In-Situ X-Ray Photoemission. *Solid State Ionics* **2015**, *273*, 51−54.
(235) Ismail, I.; Noda, A.; Nishimoto, A.; Watanabe, M. XPS Study of Lithium Surface after Contact with Lithium-Salt Doped Polymer Electrolytes. *Electrochim. Acta* **2001**, *46*, 1595−1603.
(236) Xu, C.; Sun, B.; Gustafsson, T.; Edstrom, K.; Brandell, D.; Hahlin, M. Interface Layer Formation in Solid Polymer Electrolyte Lithium Batteries: An XPS Study. *J. Mater. Chem. A* **2014**, *2*, 7256−7264.
(237) Chen, Y. C.; Ouyang, C. Y.; Song, L. J.; Sun, Z. L. Electrical and Lithium Ion Dynamics in Three Main Components of Solid Electrolyte Interphase from Density Functional Theory Study. *J. Phys. Chem. C* **2011**, *115*, 7044−7049.
(238) Xu, X.; Hou, G.; Nie, X.; Ai, Q.; Liu, Y.; Feng, J.; Zhang, L.; Si, P.; Guo, S.; Ci, L. LiP_3S_{11}/Poly(ethylene oxide) Hybrid Solid Electrolytes with Excellent Interfacial Compatibility for All-Solid-State Batteries. *J. Power Sources* **2018**, *400*, 212−217.
(239) Riphaus, N.; Stiaszny, B.; Beyer, H.; Indris, S.; Gasteiger, H. A.; Sedlmaier, S. J. Understanding Chemical Stability Issues between Different Solid Electrolytes in All-Solid-State Batteries. *J. Electrochem. Soc.* **2019**, *166*, A975−A983.
(240) Blanga, R.; Goor, M.; Burstein, L.; Rosenberg, Y.; Gladkich, A.; Logvinuk, D.; Shechtman, I.; Golodnitsky, D. The Search For a Solid Electrolyte, as a Polysulfide Barrier, for Lithium/Sulfur Batteries. *J. Solid State Electrochem.* **2016**, *20*, 3393−3404.
(241) Ma, C.; Cheng, Y. Q.; Yin, K. B.; Luo, J.; Sharafi, A.; Sakamoto, J.; Li, J. C.; More, K. L.; Dudney, N. J.; Chi, M. F. Interfacial Stability of Li Metal-Solid Electrolyte Elucidated Via in Situ Electron Microscopy. *Nano Lett.* **2016**, *16*, 7030−7036.
(242) Rettenwander, D.; Wagner, R.; Reyer, A.; Bonta, M.; Cheng, L.; Doeff, M. M.; Limbeck, A.; Wilkening, M.; Amthauer, G. Interface Instability of Fe-Stabilized $Li_7La_3Zr_2O_{12}$ Versus Li Metal. *J. Phys. Chem. C* **2018**, *122*, 3780−3785.
(243) Yang, K. Y.; Leu, I. C.; Fung, K. Z.; Hon, M. H.; Hsu, M. C.; Hsiao, Y. J.; Wang, M. C. Mechanism of the Interfacial Reaction between Cation-Deficient $La_{0.56}Li_{0.33}TiO_3$ and Metallic Lithium at Room Temperature. *J. Mater. Res.* **2008**, *23*, 1813−1825.
(244) Wu, B. B.; Wang, S. Y.; Lochala, J.; Desrochers, D.; Liu, B.; Zhang, W. Q.; Yang, J. H.; Xiao, J. The Role of the Solid Electrolyte Interphase Layer in Preventing Li Dendrite Growth in Solid-State Batteries. *Energy Environ. Sci.* **2018**, *11*, 1803−1810.
(245) Chung, H.; Kang, B. Mechanical and Thermal Failure Induced by Contact between a $Li_{1.5}Al_{0.5}Ge_{1.5}(PO_4)_3$ Solid Electrolyte and Li Metal in an All Solid-State Li Cell. *Chem. Mater.* **2017**, *29*, 8611−8619.
(246) Wang, Z. Y.; Santhanagopalan, D.; Zhang, W.; Wang, F.; Xin, H. L. L.; He, K.; Li, J. C.; Dudney, N.; Meng, Y. S. In Situ STEM-EELS Observation of Nanoscale Interfacial Phenomena in All-Solid-State Batteries. *Nano Lett.* **2016**, *16*, 3760−3767.
(247) Zhu, Y. Z.; He, X. F.; Mo, Y. F. Strategies Based on Nitride Materials Chemistry to Stabilize Li Metal Anode. *Adv. Sci.* **2017**, *4*, 1600517.
(248) Wenzel, S.; Sedlmaier, S. J.; Dietrich, C.; Zeier, W. G.; Janek, J. Interfacial Reactivity and Interphase Growth of Argyrodite Solid Electrolytes at Lithium Metal Electrodes. *Solid State Ionics* **2018**, *318*, 102−112.
(249) Munichandraiah, N.; Shukla, A. K.; Scanlon, L. G.; Marsh, R. A. On the Stability of Lithium During Ageing of Li/PEO_8LiClO_4/Li Cells. *J. Power Sources* **1996**, *62*, 201−206.
(250) Wolfenstine, J.; Allen, J. L.; Read, J.; Sakamoto, J. Chemical Stability of Cubic $Li_7La_3Zr_2O_{12}$ with Molten Lithium at Elevated Temperature. *J. Mater. Sci.* **2013**, *48*, 5846−5851.
(251) Ansell, R. O. The Chemical and Electrochemical Stability of Beta-Alumina. *J. Mater. Sci.* **1986**, *21*, 365−379.
(252) Zhu, Y. Z.; He, X. F.; Mo, Y. F. Origin of Outstanding Stability in the Lithium Solid Electrolyte Materials: Insights from Thermodynamic Analyses Based on First-Principles Calculations. *ACS Appl. Mater. Interfaces* **2015**, *7*, 23685−23693.
(253) Zhu, Y.; Connell, J. G.; Tepavcevic, S.; Zapol, P.; Garcia-Mendez, R.; Taylor, N. J.; Sakamoto, J.; Ingram, B. J.; Curtiss, L. A.; Freeland, J. W.; et al. Dopant-Dependent Stability of Garnet Solid Electrolyte Interfaces with Lithium Metal. *Adv. Energy Mater.* **2019**, *9*, 1803440.
(254) Peled, E.; Golodnitsky, D.; Ardel, G. Advanced Model for Solid Electrolyte Interphase Electrodes in Liquid and Polymer Electrolytes. *J. Electrochem. Soc.* **1997**, *144*, L208−L210.
(255) Peled, E.; Yamin, H. Solid Electrolyte Interphase (SEI) Electrodes 1. Kinetics of Lithium in $LiAlCl_4$-$SOCl_2$. *Isr. J. Chem.* **1979**, *18*, 131−135.
(256) Tsai, C. L.; Roddatis, V.; Chandran, C. V.; Ma, Q. L.; Uhlenbruck, S.; Bram, M.; Heitjans, P.; Guillon, O. $Li_7La_3Zr_2O_{12}$ Interface Modification for Li Dendrite Prevention. *ACS Appl. Mater. Interfaces* **2016**, *8*, 10617−10626.
(257) Suzuki, Y.; Kami, K.; Watanabe, K.; Watanabe, A.; Saito, N.; Ohnishi, T.; Takada, K.; Sudo, R.; Imanishi, N. Transparent Cubic Garnet-Type Solid Electrolyte of Al_2O_3-doped $Li_7La_3Zr_2O_{12}$. *Solid State Ionics* **2015**, *278*, 172−176.
(258) Ishiguro, K.; Nemori, H.; Sunahiro, S.; Nakata, Y.; Sudo, R.; Matsui, M.; Takeda, Y.; Yamamoto, O.; Imanishi, N. Ta-Doped $Li_7La_3Zr_2O_{12}$ for Water-Stable Lithium Electrode of Lithium-Air Batteries. *J. Electrochem. Soc.* **2014**, *161*, A668−A674.
(259) Ishiguro, K.; Nakata, Y.; Matsui, M.; Uechi, I.; Takeda, Y.; Yamamoto, O.; Imanishi, N. Stability of Nb-Doped Cubic $Li_7La_3Zr_2O_{12}$ with Lithium Metal. *J. Electrochem. Soc.* **2013**, *160*, A1690−A1693.
(260) Cheng, L.; Chen, W.; Kunz, M.; Persson, K.; Tamura, N.; Chen, G. Y.; Doeff, M. Effect of Surface Microstructure on Electrochemical Performance of Garnet Solid Electrolytes. *ACS Appl. Mater. Interfaces* **2015**, *7*, 2073−2081.
(261) Sudo, R.; Nakata, Y.; Ishiguro, K.; Matsui, M.; Hirano, A.; Takeda, Y.; Yamamoto, O.; Imanishi, N. Interface Behavior between Garnet-Type Lithium-Conducting Solid Electrolyte and Lithium. *Solid State Ionics* **2014**, *262*, 151−154.
(262) Wang, S. F.; Xu, H. H.; Li, W. D.; Dolocan, A.; Manthiram, A. Interfacial Chemistry in Solid-State Batteries: Formation of Interphase and Its Consequences. *J. Am. Chem. Soc.* **2018**, *140*, 250−257.
(263) Han, F.; Westover, A. S.; Yue, J.; Fan, X.; Wang, F.; Chi, M.; Leonard, D. N.; Dudney, N. J.; Wang, H.; Wang, C. High Electronic Conductivity as the Origin of Lithium Dendrite Formation within Solid Electrolytes. *Nat. Energy* **2019**, *4*, 187−196.
(264) Sakuda, A.; Kitaura, H.; Hayashi, A.; Tadanaga, K.; Tatsumisago, M. Modification of Interface between $LiCoO_2$ Electrode and Li_2S-P_2S_5 Solid Electrolyte Using Li_2O-SiO_2 Glassy Layers. *J. Electrochem. Soc.* **2009**, *156*, A27−A32.
(265) Yi, T. F.; Mei, J.; Zhu, Y. R. Key Strategies for Enhancing the Cycling Stability and Rate Capacity of $LiNi_{0.5}Mn_{1.5}O_4$ as High-Voltage Cathode Materials for High Power Lithium-Ion Batteries. *J. Power Sources* **2016**, *316*, 85−105.
(266) Wang, L.; Chen, B.; Ma, J.; Cui, G.; Chen, L. Reviving Lithium Cobalt Oxide-Based Lithium Secondary Batteries-toward a Higher Energy Density. *Chem. Soc. Rev.* **2018**, *47*, 6505−6602.
(267) Whittingham, M. S. Lithium Batteries and Cathode Materials. *Chem. Rev.* **2004**, *104*, 4271−4301.
(268) Appetecchi, G. B.; Hassoun, J.; Scrosati, B.; Croce, F.; Cassel, F.; Salomon, M. Hot-Pressed, Solvent-Free, Nanocomposite, PEO-

DOI: 10.1021/acs.chemrev.9b00268
Chem. Rev. XXXX, XXX, XXX−XXX

based electrolyte membranes II. All solid-state Li/LiFePO4 Polymer Batteries. *J. Power Sources* **2003**, *124*, 246−253.
(269) Andre, P.; Deniard, P.; Brec, R.; Lascaud, S. Study of the Interface Nickel/Composite Cathode of Industrially Made Li/V_2O_5 Polymer (POE) Batteries Working at 90 Degrees C. *J. Power Sources* **2002**, *105*, 66−74.
(270) Prosini, P. P.; Capiglia, C.; Saito, Y.; Fujieda, T.; Vellone, R.; Shikano, M.; Sakai, T. A New Composite Cathode for High-Performance Lithium-Polymer Batteries. *J. Power Sources* **2001**, *99*, 1−6.
(271) Appetecchi, G. B.; Croce, F.; Dautzenberg, G.; Mastragostino, M.; Ronci, F.; Scrosati, B.; Soavi, F.; Zanelli, A.; Alessandrini, F.; Prosini, P. P. Composite Polymer Electrolytes with Improved Lithium Metal Electrode Interfacial Properties I. Electrochemical Properties of Dry Peo-Lix Systems. *J. Electrochem. Soc.* **1998**, *145*, 4126−4132.
(272) Capuano, F.; Croce, F.; Scrosati, B. Composite Polymer Electrolytes. *J. Electrochem. Soc.* **1991**, *138*, 1918−1922.
(273) Bouchet, R.; Maria, S.; Meziane, R.; Aboulaich, A.; Lienafa, L.; Bonnet, J. P.; Phan, T. N. T.; Bertin, D.; Gigmes, D.; Devaux, D.; et al. Single-Ion BAB Triblock Copolymers as Highly Efficient Electrolytes for Lithium-Metal Batteries. *Nat. Mater.* **2013**, *12*, 452−457.
(274) Matoba, Y.; Matsui, S.; Tabuchi, M.; Sakai, T. Electrochemical Properties of Composite Polymer Electrolyte Applied to Rechargeable Lithium Polymer Battery. *J. Power Sources* **2004**, *137*, 284−287.
(275) Sylla, S.; Sanchez, J. Y.; Armand, M. Electrochemical Study of Linear and Crosslinked POE-Based Polymer Electrolytes. *Electrochim. Acta* **1992**, *37*, 1699−1701.
(276) Li, Q.; Takeda, Y.; Imanish, N.; Yang, J.; Sun, H. Y.; Yamamoto, O. Cycling Performances and Interfacial Properties of a Li/PEO-Li$(CF_3SO_2)_2$N-ceramic filler/$LiNi_{0.8}Co_{0.2}O_2$ cell. *J. Power Sources* **2001**, *97*−*98*, 795−797.
(277) Wen, Z. Y.; Itoh, T.; Ichikawa, Y.; Kubo, M.; Yamamoto, O. Blend-Based Polymer Electrolytes of Poly(ethylene oxide) and Hyperbranched Poly[bis(triethylene glycol)benzoate] with Terminal Acetyl Groups. *Solid State Ionics* **2000**, *134*, 281−289.
(278) Michael, M. S.; Jacob, M. M. E.; Prabaharan, S. R. S.; Radhakrishna, S. Enhanced Lithium Ion Transport in PEO-Based Solid Polymer Electrolytes Employing a Novel Class of Plasticizers. *Solid State Ionics* **1997**, *98*, 167−174.
(279) Zhang, J. X.; Zhao, N.; Zhang, M.; Li, Y. Q.; Chu, P. K.; Guo, X. X.; Di, Z. F.; Wang, X.; Li, H. Flexible and Ion-Conducting Membrane Electrolytes for Solid-State Lithium Batteries: Dispersion of Garnet Nanoparticles in Insulating Polyethylene Oxide. *Nano Energy* **2016**, *28*, 447−454.
(280) Wang, X. Z.; Zhang, Y. B.; Zhang, X.; Liu, T.; Lin, Y. H.; Li, L. L.; Shen, Y.; Nan, C. W. Lithium-Salt-Rich PEO/$Li_{0.3}La_{0.557}TiO_3$ Interpenetrating Composite Electrolyte with Three-Dimensional Ceramic Nano-Backbone for All-Solid-State Lithium-Ion Batteries. *ACS Appl. Mater. Interfaces* **2018**, *10*, 24791−24798.
(281) Xia, Y. Y.; Fujieda, T.; Tatsumi, K.; Prosini, P. P.; Sakai, T. Thermal and Electrochemical Stability of Cathode Materials in Solid Polymer Electrolyte. *J. Power Sources* **2001**, *92*, 234−243.
(282) Hori, S.; Suzuki, K.; Hirayama, M.; Kato, Y.; Kanno, R. Lithium Superionic Conductor $Li_{9.42}Si_{1.02}P_{2.1}S_{9.96}O_{2.04}$ with $Li_{10}GeP_2S_{12}$-Type Structure in the Li_2S-P_2S_5-SiO_2 Pseudoternary System: Synthesis, Electrochemical Properties, and Structure-Composition Relationships. *Front. Energy Res.* **2016**, *4*, 38.
(283) Hayashi, A.; Hama, S.; Mizuno, F.; Tadanaga, K.; Minami, T.; Tatsumisago, M. Characterization of Li_2S-P_2S_5 Glass-Ceramics as a Solid Electrolyte for Lithium Secondary Batteries. *Solid State Ionics* **2004**, *175*, 683−686.
(284) Boulineau, S.; Courty, M.; Tarascon, J. M.; Viallet, V. Mechanochemical Synthesis of Li-Argyrodite Li_6PS_5X (X = Cl, Br, I) as Sulfur-Based Solid Electrolytes for All Solid State Batteries Application. *Solid State Ionics* **2012**, *221*, 1−5.
(285) Han, F. D.; Gao, T.; Zhu, Y. J.; Gaskell, K. J.; Wang, C. S. A Battery Made from a Single Material. *Adv. Mater.* **2015**, *27*, 3473−3483.
(286) Ohta, S.; Kobayashi, T.; Asaoka, T. High Lithium Ionic Conductivity in the Garnet-Type Oxide $Li_{7-x}La_3(Zr_{2-x}, Nb_x)O_{12}$ (x = 0−2). *J. Power Sources* **2011**, *196*, 3342−3345.
(287) Suo, L. M.; Borodin, O.; Gao, T.; Olguin, M.; Ho, J.; Fan, X. L.; Luo, C.; Wang, C. S.; Xu, K. "Water-in-Salt" Electrolyte Enables High-Voltage Aqueous Lithium-Ion Chemistries. *Science* **2015**, *350*, 938−943.
(288) Hakari, T.; Deguchi, M.; Mitsuhara, K.; Ohta, T.; Saito, K.; Orikasa, Y.; Uchimoto, Y.; Kowada, Y.; Hayashi, A.; Tatsumisago, M. Structural and Electronic-State Changes of a Sulfide Solid Electrolyte During the Li Deinsertion-Insertion Processes. *Chem. Mater.* **2017**, *29*, 4768−4774.
(289) Hua, C. X.; Fang, X. P.; Wang, Z. X.; Chen, L. Q. Lithium Storage in Perovskite Lithium Lanthanum Titanate. *Electrochem. Commun.* **2013**, *32*, 5−8.
(290) Otoyama, M.; Ito, Y.; Hayashi, A.; Tatsumisago, M. Raman Imaging for $LiCoO_2$ Composite Positive Electrodes in All-Solid-State Lithium Batteries Using Li_2S-P_2S_5 Solid Electrolytes. *J. Power Sources* **2016**, *302*, 419−425.
(291) Wang, H.; Rus, E.; Sakuraba, T.; Kikuchi, J.; Kiya, Y.; Abruña, H. D. CO_2 and O_2 Evolution at High Voltage Cathode Materials of Li-Ion Batteries: A Differential Electrochemical Mass Spectrometry Study. *Anal. Chem.* **2014**, *86*, 6197−6201.
(292) Auvergniot, J.; Cassel, A.; Ledeuil, J. B.; Viallet, V.; Seznec, V.; Dedryvere, R. Interface Stability of Argyrodite Li_6PS_5Cl toward $LiCoO_2$, $LiNi_{1/3}Co_{1/3}Mn_{1/3}O_2$, and $LiMn_2O_4$ in Bulk All-Solid-State Batteries. *Chem. Mater.* **2017**, *29*, 3883−3890.
(293) Zhang, W. B.; Leichtweiss, T.; Culver, S. P.; Koerver, R.; Das, D.; Weber, D. A.; Zeier, W. G.; Janek, J. The Detrimental Effects of Carbon Additives in $Li_{10}GeP_2S_{12}$-Based Solid-State Batteries. *ACS Appl. Mater. Interfaces* **2017**, *9*, 35888−35896.
(294) Chu, I. H.; Nguyen, H.; Hy, S.; Lin, Y. C.; Wang, Z. B.; Xu, Z. H.; Deng, Z.; Meng, Y. S.; Ong, S. P. Insights into the Performance Limits of the $Li_7P_3S_{11}$ Superionic Conductor: A Combined First-Principles and Experimental Study. *ACS Appl. Mater. Interfaces* **2016**, *8*, 7843−7853.
(295) Sumita, M.; Tanaka, Y.; Ikeda, M.; Ohno, T. Charged and Discharged States of Cathode/Sulfide Electrolyte Interfaces in All-Solid-State Lithium Ion Batteries. *J. Phys. Chem. C* **2016**, *120*, 13332−13339.
(296) Sumita, M.; Tanaka, Y.; Ohno, T. Possible Polymerization of PS_4 at a Li_3PS_4/$FePO_4$ Interface with Reduction of the $FePO_4$ Phase. *J. Phys. Chem. C* **2017**, *121*, 9698−9704.
(297) Ma, J.; Liu, Z. L.; Chen, B. B.; Wang, L. L.; Yue, L. P.; Liu, H. S.; Zhang, J. J.; Liu, Z. H.; Cui, G. L. A Strategy to Make High Voltage $LiCoO_2$ Compatible with Polyethylene Oxide Electrolyte in All-Solid-State Lithium Ion Batteries. *J. Electrochem. Soc.* **2017**, *164*, A3454−A3461.
(298) Nagata, K.; Nanno, T. All Solid Battery with Phosphate Compounds Made through Sintering Process. *J. Power Sources* **2007**, *174*, 832−837.
(299) Kim, H. S.; Oh, Y.; Kang, K. H.; Kim, J. H.; Kim, J.; Yoon, C. S. Characterization of Sputter-Deposited $LiCoO_2$ Thin Film Grown on NASICON-Type Electrolyte for Application in All-Solid-State Rechargeable Lithium Battery. *ACS Appl. Mater. Interfaces* **2017**, *9*, 16063−16070.
(300) Hansel, C.; Afyon, S.; Rupp, J. L. M. Investigating the All-Solid-State Batteries Based on Lithium Garnets and a High Potential Cathode - $LiMn_{1.5}Ni_{0.5}O_4$. *Nanoscale* **2016**, *8*, 18412−18420.
(301) Kotobuki, M.; Suzuki, Y.; Munakata, H.; Kanamura, K.; Sato, Y.; Yamamoto, K.; Yoshida, T. Compatibility of $LiCoO_2$ and $LiMn_2O_4$ Cathode Materials for $Li_{0.55}La_{0.35}TiO_3$ Electrolyte to Fabricate All-Solid-State Lithium Battery. *J. Power Sources* **2010**, *195*, 5784−5788.
(302) Miara, L. J.; Richards, W. D.; Wang, Y. E.; Ceder, G. First-Principles Studies on Cation Dopants and Electrolytelcathode Interphases for Lithium Garnets. *Chem. Mater.* **2015**, *27*, 4040−4047.

DOI: 10.1021/acs.chemrev.9b00268
Chem. Rev. XXXX, XXX, XXX−XXX

(303) Ohta, S.; Kobayashi, T.; Seki, J.; Asaoka, T. Electrochemical Performance of an All-Solid-State Lithium Ion Battery with Garnet-Type Oxide Electrolyte. *J. Power Sources* **2012**, *202*, 332−335.
(304) Nie, K.; Hong, Y.; Qiu, J.; Li, Q.; Yu, X.; Li, H.; Chen, L. Interfaces between Cathode and Electrolyte in Solid State Lithium Batteries: Challenges and Perspectives. *Front. Chem.* **2018**, *6*, 616.
(305) Seki, S.; Kobayashi, Y.; Miyashiro, H.; Usami, A.; Mita, Y.; Terada, N. Improvement in High-Voltage Performance of All-Solid-State Lithium Polymer Secondary Batteries by Mixing Inorganic Electrolyte with Cathode Materials. *J. Electrochem. Soc.* **2006**, *153*, A1073−A1076.
(306) Seki, S.; Kobayashi, Y.; Miyashiro, H.; Yamanaka, A.; Mita, Y.; Iwahori, T. Degradation Mechanism Analysis of All-Solid-State Lithium Polymer Secondary Batteries by Using the Impedance Measurement. *J. Power Sources* **2005**, *146*, 741−744.
(307) Wood, K. N.; Steirer, K. X.; Hafner, S. E.; Ban, C. M.; Santhanagopalan, S.; Lee, S. H.; Teeter, G. Operando X-Ray Photoelectron Spectroscopy of Solid Electrolyte Interphase Formation and Evolution in Li_2S-P_2S_5 Solid-State Electrolytes. *Nat. Commun.* **2018**, *9*, 2490.
(308) Zheng, J. Y.; Zheng, H.; Wang, R.; Ben, L. B.; Lu, W.; Chen, L. W.; Chen, L. Q.; Li, H. 3d Visualization of Inhomogeneous Multi-Layered Structure and Young's Modulus of the Solid Electrolyte Interphase (SEI) on Silicon Anodes for Lithium Ion Batteries. *Phys. Chem. Chem. Phys.* **2014**, *16*, 13229−13238.
(309) Liu, T.; Lin, L.; Bi, X.; Tian, L.; Yang, K.; Liu, J.; Li, M.; Chen, Z.; Lu, J.; Amine, K.; et al. In Situ Quantification of Interphasial Chemistry in Li-Ion Battery. *Nat. Nanotechnol.* **2019**, *14*, 50.
(310) Liang, J. Y.; Zeng, X. X.; Zhang, X. D.; Wang, P. F.; Ma, J. Y.; Yin, Y. X.; Wu, X. W.; Guo, Y. G.; Wan, L. J. Mitigating Interfacial Potential Drop of Cathode-Solid Electrolyte Via Ionic Conductor Layer to Enhance Interface Dynamics for Solid Batteries. *J. Am. Chem. Soc.* **2018**, *140*, 6767−6770.
(311) Kato, T.; Hamanaka, T.; Yamamoto, K.; Hirayama, T.; Sagane, F.; Motoyama, M.; Iriyama, Y. In-Situ $Li_7La_3Zr_2O_{12}$/$LiCoO_2$ Interface Modification for Advanced All-Solid-State Battery. *J. Power Sources* **2014**, *260*, 292−298.
(312) Wu, F.; Fitzhugh, W.; Ye, L.; Ning, J.; Li, X. Advanced Sulfide Solid Electrolyte by Core-Shell Structural Design. *Nat. Commun.* **2018**, *9*, 4037.
(313) Zhao, Y.; Zheng, K.; Sun, X. Addressing Interfacial Issues in Liquid-Based and Solid-State Batteries by Atomic and Molecular Layer Deposition. *Joule* **2018**, *2*, 2583−2604.
(314) Kobayashi, Y.; Seki, S.; Yamanaka, A.; Miyashiro, H.; Mita, Y.; Iwahori, T. Development of High-Voltage and High-Capacity All-Solid-State Lithium Secondary Batteries. *J. Power Sources* **2005**, *146*, 719−722.
(315) Miyashiro, H.; Kobayashi, Y.; Seki, S.; Mita, Y.; Usami, A.; Nakayama, M.; Wakihara, M. Fabrication of All-Solid-State Lithium Polymer Secondary Batteries Using Al_2O_3-Coated $LiCoO_2$. *Chem. Mater.* **2005**, *17*, 5603−5605.
(316) Kobayashi, Y.; Seki, S.; Tabuchi, M.; Miyashiro, H.; Mita, Y.; Iwahori, T. High-Performance Genuine Lithium Polymer Battery Obtained by Fine-Ceramic-Electrolyte Coating of $LiCoO_2$. *J. Electrochem. Soc.* **2005**, *152*, A1985−A1988.
(317) Sakuda, A.; Kitaura, H.; Hayashi, A.; Tadanaga, K.; Tatsumisago, M. All-Solid-State Lithium Secondary Batteries with Oxide-Coated $LiCoO_2$ Electrode and Li_2S-P_2S_5 Electrolyte. *J. Power Sources* **2009**, *189*, 527−530.
(318) Okada, K.; Machida, N.; Naito, M.; Shigematsu, T.; Ito, S.; Fujiki, S.; Nakano, M.; Aihara, Y. Preparation and Electrochemical Properties of $LiAlO_2$-coated $Li(Ni_{1/3}Mn_{1/3}Co_{1/3})O_2$ for All-Solid-State Batteries. *Solid State Ionics* **2014**, *255*, 120−127.
(319) Ito, S.; Fujiki, S.; Yamada, T.; Aihara, Y.; Park, Y.; Kim, T. Y.; Baek, S. W.; Lee, J. M.; Doo, S.; Machida, N. A Rocking Chair Type All-Solid-State Lithium Ion Battery Adopting Li_2O-ZrO_2 Coated $LiNi_{0.8}Co_{0.15}Al_{0.05}O_2$ and a Sulfide Based Electrolyte. *J. Power Sources* **2014**, *248*, 943−950.
(320) Kim, J.; Kim, M.; Noh, S.; Lee, G.; Shin, D. Enhanced Electrochemical Performance of Surface Modified $LiCoO_2$ for All-Solid-State Lithium Batteries. *Ceram. Int.* **2016**, *42*, 2140−2146.
(321) Yubuchi, S.; Ito, Y.; Matsuyama, T.; Hayashi, A.; Tatsumisago, M. 5 V Class $LiNi_{0.5}Mn_{1.5}O_4$ positive electrode coated with Li_3PO_4 Thin Film for All-Solid-State Batteries Using Sulfide Solid Electrolyte. *Solid State Ionics* **2016**, *285*, 79−82.
(322) Ohta, N.; Takada, K.; Sakaguchi, I.; Zhang, L. Q.; Ma, R. Z.; Fukuda, K.; Osada, M.; Sasaki, T. $LiNbO_3$-coated $LiCoO_2$ as Cathode Material for All Solid-State Lithium Secondary Batteries. *Electrochem. Commun.* **2007**, *9*, 1486−1490.
(323) Ohta, N.; Takada, K.; Zhang, L. Q.; Ma, R. Z.; Osada, M.; Sasaki, T. Enhancement of the High-Rate Capability of Solid-State Lithium Batteries by Nanoscale Interfacial Modification. *Adv. Mater.* **2006**, *18*, 2226.
(324) Wang, C.; Li, X.; Zhao, Y.; Banis, M. N.; Liang, J.; Li, X.; Sun, Y.; Adair, K. R.; Sun, Q.; Liu, Y.; et al. Manipulating Interfacial Nanostructure to Achieve High-Performance All-Solid-State Lithium-Ion Batteries. *Small Methods* **2019**, *3*, 1900261.
(325) Takada, K.; Ohta, N.; Zhang, L. Q.; Fukuda, K.; Sakaguchi, I.; Ma, R.; Osada, M.; Sasaki, T. Interfacial Modification for High-Power Solid-State Lithium Batteries. *Solid State Ionics* **2008**, *179*, 1333−1337.
(326) Ohta, S.; Komagata, S.; Seki, J.; Saeki, T.; Morishita, S.; Asaoka, T. All-Solid-State Lithium Ion Battery Using Garnet-Type Oxide and Li_3BO_3 Solid Electrolytes Fabricated by Screen-Printing. *J. Power Sources* **2013**, *238*, 53−56.
(327) Zhang, Z. H.; Zhao, Y. R.; Chen, S. J.; Xie, D. J.; Yao, X. Y.; Cui, P.; Xu, X. X. An Advanced Construction Strategy of All-Solid-State Lithium Batteries with Excellent Interfacial Compatibility and Ultralong Cycle Life. *J. Mater. Chem. A* **2017**, *5*, 16984−16993.
(328) Han, X. G.; Gong, Y. H.; Fu, K.; He, X. F.; Hitz, G. T.; Dai, J. Q.; Pearse, A.; Liu, B. Y.; Wang, H.; Rublo, G.; et al. Negating Interfacial Impedance in Garnet-Based Solid-State Li Metal Batteries. *Nat. Mater.* **2017**, *16*, 572.
(329) Wang, C. H.; Zhao, Y.; Sun, Q.; Li, X.; Liu, Y. L.; Liang, J. W.; Li, X. N.; Lin, X. T.; Li, R. Y.; Adair, K. R.; et al. Stabilizing Interface between $Li_{10}SnP_2S_{12}$ and Li Metal by Molecular Layer Deposition. *Nano Energy* **2018**, *53*, 168−174.
(330) Liu, Y. J.; Li, C.; Li, B. J.; Song, H. C.; Cheng, Z.; Chen, M. R.; He, P.; Zhou, H. S. Germanium Thin Film Protected Lithium Aluminum Germanium Phosphate for Solid-State Li Batteries. *Adv. Energy Mater.* **2018**, *8*, 1702374.
(331) Luo, W.; Gong, Y. H.; Zhu, Y. Z.; Fu, K. K.; Dai, J. Q.; Lacey, S. D.; Wang, C. W.; Liu, B. Y.; Han, X. G.; Mo, Y. F.; et al. Transition from Superlithiophobicity to Superlithiophilicity of Garnet Solid-State Electrolyte. *J. Am. Chem. Soc.* **2016**, *138*, 12258−12262.
(332) Krauskopf, T.; Dippel, R.; Hartmann, H.; Peppler, K.; Mogwitz, B.; Richter, F. H.; Zeier, W. G.; Janek, J. Lithium-Metal Growth Kinetics on LLZO Garnet-Type Solid Electrolytes. *Joule* **2019**, *3*, 2030−2049.
(333) Liu, J. Y.; Liu, T.; Pu, Y. J.; Guan, M. M.; Tang, Z. Y.; Ding, F.; Xu, Z. B.; Li, Y. Facile Synthesis of NASICON-type $Li_{1.3}Al_{0.3}Ti_{1.7}(PO_4)_3$ Solid Electrolyte and its Application for Enhanced Cyclic Performance in Lithium Ion Batteries through the Introduction of an Artificial Li_3PO_4 SEI Layer. *RSC Adv.* **2017**, *7* (74), 46545.
(334) Liu, Y. L.; Sun, Q.; Zhao, Y.; Wang, B. Q.; Kaghazchi, P.; Adair, K. R.; Li, R. Y.; Zhang, C.; Liu, J. R.; Kuo, L. Y.; et al. Stabilizing the Interface of NASICON Solid Electrolyte against Li Metal with Atomic Layer Deposition. *ACS Appl. Mater. Interfaces* **2018**, *10* (37), 31240.
(335) Hou, G. M.; Ma, X. X.; Sun, Q. D.; Ai, Q.; Xu, X. Y.; Chen, L. N.; Li, D. P.; Chen, J. H.; Zhong, H.; Li, Y.; et al. Lithium Dendrite Suppression and Enhanced Interfacial Compatibility Enabled by an Ex Situ SEI on Li Anode for LAGP-Based All-Solid-State Batteries. *ACS Appl. Mater. Interfaces* **2018**, *10*, 18610.
(336) Hao, X. G.; Zhao, Q.; Su, S. M.; Zhang, S. Q.; Ma, J. B.; Shen, L.; Yu, Q. P.; Zhao, L.; Liu, Y.; Kang, F. Y.; He, Y. B. Constructing

DOI: 10.1021/acs.chemrev.9b00268
Chem. Rev. XXXX, XXX, XXX−XXX

Multifunctional Interphase between $Li_{1.4}Al_{0.4}Ti_{1.6}(PO_4)_3$ and Li Metal by Magnetron Sputtering for Highly Stable Solid-State Lithium Metal Batteries. *Adv. Energy Mater.* **2019**, *9*, 1901604.
(337) Li, N. W.; Yin, Y. X.; Yang, C. P.; Guo, Y. G. An Artificial Solid Electrolyte Interphase Layer for Stable Lithium Metal Anodes. *Adv. Mater.* **2016**, *28*, 1853−1858.
(338) Gao, Y.; Wang, D.; Li, Y. C.; Yu, Z.; Mallouk, T. E.; Wang, D. Salt-Based Organic−Inorganic Nanocomposites: Towards a Stable Lithium Metal/$Li_{10}GeP_2S_{12}$ Solid Electrolyte Interface. *Angew. Chem., Int. Ed.* **2018**, *57*, 13608−13612.
(339) Wang, C.; Adair, K. R.; Liang, J.; Li, X.; Sun, Y.; Li, X.; Wang, J.; Sun, Q.; Zhao, F.; Lin, X.; et al. Solid-State Plastic Crystal Electrolytes: Effective Protection Interlayers for Sulfide-Based All-Solid-State Lithium Metal Batteries. *Adv. Funct. Mater.* **2019**, *29*, 1900392.
(340) Nakamura, T.; Amezawa, K.; Kulisch, J.; Zeier, W. G.; Janek, J. Guidelines for All-Solid-State Battery Design and Electrode Buffer Layers Based on Chemical Potential Profile Calculation. *ACS Appl. Mater. Interfaces* **2019**, *11*, 19968−19976.
(341) Sang, L.; Bassett, K. L.; Castro, F. C.; Young, M. J.; Chen, L.; Haasch, R. T.; Elam, J. W.; Dravid, V. P.; Nuzzo, R. G.; Gewirth, A. A. Understanding the Effect of Interlayers at the Thiophosphate Solid Electrolyte/Lithium Interface for All-Solid-State Li Batteries. *Chem. Mater.* **2018**, *30*, 8747−8756.
(342) West, W. C.; Whitacre, J. F.; Lim, J. R. Chemical Stability Enhancement of Lithium Conducting Solid Electrolyte Plates Using Sputtered LiPON Thin Films. *J. Power Sources* **2004**, *126*, 134−138.
(343) Basappa, R. H.; Ito, T.; Yamada, H. Contact between Garnet-Type Solid Electrolyte and Lithium Metal Anode: Influence on Charge Transfer Resistance and Short Circuit Prevention. *J. Electrochem. Soc.* **2017**, *164*, A666−A671.
(344) Luo, W.; Gong, Y. H.; Zhu, Y. Z.; Li, Y. J.; Yao, Y. G.; Zhang, Y.; Fu, K.; Pastel, G.; Lin, C. F.; Mo, Y. F.; et al. Reducing Interfacial Resistance between Garnet-Structured Solid-State Electrolyte and Li-Metal Anode by a Germanium Layer. *Adv. Mater.* **2017**, *29*, 1606042.
(345) He, M. H.; Cui, Z. H.; Chen, C.; Li, Y. Q.; Guo, X. X. Formation of Self-Limited, Stable and Conductive Interfaces between Garnet Electrolytes and Lithium Anodes for Reversible Lithium Cycling in Solid-State Batteries. *J. Mater. Chem. A* **2018**, *6*, 11463−11470.
(346) Xu, H. H.; Li, Y. T.; Zhou, A. J.; Wu, N.; Xin, S.; Li, Z. Y.; Goodenough, J. B. Li_3N-Modified Garnet Electrolyte for All-Solid-State Lithium Metal Batteries Operated at 40 Degrees C. *Nano Lett.* **2018**, *18*, 7414−7418.
(347) Shao, Y. J.; Wang, H. C.; Gong, Z. L.; Wang, D. W.; Zheng, B. Z.; Zhu, J. P.; Lu, Y. X.; Hu, Y. S.; Guo, X. X.; Li, H.; et al. Drawing a Soft Interface: An Effective Interfacial Modification Strategy for Garnet Type Solid-State Li Batteries. *ACS Energy Lett.* **2018**, *3*, 1212−1218.
(348) Wang, C. W.; Gong, Y. H.; Liu, B. Y.; Fu, K.; Yao, Y. G.; Hitz, E.; Li, Y. J.; Dai, J. Q.; Xu, S. M.; Luo, W.; et al. Conformal, Nanoscale Zno Surface Modification of Garnet-Based Solid-State Electrolyte for Lithium Metal Anodes. *Nano Lett.* **2017**, *17*, 565−571.
(349) Feng, W.; Dong, X.; Lai, Z.; Zhang, X.; Wang, Y.; Wang, C.; Luo, J.; Xia, Y. Building an Interfacial Framework: Li/Garnet Interface Stabilization through a Cu_6Sn_5 Layer. *ACS Energy Lett.* **2019**, *4*, 1725−1731.
(350) Zheng, B. Z.; Zhu, J. P.; Wang, H. C.; Feng, M.; Umeshbabu, E.; Li, Y. X.; Wu, Q. H.; Yang, Y. Stabilizing $Li_{10}SnP_2S_{12}$/Li Interface Via an in Situ Formed Solid Electrolyte Interphase Layer. *ACS Appl. Mater. Interfaces* **2018**, *10*, 25473−25482.
(351) Xu, R. C.; Han, F. D.; Ji, X.; Fan, X. L.; Tu, J. P.; Wang, C. S. Interface Engineering of Sulfide Electrolytes for All-Solid-State Lithium Batteries. *Nano Energy* **2018**, *53*, 958−966.
(352) Kato, A.; Suyama, M.; Hotehama, C.; Kowada, H.; Sakuda, A.; Hayashi, A.; Tatsumisago, M. High-Temperature Performance of All-Solid-State Lithium-Metal Batteries Having Li/Li_3PS_4 Interfaces Modified with Au Thin Films. *J. Electrochem. Soc.* **2018**, *165*, A1950−A1954.
(353) Whiteley, J. M.; Woo, J. H.; Hu, E. Y.; Nam, K. W.; Lee, S. H. Empowering the Lithium Metal Battery through a Silicon-Based Superionic Conductor. *J. Electrochem. Soc.* **2014**, *161*, A1812−A1817.
(354) Brissot, C.; Rosso, M.; Chazalviel, J. N.; Lascaud, S. Dendritic Growth Mechanisms in Lithium/Polymer Cells. *J. Power Sources* **1999**, *81*, 925−929.
(355) Builes, D. H.; Hernández-Ortiz, J. P.; Corcuera, M. A.; Mondragon, I.; Tercjak, A. Effect of Poly(ethylene oxide) Homopolymer and Two Different Poly(ethylene oxide-b-poly-(propylene oxide)-b-poly(ethylene oxide) Triblock Copolymers on Morphological, Optical, and Mechanical Properties of Nanostructured Unsaturated Polyester. *ACS Appl. Mater. Interfaces* **2014**, *6*, 1073−1081.
(356) Ramesh, S.; Winie, T.; Arof, A. K. Investigation of Mechanical Properties of Polyvinyl Chloride−Polyethylene Oxide (PVC−PEO) Based Polymer Electrolytes for Lithium Polymer Cells. *Eur. Polym. J.* **2007**, *43*, 1963−1968.
(357) McGrogan, F. P.; Swamy, T.; Bishop, S. R.; Eggleton, E.; Porz, L.; Chen, X.; Chiang, Y.-M.; Van Vliet, K. J. Compliant yet Brittle Mechanical Behavior of Li_2S−P_2S_5 Lithium-Ion-Conducting Solid Electrolyte. *Adv. Energy Mater.* **2017**, *7*, 1602011.
(358) Kato, A.; Nose, M.; Yamamoto, M.; Sakuda, A.; Hayashi, A.; Tatsumisago, M. Mechanical Properties of Sulfide Glasses in All-Solid-State Batteries. *J. Ceram. Soc. Jpn.* **2018**, *126*, 719−727.
(359) Deng, Z.; Wang, Z. B.; Chu, I. H.; Luo, J.; Ong, S. P. Elastic Properties of Alkali Superionic Conductor Electrolytes from First Principles Calculations. *J. Electrochem. Soc.* **2016**, *163*, A67−A74.
(360) Jackman, S. D.; Cutler, R. A. Effect of Microcracking on Ionic Conductivity in LATP. *J. Power Sources* **2012**, *218*, 65−72.
(361) Cho, Y.-H.; Wolfenstine, J.; Rangasamy, E.; Kim, H.; Choe, H.; Sakamoto, J. Mechanical Properties of the Solid Li-Ion Conducting Electrolyte: $Li_{0.33}La_{0.57}TiO_3$. *J. Mater. Sci.* **2012**, *47*, 5970−5977.
(362) Yu, S.; Schmidt, R. D.; Garcia-Mendez, R.; Herbert, E.; Dudney, N. J.; Wolfenstine, J. B.; Sakamoto, J.; Siegel, D. J. Elastic Properties of the Solid Electrolyte $Li_7La_3Zr_2O_{12}$ (LLZO). *Chem. Mater.* **2016**, *28*, 197−206.
(363) Ni, J. E.; Case, E. D.; Sakamoto, J. S.; Rangasamy, E.; Wolfenstine, J. B. Room Temperature Elastic Moduli and Vickers Hardness of Hot-Pressed LLZO Cubic Garnet. *J. Mater. Sci.* **2012**, *47*, 7978−7985.
(364) Kim, Y.; Jo, H.; Allen, J. L.; Choe, H.; Wolfenstine, J.; Sakamoto, J. The Effect of Relative Density on the Mechanical Properties of Hot-Pressed Cubic $Li_7La_3Zr_2O_{12}$. *J. Am. Ceram. Soc.* **2016**, *99*, 1367−1374.
(365) Boresi, A. P. *Advanced Mechanics of Materials*, 6th ed.; John Wiley & Sons, 2003.
(366) Pugh, S. F. Relations between the Elastic Moduli and the Plastic Properties of Polycrystalline Pure Metals. *Philos. Mag.* **1954**, *45*, 823−843.
(367) Koerver, R.; Aygun, I.; Leichtweiss, T.; Dietrich, C.; Zhang, W. B.; Binder, J. O.; Hartmann, P.; Zeier, W. G.; Janek, J. Capacity Fade in Solid-State Batteries: Interphase Formation and Chemo-mechanical Processes in Nickel-Rich Layered Oxide Cathodes and Lithium Thiophosphate Solid Electrolytes. *Chem. Mater.* **2017**, *29*, 5574−5582.
(368) Gilman, J. The Plastic Resistance of Crystals. *Aust. J. Phys.* **1960**, *13*, 327−346.
(369) Mukhopadhyay, A.; Sheldon, B. W. Deformation and Stress in Electrode Materials for Li-Ion Batteries. *Prog. Mater. Sci.* **2014**, *63*, 58−116.
(370) Swallow, J. G.; Woodford, W. H.; McGrogan, F. P.; Ferralis, N.; Chiang, Y. M.; Van Vliet, K. J. Effect of Electrochemical Charging on Elastoplastic Properties and Fracture Toughness of Li_xCoO_2. *J. Electrochem. Soc.* **2014**, *161*, F3084−F3090.
(371) Cheng, E. J.; Taylor, N. J.; Wolfenstine, J.; Sakamoto, J. Elastic Properties of Lithium Cobalt Oxide ($LiCoO_2$). *J. Asian Ceram. Soc.* **2017**, *5*, 113−117.

DOI: 10.1021/acs.chemrev.9b00268
Chem. Rev. XXXX, XXX, XXX−XXX

(372) Chong, X. Y.; Jiang, Y.; Feng, J. Mechanical Properties, Electronic Structure and Alkali-ion Diffusion of Eldfellite-type $AFe(SO_4)_2$ (A = Li, Na, K) as Potential Cathode Materials Comparing with $LiFePO_4$. *J. Micromech. Mol. Phys.* **2017**, *02*, 1750002.
(373) Mughal, M. Z.; Moscatelli, R.; Amanieu, H. Y.; Sebastiani, M. Effect of Lithiation on Micro-Scale Fracture Toughness of $Li_xMn_2O_4$ Cathode. *Scr. Mater.* **2016**, *116*, 62−66.
(374) Li, W. J.; Hirayama, M.; Suzuki, K.; Kanno, R. Fabrication and All Solid-State Battery Performance of $TiS_2/Li_{10}GeP_2S_{12}$ Composite Electrodes. *Mater. Trans.* **2016**, *57* (4), 549.
(375) Qi, Y.; Guo, H. B.; Hector, L. G.; Timmons, A. Threefold Increase in the Young's Modulus of Graphite Negative Electrode During Lithium Intercalation. *J. Electrochem. Soc.* **2010**, *157*, A558−A566.
(376) Slotwinski, T.; Trivisonno, J. Temperature Dependence of the Elastic Constants of Single Crystal Lithium. *J. Phys. Chem. Solids* **1969**, *30*, 1276−1278.
(377) Porz, L.; Swamy, T.; Sheldon, B. W.; Rettenwander, D.; Froemling, T.; Thaman, H. L.; Berendts, S.; Uecker, R.; Carter, W. C.; Chiang, Y.-M. Mechanism of Lithium Metal Penetration through Inorganic Solid Electrolytes. *Adv. Energy Mater.* **2017**, *7*, 1701003.
(378) Swamy, T.; Park, R.; Sheldon, B. W.; Rettenwander, D.; Porz, L.; Berendts, S.; Uecker, R.; Carter, W. C.; Chiang, Y.-M. Lithium Metal Penetration Induced by Electrodeposition through Solid Electrolytes: Example in Single-Crystal $Li_6La_3ZrTaO_{12}$ Garnet. *J. Electrochem. Soc.* **2018**, *165*, A3648−A3655.
(379) Tian, H.-K.; Xu, B.; Qi, Y. Computational Study of Lithium Nucleation Tendency in $Li_7La_3Zr_2O_{12}$ (LLZO) and Rational Design of Interlayer Materials to Prevent Lithium Dendrites. *J. Power Sources* **2018**, *392*, 79−86.
(380) Monroe, C.; Newman, J. The Impact of Elastic Deformation on Deposition Kinetics at Lithium/Polymer Interfaces. *J. Electrochem. Soc.* **2005**, *152*, A396−A404.
(381) Wolfenstine, J.; Allen, J. L.; Sakamoto, J.; Siegel, D. J.; Choe, H. Mechanical Behavior of Li-Ion-Conducting Crystalline Oxide-Based Solid Electrolytes: A Brief Review. *Ionics* **2018**, *24*, 1271−1276.
(382) Xu, S.; McOwen, D. W.; Wang, C.; Zhang, L.; Luo, W.; Chen, C.; Li, Y.; Gong, Y.; Dai, J.; et al. Three-Dimensional, Solid-State Mixed Electron−Ion Conductive Framework for Lithium Metal Anode. *Nano Lett.* **2018**, *18*, 3926−3933.
(383) Tian, H. K.; Qi, Y. Simulation of the Effect of Contact Area Loss in All-Solid-State Li-Ion Batteries. *J. Electrochem. Soc.* **2017**, *164*, E3512−E3521.
(384) Bucci, G.; Swamy, T.; Chiang, Y. M.; Carter, W. C. Modeling of Internal Mechanical Failure of All-Solid-State Batteries During Electrochemical Cycling, and Implications for Battery Design. *J. Mater. Chem. A* **2017**, *5*, 19422−19430.
(385) Zhang, W. B.; Schroder, D.; Arlt, T.; Manke, I.; Koerver, R.; Pinedo, R.; Weber, D. A.; Sann, J.; Zeier, W. G.; Janek, J. (Electro)Chemical Expansion During Cycling: Monitoring the Pressure Changes in Operating Solid-State Lithium Batteries. *J. Mater. Chem. A* **2017**, *5*, 9929−9936.
(386) Monroe, C.; Newman, J. The Effect of Interfacial Deformation on Electrodeposition Kinetics. *J. Electrochem. Soc.* **2004**, *151*, A880−A886.
(387) Pervez, S. A.; Ganjeh-Anzabi, P.; Farooq, U.; Trifkovic, M.; Roberts, E. P. L.; Thangadurai, V. Fabrication of a Dendrite-Free All Solid-State Li Metal Battery Via Polymer Composite/Garnet/Polymer Composite Layered Electrolyte. *Adv. Mater. Interfaces* **2019**, *6*, 1900186.
(388) Kalnaus, S.; Sabau, A. S.; Tenhaeff, W. E.; Dudney, N. J.; Daniel, C. Design of Composite Polymer Electrolytes for Li Ion Batteries Based on Mechanical Stability Criteria. *J. Power Sources* **2012**, *201*, 280−287.
(389) Kumar, J.; Kichambare, P.; Rai, A. K.; Bhattacharya, R.; Rodrigues, S.; Subramanyam, G. A High Performance Ceramic-Polymer Separator for Lithium Batteries. *J. Power Sources* **2016**, *301*, 194−198.
(390) Shi, J.; Xia, Y.; Han, S.; Fang, L.; Pan, M.; Xu, X.; Liu, Z. Lithium Ion Conductive $Li_{1.5}Al_{0.5}Ge_{1.5}(PO_4)_3$ Based Inorganic-Organic Composite Separator with Enhanced Thermal Stability and Excellent Electrochemical Performances in 5 V Lithium Ion Batteries. *J. Power Sources* **2015**, *273*, 389−395.
(391) Wu, J. Y.; Ling, S. G.; Yang, Q.; Li, H.; Xu, X. X.; Chen, L. Q. Forming Solid Electrolyte Interphase in Situ in an Ionic Conducting $Li_{1.5}Al_{0.5}Ge_{1.5}(PO_4)_3$-Polypropylene (PP) Based Separator for Li-Ion Batteries. *Chin. Phys. B* **2016**, *25*, 078204.
(392) Fu, K.; Gong, Y. H.; Hitz, G. T.; McOwen, D. W.; Li, Y. J.; Xu, S. M.; Wen, Y.; Zhang, L.; Wang, C. W.; Pastel, G.; et al. Three-Dimensional Bilayer Garnet Solid Electrolyte Based High Energy Density Lithium Metal-Sulfur Batteries. *Energy Environ. Sci.* **2017**, *10*, 1568−1575.
(393) Yang, C.; Zhang, L.; Liu, B.; Xu, S.; Hamann, T.; McOwen, D.; Dai, J.; Luo, W.; Gong, Y.; Wachsman, E. D.; et al. Continuous Plating/Stripping Behavior of Solid-State Lithium Metal Anode in a 3d Ion-Conductive Framework. *Proc. Natl. Acad. Sci. U. S. A.* **2018**, *115*, 3770−3775.
(394) Huo, H.; Chen, Y.; Luo, J.; Yang, X.; Guo, X.; Sun, X. Rational Design of Hierarchical "Ceramic-in-Polymer" and "Polymer-in-Ceramic" Electrolytes for Dendrite-Free Solid-State Batteries. *Adv. Energy Mater.* **2019**, *9*, 1804004.
(395) Xu, R.; Yue, J.; Liu, S.; Tu, J.; Han, F.; Liu, P.; Wang, C. Cathode-Supported All-Solid-State Lithium-Sulfur Batteries with High Cell-Level Energy Density. *ACS Energy Lett.* **2019**, *4*, 1073−1079.
(396) Li, Q.; Yi, T.; Wang, X.; Pan, H.; Quan, B.; Liang, T.; Guo, X.; Yu, X.; Wang, H.; Huang, X.; et al. In-Situ Visualization of Lithium Plating in All-Solid-State Lithium-Metal Battery. *Nano Energy* **2019**, *63*, 103895.
(397) Park, K. H.; Bai, Q.; Kim, D. H.; Oh, D. Y.; Zhu, Y. Z.; Mo, Y. F.; Jung, Y. S. Design Strategies, Practical Considerations, and New Solution Processes of Sulfide Solid Electrolytes for All-Solid-State Batteries. *Adv. Energy Mater.* **2018**, *8*, 1800035.
(398) Kim, D. H.; Oh, D. Y.; Park, K. H.; Choi, Y. E.; Nam, Y. J.; Lee, H. A.; Lee, S.-M.; Jung, Y. S. Infiltration of Solution-Processable Solid Electrolytes into Conventional Li-Ion-Battery Electrodes for All-Solid-State Li-Ion Batteries. *Nano Lett.* **2017**, *17*, 3013−3020.
(399) Sakuda, A.; Kuratani, K.; Yamamoto, M.; Takahashi, M.; Takeuchi, T.; Kobayashi, H. All-Solid-State Battery Electrode Sheets Prepared by a Slurry Coating Process. *J. Electrochem. Soc.* **2017**, *164*, A2474−A2478.
(400) Nam, Y. J.; Oh, D. Y.; Jung, S. H.; Jung, Y. S. Toward Practical All-Solid-State Lithium-Ion Batteries with High Energy Density and Safety: Comparative Study for Electrodes Fabricated by Dry- and Slurry-Mixing Processes. *J. Power Sources* **2018**, *375*, 93−101.
(401) Chen, X.; He, W.; Ding, L.-X.; Wang, S.; Wang, H. Enhancing Interfacial Contact in All Solid State Batteries with a Cathode-Supported Solid Electrolyte Membrane Framework. *Energy Environ. Sci.* **2019**, *12*, 938−944.
(402) Li, H. M.; Yin, H. Y.; Wang, K. L.; Cheng, S. J.; Jiang, K.; Sadoway, D. R. Liquid Metal Electrodes for Energy Storage Batteries. *Adv. Energy Mater.* **2016**, *6*, 1600483.
(403) Lu, X. C.; Li, G. S.; Kim, J. Y.; Mei, D. H.; Lemmon, J. P.; Sprenkle, V. L.; Liu, J. Liquid-Metal Electrode to Enable Ultra-Low Temperature Sodium-Beta Alumina Batteries for Renewable Energy Storage. *Nat. Commun.* **2014**, *5*, 4578.
(404) Jin, Y.; Liu, K.; Lang, J. L.; Zhuo, D.; Huang, Z. Y.; Wang, C. A.; Wu, H.; Cui, Y. An Intermediate Temperature Garnet-Type Solid Electrolyte-Based Molten Lithium Battery for Grid Energy Storage. *Nat. Energy* **2018**, *3*, 732−738.
(405) Yu, J. Z.; Hu, Y. S.; Pan, F.; Zhang, Z. Z.; Wang, Q.; Li, H.; Huang, X. J. E.; Chen, L. Q. A Class of Liquid Anode for Rechargeable Batteries with Ultralong Cycle Life. *Nat. Commun.* **2017**, *8*, 14629.
(406) Perea, A.; Dontigny, M.; Zaghib, K. Safety of Solid-State Li Metal Battery: Solid Polymer Versus Liquid Electrolyte. *J. Power Sources* **2017**, *359*, 182−185.

DOI: 10.1021/acs.chemrev.9b00268
Chem. Rev. XXXX, XXX, XXX−XXX

(407) Inoue, T.; Mukai, K. Are All-Solid-State Lithium-Ion Batteries Really Safe?-Verification by Differential Scanning Calorimetry with an All-Inclusive Microcell. *ACS Appl. Mater. Interfaces* **2017**, *9*, 1507−1515.
(408) Liu, K.; Liu, Y.; Lin, D.; Pei, A.; Cui, Y. Materials for Lithium-Ion Battery Safety. *Sci. Adv.* **2018**, *4*, eaas9820.
(409) Feng, X.; Ouyang, M.; Liu, X.; Lu, L.; Xia, Y.; He, X. Thermal Runaway Mechanism of Lithium Ion Battery for Electric Vehicles: A Review. *Energy Storage Mater.* **2018**, *10*, 246−267.
(410) Chen, H. P.; Tao, H. Z.; Wu, Q. D.; Zhao, X. J. Thermal Behavior and Lithium Ion Conductivity of L_2O-Al_2O_3-TiO_2-SiO_2-P_2O_5 Glass-Ceramics. *J. Wuhan Univ. Technol., Mater. Sci. Ed.* **2012**, *27*, 67−72.
(411) Tsukasaki, H.; Otoyama, M.; Mori, Y.; Mori, S.; Morimoto, H.; Hayashi, A.; Tatsumisago, M. Analysis of Structural and Thermal Stability in the Positive Electrode for Sulfide-Based All-Solid-State Lithium Batteries. *J. Power Sources* **2017**, *367*, 42−48.
(412) Singh, V. K.; Shalu; Balo, L.; Gupta, H.; Singh, S. K.; Singh, R. K. Solid Polymer Electrolytes Based on Li^+/Ionic Liquid for Lithium Secondary Batteries. *J. Solid State Electrochem.* **2017**, *21*, 1713−1723.
(413) Katayama, N.; Kawamura, T.; Baba, Y.; Yamaki, J.-i. Thermal Stability of Propylene Carbonate and Ethylene Carbonate-Propylene Carbonate-Based Electrolytes for Use in Li Cells. *J. Power Sources* **2002**, *109*, 321−326.
(414) Sasaki, Y.; Handa, M.; Kurashima, K.; Tonuma, T.; Usami, K. Application of Lithium Organoborate with Salicylic Ligand to Lithium Battery Electrolyte. *J. Electrochem. Soc.* **2001**, *148*, A999−A1003.
(415) Rodrigues, A. M.; Narvaez-Semanate, J. L.; Cabral, A. A.; Rodrigues, A. C. M. Determination of Crystallization Kinetics Parameters of a $Li_{1.5}Al_{0.5}Ge_{1.5}(PO_4)_3$ (LAGP) Glass by Differential Scanning Calorimetry. *Mater. Res.* **2013**, *16*, 811−816.
(416) Narvaez-Semanate, J. L.; Rodrigues, A. C. M. Microstructure and Ionic Conductivity of $Li_{1+x}Al_xTi_{2-x}(PO_4)_3$ Nasicon Glass-Ceramics. *Solid State Ionics* **2010**, *181*, 1197−1204.
(417) Cruz, A. M.; Ferreira, E. B.; Rodrigues, A. C. M. Controlled Crystallization and Ionic Conductivity of a Nanostructured $LiAlGePO_4$ Glass-Ceramic. *J. Non-Cryst. Solids* **2009**, *355*, 2295−2301.
(418) Bron, P.; Johansson, S.; Zick, K.; Schmedt auf der Gunne, J. S.; Dehnen, S.; Roling, B. $Li_{10}SnP_2S_{12}$: An Affordable Lithium Superionic Conductor. *J. Am. Chem. Soc.* **2013**, *135*, 15694−15697.
(419) Brant, J. A.; Massi, D. M.; Holzwarth, N. A. W.; MacNeil, J. H.; Douvalis, A. P.; Bakas, T.; Martin, S. W.; Gross, M. D.; Aitken, J. A. Fast Lithium Ion Conduction in Li_2SnS_3: Synthesis, Physicochemical Characterization, and Electronic Structure. *Chem. Mater.* **2015**, *27*, 189−196.
(420) Zhang, X.; Liu, T.; Zhang, S. F.; Huang, X.; Xu, B. Q.; Lin, Y. H.; Xu, B.; Li, L. L.; Nan, C. W.; Shen, Y. Synergistic Coupling between $Li_{6.75}La_3Zr_{1.75}Ta_{0.25}O_{12}$ and Poly(vinylidene fluoride) Induces High Ionic Conductivity, Mechanical Strength, and Thermal Stability of Solid Composite Electrolytes. *J. Am. Chem. Soc.* **2017**, *139*, 13779−13785.
(421) Nippani, S. K.; Kuchhal, P.; Anand, G.; Kumar Kambila, V. Structural, Thermal and Conductivity Studies of PAN-$LIBF_4$ Polymer Electrolytes. *J. Eng. Sci. Technol.* **2016**, *11*, 1595−1608.
(422) You, D. J.; Yin, Z.; Ahn, Y. K.; Cho, S.; Kim, H.; Shin, D.; Yoo, J.; Kim, Y. S. A High-Performance Polymer Composite Electrolyte Embedded with Ionic Liquid for All Solid Lithium Based Batteries Operating at Ambient Temperature. *J. Ind. Eng. Chem.* **2017**, *52*, 1−6.
(423) Maleki, H.; Deng, G. P.; Anani, A.; Howard, J. Thermal Stability Studies of Li-Ion Cells and Components. *J. Electrochem. Soc.* **1999**, *146*, 3224−3229.
(424) Biensan, P.; Simon, B.; Pérès, J. P.; de Guibert, A.; Broussely, M.; Bodet, J. M.; Perton, F. On Safety of Lithium-Ion Cells. *J. Power Sources* **1999**, *81*−*82*, 906−912.
(425) Yue, J.; Yan, M.; Yin, Y. X.; Guo, Y. G. Progress of the Interface Design in All-Solid-State Li-S Batteries. *Adv. Funct. Mater.* **2018**, *28*, 1707533.
(426) Zhang, Z.; Shao, Y.; Lotsch, B.; Hu, Y.-S.; Li, H.; Janek, J.; Nazar, L. F.; Nan, C.-W.; Maier, J.; Armand, M.; et al. New Horizons for Inorganic Solid State Ion Conductors. *Energy Environ. Sci.* **2018**, *11*, 1945−1976.
(427) Yu, X.; Manthiram, A. Electrode-Electrolyte Interfaces in Lithium-Based Batteries. *Energy Environ. Sci.* **2018**, *11*, 527−543.
(428) Goodenough, J. B.; Singh, P. Review—Solid Electrolytes in Rechargeable Electrochemical Cells. *J. Electrochem. Soc.* **2015**, *162*, A2387−A2392.
(429) Zhang, B.; Tan, R.; Yang, L.; Zheng, J.; Zhang, K.; Mo, S.; Lin, Z.; Pan, F. Mechanisms and Properties of Ion-Transport in Inorganic Solid Electrolytes. *Energy Storage Mater.* **2018**, *10*, 139−159.
(430) Kwon, O.; Hirayama, M.; Suzuki, K.; Kato, Y.; Saito, T.; Yonemura, M.; Kamiyama, T.; Kanno, R. Synthesis, Structure, and Conduction Mechanism of the Lithium Superionic Conductor $Li_{10+\delta}Ge_{1+\delta}P_{2-\delta}S_{12}$. *J. Mater. Chem. A* **2015**, *3*, 438−446.
(431) Arbi, K.; Hoelzel, M.; Kuhn, A.; García-Alvarado, F.; Sanz, J. Structural Factors That Enhance Lithium Mobility in Fast-Ion $Li_{1+x}Ti_{2-x}Al_x(PO_4)_3$ ($0 \leq x \leq 0.4$) Conductors Investigated by Neutron Diffraction in the Temperature Range 100−500 K. *Inorg. Chem.* **2013**, *52*, 9290−9296.
(432) Cheng, L.; Wu, C. H.; Jarry, A.; Chen, W.; Ye, Y.; Zhu, J.; Kostecki, R.; Persson, K.; Guo, J.; Salmeron, M.; et al. Interrelationships among Grain Size, Surface Composition, Air Stability, and Interfacial Resistance of Al-Substituted $Li_7La_3Zr_2O_{12}$ Solid Electrolytes. *ACS Appl. Mater. Interfaces* **2015**, *7*, 17649−17655.
(433) Kitazawa, Y.; Iwata, K.; Kido, R.; Imaizumi, S.; Tsuzuki, S.; Shinoda, W.; Ueno, K.; Mandai, T.; Kokubo, H.; Dokko, K.; et al. Polymer Electrolytes Containing Solvate Ionic Liquids: A New Approach to Achieve High Ionic Conductivity, Thermal Stability, and a Wide Potential Window. *Chem. Mater.* **2018**, *30*, 252−261.
(434) Tu, Z.; Choudhury, S.; Zachman, M. J.; Wei, S.; Zhang, K.; Kourkoutis, L. F.; Archer, L. A. Designing Artificial Solid-Electrolyte Interphases for Single-Ion and High-Efficiency Transport in Batteries. *Joule* **2017**, *1*, 394−406.
(435) Thompson, T.; Yu, S.; Williams, L.; Schmidt, R. D.; Garcia-Mendez, R.; Wolfenstine, J.; Allen, J. L.; Kioupakis, E.; Siegel, D. J.; Sakamoto, J. Electrochemical Window of the Li-Ion Solid Electrolyte $Li_7La_3Zr_2O_{12}$. *ACS Energy Lett.* **2017**, *2*, 462−468.
(436) Thangadurai, V.; Pinzaru, D.; Narayanan, S.; Baral, A. K. Fast Solid-State Li Ion Conducting Garnet-Type Structure Metal Oxides for Energy Storage. *J. Phys. Chem. Lett.* **2015**, *6*, 292−299.
(437) Murugan, R.; Weppner, W.; Schmid-Beurmann, P.; Thangadurai, V. Structure and Lithium Ion Conductivity of Bismuth Containing Lithium Garnets $Li_5La_3Bi_2O_{12}$ and $Li_6SrLa_2Bi_2O_{12}$. *Mater. Sci. Eng., B* **2007**, *143*, 14−20.
(438) Nishimura, S.-i.; Kobayashi, G.; Ohoyama, K.; Kanno, R.; Yashima, M.; Yamada, A. Experimental Visualization of Lithium Diffusion in Li_xFePO_4. *Nat. Mater.* **2008**, *7*, 707.
(439) Dai, J.; Yang, C.; Wang, C.; Pastel, G.; Hu, L. Interface Engineering for Garnet-Based Solid-State Lithium-Metal Batteries: Materials, Structures, and Characterization. *Adv. Mater.* **2018**, *30*, 1802068.
(440) Maier, J. Space Charge Regions in Solid Two-Phase Systems and Their Conduction Contribution I. Conductance Enhancement in the System Ionic Conductor-"Inert" Phase and Application on $AgCl:Al_2O_3$ and $AgCl:SiO_2$. *J. Phys. Chem. Solids* **1985**, *46*, 309−320.
(441) Maier, J. Ionic Conduction in Space Charge Regions. *Prog. Solid State Chem.* **1995**, *23*, 171−263.
(442) Zheng, J.; Tang, M.; Hu, Y.-Y. Lithium Ion Pathway within $Li_7La_3Zr_2O_{12}$-Polyethylene Oxide Composite Electrolytes. *Angew. Chem., Int. Ed.* **2016**, *55*, 12538−12542.
(443) Brazier, A.; Dupont, L.; Dantras-Laffont, L.; Kuwata, N.; Kawamura, J.; Tarascon, J. M. First Cross-Section Observation of an All Solid-State Lithium-Ion "Nanobattery" by Transmission Electron Microscopy. *Chem. Mater.* **2008**, *20*, 2352−2359.
(444) Okumura, T.; Nakatsutsumi, T.; Ina, T.; Orikasa, Y.; Arai, H.; Fukutsuka, T.; Iriyama, Y.; Uruga, T.; Tanida, H.; Uchimoto, Y.; et al. Depth-Resolved X-Ray Absorption Spectroscopic Study on Nanoscale

DOI: 10.1021/acs.chemrev.9b00268
Chem. Rev. XXXX, XXX, XXX−XXX

Observation of the Electrode-Solid Electrolyte Interface for All Solid State Lithium Ion Batteries. *J. Mater. Chem.* **2011**, *21*, 10051−10060.
(445) Louli, A. J.; Li, J.; Trussler, S.; Fell, C. R.; Dahn, J. R. Volume, Pressure and Thickness Evolution of Li-Ion Pouch Cells with Silicon-Composite Negative Electrodes. *J. Electrochem. Soc.* **2017**, *164*, A2689−A2696.
(446) Louli, A. J.; Ellis, L. D.; Dahn, J. R. Operando Pressure Measurements Reveal Solid Electrolyte Interphase Growth to Rank Li-Ion Cell Performance. *Joule* **2019**, *3*, 745−761.
(447) Wang, C.; Gong, Y.; Dai, J.; Zhang, L.; Xie, H.; Pastel, G.; Liu, B.; Wachsman, E.; Wang, H.; Hu, L. In Situ Neutron Depth Profiling of Lithium Metal-Garnet Interfaces for Solid State Batteries. *J. Am. Chem. Soc.* **2017**, *139*, 14257−14264.
(448) Liu, X.; Wang, D.; Liu, G.; Srinivasan, V.; Liu, Z.; Hussain, Z.; Yang, W. Distinct Charge Dynamics in Battery Electrodes Revealed by in Situ and Operando Soft X-Ray Spectroscopy. *Nat. Commun.* **2013**, *4*, 2568.
(449) Yamamoto, K.; Iriyama, Y.; Asaka, T.; Hirayama, T.; Fujita, H.; Nonaka, K.; Miyahara, K.; Sugita, Y.; Ogumi, Z. Direct Observation of Lithium-Ion Movement around an In-situ-Formed-Negative-Electrode/Solid-State-Electrolyte Interface During Initial Charge−Discharge Reaction. *Electrochem. Commun.* **2012**, *20*, 113−116.
(450) Wang, L.; Wu, Z.; Zou, J.; Gao, P.; Niu, X.; Li, H.; Chen, L. Li-Free Cathode Materials for High Energy Density Lithium Batteries. *Joule* **2019**, *3*, 2086.
(451) Liu, L.; Xu, J.; Wang, S.; Wu, F.; Li, H.; Chen, L. Practical Evaluation of Energy Densities for Sulfide Solid-State Batteries. *eTransportation* **2019**, *1*, 100010.
(452) Liang, J.; Li, X.; Zhao, Y.; Goncharova, L. V.; Li, W.; Adair, K. R.; Banis, M. N.; Hu, Y.; Sham, T.-K.; et al. An Air-Stable and Dendrite-Free Li Anode for Highly Stable All-Solid-State Sulfide-Based Li Batteries. *Adv. Energy Mater.* **2019**, *9*, 1902125.
(453) McCloskey, B. D. Attainable Gravimetric and Volumetric Energy Density of Li−S and Li Ion Battery Cells with Solid Separator-Protected Li Metal Anodes. *J. Phys. Chem. Lett.* **2015**, *6*, 4581−4588.

DOI: 10.1021/acs.chemrev.9b00268
Chem. Rev. XXXX, XXX, XXX−XXX